ABSTRACT

Title of dissertation: CAVITY QUANTUM ELECTRODYNAMICS OF NANOSCALE TWO-LEVEL SYSTEMS

Bahman Sarabi, Doctor of Philosophy, 2014

Dissertation directed by: Dr. Kevin D. Osborn
Laboratory for Physical Sciences

Professor Frederick C. Wellstood
Department of Physics

In this dissertation, I introduce a novel method for measuring individual nanoscale two-level systems (TLSs) in amorphous solids based on strong direct coupling between a TLS and a cavity. I describe power- and temperature-dependent analysis of individual TLSs using a theoretical model based on cavity quantum electrodynamics (CQED). This method allows for measuring individual TLSs in different insulators and over a wide range of film thicknesses. For a silicon nitride film at 25 mK and a lumped-element cavity resonance at 6.9 GHz, I find TLSs with coherence times on the order of microseconds which can potentially be used as coherent resources.

Furthermore, I introduce a device which enables spectroscopy of TLSs in insulating films by DC-tuning the TLSs. I present measurement results on 60 TLSs accompanied by theoretical analysis and extraction of distribution statistics of the TLS parameters. I find evidence for at least two TLS dipole sizes.

I also investigate the role of RF-induced DC bias voltage on the growth of titanium nitride films on silicon (100) substrates deposited by DC magnetron reactive sputtering. I present hybrid designs of TiN coplanar resonators which were fabricated with an aluminum transmission line to avoid impedance mismatches due to large kinetic inductance of TiN films. I observe remarkably large kinetic inductance at certain substrate DC bias voltages.

Finally, I describe several trilayer resonators designed to measure TLS ensembles within atomic layer deposition (ALD) grown aluminum oxide. Each resonator is unique in trilayer capacitor perimeter and hence the alumina air-exposed cross section. I compare the measured loss tangents of the resonators and investigate the effect of the capacitor perimeter on TLS defect density at different temperatures.

CAVITY QUANTUM ELECTRODYNAMICS OF NANOSCALE TWO-LEVEL SYSTEMS

by

BAHMAN SARABI

Dissertation submitted to the Faculty of the Graduate School of the
University of Maryland, College Park in partial fulfillment
of the requirements for the degree of
Doctor of Philosophy
2014

Advisory Committee:
Professor Frederick C. Wellstood, Chair/Advisor
Dr. Kevin D. Osborn, Advisor/Principal Investigator
Professor Christopher J. Lobb
Professor Ichiro Takeuchi
Dr. Benjamin S. Palmer

Dedication

To my wonderful parents for their love and support.

Acknowledgments

Foremost, I want to acknowledge my sincere thanks to my two great advisors, Dr. Kevin D. Osborn (Laboratory for Physical Sciences - LPS) and Prof. Frederick C. Wellstood (University of Maryland - UMD).

I owe Kevin the opportunity to work in the Quantum Computing group at LPS, which truly made one of my greatest experiences. Every time I knocked on his door, he gave me invaluable ideas, advice on my research and direction so I and the rest of the group could achieve our goals. Not only it has been an immense pleasure to learn from him as my advisor, but it was extremely enjoyable to work with him in his group.

Fred's insight and his depth of knowledge had an invaluable effect in my work. He spent a lot of time to go through every detail of my results and to give me extraordinary ideas and advice for my experiments and analyses. I can not thank him enough for the time that he spent to help me interpret my results, and for his crucial contribution to my work, both during my first year at UMD, and throughout the rest of my studies at LPS.

I also have to thank Dr. Anna Herr for her advice and support during my first year at UMD. I learned a lot from her expertise in superconducting digital electronics, and I was inspired by her motivation and curiosity in research.

I would also like to thank Prof. Christopher J. Lobb for his continuous support throughout my studies. He shared his ideas and and gave me comments in many discussions and meetings that we had during my studies.

I also have to acknowledge my thanks to Dr. Benjamin S. Palmer for his help and support. I learned a lot of experimental skills from Ben during our discussions on low-temperature measurements and dilution refrigerator setup.

I also want to thank Prof. Ichiro Takeuchi for his time, and for agreeing to serve as Deans representative at my thesis defense.

I also owe my gratitude to the people that I enjoyed working with as a group: Dr. Aruna Ramanayaka, Dr. Moe Khalil, Dr. Micah Stoutimore, Dr. Yaniv Rosen and Dr. Sergiy Gladchenko. I was very lucky to have such knowledgable and friendly colleagues. Our countless discussions and meetings were extremely helpful in choosing the best path towards my objectives. I also want to thank Iftekhar Jaim and Jonathan Aguilar who, despite their relatively short time at LPS, significantly contributed to the titanium nitride project.

I should also thank many great people at LPS who made it the most enjoyable work environment I could ask for: Dr. Anita Roychowdhury, Dr. Vitaley Zaretskey, Dr. Nathan Siwak, Sergey Novikov, Baladitya Suri, Dr. John Bavier, Joyce Coppock, Pavel Nagornykh and Dr. Zaeill Kim. I also want to acknowledge many useful discussions with Kristen Voigt, Rangga Budoyo and Dr. Jared Hertzberg, members of the Joint Quantum Institute (JQI).

I would also like to thank the great collaborators that I had the chance to work with: Prof. Alexander Burin (Tulane University), Dr. Christopher Richardson (LPS), Dr. Evgeniya Lock (Naval Research Laboratory), Prof. Gary Rubloff (University of Maryland) and Alexander Kozen (University of Maryland). I want to send special thanks to Prof. Alexander Burin for his significant contribution in the

theoretical cavity-QED analysis and for sharing his thoughts on many of my results.

I am also grateful to engineers and staff of the clean room at LPS for their continuous support: Scott Horst, Dan Hinkel, Warren Berk, Toby Olver, Steve Brown, Sean Flannery and Curt Walsh. I received much helpful advice from them on the fabrication part of my work. I would also like to thank LPS staff Paul Hannah, Greg Latini and Althia Kirlew for their help during my time at LPS.

There are many friends - more than I can enumerate - to whom I am very grateful. Thank you for making my life and studies a lot more enjoyable during these years.

Finally, I want to acknowledge my deepest thanks to my beloved family, especially my parents Javad Sarabi and Fahimeh Ghoreishi, and my brother Behrooz Sarabi. Without your love and continuous support from the farthest distances, this thesis would have been a faraway dream. Thank you for being a constant source of love, care, strength and patience throughout my life.

I owe my gratitude to so many people and it is impossible to name them all. I apologize to those I have inadvertently left out.

Table of Contents

List of Figures

Chapter 1: Introduction

1.1 Quantum computing

1.1.1 Ideas in classical and quantum superconducting logic

Digital CMOS-based computers use irreversible logic, meaning that energy is dissipated as information is being processed. Thanks to continuous progress in fabrication technology, such computers today can run with more and smaller logic elements at lower drive powers than was possible a decade ago. But there is a limit to which these circuits can be scaled down. At the nanometer scale, statistical fluctuations in the number of carriers and quantum mechanical effects such as tunneling start to influence the circuit behavior. Although CMOS technology has great advantages and is very well established, the apparent physical limitations have motivated the research community to propose new hardware schemes.

The theoretical prediction of tunneling supercurrents in superconductor-insulator-superconductor (SIS) junctions, known as the Josephson effect [1], and the subsequent verification [2,3], marked the advent of new technologies with the potential to improve computational capabilities. Among these, I should emphasize rapid single flux quantum (RSFQ) logic, which was developed in early 1990's [4]. RSFQ circuits

have been operated at clock frequencies of 30-40 GHz, and have the potential to operate at hundreds of GHz [5]. An RSFQ-based circuit can consume approximately 5 orders of magnitude less power than a typical CMOS-based circuit (excluding the cooling power) to do the same operations. This is mostly due to propagation of the signals in non-dissipative (superconducting) lines and the relatively small power requirement for switching Josephson junctions (JJs), which are the active elements in RSFQ circuits. RSFQ is a fairly well-developed scheme allowing to construct a wide variety of circuits. However, for sizable RSFQ circuits, signal timing is a difficult problem at high clock frequencies [6]. In order to compensate for jitter and clock skew in RSFQ circuits, in 2009 I designed and successfully measured a FIFO register using this technology, in collaboration with Hypres Inc. [7, 8].

Although RSFQ remains an excellent candidate for some applications (*e.g.* digital signal processing), complications arise when the circuits are scaled up. Large number of resistors for current biasing the JJs result in a significant dc parasitic heat load which was not always included in comparisons between RSFQ and CMOS. This problem can be solved by removing the bias resistors and inductively coupling the bias lines to an AC transmission line. This is the basis for reciprocal quantum logic (RQL) which was developed in 2011 by Q. Herr *et al.* [9]. Also, by modifying gate biasing using junction-based current distribution techniques, ERSFQ/eSFQ logics have been developed which, in a sense, update RSFQ logic by removing the major component of the resistive energy loss [10].

I note that all of the above mentioned technologies (CMOS, RSFQ, RQL, ERSFQ and eSFQ) are examples of binary (classical) computing, despite the fact

that the latter two take advantage of quantum phenomenon of supercurrent (Josephson) tunneling. Furthermore, the energy consumption for a single computational step is a few orders of magnitude larger than the Landauer limit as they operate irreversibly. Basically, irreversible computing results in an unavoidable (and relatively large) minimum for power dissipation which includes switching events. These switchings which are included in the design, can act as a noise source causing computational errors since there is some random aspect of the switching which is generally damped [11]. Some very interesting studies have been performed on binary reversible gates [12–14], but even these gates will not perform quantum information processing by definition because of the necessarily binary states of their bits.

Quantum information theory emerged in the 1970's [15] and the idea of a quantum computer was suggested in the early 1980's [16, 17]. Quantum computers potentially have the ability to perform certain tasks exponentially faster than classical computers, making them a hot topic of research. A quantum computer is distinguished by two fundamental properties: it contains reversible gates *and* quantum coherent states. This follows because quantum computers would apply unitary operations on entangled quantum states of their fundamental building blocks - the qubits [18].

A qubit is a quantum two-level system which can be in state $|0\rangle$ or $|1\rangle$ (like a classical bit), or a superposition of $|0\rangle$ and $|1\rangle$ (in contrast to a classical bit). A state of a single qubit can be mathematically represented by a vector $|\psi\rangle$ in a

two-dimensional Hilbert space, with basis vectors $|0\rangle$ and $|1\rangle$, namely,

$$|\psi\rangle = \alpha\,|0\rangle + \beta\,|1\rangle\,, \tag{1.1}$$

where α and β are, in general, complex numbers and $|\alpha|^2 + |\beta|^2 = 1$. A qubit state can always be rewritten as

$$|\psi\rangle = e^{i\gamma}\left(\cos\frac{\theta}{2}\,|0\rangle + e^{i\phi}\sin\frac{\theta}{2}\,|1\rangle\right), \tag{1.2}$$

where θ, ϕ and γ are (real) angles determining the state $|\psi\rangle$. Since the factor of $e^{i\gamma}$ has no observable effect, Eq. 1.2 can be simplified to

$$|\psi\rangle = \cos\frac{\theta}{2}\,|0\rangle + e^{i\phi}\sin\frac{\theta}{2}\,|1\rangle\,. \tag{1.3}$$

With this choice, the state $|\psi\rangle$ can be represented as a point on the surface of the Bloch sphere, as shown in Fig. 1.1. In particular, there is a one-to-one mapping between possible states $|\psi\rangle$ and the angles θ and ϕ, or the points on the surface of the sphere.

Since there are infinitely many points on the surface of a sphere, in theory infinite information can be stored in a qubit. However, according to a fundamental postulate of quantum mechanics, the *measured* state of a qubit along the z axis of the Bloch sphere can can only be either $|0\rangle$ or $|1\rangle$, meaning that only one bit of information can be extracted by measurement of the qubit state. Although not measurable in one measurement on a single qubit, this *hidden* information does exist, and in a real sense nature "knows" the continuous variables (*e.g.* θ and ϕ) that describe the qubit state. Furthermore, the amount of information that can be stored in multiple qubits grows superexponentially with the number of qubits, *i.e.*

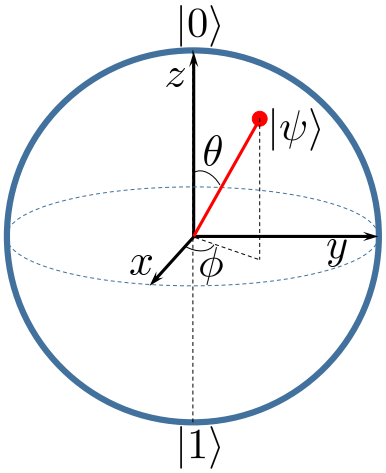

Figure 1.1: Bloch sphere representation of the qubit state.

the effective number of classical bits grows exponentially with the number of qubits. This is a result of quantum entanglement of qubits - a unique capability of quantum systems to exist in entangled states.

In principle, any quantum system with two isolated states can potentially be operated as a qubit. A few examples of such systems are: (i) an electronic spin [19] or nuclear spin [20] where eigenstates correspond to spin-up and spin-down, (ii) photon polarization [21] where the vertical- and horizontal polarizations form the eigenstates and finally (iii) superconducting qubits [22–24] where the eigenvectors are represented by the charge, current or energy states depending on the qubit type.

1.1.2 Requirements and criteria

A natural question is, aside from a collection of two-level quantum systems, what else would be needed to build a quantum computer? Five requirements for im-

plementing quantum computation have been described by DiVincenzo [25–27]. DiVincenzo also gave two additional requirements for quantum communication, which are not discussed here. According to DiVincenzo, the conditions to be fulfilled in order for quantum computation to become possible are:

(a) A scalable physical system containing a collection of well characterized qubits. Characterization of the qubit means that the internal and external properties of the qubit are well-determined. These properties include the internal Hamiltonian, interaction parameters with other qubits and coupling conditions to external fields for manipulating the qubit.

(b) The ability to initialize the state of the qubits to a known well-defined state, such as $|000...\rangle$. This is equivalent to initialization of registers, CPUs and other building blocks of a conventional computer.

(c) Sufficiently long coherence times of the qubits. I highlight this requirement as it is the most relevant to this thesis and is considered to be a particularly challenging requirement for superconducting qubits [28]. A long coherence time is crucial for quantum computing as computation can only take place while all the qubits are in a coherent state. As DiVincenzo states, decoherence is "the principal mechanism for the emergence of classical behavior" [29], and fast decoherence means only classical operations can be performed. We will see in section 1.3 that the basic source of decoherence is the qubit's coupling to the environment. Ideally, a qubit would only be coupled to other qubits and manipulation/readout circuitry while being isolated from the rest of the

universe.

(d) Accurate operation of a complete set of quantum gates. Since quantum algorithms consist of sequences of unitary transformations, for universal computation it must be possible to apply a set of gate operations to reach any point in the multi-qubit Hilbert space, or at least get arbitrarily close to any point.

(e) The ability to perform "strong" quantum measurements. Once a computation is completed by the system, the results must be measurable with high accuracy (in quantum computing language: high fidelity). Also, ideally, reading out the state of each qubit should not disturb the state of the rest of the system.

1.1.3 Quantum algorithms

The first efficiency comparison between quantum algorithms versus their classical counterpart dates back to 1985, when Deutsch [30] demonstrated that to solve the "black-box problem" on a quantum computer, only one query is needed, whereas classical algorithms require two queries. This idea was later developed into the Deutsch-Jozsa algorithm [31]. Simon's algorithm [32] for solving the black-box equation was shown to be exponentially faster than a classical algorithm, and became a motivation for Shor's algorithm [33]. Shor's algorithm calculates the prime factors of an integer in polynomial time, making it exponentially faster than the fastest known classical algorithm. This quantum speedup is a result of using a unitary algebraic operation called the quantum fourier transform (QFT) [34]. Other operations have been used to developed a number of different quantum algorithms, such as

algorithms based on quantum walks [35] and quantum amplitude amplification [36]. Detailed description of quantum algorithms is beyond the scope of this thesis, but can be found in the above citations.

1.2 Cavity quantum electrodynamics

The theory of quantum electrodynamics (QED) involves the combination of special relativity and quantum mechanics. Many interesting effects occur. For example, it was predicted in 1946 that the spontaneous emission probability (and hence the emission rate Γ_0) of an atom changes when it is placed in an electromagnetic cavity that is resonant with the atomic transition [37]. In such a system, a very long atomic relaxation time will be divided by a factor of

$$\nu = \frac{3Q\lambda^3}{4\pi^2 V}, \tag{1.4}$$

where Q is the cavity's quality factor, λ is the free-space wavelength of the emitted light and V is the cavity volume. At optical frequencies, Fabry-Pérot cavities typically have $V \gg \lambda^3$ and observation of such effects are challenging even with high-Q cavities. At microwave RF frequencies, cavities with $V \sim \lambda^3$ are easily realized, however, the atomic transition rate Γ_0 is usually very small in this frequency range, making it difficult to detect changes in Γ_0. Given the physical constraints it is perhaps not surprising that the experimental verification of this effect did not happen until 1983, when an enhanced atomic spontaneous emission was observed from Rydberg states of Na atoms excited in a niobium superconducting cavity resonant at 340 GHz [38]. When an atom is in a Rydberg state, the outermost electron

is bound very weakly. Therefore, transitions can happen between closely-spaced energy states resulting in emission of a range of relatively long wavelengths, from less than a millimeter up to a few centimeters [39].

Understanding the dynamics of a two-level atom in a small volume (cavity) that confines the electric field requires a fully quantum mechanical treatment of the light-matter interaction. The atomic dynamics is affected by the number of photons in the cavity (even at *zero* photons) and is the subject of the field of cavity quantum electrodynamics (CQED). Aside from many interesting physical effects that occur in CQED, it plays an important role in superconducting qubit readout and analysis. Also, as I discuss in full detail in Chapter 5, measurement of CQED effects can be used to characterize a (nanoscale) atomic tunneling two-level system. For the rest of this section, I briefly review field quantization and the Jaynes-Cummings model for the light-matter interaction. For this review I found Refs. [40–49] to be extremely helpful for understanding CQED analysis.

1.2.1 Quantization of the electromagnetic field

To investigate the dynamics of a two-level atom coupled to a cavity, I begin with Maxwell's equations and show how the electromagnetic field in a cavity is quantized.

In the absence of charge or current sources, Maxwell's equations simplify to

$$\nabla \times \mathbf{E} = -\frac{1}{c}\frac{\partial \mathbf{B}}{\partial t}, \tag{1.5a}$$

$$\nabla \times \mathbf{B} = \frac{1}{c}\frac{\partial \mathbf{E}}{\partial t}, \tag{1.5b}$$

$$\nabla \cdot \mathbf{B} = 0, \tag{1.5c}$$

$$\nabla \cdot \mathbf{E} = 0, \tag{1.5d}$$

in CGS units. The electric field $\mathbf{E}$ and magnetic field $\mathbf{B}$ can be written in terms of scalar and vector potentials Φ and $\mathbf{A}$, respectively, *i.e.*

$$\mathbf{E} = -\nabla\Phi - \frac{1}{c}\frac{\partial \mathbf{A}}{\partial t}, \tag{1.6a}$$

$$\mathbf{B} = \nabla \times \mathbf{A}. \tag{1.6b}$$

From the Lagrangian density of a free electromagnetic field,

$$\mathbb{L}_{em} = \frac{1}{8\pi}\left[\mathbf{E}^2 - \mathbf{B}^2\right], \tag{1.7}$$

one can show the canonical momenta p_i for the coordinates $q = (\Phi, A_x, A_y, A_z)$ are

$$p_i = \frac{\partial \mathbb{L}_{em}}{\partial \dot{A}_i} = \frac{1}{4\pi c}\left(\frac{\partial \Phi}{\partial x_i} + \frac{1}{c}\frac{\partial A_i}{\partial t}\right) = -\frac{1}{4\pi c}E_i, \quad i = 1, 2, 3. \tag{1.8}$$

Note that the Lagrangian density is independent of $\dot{\Phi}$, eliminating one of the four momentum coordinates. The Hamiltonian density $\mathbb{H}_{em} = p_i\dot{q}^i - \mathbb{L}$ becomes

$$\mathbb{H}_{em} = \mathbf{p} \cdot \frac{\partial \mathbf{A}}{\partial t} - \mathbb{L}_{em} = 2\pi c^2\mathbf{p}^2 + \frac{1}{8\pi}\left(\nabla \times \mathbf{A}\right)^2 - c\mathbf{p} \cdot \nabla\Phi. \tag{1.9}$$

As a result of Eq. 1.5d, we get

$$\int d^3r\left[\mathbf{p}.\nabla\Phi\right] = -\frac{1}{4\pi c}\int d^3r\left[\mathbf{E} \cdot \nabla\Phi\right] = 0. \tag{1.10}$$

Therefore, the Hamiltonian is

$$\mathcal{H}_{em} = \int d^3r\left[\frac{1}{8\pi}\left(\mathbf{E}^2 + \mathbf{B}^2\right)\right] = \int d^3r\left[2\pi c^2\mathbf{p}^2 + \frac{1}{8\pi}\left(\nabla \times \mathbf{A}\right)^2\right]. \tag{1.11}$$

From

$$\dot{q}_i = \frac{\delta \mathbb{H}_{em}}{\delta p_i}, \quad \dot{p}_i = -\frac{\delta \mathbb{H}_{em}}{\delta q_i}, \tag{1.12}$$

for each coordinate we obtain

$$\frac{\partial A_i}{\partial t} = 4\pi c^2 p_i, \quad \frac{\partial p_i}{\partial t} = \frac{1}{4\pi}\nabla^2 A_i, \tag{1.13}$$

which results in the wave equation

$$\nabla^2 \mathbf{A} - \frac{1}{c^2}\frac{\partial^2 \mathbf{A}}{\partial t^2} = 0. \tag{1.14}$$

Equation 1.14 has planar wave solutions of the form $e^{i\mathbf{k}\cdot\mathbf{r}-\omega_k t}$ with angular frequency $\omega_{\mathbf{k}}$ and wave vector $\mathbf{k}$ and a linear dispersion relation $\omega_{\mathbf{k}} = c|\mathbf{k}|$. Assuming periodic boundary conditions for the total field in volume V, we can Fourier-expand the modes as

$$\mathbf{A}(\mathbf{r}, t) = \frac{1}{\sqrt{V}} \sum_{\mathbf{k}} \mathbf{A}_{\mathbf{k}}(t)\, e^{i\mathbf{k}\cdot\mathbf{r}} \tag{1.15}$$

with the normalization condition

$$\int d^3\mathbf{r} \left[e^{i\mathbf{k}\cdot\mathbf{r}} e^{-i\mathbf{k}'\cdot\mathbf{r}} \right] = V\delta_{\mathbf{k}\mathbf{k}'}. \tag{1.16}$$

Assuming the gauge $\nabla \cdot \mathbf{A} = 0$, we get $\mathbf{k} \cdot \mathbf{A}_{\mathbf{k}} = 0$ which gives two transverse polarization directions identified by transverse unit vectors $\mathbf{e}_{\mathbf{k}\alpha}$, where $\alpha = 1, 2$. Therefore,

$$\mathbf{A}_{\mathbf{k}} = \sum_{\alpha=1}^{2} \mathbf{e}_{\mathbf{k}\alpha} A_{\mathbf{k}\alpha}. \tag{1.17}$$

Also from the wave equation, the time dependence of each mode (and also each polarization) is an oscillatory one,

$$\mathbf{A}_{\mathbf{k}}(t) = \mathbf{A}_{\mathbf{k}} e^{-i\omega_{\mathbf{k}} t}. \tag{1.18}$$

In order to have a real field rather than a complex one, Eq. 1.15 can be equivalently written in the form

$$\mathbf{A}(\mathbf{r},t)=\frac{1}{2\sqrt{V}}\sum_{\mathbf{k}}\left[\mathbf{A}_{\mathbf{k}}(t)\,e^{i\mathbf{k}\cdot\mathbf{r}}+\mathbf{A}_{\mathbf{k}}^{*}(t)\,e^{-i\mathbf{k}\cdot\mathbf{r}}\right]. \tag{1.19}$$

From Eq. 1.19 the fields can now be simply obtained as

$$\mathbf{E}(\mathbf{r},t)=\frac{i}{2c\sqrt{V}}\sum_{\mathbf{k}}\omega_{\mathbf{k}}\left[\mathbf{A}_{\mathbf{k}}(t)\,e^{i\mathbf{k}\cdot\mathbf{r}}-\mathbf{A}_{\mathbf{k}}^{*}(t)\,e^{-i\mathbf{k}\cdot\mathbf{r}}\right], \tag{1.20a}$$

$$\mathbf{B}(\mathbf{r},t)=\frac{i}{2\sqrt{V}}\sum_{\mathbf{k}}\mathbf{k}\times\left[\mathbf{A}_{\mathbf{k}}(t)\,e^{i\mathbf{k}\cdot\mathbf{r}}-\mathbf{A}_{\mathbf{k}}^{*}(t)\,e^{-i\mathbf{k}\cdot\mathbf{r}}\right]. \tag{1.20b}$$

According to Eq. 1.11 and using $\mathbf{k}^2=\omega_{\mathbf{k}}^2/c^2$, the total energy of the field is then

$$\mathcal{H}_{em}=\frac{1}{8\pi}\int d^3r\,(\mathbf{E}\cdot\mathbf{E}^{*}+\mathbf{B}\cdot\mathbf{B}^{*})=\frac{1}{8\pi}\sum_{\mathbf{k}}k^2|\mathbf{A}_{\mathbf{k}}|^2=\frac{1}{8\pi}\sum_{\mathbf{k}\alpha}k^2|A_{\mathbf{k}\alpha}|^2. \tag{1.21}$$

In order to quantize the modes, we note that each mode is analogous to a harmonic oscillator and introduce real canonical variables $\mathbf{Q}_{\mathbf{k}}(t)$ and $\mathbf{P}_{\mathbf{k}}(t)$

$$\mathbf{Q}_{\mathbf{k}}(t)=\frac{1}{2c\sqrt{4\pi}}\left[\mathbf{A}_{\mathbf{k}}(t)+\mathbf{A}_{\mathbf{k}}^{*}(t)\right], \tag{1.22a}$$

$$\mathbf{P}_{\mathbf{k}}(t)=\frac{-ik}{2\sqrt{4\pi}}\left[\mathbf{A}_{\mathbf{k}}(t)-\mathbf{A}_{\mathbf{k}}^{*}(t)\right], \tag{1.22b}$$

so that

$$\mathbf{A}_{\mathbf{k}}(t)=2c\sqrt{\pi}\left[\mathbf{Q}_{\mathbf{k}}(t)+\frac{i}{\omega_k}\mathbf{P}_{\mathbf{k}}(t)\right] \tag{1.23}$$

and

$$\mathcal{H}_{em}=\frac{1}{2}\sum_{\mathbf{k}\alpha}\left(P_{\mathbf{k}\alpha}^2+\omega_{\mathbf{k}}^2Q_{\mathbf{k}\alpha}^2\right). \tag{1.24}$$

The standard quantization procedure includes the commutation relations

$$[P_{\mathbf{k}\alpha},P_{\mathbf{k}'\alpha'}]=0,\quad [Q_{\mathbf{k}\alpha},Q_{\mathbf{k}'\alpha'}]=0,\quad [Q_{\mathbf{k}\alpha},P_{\mathbf{k}'\alpha'}]=i\hbar\delta_{\mathbf{k}\mathbf{k}'}\delta_{\alpha\alpha'}. \tag{1.25}$$

It is also useful to identify $a_{\mathbf{k}\alpha}$ and $a^*_{\mathbf{k}\alpha}$

$$a_{\mathbf{k}\alpha} = \frac{\omega_{\mathbf{k}} Q_{\mathbf{k}\alpha} + iP_{\mathbf{k}\alpha}}{\sqrt{2\hbar\omega_{\mathbf{k}}}}, \tag{1.26a}$$

$$a^*_{\mathbf{k}\alpha} = \frac{\omega_{\mathbf{k}} Q_{\mathbf{k}\alpha} - iP_{\mathbf{k}\alpha}}{\sqrt{2\hbar\omega_{\mathbf{k}}}}. \tag{1.26b}$$

Obviously,

$$Q_{\mathbf{k}\alpha} = \sqrt{\frac{\hbar}{2\omega_{\mathbf{k}}}} \left(a_{\mathbf{k}\alpha} + a^*_{\mathbf{k}\alpha}\right), \tag{1.27a}$$

$$P_{\mathbf{k}\alpha} = -i\sqrt{\frac{\hbar\omega_{\mathbf{k}}}{2}} \left(a_{\mathbf{k}\alpha} - a^*_{\mathbf{k}\alpha}\right), \tag{1.27b}$$

which we will refer to later.

We now replace $a_{\mathbf{k}\alpha}$ and $a^*_{\mathbf{k}\alpha}$ with the annihilation and creation operators $\hat{a}_{\mathbf{k}\alpha}$ and $\hat{a}^\dagger_{\mathbf{k}\alpha}$

$$a_{\mathbf{k}\alpha} \to \hat{a}_{\mathbf{k}\alpha}, \tag{1.28a}$$

$$a^*_{\mathbf{k}\alpha} \to \hat{a}^\dagger_{\mathbf{k}\alpha}, \tag{1.28b}$$

which satisfy the commutation relations

$$[\hat{a}_{\mathbf{k}\alpha}, \hat{a}_{\mathbf{k}'\alpha'}] = 0, \quad [\hat{a}^\dagger_{\mathbf{k}\alpha}, \hat{a}^\dagger_{\mathbf{k}'\alpha'}] = 0, \quad [\hat{a}_{\mathbf{k}\alpha}, \hat{a}^\dagger_{\mathbf{k}'\alpha'}] = \delta_{\mathbf{k}\mathbf{k}'}\delta_{\alpha\alpha'}. \tag{1.29}$$

The operator $\hat{n}_{\mathbf{k}\alpha} = \hat{a}^\dagger_{\mathbf{k}\alpha}\hat{a}_{\mathbf{k}\alpha}$ is the number operator and counts the number of excitations (quanta) in mode $\mathbf{k}, \alpha$. The total energy of the electromagnetic field becomes

$$\hat{\mathcal{H}}_{em} = \sum_{\mathbf{k}\alpha} \hbar\omega_{\mathbf{k}} \left(\hat{a}^\dagger_{\mathbf{k}\alpha}\hat{a}_{\mathbf{k}\alpha} + \frac{1}{2}\right) = \sum_{\mathbf{k}\alpha} \hbar\omega_{\mathbf{k}} \left(\hat{n}_{\mathbf{k}\alpha} + \frac{1}{2}\right). \tag{1.30}$$

From Eq. 1.27a, 1.27b and 1.19 and including the oscillatory time dependence, we can write the vector potential operator as

$$\hat{\mathbf{A}}\left(\mathbf{r}, t\right) = \sqrt{\frac{2\pi\hbar c^2}{V}} \sum_{\mathbf{k}\alpha} \frac{1}{\sqrt{\omega_{\mathbf{k}}}} \left[\hat{a}_{\mathbf{k}\alpha}\mathbf{e}_{\mathbf{k}\alpha} e^{i(\mathbf{k}\cdot\mathbf{r} - \omega_{\mathbf{k}}t)} + \hat{a}^\dagger_{\mathbf{k}\alpha}\mathbf{e}_{\mathbf{k}\alpha} e^{-i(\mathbf{k}\cdot\mathbf{r} - \omega_{\mathbf{k}}t)}\right]. \tag{1.31}$$

The electric field and magnetic field operators are then

$$\hat{\mathbf{E}}(\mathbf{r},t) = i\sqrt{\frac{2\pi\hbar}{V}}\sum_{\mathbf{k}\alpha}\sqrt{\omega_{\mathbf{k}}}\left[\hat{a}_{\mathbf{k}\alpha}\mathbf{e}_{\mathbf{k}\alpha}e^{i(\mathbf{k}\cdot\mathbf{r}-\omega_{\mathbf{k}}t)} - \hat{a}^{\dagger}_{\mathbf{k}\alpha}\mathbf{e}_{\mathbf{k}\alpha}e^{-i(\mathbf{k}\cdot\mathbf{r}-\omega_{\mathbf{k}}t)}\right], \tag{1.32a}$$

$$\hat{\mathbf{B}}(\mathbf{r},t) = i\sqrt{\frac{2\pi\hbar c^2}{V}}\sum_{\mathbf{k}\alpha}\frac{\mathbf{k}\times\mathbf{e}_{\mathbf{k}\alpha}}{\sqrt{\omega_{\mathbf{k}}}}\left[\hat{a}_{\mathbf{k}\alpha}e^{i(\mathbf{k}\cdot\mathbf{r}-\omega_{\mathbf{k}}t)} - \hat{a}^{\dagger}_{\mathbf{k}\alpha}e^{-i(\mathbf{k}\cdot\mathbf{r}-\omega_{\mathbf{k}}t)}\right]. \tag{1.32b}$$

For a single-mode field with one polarization direction, Eq. 1.30 simplifies to

$$\hat{\mathcal{H}}_{em} = \hbar\omega\left(\hat{a}^{\dagger}\hat{a} + \frac{1}{2}\right). \tag{1.33}$$

Analogous to a harmonic oscillator, photon number states $|n\rangle$ become eigenstates of the Hamiltonian and

$$\hat{\mathcal{H}}_{em}|n\rangle = \hbar\omega\left(n + \frac{1}{2}\right)|n\rangle. \tag{1.34}$$

The operators $\hat{a}$ and $\hat{a}^{\dagger}$ cause destruction or addition of a photon to the field mode, as described by

$$\hat{a}|n\rangle = \sqrt{n}\,|n-1\rangle, \tag{1.35a}$$

and

$$\hat{a}^{\dagger}|n\rangle = \sqrt{n+1}\,|n+1\rangle. \tag{1.35b}$$

1.2.2 Jaynes-Cummings model

To understand the interaction of an atom with an electromagnetic field, I first consider an isolated two-level atom with no fields present. This situation is exactly analogous to a spin-$\frac{1}{2}$ system in an applied static field. The two atomic energy eigenstates can be written as

$$|\mathrm{e}\rangle = \begin{pmatrix} 1 \\ \\ 0 \end{pmatrix}, \quad |\mathrm{g}\rangle = \begin{pmatrix} 0 \\ \\ 1 \end{pmatrix}. \tag{1.36}$$

The Hamiltonian is the sum over all accessible energies, *i.e.*

$$\begin{aligned}\hat{\mathcal{H}}_{atom} &= E_{\mathrm{e}} \left|\mathrm{e}\right\rangle \left\langle \mathrm{e}\right| + E_{\mathrm{g}} \left|\mathrm{g}\right\rangle \left\langle \mathrm{g}\right| \\ &= \begin{pmatrix} E_{\mathrm{e}} & 0 \\ 0 & E_{\mathrm{g}} \end{pmatrix} = \frac{1}{2} \begin{pmatrix} E_{\mathrm{e}} + E_{\mathrm{g}} & 0 \\ 0 & E_{\mathrm{e}} + E_{\mathrm{g}} \end{pmatrix} + \frac{1}{2} \begin{pmatrix} E_{\mathrm{e}} - E_{\mathrm{g}} & 0 \\ 0 & E_{\mathrm{g}} - E_{\mathrm{e}} \end{pmatrix} \\ &= \frac{1}{2} \left(E_{\mathrm{e}} + E_{\mathrm{g}}\right) \hat{\mathbf{I}} + \frac{1}{2} \left(E_{\mathrm{e}} - E_{\mathrm{g}}\right) \hat{\sigma}_z,\end{aligned} \tag{1.37}$$

where $\hat{\mathbf{I}}$ is the identity operator and $\hat{\sigma}_z$ is the Pauli z-operator. By defining $E_{\mathrm{e}} - E_{\mathrm{g}} \equiv \hbar\omega_0$ and setting $(E_{\mathrm{e}} + E_{\mathrm{g}})/2 = 0$, we can write

$$\hat{\mathcal{H}}_{atom} = \frac{1}{2} \hbar\omega_0 \hat{\sigma}_z. \tag{1.38}$$

Typically we can assume that the electric field is uniform across an atom, as the atomic dipole length is much smaller than the wavelengths of interest. This allows us to use the dipole approximation to describe the interaction between the atom and the electric field ($\hat{\mathbf{E}}$) and write the coupling (interaction) Hamiltonian as

$$\hat{\mathcal{H}}_{int} = -\hat{\mathbf{p}} \cdot \hat{\mathbf{E}}, \tag{1.39}$$

where the electric dipole operator $\hat{\mathbf{p}}$ (not to be confused with the momentum) is responsible for atomic transitions. The diagonal dipole matrix elements vanish as a result of parity, *i.e.*

$$\left\langle \mathrm{e}\right| \hat{p} \left|\mathrm{e}\right\rangle = \left\langle \mathrm{g}\right| \hat{p} \left|\mathrm{g}\right\rangle = 0, \tag{1.40}$$

and $\hat{\mathbf{p}}$, which is a real vector, can be written as

$$\hat{\mathbf{p}} = \mathbf{p}^* \hat{\sigma}_+ + \mathbf{p} \hat{\sigma}_- = \mathbf{p} \left(\hat{\sigma}_+ + \hat{\sigma}_-\right), \tag{1.41}$$

where $\hat{\sigma}_+$ and $\hat{\sigma}_-$ are the raising and lowering operators and

$$\hat{\sigma}_+ = \begin{pmatrix} 0 & 1 \\ \\ 0 & 0 \end{pmatrix} = |\mathrm{e}\rangle \langle \mathrm{g}|, \quad \hat{\sigma}_+ |\mathrm{g}\rangle = |\mathrm{e}\rangle, \quad \hat{\sigma}_+ |\mathrm{e}\rangle = 0, \tag{1.42a}$$

$$\hat{\sigma}_- = \begin{pmatrix} 0 & 0 \\ \\ 1 & 0 \end{pmatrix} = |\mathrm{g}\rangle \langle \mathrm{e}|, \quad \hat{\sigma}_- |\mathrm{e}\rangle = |\mathrm{g}\rangle, \quad \hat{\sigma}_- |\mathrm{g}\rangle = 0. \tag{1.42b}$$

From Eq. 1.32a, a single-mode electric field polarized in direction $\mathbf{u}$ can be described by

$$\hat{\mathbf{E}} = i\mathbf{u}(\mathbf{r}) \sqrt{\frac{2\pi\hbar\omega}{V}} \left(\hat{a} - \hat{a}^\dagger\right). \tag{1.43}$$

We can now rewrite Eq. 1.39 as

$$\begin{aligned} \hat{\mathcal{H}}_{int} &= -\mathbf{p}(\hat{\sigma}_+ + \hat{\sigma}_-) \cdot i\mathbf{u}(\mathbf{r}) \sqrt{\frac{2\pi\hbar\omega}{V}} (\hat{a} - \hat{a}^\dagger) \\ &= -i\hbar\mathbf{p} \cdot \mathbf{u}(\mathbf{r}) \sqrt{\frac{2\pi\hbar\omega}{V}} (\hat{\sigma}_+ + \hat{\sigma}_-)(\hat{a} - \hat{a}^\dagger). \end{aligned} \tag{1.44}$$

By defining

$$g = \mathbf{p} \cdot \mathbf{u}(\mathbf{r}) \sqrt{\frac{2\pi\hbar\omega}{V}} \tag{1.45}$$

as a measure of the atom-field coupling strength (see Fig. 1.2), the interaction Hamiltonian becomes

$$\hat{\mathcal{H}}_{int} = -i\hbar g(\hat{\sigma}_+ + \hat{\sigma}_-)(\hat{a} - \hat{a}^\dagger) = -i\hbar g(\hat{\sigma}_+\hat{a} + \hat{\sigma}_-\hat{a} + \hat{\sigma}_+\hat{a}^\dagger + \hat{\sigma}_-\hat{a}^\dagger). \tag{1.46}$$

In the interaction picture, the operators gain time dependence such that

$$\hat{a}^\dagger(t) = \hat{a}^\dagger e^{i\omega t}, \quad \hat{a}(t) = \hat{a}e^{-i\omega t}, \quad \hat{\sigma}_+(t) = \hat{\sigma}_+ e^{i\omega_0 t}, \quad \hat{\sigma}_-(t) = \hat{\sigma}_- e^{-i\omega_0 t}, \tag{1.47}$$

and

$$\hat{\mathcal{H}}_{int} = -i\hbar g \left(\hat{\sigma}_+\hat{a}e^{-i(\omega-\omega_0)t} + \hat{\sigma}_-\hat{a}e^{-i(\omega+\omega_0)t} + \hat{\sigma}_+\hat{a}^\dagger e^{i(\omega+\omega_0)t} + \hat{\sigma}_-\hat{a}^\dagger e^{i(\omega-\omega_0)t}\right). \tag{1.48}$$

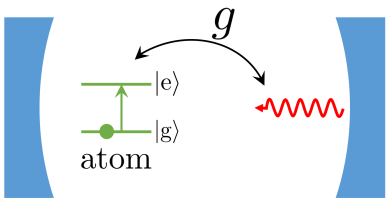

Figure 1.2: Cavity field interacting with a two-level atom. The atom-field coupling strength is determined by g.

Near resonance ($\omega \simeq \omega_0$), the $e^{\pm i(\omega-\omega_0)t}$ terms in Eq. 1.48 vary slowly, thus allowing these terms to accumulate effects from the atom-cavity interaction. On the other hand, the effects of the rapidly varying terms $e^{\pm i(\omega+\omega_0)t}$ tend to cancel out since they are far from resonance. By using this rotating wave approximation (RWA), the interaction Hamiltonian in the Schrödinger picture reduces to

$$\hat{\mathcal{H}}_{int} = -i\hbar g(\hat{\sigma}_+\hat{a} + \hat{\sigma}_-\hat{a}^\dagger). \tag{1.49}$$

Clearly, $\hat{\mathcal{H}}_{int}$ describes the conversion of atomic excitations to photonic excitations and vice versa. The Jaynes-Cummings Hamiltonian [40], describing the full atom-field system, is obtained by adding up the field, atom and the interaction terms, *i.e.*

$$\hat{\mathcal{H}}_{JC} = \hbar\omega\hat{a}^\dagger\hat{a} + \frac{1}{2}\hbar\omega_0\hat{\sigma}_z - i\hbar g(\hat{\sigma}_+\hat{a} + \hat{\sigma}_-\hat{a}^\dagger). \tag{1.50}$$

Equation 1.50 is one of the few exactly solvable Hamiltonians in quantum optics. I start by introducing the combined occupation number

$$\hat{n}_{com} = \hat{n} + \hat{n}_{atom} = \hat{a}^\dagger\hat{a} + \hat{\sigma}_+\hat{\sigma}_-. \tag{1.51}$$

Performing simple algebra, one can show that $[\hat{n}_{com}, \hat{\sigma}_+\hat{\sigma}_-] = \left[\hat{n}_{com}, \hat{a}^\dagger\hat{a}\right] = 0$ and

hence

$$[\hat{n}_{com}, \hat{\mathcal{H}}_{JC}] = -i\hbar g \left([\hat{n}_{com}, \hat{a}\hat{\sigma}_+] + \left[\hat{n}_{com}, \hat{a}^\dagger \hat{\sigma}_-\right] \right). \tag{1.52}$$

Also, since

$$\begin{aligned} \left[\hat{a}^\dagger \hat{a}, \hat{a}^\dagger \hat{\sigma}_-\right] &= \hat{a}^\dagger \hat{\sigma}_-, \\ \left[\hat{a}^\dagger \hat{\sigma}_-, \hat{\sigma}_+ \hat{\sigma}_-\right] &= \hat{\sigma}_- \hat{a}^\dagger, \\ [\hat{\sigma}_+ \hat{\sigma}_-, \hat{a}\hat{\sigma}_+] &= \hat{a}\hat{\sigma}_+, \\ \left[\hat{a}\hat{\sigma}_+, \hat{a}^\dagger \hat{a}\right] &= \hat{\sigma}_+ \hat{a}, \end{aligned} \tag{1.53}$$

we obtain

$$[\hat{n}_{com}, \hat{\mathcal{H}}_{JC}] = 0. \tag{1.54}$$

This means that $\hat{n}_{com}$ and $\hat{\mathcal{H}}_{JC}$ share the same set of eigenstates.

In order to find the eigenstates of $\hat{\mathcal{H}}_{JC}$, we first note that $[\hat{n}, \hat{n}_{atom}] = 0$ as they operate on different subspaces. Therefore, $\hat{n}$ and $\hat{n}_{atom}$ also share a common set of eigenstates, but they have distinct sets of eigenvalues. This suggests that an interesting set of basis states for the total Hamiltonian is

$$|n, s\rangle = |n\rangle \otimes |s\rangle = \{|n, \mathrm{g}\rangle, \ |n, \mathrm{e}\rangle, \ n = 0, 1, 2, ...\}, \tag{1.55}$$

These are called the *bare states*. Also, the eigenvalue equation

$$\hat{n}_{com} |n, s\rangle = (n + n_{atom}) |n, s\rangle \tag{1.56}$$

holds, but since $n_{atom} \in \{0, 1\}$, there are two states that contribute to a fixed $n + n_{atom}$ except for the special case $n_{com} = 0$. We can now write the Hamiltonian of Eq. 1.50 in the bare-state basis as

$$\hat{\mathcal{H}}_{JC} = \sum_{n,n'=0}^{\infty} \sum_{s,s'=\mathrm{e,g}} |n, s\rangle \langle n, s| \hat{\mathcal{H}}_{JC} |n', s'\rangle \langle n', s'|. \tag{1.57}$$

Using Eqs. 1.35a, 1.35b, 1.42a and 1.42b we find

$$\begin{aligned}
&\hat{\sigma}_+\hat{\sigma}_- \left|n+1,\mathrm{g}\right\rangle = \hat{a}\hat{\sigma}_+ \left|n,\mathrm{e}\right\rangle = \hat{a}^\dagger\hat{\sigma}_- \left|n+1,\mathrm{g}\right\rangle = 0,\\
&\hat{a}^\dagger\hat{a}\left|n+1,\mathrm{g}\right\rangle = (n+1)\left|n+1,\mathrm{g}\right\rangle, \quad \hat{a}^\dagger\hat{a}\left|n,\mathrm{e}\right\rangle = n\left|n,\mathrm{e}\right\rangle,\\
&\hat{\sigma}_+\hat{\sigma}_- \left|n,\mathrm{e}\right\rangle = \left|n,\mathrm{e}\right\rangle, \quad \hat{a}\hat{\sigma}_+ \left|n+1,\mathrm{g}\right\rangle = \sqrt{n+1}\left|n,\mathrm{e}\right\rangle,\\
&\hat{a}^\dagger\hat{\sigma}_- \left|n,\mathrm{e}\right\rangle = \sqrt{n+1}\left|n+1,\mathrm{g}\right\rangle.
\end{aligned} \tag{1.58}$$

Since the interaction Hamiltonian only couples pairs of bare states, for $n > 0$ the Jaynes-Cummings Hamiltonian decouples into an infinite direct product of 2×2-matrix Hamiltonians with the elements

$$\begin{aligned}
\mathcal{H}_{n,11} &= \hbar\omega n + \frac{1}{2}\hbar\omega_0,\\
\mathcal{H}_{n,22} &= \hbar\omega\,(n+1) - \frac{1}{2}\hbar\omega_0,\\
\mathcal{H}_{n,12} &= \mathcal{H}_{n,21} = \hbar g\sqrt{n+1}.
\end{aligned} \tag{1.59}$$

Thus the form of the n-th 2×2-matrix is

$$\hat{\mathcal{H}}_n = \begin{pmatrix} \hbar\omega n + \frac{1}{2}\hbar\omega_0 & \hbar g\sqrt{n+1} \\ \hbar g\sqrt{n+1} & \hbar\omega\,(n+1) - \frac{1}{2}\hbar\omega_0 \end{pmatrix}. \tag{1.60}$$

Upon diagonalization, the eigenenergies are obtained as

$$E_\pm(n) = \hbar\omega\left(n+\frac{1}{2}\right) \pm \frac{1}{2}\hbar\omega_{R,n} \tag{1.61}$$

and the eigenfrequencies are $\omega_\pm = E_\pm/\hbar$, where

$$\omega_{R,n} = \sqrt{\Delta_\omega^2 + 4g^2(n+1)} \tag{1.62}$$

is the Rabi frequency and $\Delta_\omega = \omega - \omega_0$ is the detuning. The Rabi frequency is the energy (photon) exchange rate between the atom and the field, and obviously, an

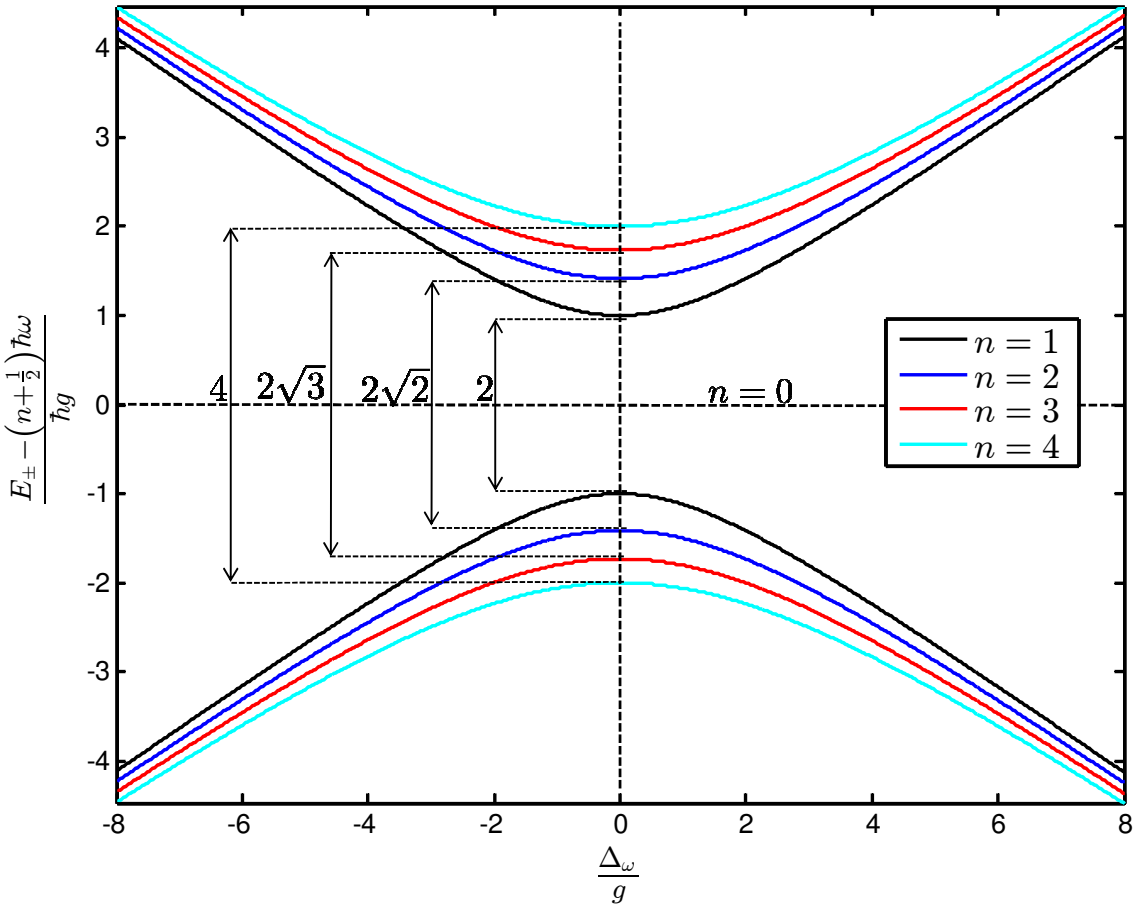

Figure 1.3: Plot of $E_\pm - \left(n + \frac{1}{2}\right)\hbar\omega$ as a function of detuning Δ_ω for $n = 0 - 4$.

indication of the atom-field coupling strength. Figure 1.3 shows a few of the lowest eigenenergies as a function of detuning. The eigenstates (the *dressed states*) are

$$\begin{aligned} |n+1,+\rangle &= \left(\frac{\omega_{R,n}+\Delta_\omega}{2\omega_{R,n}}\right)^{1/2} |n+1,\mathrm{e}\rangle + \left(\frac{\omega_{R,n}-\Delta_\omega}{2\omega_{R,n}}\right)^{1/2} |n+2,\mathrm{g}\rangle\,, \\ |n+1,-\rangle &= -\left(\frac{\omega_{R,n}-\Delta_\omega}{2\omega_{R,n}}\right)^{1/2} |n+1,\mathrm{e}\rangle + \left(\frac{\omega_{R,n}+\Delta_\omega}{2\omega_{R,n}}\right)^{1/2} |n+2,\mathrm{g}\rangle\,. \end{aligned} \tag{1.63}$$

For the special case of $|0,+\rangle$ and $|0,-\rangle$, $|0,+\rangle = |0,-\rangle = |0,\mathrm{g}\rangle$.

From Eqs. 1.61-1.63 we can understand how the unperturbed atomic eigenstates ($|\mathrm{g}\rangle$ and $|\mathrm{e}\rangle$) are modified. For zero detuning ($\Delta_\omega = 0$), the interaction with

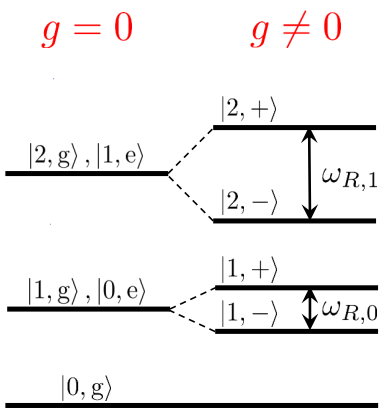

Figure 1.4: Diagram showing how the degeneracy of the unperturbed states is lifted as a result of atom-field coupling ($\Delta_\omega = 0$).

the field causes excited state eigenfrequencies to shift by an amount proportional to the coupling strength g. Thus in the case of zero detuning, the eigenfrequencies of the states $|n+1, \mathrm{g}\rangle$ and $|n, \mathrm{e}\rangle$ which are $(n+1/2)\omega$ (degenerate) when unperturbed, get split by $\omega_{R,n} = 2g\sqrt{n+1}$ as a result of interaction. I emphasize here that the uncoupled $|0, \mathrm{e}\rangle$ and $|1, \mathrm{g}\rangle$ are split by $\omega_{R,0} = 2g$ (called the *vacuum Rabi splitting*) in the coupled atom-field system (Fig. 1.4). This is a purely quantum-mechanical phenomenon that is not predicted by classical physics.

It is also useful to consider the time evolution of the state of the combined system. If an atom in the excited state interacts with a single-mode field that was produced by an external drive under the Jaynes-Cummings Hamiltonian the state of the system can be written as [43]

$$|\psi(t)\rangle = \sum_{n=0}^{\infty} C_{\mathrm{e}}(t) \frac{e^{-|\alpha|^2/2}\alpha^n}{\sqrt{n!}} |n, \mathrm{e}\rangle + \sum_{n=0}^{\infty} C_{\mathrm{g}}(t) \frac{e^{-|\alpha|^2/2}\alpha^n}{\sqrt{n!}} |n+1, \mathrm{g}\rangle \,, \tag{1.64}$$

where α is the coherent state amplitude and the factor of $e^{-|\alpha|^2/2}\alpha^n/\sqrt{n!}$ comes

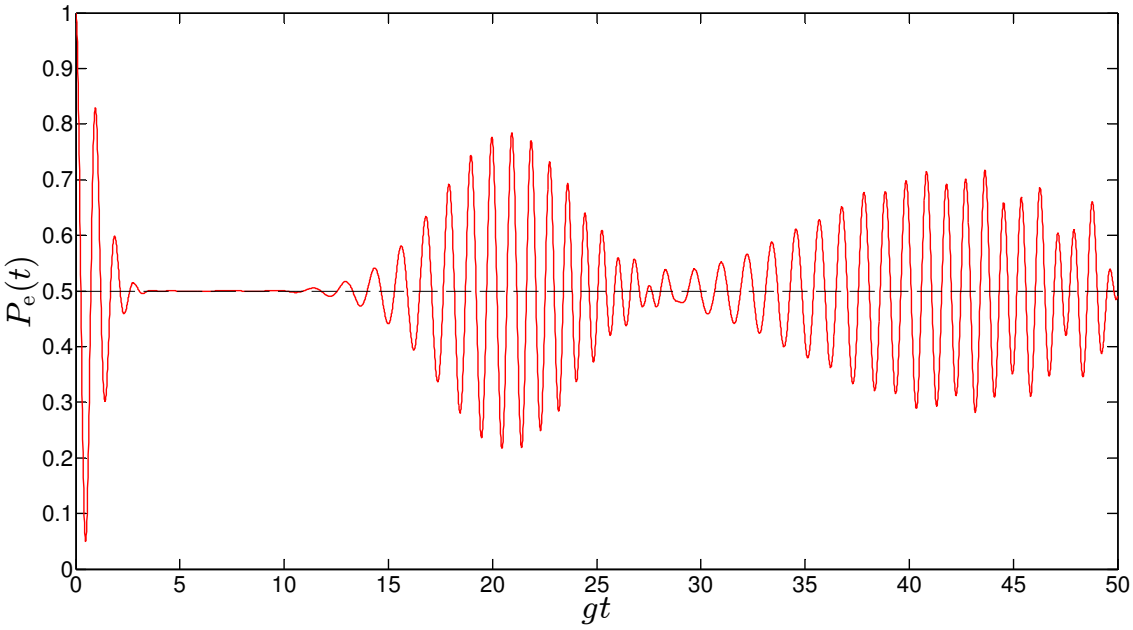

Figure 1.5: Plot of the probability of the atomic excited state occupancy $P_{\rm e}(t)$ as a function of the scaled time gt for $|\alpha|^2 = \bar{n} = 10$ with $P_{\rm e}(0) = 1$. The oscillations start to damp out (collapse) immediately after $t = 0$, but they reappear after a few Rabi cycles (revival), although not with the full amplitude. These sequential collapses and revivals continue, but the revivals generally show smaller amplitudes as time increases.

from the Poissonian distribution of photon numbers. Also, $|\alpha|^2 = \bar{n}$, where $\bar{n}$ is the average number of photons in the volume (cavity). From Schrödinger's equation,

$$i\hbar \frac{d}{dt} |\psi(t)\rangle = \hat{\mathcal{H}}_{JC} |\psi(t)\rangle . \tag{1.65}$$

Using $C_{\rm e}(0) = 1$ and $C_{\rm g}(0) = 0$, at resonance ($\omega = \omega_0$) we find

$$\begin{aligned} C_{\rm e}(t) &= \cos(g\sqrt{n+1}t), \\ C_{\rm g}(t) &= i\sin(g\sqrt{n+1}t). \end{aligned} \tag{1.66}$$

The probability of finding the atom in the excited state is

$$P_{\rm e}(t) = \sum_{m=0}^{\infty} |\langle m, {\rm e}|\psi(t)\rangle|^2 = e^{-|\alpha|^2} \sum_{n=0}^{\infty} \frac{|\alpha|^{2n}}{n!} \cos^2(g\sqrt{n+1}t). \tag{1.67}$$

Figure 1.5 shows $P_e(t)$ as a function of the scaled time gt for $\bar{n} = 10$. We note that in this fully-quantum-mechanical approach, $P_e(t)$ has a general oscillatory form with the Rabi frequency, as in the semiclassical approach [50]. But there is a clear and significant difference in the results of the two approaches. In the fully-quantum model, the oscillations undergo a series of *collapses* and *revivals* [51], as opposed to the semiclassical model where the Rabi oscillations have a constant amplitude.

1.3 Superconducting qubits and resonators

As I noted earlier, any quantum system with two isolated states can potentially serve as a qubit. Ideally, it should only be coupled to the read, write and control lines, and completely decoupled from everything else. Isolation from the environment can be done relatively easily when the qubit is an atom or ion, or an electronic or nuclear spin. However, the qubit-qubit coupling in these systems is challenging, making it hard to realize efficient multi-qubit circuits [52]. Superconducting qubits, which are circuit-based quantum systems, have a potential advantage in that they can be efficiently and relatively easily coupled to each other and/or other circuits via microwave cavities, inductors, capacitors, *etc.* However, they also tend to couple to nanoscale defects, parasitic microwave resonances and environmental noise, which cause decoherence. Since qubits need to operate coherently to be useful for quantum computation, decoherence is a serious short-coming. This is why this thesis is focused on understanding sources of decoherence in superconducting qubits.

1.3.1 Basic qubit types

All superconducting qubits take advantage of the nonlinear inductance of the Josephson junctions (JJs). Superconducting qubits are designed so that the two lowest energy levels have an energy difference that is distinct from all others, in contrast to a harmonic oscillator. One of the qubit types, named the phase qubit, can be represented by a current-biased JJ [53, 54] where the phase difference across the junction can be represented by a particle in a single anharmonic well of the tilted washboard potential [55–57]. The tunneling of the particle from one well to an adjacent well can be significant if there is a tilt and the tunneling probability is never zero. However, by operating the qubit at relatively low tilts and choosing the circuit parameters appropriately, the particle can be made to stay close to the bottom of the well with negligible tunneling probability and the two lowest levels can be used as qubit states.

A phase qubit can be realized by current biasing a JJ which is operated at zero voltage [58]. In contrast, a charge qubit or a Cooper pair box uses the charge states of a small superconducting island. The two qubit states correspond to the existence or absence of an excess Cooper pair on the island [59, 60]. The island is connected to a relatively large superconducting reservoir via an ultra-small JJ. By controlling the voltage on a gate capacitor, Cooper pairs can be transferred to and from the island [61]. A major complication with conventional charge qubits is that charge noise from nanoscale defects limits the coherence time even when the device is operated at millikelvin temperatures and biased at the charge sweet spot [62].

The coherence time of charge qubit can be significantly improved by shunting the JJ with a large capacitor, which increases the ratio of the Josephson energy E_J and the charging energy E_C, leading to a device called the transmon [63]. For a transmon or a phase qubit $E_J \gg E_C$, while for a typical charge qubit $E_J \simeq E_C$ [64].

Flux qubits are another type of superconducting qubit [65]. They are essentially a type of RF-SQUID - a loop interrupted by one or more ultra-small JJs. The flux qubit is coupled to an auxiliary coil which enables flux biasing of the loop. With careful selection of the parameters and by flux biasing the loop at half a flux quantum, the system has a double-well potential with two degenerate states (one in each well) that are separated by a shallow barrier. Ideally, the tunneling energy between these two states is not too small, but much smaller than the level spacing of each well, allowing two well-isolated quantum levels.

1.3.2 Qubit decoherence and superconducting resonators

Superconducting microwave resonators have been playing increasingly important roles in superconducting qubit circuits. An important early example was the use of resonators for a CQED readout of a Cooper pair box [22]. This technique is based on the CQED model discussed in section 1.2. In this dispersive readout scheme, a high-quality superconducting resonator is coupled to the charge qubit such that the qubit-resonator coupling rate is much larger than the relaxation rate of the Cooper pair box. If the transition frequency of the charge qubit is detuned from the resonator's frequency, the coupling gives rise to a resonator frequency that

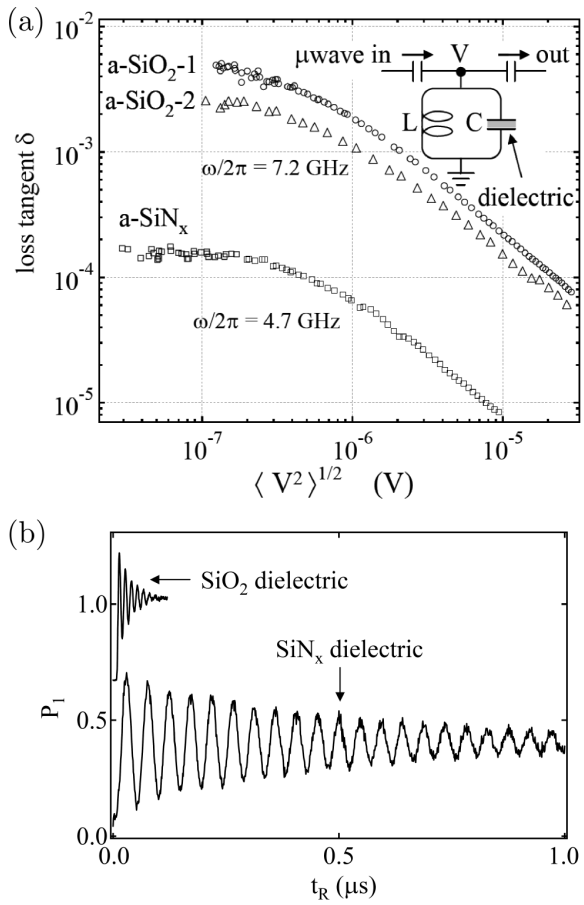

Figure 1.6: From Ref. [66] (a) Measured loss tangent versus the RMS microwave voltage across SiO_2 and SiN_x dielectric in a thin film capacitor. (b) Measured Rabi oscillations in a phase qubit showing a faster decay when a lossier dielectric is used.

depends on the qubit state. Superconducting resonators can also be used to control qubit-qubit interactions, to couple two remote qubits, or to connect several qubits [18].

Another application of superconducting resonators is as a tool to measure loss in materials used in superconducting qubit circuitry (see Fig. 1.6). Qubit decoherence is due to unwanted coupling to the environment, which causes loss and

dephasing. It is now well known that dielectrics are a major source of loss in superconducting qubits [66,67]. This includes dielectrics that are used deliberately in the qubit (*e.g.* the substrate, insulating layers, JJ barriers) or present unintentionally (*e.g.* native oxide on the superconductor or adsorbed surface layers).

Dielectrics contain nanoscale tunneling two-level systems (sometimes known as two-level system defects) which couple to the electric fields of the qubit circuit, thus absorbing energy and causing qubit decoherence. The precise identity of these two-level systems (TLSs) is generally unknown, but significant progress has been made in recent years to understand their ensemble-averaged and individual behavior. I discuss the physics of nanoscale TLSs in detail in Chapter 2. In 2005, the Martinis group showed that longer qubit coherence times can be obtained by using higher quality dielectrics [66] (see Fig. 1.6). Another key result from this work was the realization that one does not necessarily need to measure a qubit to study dielectric loss - dielectric loss can be measured using a superconducting microwave resonator instead. If a known fraction of the electric field energy (the filling factor) at resonance penetrates into the dielectric under study, the resulting measurements can be analyzed quantitatively to find dielectric loss. If the dielectric is used as the insulator inside a parallel-plate capacitor, the filling factor is approximately 1, meaning almost all of the electric energy density is confined within the dielectric. In contrast to typical room-temperature circuit resonators where the capacitor is often the least lossy element of the circuit, it is often the most dissipative element in a superconducting resonator because resistive loss is negligible. Therefore, by measuring the resonator's internal quality factor (Q_i), the dielectric loss can be determined.

Superconducting microwave resonators also have applications in astronomical radiation detection. Microwave kinetic inductance detectors (MKIDs) are superconducting resonators specially designed for detection of photons from far-infrared frequencies up to X-ray frequencies [68]. When a photon hits the MKID, it can break Cooper pairs and thus create excess quasi-particles. This changes the kinetic inductance of the MKID which in turn causes a detectable shift in its resonance frequency. Although I will not be examining MKIDs in this thesis, these detectors also are affected by two-level systems and my results will be of interest to researchers from that community as well as the superconducting quantum computing community.

1.4 Overview of thesis

The main aim of my thesis is to increase the understanding of nanoscale TLSs and search for materials with reduced loss or long TLS coherence time. The thesis can be divided into two main parts:

(a) Characterization and analysis of individual nanoscale TLSs in amorphous solids, including the extraction of some of their distribution statistics and the introduction of a new method to measure individual TLSs (based on CQED).

(b) Measurement and analysis of the averaged response of many TLSs in silicon nitride (SiN_x), aluminum oxide (Al_2O_3) and surfaces of titanium nitride (TiN).

All of this work involved measurements on superconducting resonators.

In Chapter 2, I describe the standard model of TLS loss together with some background work on ensemble-averaged TLS measurements and individual TLS

characterization. In Chapter 3, I describe the methods I used to analyze my loss measurements and introduce a novel model for ensemble-averaged TLS analysis using superconducting microwave resonators. The experimental setup is described in detail in Chapter 4, along with the equipment that I have used to fabricate my devices. In Chapter 5, I discuss the CQED measurement, analysis and characterization of individual TLSs. A theoretical model for a strongly-coupled TLS in a cavity is also introduced in this chapter. In Chapter 6, I introduce a device that I designed for spectroscopy of individual TLSs in insulating amorphous solids. In addition to the measurement and analysis of this device, I describe a simulation for CQED spectroscopy of TLSs. Chapter 7 describes the low-temperature and room-temperature characterization of titanium nitride films grown using different recipes. I report measurements of the film quality factor, kinetic inductance, stress, critical temperature T_c, film composition and stoichiometry, *etc.* In Chapter 8, I describe my loss measurements on Al_2O_3 grown by atomic layer deposition (ALD) using trilayer superconducting microwave resonators. Finally, I summarize and conclude the thesis in Chapter 9.

Chapter 2: Nanoscale two-level systems

2.1 Low-temperature properties of amorphous solids

In 1959, measurements of the specific heat in silica at temperatures T from 2.3 K to 19 K showed a significant difference compared to that of single crystals [69]. In the early 1970's, Zeller and Pohl [70] reported measurements of the thermal conductivity of several amorphous solids (SiO_2, Se, silica- and germania-based glasses) in the 50 mK to 1 K temperature range and noticed that it was significantly smaller than that of crystalline solids. Other experiments showed that the heat capacity of amorphous solids varied approximately linearly with T and the thermal conductivity was proportional to T^2 [71]. This was surprising as it was believed that Debye's theory for specific heat [72] was applicable to both crystalline and amorphous materials at low temperatures. Debye predicted that the specific heat and thermal conductivity should be proportional to T^3 at low temperatures. Finally, experiments also showed that acoustic attenuation in amorphous silica at millikelvin temperatures depended on the acoustic intensity and saturated at sufficiently high intensities [73].

Several models were proposed to explain these discrepancies. Among them, a microscopic model proposed independently by Phillips [74] and Anderson *et al.* [75], was the most successful. According to this model, Debye-like phonons are in-

elastically scattered by defects that behave as tunneling two-level systems (TLSs). These low-energy defect states are present in amorphous solids and strongly affect their thermal, acoustic and dielectric properties at very low temperatures.

As mentioned in section 1.3.2, charged nanoscale tunneling TLSs will also couple to electric fields in a superconducting qubit or microwave resonator circuit. In 2005, Martinis *et al.* [66] reported that TLSs in the dielectrics were the dominant loss mechanism in their superconducting phase qubits, and showed that by using higher quality dielectrics and/or JJs with smaller areas (hence fewer TLSs in the tunneling barrier) one can increase the coherence time of a qubit. More specifically, it was shown that using low-loss SiN_x rather than SiO_2 as the crossover wiring dielectric, significantly improved the coherence time. Finally, the group also showed that when the same dielectrics were used to fabricate superconducting resonator circuits, the former resulted in a higher resonator quality factor (Q).

2.2 The tunneling TLS model

In this section, I review the standard model of microwave dielectric loss due to nanoscale TLS defects. Note that any anharmonic oscillator with sufficiently sharp levels at sufficiently low temperatures and low powers acts effectively as a two-level system as the levels are spaced unequally. The standard TLS model assumes that in disordered solids, certain atoms or a group of atoms have available two (or possibly more) accessible potential minima [76]. For simplicity, we assume a double-well potential V for the TLS, as shown in Fig. 2.1. At millikelvin temperatures, we

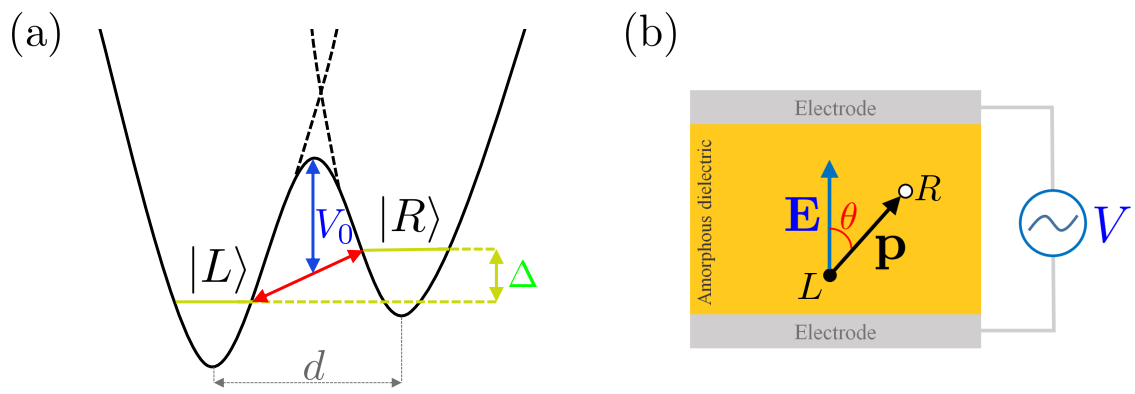

Figure 2.1: (a) Double well potential of a nanoscale TLS. V_0 is the barrier height separating the two wells, Δ is the asymmetry energy, Δ_0 is the tunneling energy and d is the spatial separation of the potential minima. (b) A nanoscale TLS, represented by the dipole moment $\mathbf{p} = q\mathbf{d}/2$, in an amorphous dielectric exposed to an external AC electric field $\mathbf{E}$.

assume that the particle is restricted to the ground states of the two wells ($|L\rangle$ and $|R\rangle$), and only the two lowest energy levels are important. If there is no applied field, the energy difference of these two states is set by the tunneling energy through the barrier (Δ_0) and the asymmetry energy of the wells (Δ). For simplicity, the wells may be considered to be quasi-harmonic with potentials V_L and V_R and Hamiltonians $\hat{\mathcal{H}}_L$ and $\hat{\mathcal{H}}_R$. When a potential $V(x)$ is applied in addition to the potentials V_L and V_R, the Hamiltonian for the particle is

$$\hat{\mathcal{H}}_0 = \hat{\mathcal{H}}_L + \hat{\mathcal{H}}_R + qV(x), \tag{2.1}$$

where we have assumed the particle has charge q. This is equivalent to

$$\hat{\mathcal{H}}_0 = \begin{pmatrix} \mathcal{E}_L + \langle L| V |L\rangle & \langle L| \hat{\mathcal{H}}_0 |R\rangle \\ \langle R| \hat{\mathcal{H}}_0 |L\rangle & \mathcal{E}_R + \langle R| V |R\rangle \end{pmatrix} \tag{2.2}$$

in the $\{|L\rangle, |R\rangle\}$ basis. Ignoring the two terms $\langle L| V |L\rangle$ and $\langle R| V |R\rangle$ for now, I choose the zero of energy as the mean of $\mathcal{E}_L$ and $\mathcal{E}_R$, and define $\Delta_0 = -2 \langle L| \hat{\mathcal{H}}_0 |R\rangle$ and $\Delta = \mathcal{E}_L - \mathcal{E}_R$. The Hamiltonian then becomes

$$\hat{\mathcal{H}}_0 = \frac{1}{2} \begin{pmatrix} \Delta & -\Delta_0 \\ -\Delta_0 & -\Delta \end{pmatrix}. \tag{2.3}$$

By diagonalizing the Hamiltonian, we obtain

$$\hat{\mathcal{H}}_0 = \frac{1}{2} \begin{pmatrix} \mathcal{E} & 0 \\ 0 & -\mathcal{E} \end{pmatrix}, \tag{2.4}$$

where $\mathcal{E} = \sqrt{\Delta^2 + \Delta_0^2}$. Clearly, the energy eigenvalues are $\pm\mathcal{E}/2$ and the energy difference between the two energy eigenstates is $\mathcal{E}$. The energy eigenstates are

$$\begin{aligned} |\psi_1\rangle &= \cos\theta |L\rangle - \sin\theta |R\rangle, \\ |\psi_2\rangle &= \sin\theta |L\rangle + \cos\theta |R\rangle, \end{aligned} \tag{2.5}$$

where $\tan 2\theta = \Delta_0/\Delta$.

One can evaluate Δ_0 for specific potentials. For two identical truncated 3-dimensional harmonic wells with $\Delta = 0$ and barrier height V_0 (see Fig. 2.1a)

$$\Delta_0 = \hbar\omega_0 \left[3 - \sqrt{\frac{8V_0}{\pi\hbar\omega_0}}\right] e^{-2V_0/\hbar\omega_0}, \tag{2.6}$$

where $\hbar\omega_0 = 2\mathcal{E}_L = 2\mathcal{E}_R$ [76]. Assuming that the tunneling particle has a mass m and $V_0 \gg \hbar\omega_0$, which is valid for our purposes, Eq. 2.6 becomes

$$\Delta_0 \simeq -4 \left(\frac{2\hbar^2 V_0^3}{md^2}\right)^{1/4} e^{-\left(2mV_0/\hbar^2\right)^{1/2} d/2}, \tag{2.7}$$

where d is the distance between the two minima. Needless to say, the actual microscopic form of the potential for the TLSs in amorphous solids is not well understood.

For simplicity, we assume an expression of the form

$$\Delta_0 = \hbar\Omega e^{-d\left(2mV_0/\hbar^2\right)^{1/2}}, \tag{2.8}$$

where $\Omega \sim \omega_0$ is a reasonable approximation for the case of amorphous solids.

The TLSs are believed to have a uniform spatial distribution in the bulk of an amorphous dielectric. Also, in the standard model, the TLS distributions in the asymmetry energy Δ and the barrier height V_0 are assumed to be uniform, and the latter gives rise to a logarithmic distribution in the tunneling energy Δ_0 as a result of Eq. 2.8. Therefore, the energy and space distribution of TLSs (the standard TLS distribution) can be written as

$$d^2n = (P_0/\Delta_0)\, d\Delta d\Delta_0, \tag{2.9}$$

where P_0 is a material-related constant denoting the TLS spectral and spatial density. For a typical amorphous dielectric, $P_0 \sim 10^{44}$ $\mathrm{J}^{-1}\mathrm{m}^{-3}$ [74]. Since the total number of TLSs in a sample is finite, the distribution must be restricted to a range $\Delta_{min} < \Delta < \Delta_{max}$ and $\Delta_{0,min} < \Delta_0 < \Delta_{0,max}$.

2.3 TLS-field interaction

When a TLS couples to electric or strain fields, the Hamiltonian of Eq. 2.3 is perturbed and the parameters Δ and Δ_0 are changed. I can write:

$$\hat{\mathcal{H}} = \hat{\mathcal{H}}_0 + \hat{\mathcal{H}}', \tag{2.10}$$

where

$$\hat{\mathcal{H}}' = \frac{1}{2}\begin{pmatrix} \delta\Delta & -\delta\Delta_0 \\ -\delta\Delta_0 & -\delta\Delta \end{pmatrix}. \tag{2.11}$$

For simplicity, I will assume that under the influence of external fields, the separation d between the wells and the barrier hight V_0 remain unchanged, *i.e.* $|\delta\Delta| \gg |\delta\Delta_0| \simeq 0$ [77]. For an external electric field $\mathbf{E}$ and a charged TLS with electric dipole $\mathbf{p} = q\mathbf{d}/2$ (see Fig. 2.1b) and for sufficiently small perturbations, we have

$$\delta\Delta = 2\mathbf{p}\cdot\mathbf{E}. \tag{2.12a}$$

For a strain field $\overleftrightarrow{\mathbf{e}}$ I assign the deformation potential $\overleftrightarrow{\mathbf{D}}$ to the TLS, and I can write

$$\delta\Delta = 2\,\overleftrightarrow{\mathbf{D}}\cdot\overleftrightarrow{\mathbf{e}}\,. \tag{2.12b}$$

If we transfer $\hat{\mathcal{H}}'$ into the basis of $\hat{\mathcal{H}}_0$, we get [77]

$$\hat{\mathcal{H}}' = \frac{1}{\mathcal{E}}\begin{pmatrix} \Delta & -\Delta_0 \\ -\Delta_0 & -\Delta \end{pmatrix}(\mathbf{p}\cdot\mathbf{E} + D\tilde{e})\,, \tag{2.13}$$

where we have ignored the tensorial character of $\overleftrightarrow{\mathbf{D}}$ and $\overleftrightarrow{\mathbf{e}}$ and used D and $\tilde{e}$ instead. According to Eq. 2.13, the change in the level splitting is

$$\delta\mathcal{E} = \frac{2\Delta}{\mathcal{E}}\mathbf{p}\cdot\mathbf{E} \tag{2.14}$$

if it is caused by $\mathbf{E}$, and

$$\delta\mathcal{E} = \frac{2\Delta}{\mathcal{E}}D\tilde{e} \tag{2.15}$$

if it is caused by $\overleftrightarrow{\mathbf{e}}$.

For the rest of this section, I will describe the acoustic wave interaction first, and then discuss the analogous electric field interaction, as it was worked out historically. Needless to say, the focus of the rest of this thesis is on effects due to external electric fields.

The dynamics of a TLS in an external electric field or in the presence of an acoustic waves is equivalent to that of a spin-$\frac{1}{2}$ particle in a magnetic field. Consider a static magnetic field $\mathbf{B}_0$ in the z direction and an oscillatory perturbing field $\mathbf{B}'$. The Hamiltonian of a spin-$\frac{1}{2}$ particle in a magnetic field $\mathbf{B} = \mathbf{B}_0 + \mathbf{B}'$ is given by [71, 78]

$$\hat{H} = -\hbar\gamma\left(\mathbf{B}\cdot\mathbf{S}\right) = -\hbar\gamma\left(\mathbf{B}_0\cdot\mathbf{S}\right) - \hbar\gamma\left(\mathbf{B}'\cdot\mathbf{S}\right) = \hat{H}_0 + \hat{H}', \tag{2.16}$$

where γ is the gyromagnetic ratio and $\mathbf{S}$ is the spin.

In the analogous case of a TLS in the presence of an acoustic wave, let $\mathcal{E}$ be the energy splitting of the two levels in the unperturbed case and D and M be the deformation potentials and the coupling constants in the perturbation. We then have

$$\hat{H}_0 = \frac{1}{2}\begin{pmatrix} \mathcal{E} & 0 \\ 0 & -\mathcal{E} \end{pmatrix}, \quad \hat{H}' = \frac{e}{2}\begin{pmatrix} D & 2M \\ 2M & -D \end{pmatrix} \tag{2.17}$$

Basically, D expresses the energy shift of the relaxing states in a strain field of unit strength, and the elements $2M$ describe the TLS-phonon coupling strength for the resonant interaction. Using the Pauli matrices

$$\sigma_x = \begin{pmatrix} 0 & 1 \\ 1 & 0 \end{pmatrix}, \quad \sigma_y = \begin{pmatrix} 0 & -i \\ i & 0 \end{pmatrix}, \quad \sigma_z = \begin{pmatrix} 1 & 0 \\ 0 & -1 \end{pmatrix}, \tag{2.18}$$

one can write the effective fields $\mathbf{S}$, $\mathbf{B}_0$ and $\mathbf{B}'$ as

$$\mathbf{S} = \frac{1}{2}\boldsymbol{\sigma}, \quad -\hbar\gamma\mathbf{B}_0 = (0, 0, \mathcal{E}), \quad -\hbar\gamma\mathbf{B}' = e\,(2M, 0, D). \tag{2.19}$$

This is equivalent to

$$-\hbar\gamma\mathbf{B}_0 = (0, 0, \mathcal{E}), \quad -\hbar\gamma\mathbf{B}' = \left(\frac{2\Delta_0}{\mathcal{E}}\mathbf{p}\cdot\mathbf{E}, 0, \frac{2\Delta}{\mathcal{E}}\mathbf{p}\cdot\mathbf{E}\right) \tag{2.20}$$

for a TLS exposed to an external electric field (see Eq. 2.13).

If we assume zero loss/noise and hence infinite TLS (spin) lifetime, the dynamics is described by the well known equation

$$\frac{d}{dt}\mathbf{S}(t) = \gamma\mathbf{S}\times\mathbf{B}. \tag{2.21}$$

For a finite TLS (spin) lifetime, the situation is more complex. In 1946, Felix Bloch developed a set of differential equations in the context of nuclear magnetic resonance (NMR), which described the dynamics of a TLS (spin) ensemble including relaxation [79]. These equations, known as the Bloch equations, are

$$\frac{d}{dt}\langle S_x(t)\rangle = \gamma\left(\langle S_y\rangle B_z - \langle S_z\rangle B_y\right) - \mathrm{T}_2^{-1}\langle S_x\rangle, \tag{2.22a}$$

$$\frac{d}{dt}\langle S_y(t)\rangle = \gamma\left(\langle S_z\rangle B_x - \langle S_x\rangle B_z\right) - \mathrm{T}_2^{-1}\langle S_y\rangle, \tag{2.22b}$$

$$\frac{d}{dt}\langle S_z(t)\rangle = \gamma\left(\langle S_x\rangle B_y - \langle S_y\rangle B_x\right) - \mathrm{T}_1^{-1}\langle S_z\rangle + \mathrm{T}_1^{-1}S_z^l\left[B_z(t)\right], \tag{2.22c}$$

where T_1 and T_2 are the longitudinal and transverse relaxation times respectively, and

$$S_z^l\left[B_z(t)\right] = \frac{1}{2}\tanh\left(\frac{\hbar\gamma B_z(t)}{2k_BT}\right) \tag{2.23}$$

is the difference in the population of the two levels due to thermal excitations.

The relaxation rate T_1^{-1} denotes the rate at which a non-equilibrium population relaxes into equilibrium through absorption or emission of phonons or photons. The emission/absorption rates are always such that they pull the system into equilibrium. Obviously, in equilibrium, the emission rate equals the absorption rate. For a tunneling TLS, it can be shown that phonon emission yields [71, 80]

$$T_1^{-1} = \left(\frac{\Delta_0}{\mathcal{E}}\right)^2 T_{1,min}^{-1}, \tag{2.24}$$

where

$$T_{1,min}^{-1} = \left[\frac{M_L^2}{v_L^5} + \frac{2M_T^2}{v_T^5}\right] \frac{\mathcal{E}^3}{2\pi\rho\hbar^4} \coth\left(\frac{\mathcal{E}}{2k_BT}\right). \tag{2.25}$$

Here $T_{1,min}$ is the minimum T_1 time for a TLS with energy $\mathcal{E}$, M_L and M_T are the longitudinal and transverse phonon deformation potentials, v_L and v_T are the longitudinal and transverse sound velocity, and ρ is the mass density of the material.

T_2 is the coherence time and the quantity $2T_2^{-1}$ in the Bloch equations is the intrinsic spectral linewidth of an ensemble of homogeneous TLSs that take part in the resonant absorption process at a given frequency. Several phenomena can limit the coherence time. The most important ones are the relaxation of each TLS and any interaction between TLSs, which causes the broadening of the spectral linewidth. In general, one can divide the sources of this homogeneous broadening into two categories: some arise from longitudinal relaxation processes (set by T_1), and some arise from phenomena that affect the phase of the precessing TLSs (set by the dephasing time T_ϕ). T_2 is related to T_1 and T_ϕ by [76]

$$T_2^{-1} = \frac{1}{2}T_1^{-1} + T_\phi^{-1}. \tag{2.26}$$

Using the Bloch equations and the spin-TLS analogy, it can be shown that the TLS-induced acoustic attenuation length l_{res} in an amorphous solid at frequency ω and acoustic intensity J obeys [71]

$$l_{res}^{-1} = l_0^{-1} \frac{\tanh(\hbar\omega/2k_BT)}{\sqrt{1 + J/J_c}}, \tag{2.27}$$

where

$$l_0^{-1} = \pi n_0 M^2 \omega/\rho v^3 \tag{2.28}$$

is the low-intensity limit of the attenuation length at zero temperature in terms of the constant density of states (n_0) of TLS energy splitting, and

$$J_c = \hbar^2 \rho v^3/2M^2 \mathrm{T}_1 \mathrm{T}_2 \tag{2.29}$$

is the critical intensity.

In analogy to the acoustic attenuation, the loss tangent of an amorphous dielectric, caused by the standard distribution of randomly oriented TLS dipoles coupled to an AC electric field with frequency ω, is found to be [81]

$$\tan\delta = \tan\delta_0 \frac{\tanh(\hbar\omega/2k_BT)}{\sqrt{1 + \bar{\omega}_R^2 \mathrm{T}_{1,min} \mathrm{T}_2}}, \tag{2.30}$$

where

$$\tan\delta_0 = \frac{\pi P_0 p^2}{3\epsilon} \tag{2.31}$$

is the low-power limit of the loss tangent, and $\bar{\omega}_R$ is the characteristic Rabi frequency of the TLS ensemble:

$$\bar{\omega}_R = \frac{2pE}{\sqrt{3}\hbar}. \tag{2.32}$$

Here E is the electric field amplitude. $\bar{\omega}_R$ can be viewed as an *effective* Rabi frequency for a distribution of TLSs in energy (as described by Eq. 2.9) and space (uniformly). It is derived from the Rabi frequency of an individual TLS, *i.e.*

$$\omega_R = \frac{\Delta_0}{\mathcal{E}} \frac{2\mathbf{p} \cdot \mathbf{E}}{\hbar}. \tag{2.33}$$

One can also define a characteristic electric field amplitude E_c (also called the critical field) as

$$E_c = \frac{\sqrt{3}\hbar}{2p\sqrt{\mathrm{T}_{1,min}\mathrm{T}_2}}. \tag{2.34}$$

Equation 2.30 can now be written in terms of the electric field amplitude as

$$\tan\delta = \tan\delta_0 \frac{\tanh(\hbar\omega/2k_BT)}{\sqrt{1+(E/E_c)^2}}. \tag{2.35}$$

The physical interpretation of the Eq. 2.35 is straight forward. At zero temperature and low drive powers (low field amplitudes, $E \ll E_c$) the TLSs are generally in the ground state and actively participate in photon absorption/emission processes, hence causing maximum dielectric loss ($\tan\delta = \tan\delta_0$). For increasing drive power, the TLSs with $\mathcal{E} \simeq \hbar\omega$ interact most strongly with the field and become more likely to be in the excited state. This reduces the number of TLSs in the ground state available for additional photon absorption, and the loss tangent decreases. In the high-power limit, $E \gg E_c$, loss tangent decreases as E^{-1} due to saturation of the TLSs. I use Eq. 2.35 throughout this thesis to characterize ensembles of weakly-coupled TLSs in different materials and structures.

2.4 Measurement of TLSs: ensemble-averaged and individual

While significant theoretical and experimental effort has been made to study nanoscale TLSs, their precise microscopic nature in a given material remains generally unknown. Studying TLS ensembles has been performed using superconducting resonators in many previous studies [66, 82, 83]. The dependence of loss tangent on the microwave drive power and temperature has been measured for several amorphous solids, and in some cases, have lead to clues about the nature of the TLSs. For example, in 1976, it was shown that the loss tangent of amorphous silica is correlated with the density of OH^- ions [84], whereas this density had nearly no influence in acoustic measurements. In a more recent experiment, Paik and Osborn showed that the loss tangent in different types of SiN_x, deposited using PECVD, was correlated with the nitrogen flow during film deposition [82]. In the same study, FT-IR measurements of the SiN_x films revealed that lossier films had a higher density of N-H bonds, suggesting that this impurity plays an important role in the TLS-induced dielectric loss.

Although ensemble measurements can provide useful data about TLSs, they lack the ability to provide accurate information on individual TLS properties. These properties include the individual TLS coherence times, asymmetry energy, dipole size, dipole orientation, tunneling energy, *etc.* as well as the distribution of these properties. As mentioned in Chapter 1, TLSs can couple to a superconducting qubit and limit its coherence time. Using superconducting qubits, one can reach the strong TLS-qubit coupling regime with the TLSs in the tunneling barrier and measure them

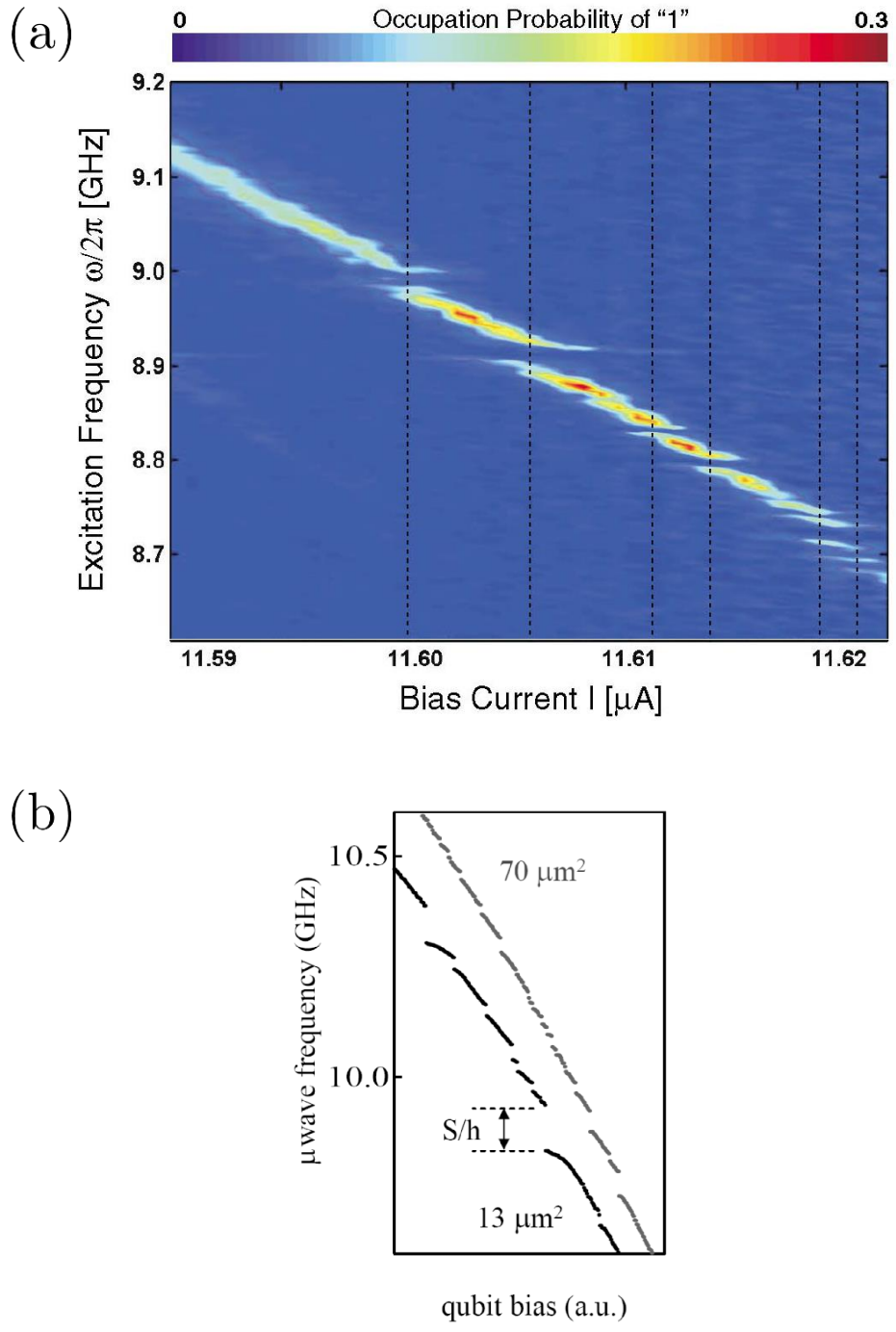

Figure 2.2: Figures from Refs. [66, 67] (a) Measured probability of phase qubit state "1" versus microwave excitation frequency $\omega/2\pi$ and bias current I for a fixed microwave power. (b) Spectroscopy of the $0 \rightarrow 1$ qubit transition as a function of junction bias for two phase qubits with junction areas 13 μm^2 and 70 μm^2. S represents the splitting size. Larger number of TLSs were found in the JJ with larger area.

individually. It was shown in 2004 by Martinis group at NIST that level splittings can occur as a result of strong TLS-qubit interaction (see Fig. 2.2a), causing loss in the qubit [67]. Each splitting is caused by the quantum entanglement of the qubit and a TLS within its JJ barrier, resulting in a so-called "avoided crossing". In other individual TLS measurements, the qubit coherence times were improved by using junctions of smaller areas (smaller tunneling barrier volumes) to reduce TLS spectral density [66] (see Figs. 1.6 and 2.2b). More recently, measurements of the lifetimes of individual TLSs in an alumina tunnel barrier have revealed that these TLSs can have substantially different coherence times [85]. Also, a JJ has been used to make a nearly-harmonic resonator, which can operate as a defect spectrometer to study the TLSs within its tunneling barrier [86].

As mentioned in Chapter 1, any quantum system with two isolated states can potentially be operated as a qubit [87]. This suggests the possibility of using the nanoscale TLSs as qubits or quantum memory bits. Obviously, the inherent randomness of the TLS distribution in energy and space and the difficulties in achieving strong coupling to the TLSs are serious challenges. In an interesting example of this approach, Neeley *et al.* used a TLS within the tunnel barrier of a Josephson-phase qubit as a quantum memory bit [88]. In their study, an arbitrary quantum state was transferred to the TLS, stored there for some time, and retrieved.

I should note that the above experiments on individual TLSs, and other similar experiments, have a few common limitations, *i.e.*

(a) they monitor individual TLSs only through coupling to a qubit or JJ,

(b) the volume of the dielectric under study is extremely small ($\ll 1\,\mu\mathrm{m}^3$), as only TLSs in tunneling barriers are individually measured,

(c) all the individually measured TLSs were in alumina, and no other material was investigated as a result of limitations in material choice for JJ barrier fabrication.

In Chapters 5 and 6 I show how these limitations can be removed, thereby allowing the measurement of individual TLSs to be achieved in different materials without using JJs.

Chapter 3: Resonance lineshape analysis

Thin-film superconducting microwave resonators have been widely used in superconducting qubit circuits, microwave kinetic inductance detectors and in studies of TLS-induced loss in dielectrics. In my thesis research, I used superconducting resonators as a tool for looking at the behavior of both ensembles of TLSs and individual TLSs. In this Chapter, I describe the analysis methods I used for TLS ensemble measurements. The analysis of the devices that I used for individual TLS measurements (micro-V devices) is covered in Chapter 5.

In all my experiments, the resonators were coupled to a coplanar waveguide (CPW) both capacitively and inductively, in general. The CPW's transmission S-parameter (S_{21}) was measured and fit to theoretical expressions described in this Chapter and Chapter 5.

3.1 Symmetric resonance lineshape

The derivation I give below for $S_{21} = V_{out}/V_{in}$ for superconducting coplanar resonators follows on analysis that was originally performed by Dr. K. Osborn and described by Dr. M. Khalil [89]. I review this result and provide a slightly different derivation.

Fig. 3.1a shows a schematic of a linear superconducting resonator coupled to a CPW. The resonator is composed of a lossless (superconducting) inductor L, and a lossy capacitor $\tilde{C}$ which is considered to be complex to account for the TLS-induced loss. All other elements in the circuit are assumed to be ideal. Assuming a negligible coupling impedance ($\sqrt{L_1/C_c} \ll Z_0 = 50\,\Omega$), an equivalent circuit can be constructed, as shown in Fig. 3.1b. For the equivalent circuit I can write

$$2V_{in} - V_{out} = I_1(Z_0 + i\omega L_1) - i\omega M I_L, \tag{3.1a}$$

$$V_{\tilde{C}} - V_{out} = \frac{I_2}{i\omega C_c}, \tag{3.1b}$$

$$i\omega M I_1 - i\omega L I_L = (I_2 + I_L)\,\frac{1}{i\omega\tilde{C}}, \tag{3.1c}$$

$$V_{out} = Z_0(I_1 + I_2). \tag{3.1d}$$

Using the approximations $\omega\mathrm{Re}(\tilde{C}) \ll 1/Z_0$, $\omega L_1 \ll Z_0$ and $\omega M^2/L \ll Z_0$, we get [89]

$$S_{21} = \frac{V_{out}}{V_{in}} = 1 + \frac{V_{\tilde{C}}}{2V_{in}}\left(\frac{M}{L} + i\omega C_c Z_0\right). \tag{3.2}$$

Also, from Eqs. 3.1 we can obtain a Norton equivalent current described by

$$I_N = V_{\tilde{C}} G_N, \tag{3.3}$$

where

$$I_N = -\frac{V_{in}}{Z_0}\left(\frac{M}{L} - \frac{i\omega C_c Z_0}{i\omega C_c Z_0 + 1}\right), \tag{3.4a}$$

and

$$G_N = \frac{1}{i\omega L} + i\omega\tilde{C} + G_T, \tag{3.4b}$$

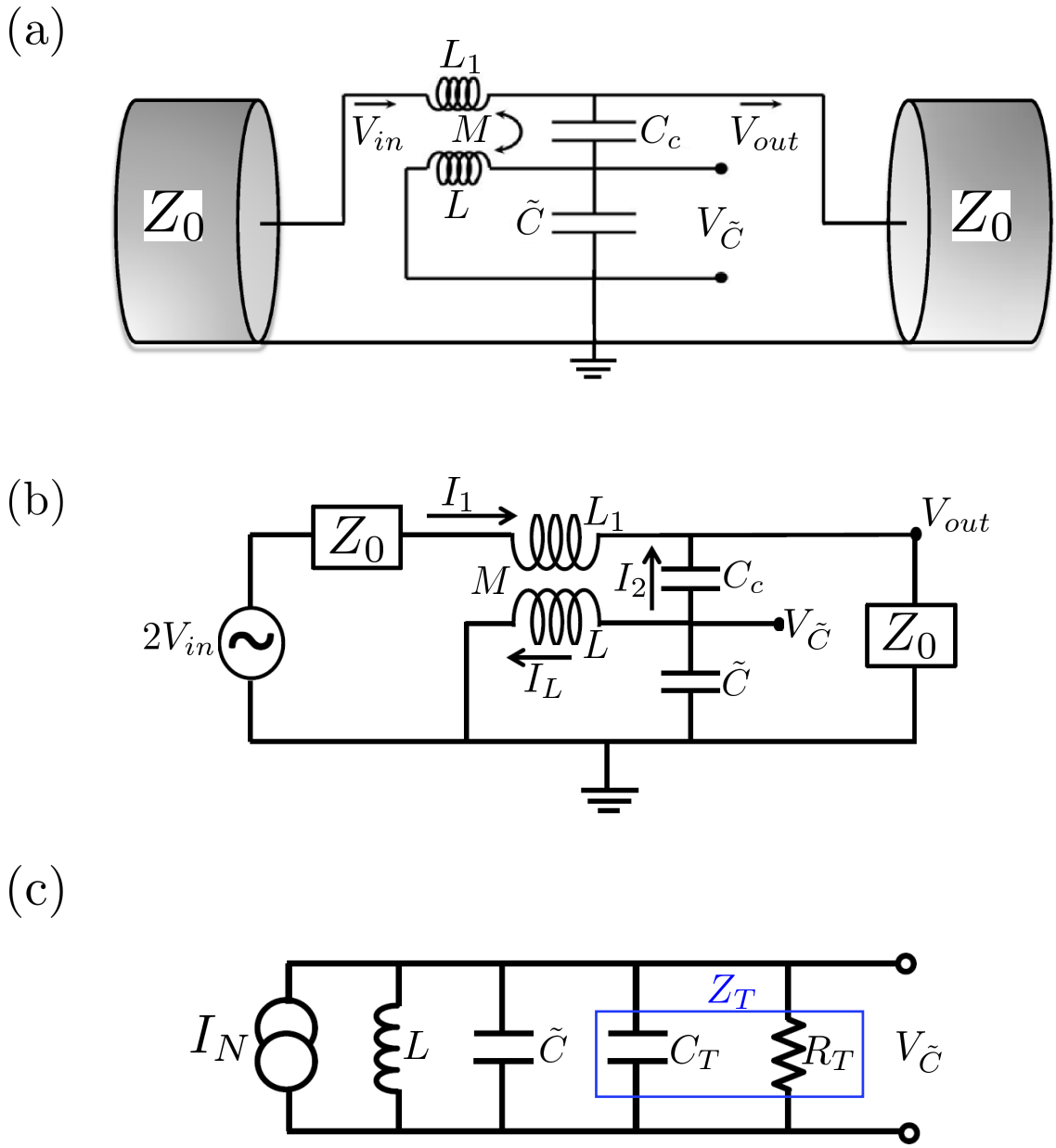

Figure 3.1: From Ref. [90] (a) Superconducting LC resonator coupled to a microwave transmission line. V_{in} and V_{out} are the voltage amplitude of the input and output waves, respectively. The resonator has inductance L and complex capacitance $\tilde{C}$, and is coupled to the CPW center by the coupling capacitor C_c and mutual inductance M. Ideally, the input and output impedance of the CPW is $Z_0 = 50\ \Omega$. (b) An equivalent circuit. (c) The Norton equivalent circuit.

with

$$G_T = Z_T^{-1} \equiv \frac{i\omega C_c}{i\omega C_c Z_0 + 1} + \frac{1}{2Z_0}\left(\frac{M}{L} - \frac{i\omega C_c Z_0}{i\omega C_c Z_0 + 1}\right). \tag{3.4c}$$

I note that this definition of G_N is different from that of Refs. [89] and [90]. The Norton equivalent circuit is shown in Fig. 3.1c.

Assuming relatively low loss, $\mathrm{Im}(\tilde{C}) \ll \mathrm{Re}(\tilde{C})$, the lossy capacitance can be split into an ideal capacitance $C \equiv \mathrm{Re}(\tilde{C})$ and a parallel resistance $R \equiv 1/\omega \mathrm{Im}(\tilde{C})$. Also, we define

$$R_T^{-1} \equiv \mathrm{Re}(G_T), \quad C_T \equiv \frac{1}{\omega}\mathrm{Im}(G_T), \tag{3.5a}$$

$$R_{eff}^{-1} \equiv R^{-1} + R_T^{-1}, \tag{3.5b}$$

and the total quality factor

$$Q \equiv R_{eff}\omega_0(C + C_T), \tag{3.5c}$$

and

$$\omega_0 \equiv \frac{1}{\sqrt{L(C + C_T)}}. \tag{3.5d}$$

Expanding Eq. 3.4c in terms of M/L and $\omega C_c Z_0$, which are much smaller than unity, gives

$$C_T = C_c, \tag{3.6a}$$

and

$$R_T^{-1} \simeq \frac{1}{2Z_0}\left[\left(\frac{M}{L}\right)^2 + \omega^2 C_c^2 Z_0^2\right]. \tag{3.6b}$$

Near resonance ($\omega \simeq \omega_0$), Eq. 3.2 can be written as

$$S_{21} = 1 - \frac{R_{eff}/R_T}{1 + 2iQ(\omega - \omega_0)/\omega_0}. \tag{3.7}$$

The external quality factor Q_e is inversely related to the resonator's photon decay rate due to coupling to the CPW, and can be written as

$$Q_e = \omega_0 R_T (C + C_T). \tag{3.8}$$

Equation 3.7 can be written as [89]

$$S_{21} = 1 - \frac{Q/Q_e}{1 + 2iQ(\omega - \omega_0)/\omega_0}. \tag{3.9}$$

This equation describes a Lorentzian resonance determined by the three parameters ω_0, Q and Q_e. Fitting Eq. 3.9 to a measured $S_{21}(\omega)$ lets us extract these parameters. The total quality factor Q depends on the external quality factor Q_e and the internal quality factor Q_i. From Eqs. 3.5b, 3.5c and 3.8 we can write

$$\frac{1}{Q} = \frac{1}{Q_i} + \frac{1}{Q_e}, \tag{3.10}$$

where $Q_i = R\omega_0 C$. After extracting Q and Q_e from the Lorentzian fit, Q_i can be found from Eq. 3.10.

While Q_e is determined by the energy loss due to coupling to the transmission line, Q_i is due to all other loss mechanisms, including resistive loss, radiative loss, dielectric loss, *etc.* For superconducting resonators operating at millikelvin temperatures and relatively low powers with well-filtered leads, the number of quasiparticles and hence the resistive loss is expected to be negligible. Also, resonators can be designed and packaged so that there is negligible radiative loss at the frequencies of interest. Typically, the interaction of the resonator with TLSs is the dominant loss mechanism at low temperatures and powers. In this case, Q_i is inversely related to

the dielectric loss tangent by

$$\tan\delta = \frac{1}{FQ_i}, \tag{3.11}$$

where F is the filling factor - the fraction of the total electric energy stored within the lossy dielectric under study. For a resonator with a parallel plate capacitor we have $F \simeq 1$, as, ideally, all the electric field energy is confined within the dielectric between the plates. However, for coplanar resonators, $F < 1$ and one typically would need to obtain F from calculation or simulation.

3.2 Asymmetric resonance lineshape

Equation 3.9 was derived assuming that the CPW was impedance-matched to the input and output leads. However, asymmetric resonance lineshapes can occur from impedance mismatches, *e.g.* between the cables and the PCB of the sample box or the PCB and the on-chip CPW. One can reduce this asymmetry to a great extent by optimizing the experimental setup and the resonator design so that the impedances are matched. However, as I will describe in Chapter 7, using superconducting materials with an unknown kinetic inductance can cause significant impedance mismatches. In general, to obtain a good fit to a measured $S_{21}(\omega)$ and extract accurate values for Q_i and Q_e, one needs to account for impedance mismatch. The next sections describe two methods for handling this situation.

3.2.1 Diameter Correction Method

I used the Diameter Correction Method (DCM) in some of the analysis in this thesis. A full description of this method can be found in Ref. [90], and I briefly describe it here. Assuming generally-mismatched input- and output impedances for the transmission line (Z_{in} and Z_{out}), and non-negligible coupling impedance, Khalil *et al.* showed that

$$S_{21} = (1+\hat{\epsilon})\left[1 + \frac{V_{\tilde{C}}}{2V_{in}}\left(\frac{M}{L} + i\omega C_c Z'_{in}\right)\right], \tag{3.12}$$

where

$$1 + \hat{\epsilon} \equiv \frac{2}{1 + \left(i\omega C_c + \frac{1}{Z_{out}}\right) + Z'_{in}} \tag{3.13}$$

and

$$Z'_{in} \equiv Z_{in} + i\omega L_1 - i\omega\frac{M^2}{L}, \tag{3.14}$$

assuming $|\hat{\epsilon}| \ll 1$. Subsequently, the Norton equivalent current becomes (see Fig. 3.1c)

$$I_N = -2V_{in}\left[\frac{\frac{M}{L} - \frac{i\omega C_c Z_{out}}{i\omega C_c Z_{out}+1}}{Z'_{out} + Z_{in} + i\omega\left(L_1 - \frac{M^2}{L}\right)}\right], \tag{3.15}$$

where

$$Z'_{out} \equiv \frac{Z_{out}}{i\omega C_c Z_{out} + 1}, \tag{3.16}$$

and we have

$$G_T = \frac{i\omega C_c}{i\omega C_c Z_{out} + 1} + \frac{\left(\frac{M}{L} - \frac{i\omega C_c Z_{out}}{i\omega C_c Z_{out}+1}\right)^2}{Z'_{out} + Z_{in} + i\omega\left(L_1 - \frac{M^2}{L}\right)}. \tag{3.17}$$

While the definitions in Eqs. 3.5a,3.5b and 3.5c still hold, we introduce

$$G' \equiv -\frac{I_N}{2V_{in}}\left(\frac{M}{L} + i\omega C_c Z'_{in}\right). \tag{3.18}$$

Equation 3.12 can now be rewritten as

$$S_{21} = (1 + \hat{\epsilon}) \left[1 - \frac{G' R_{eff}}{1 + 2iQ\frac{\omega - \omega 0}{\omega_0}} \right]. \tag{3.19}$$

Expanding in the small parameters M/L and $\omega C_c Z_{out}$ to second-order gives $G' = R_T^{-1}$, and hence higher orders are required to see effects from impedance mismatch. Taking $G_D \equiv G' - R_T^{-1}$, gives a purely imaginary term "creating" the asymmetry, and Eq. 3.19 becomes

$$S_{21} = (1 + \hat{\epsilon}) \left[1 - \frac{\left(G_D + R_T^{-1}\right) R_{eff}}{1 + 2iQ\frac{\omega - \omega 0}{\omega_0}} \right]. \tag{3.20}$$

By expanding to third order in G_D we find [90]

$$S_{21} = 1 - \frac{Q\hat{Q}_e^{-1}}{1 + 2iQ\frac{\omega - \omega 0}{\omega_0}}, \tag{3.21}$$

where

$$\hat{Q}_e \equiv \frac{\omega_0 \left(C + C_T\right)}{R_T^{-1} + G_D}, \tag{3.22}$$

and

$$Q_i^{-1} = Q^{-1} - Q_e^{-1} = Q^{-1} - \mathrm{Re}(\hat{Q}_e^{-1}), \tag{3.23}$$

and we have used $Q_e \equiv \mathrm{Re}(\hat{Q}_e^{-1})$ and the approximation $C_T \ll C$. The prefactor $1 + \hat{\epsilon}$ has been dropped in Eq. 3.21 as it only adds a constant phase and a constant multiplicative factor to the amplitude of S_{21}.

I should note that, for the fitting purposes, Eq. 3.21 requires one extra fitting parameter compared to the symmetric transmission case (Eq. 3.9), as $\hat{Q}_e$ is complex. This parameter can be defined as phase ϕ or frequency $\delta\omega$, depending on the format of Eq. 3.21, *i.e.*

$$S_{21} = 1 - \frac{Q|\hat{Q}_e^{-1}|e^{i\phi}}{1 + 2iQ(\omega - \omega_0)/\omega_0}, \tag{3.24}$$

or

$$S_{21} = 1 - \frac{Q}{Q_e} \frac{1 + 2iQ(\delta\omega/\omega_0)}{1 + 2iQ(\omega - \omega_0)/\omega_0}. \tag{3.25}$$

These different representations are discussed in more detail in Refs. [89, 90].

3.2.2 Dual-Cavity Method

In this method, we consider two cavities coupled to each other. One of the cavities (cavity c) represents the resonator, and the other (cavity d) models the mismatched transmission line. The insertion of cavity d into the model provides a degree of freedom to create asymmetric transmissions, and there is a one-to-one mapping of the fitting parameters to those introduced in section 3.2.1. This model follows from the technique of Collett and Gardiner [91].

Figure 3.2 depicts the model in a simple block diagram. Cavity d is a two-sided cavity with photon decay rates γ_1 and γ_2, representing coupling to semi-infinite input (1) and output (2) transmission lines allowing for transmission measurements. Cavity d is assumed to be a low-Q cavity that represents one mode. Physically, this mode would correspond to a standing wave on the chip and this has been found to produce the same transmission lineshape as described in the previous section [92]. Even though a full description of the standing wave is generally not available in practice, it is reasonable to assume that cavity d has a low-Q mode that represents a standing wave on chip and can be used to match boundary conditions. With the assumption that cavity d has one low-Q mode, I next show that the transmission lineshape has the same form as that found in Section 3.2.1.

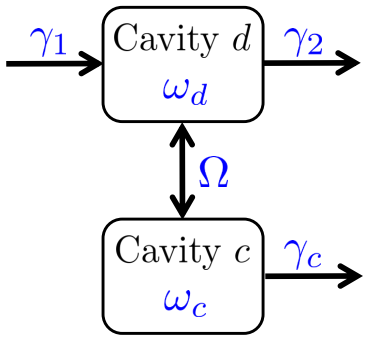

Figure 3.2: The Dual-Cavity Model.

I proceed by assuming a low-Q mode in cavity d that is coupled to the transmission line halves through γ_1 and γ_2. Cavities c and d are coupled to each other with rate Ω. Ignoring γ_1, γ_2, and γ_c, the Hamiltonian for this system is

$$\mathcal{H}_{sys} = \hbar\omega_c cc^\dagger + \hbar\omega_d dd^\dagger + \hbar\Omega\left(cd^\dagger + dc^\dagger\right), \tag{3.26}$$

where c and d are the photon annihilation operators of the corresponding cavities. Similar to Eq. 1.29,

$$\begin{aligned} \left[d, d^\dagger\right] &= \left[c, c^\dagger\right] = 1, \\ \left[c, d^\dagger d\right] &= \left[d, c^\dagger c\right] = 0, \\ [c, d] &= \left[c, d^\dagger\right] = \left[d, c^\dagger\right] = 0. \end{aligned} \tag{3.27}$$

The Heisenberg equations give the solution for *lossless* coupled light modes as [93]

$$\frac{d}{dt}c = -i\omega c = -\frac{i}{\hbar}\left[c, \mathcal{H}_{sys}\right], \tag{3.28a}$$

$$\frac{d}{dt}d = -i\omega d = -\frac{i}{\hbar}\left[d, \mathcal{H}_{sys}\right]. \tag{3.28b}$$

Including loss, one can obtain the quantum-mechanical Langevin equations [94] for the one-sided one-mode cavity c as

$$\frac{d}{dt}c = -i\omega c = -\frac{i}{\hbar}\left[c, \mathcal{H}_{sys}\right] - \frac{\gamma_c}{2}c + \sqrt{\gamma_c}c_{in}, \tag{3.29}$$

and

$$\frac{d}{dt}c = -i\omega c = -\frac{i}{\hbar}\left[c, \mathcal{H}_{sys}\right] + \frac{\gamma_c}{2}c - \sqrt{\gamma_c}c_{out}, \tag{3.30}$$

where γ_c, c_{in} and c_{out} are the decay rate, the input field and the output field of cavity c, respectively, and $\sqrt{\gamma_c}$ in the last term appears due to a quantum fluctuation-dissipation theorem [91,95]. Similarly, considering $d_{1,in}$, $d_{1,out}$, $d_{2,in}$ and $d_{2,out}$ as the input and output fields of the two-sided cavity d, we get

$$\frac{d}{dt}d = -i\omega d = -\frac{i}{\hbar}\left[d, \mathcal{H}_{sys}\right] - \frac{\gamma_1}{2}d - \frac{\gamma_2}{2}d + \sqrt{\gamma_1}d_{1,in} + \sqrt{\gamma_2}d_{2,in}, \tag{3.31}$$

and

$$\frac{d}{dt}d = -i\omega d = -\frac{i}{\hbar}\left[d, \mathcal{H}_{sys}\right] + \frac{\gamma_1}{2}d + \frac{\gamma_2}{2}d - \sqrt{\gamma_1}d_{1,out} - \sqrt{\gamma_2}d_{2,out}. \tag{3.32}$$

The boundary conditions which relate the input and output fields to photon annihilation in each cavity, can be written as

$$c_{in} + c_{out} = \sqrt{\gamma_c}c, \tag{3.33}$$

$$d_{1,in} + d_{1,out} = \sqrt{\gamma_1}d, \tag{3.34}$$

and

$$d_{2,in} + d_{2,out} = \sqrt{\gamma_2}d. \tag{3.35}$$

We assume only one input field ($d_{1,in}$) and set $d_{2,in} = c_{in} = 0$. By using the above boundary conditions, we obtain

$$c = \frac{-2i\Omega d}{\gamma_c - 2i\left(\omega - \omega_c\right)}, \tag{3.36}$$

$$c = \frac{2\gamma_c c + 2i\Omega d}{\gamma_c + 2i\left(\omega - \omega_c\right)}, \tag{3.37}$$

$$d = \frac{2\sqrt{\gamma_1} d_{1,in} - 2i\Omega c}{\gamma_1 + \gamma_2 - 2i\left(\omega - \omega_d\right)}, \tag{3.38}$$

and thus

$$d = \frac{2\gamma_1 d - 2\sqrt{\gamma_1} d_{1,in} + 2\sqrt{\gamma_2} d_{2,out} + 2i\Omega c}{\gamma_1 + \gamma_2 + 2i\left(\omega - \omega_d\right)}. \tag{3.39}$$

Solving for $d_{2,out}$ we get

$$d_{2,out} = \frac{2\sqrt{\gamma_1\gamma_2} d_{1,in}\left(\gamma_c - 2i\left(\omega - \omega_c\right)\right)}{\left(\gamma_c - 2i\left(\omega - \omega_c\right)\right)\left(\gamma_1 + \gamma_2 - 2i\left(\omega - \omega_d\right)\right) + 4\Omega^2}. \tag{3.40}$$

The classical S-parameter (transmission) for the wave amplitudes is then defined as the ratio of the output field to the input field, *i.e.*

$$S_{21} = \frac{\langle d_{2,out}\rangle}{\langle d_{1,in}\rangle}, \tag{3.41}$$

and thus

$$S_{21} = \frac{\sqrt{\gamma_1\gamma_2}}{\frac{\gamma_1+\gamma_2}{2} + i\left(\omega - \omega_d\right) + \frac{\Omega^2}{\gamma_c/2 + i(\omega - \omega_c)}}. \tag{3.42}$$

I note that in going from Eq. 3.40 to Eq. 3.42, I have conjugated the final expression to better match the experimental data, and note that the sign of ω can be chosen according to the convention used.

We can now see that there is a one-to-one mapping between the fit parameters in Eqs. 3.42 and 3.21 if certain assumptions are made. This correspondence was first pointed out to me by Dr. Osborn. As mentioned before, Eq. 3.21 has four

fit parameters. On the other hand, Eq. 3.42 has six. However, without loss of generality, I assume

$$\gamma_1 = \gamma_2 = \frac{\gamma_d}{2}, \tag{3.43}$$

which eliminates one of the extra fit parameters. Also, analysis of Eq. 3.42 near ω_c shows that we can take $Q_d \equiv \omega_d/\gamma_d$ to be a constant as long as it is much smaller than $Q_c \equiv \omega_c/\gamma_c$. In order to check this, I fit a transmission curve with $Q_d \in \{20, 10, 1, 0.1\}$ and found that the extracted parameters are indeed independent of Q_d to better than 0.1%. These assumptions reduce the number of fitting parameters in Eq. 3.42 to four.

In order to find the parameters ω_0, Q_i and Q_e in terms of the Dual-Cavity parameters, I can write Eq. 3.42 in the same form as Eq. 3.21. In this procedure, I found Eqs. 23 and 26 of Ref. [92] very helpful. The relationships between the parameters are

$$\omega_0 = \omega_c, \tag{3.44}$$

$$Q_i = Q_c = \frac{\omega_c}{\gamma_c}, \tag{3.45}$$

$$Q_e = \frac{\gamma_1 + \gamma_2}{4\Omega^2}\omega_c = \frac{\gamma_d \omega_c}{4\Omega^2}. \tag{3.46}$$

I skip the relations for the fourth parameter which can be defined differently depending on the S_{21} format used.

Equation 3.42 can be used to analyze the response of a resonator that is coupled to TLSs in an ensemble-averaged manner. I wrote a fully-automated Matlab code that used this equation to fit my experimental data and extract the resonance parameters. In the code, a Least-Squares Monte Carlo (LSM) method is used to

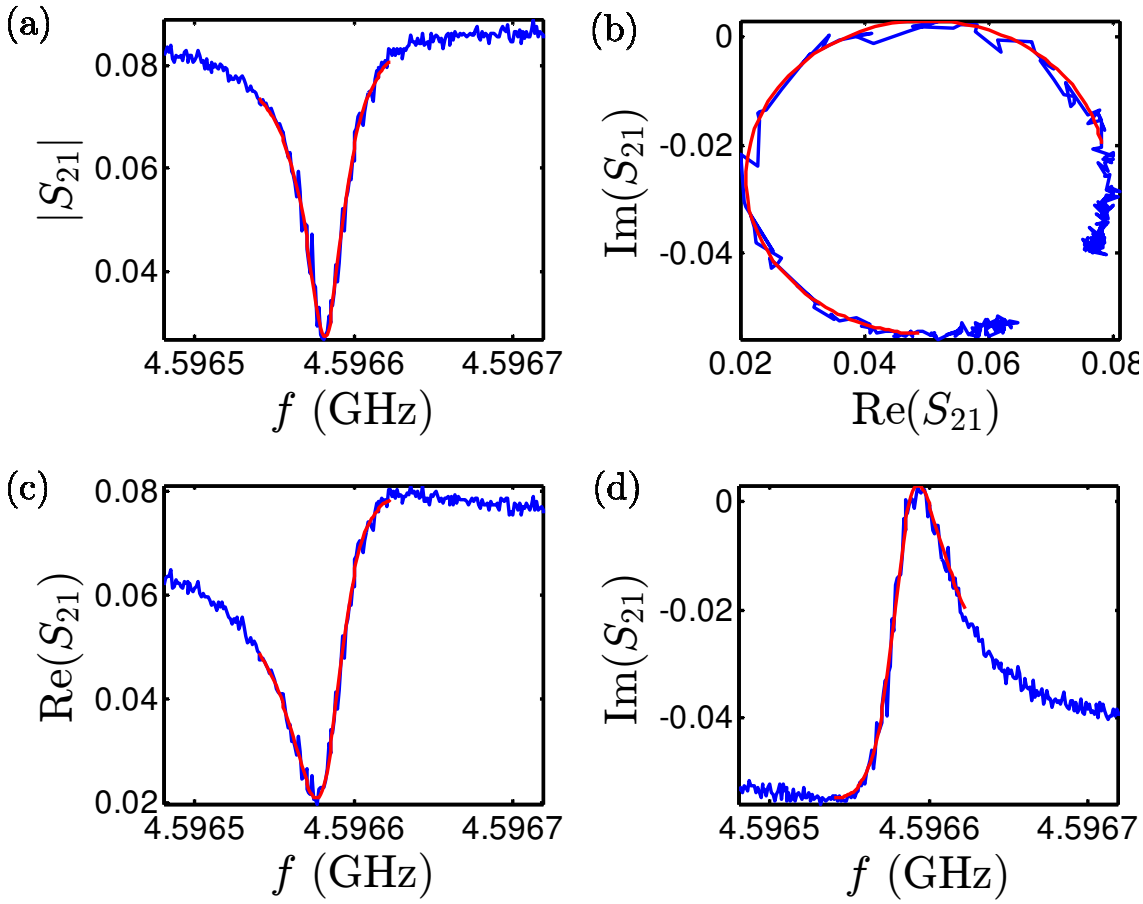

Figure 3.3: Sample fit (red) to a resonance lineshape using the combination of the Dual-Cavity Model and the LSM method. The data was taken on Res1 of TiN-RF-54 (see Chapter 7). The power at which this data (blue) was taken corresponds to an average photon number of $\bar{n} \simeq 9$ in the cavity. The fit yielded $\omega_0 = 4.596581985$ GHz, $Q_i = (\tan\delta)^{-1} = 3.48 \times 10^5$ and $Q_e = 1.67 \times 10^5$. (a) $|S_{21}|$ versus frequency f, (b) $\mathrm{Im}(S_{21})$ versus $\mathrm{Re}(S_{21})$, (c) $\mathrm{Re}(S_{21})$ versus frequency f and (d) $\mathrm{Im}(S_{21})$ versus frequency f.

find the optimum fits to $\mathrm{Re}(S_{21})$ and $\mathrm{Im}(S_{21})$ separately but simultaneously (see Fig. 3.3). I usually start by assuming $Q_d = 1$ and input initial guesses for γ_d, ω_c, γ_c, Ω and Θ. The Θ parameter accounts for a constant rotation angle of the experimental S_{21} with respect to the theoretical S_{21}, and appears as an extra multiplicative factor $e^{i\Theta}$ applied to the right hand side of Eq. 3.42. Next, a Monte Carlo guess in the form $x = x_0 e^{\xi\zeta}$ is made for each fit parameter, where x_0 is the previous (initial) guess for the fit parameter x, ζ is a randomly generated number between -1 and 1, and ξ is a parameter determining the guessing range. Usually, I take $\xi = 0.1$ for γ_d, γ_c, Ω and Θ and $\xi = 10^{-5}$ for ω_c. After this randomly generated guess, the theoretical S_{21} is calculated and subtracted from the experimental data, and then squared to obtain the error. If this error is smaller than the previous (initial) error, the new parameter values replace the previous (initial) ones. This procedure is repeated 10^4 times, and a reasonably good *preliminary fit* is obtained, from which the bandwidth of the resonance is calculated as $B = \omega_c/Q$. Next, a span of $2B$ is considered around ω_c and the rest of the data is ignored for the fitting to increase parameter extraction accuracy. Finally, the LSM method is used once again, this time with 10^5 (or more) steps, to obtain the *optimum fit*.

Figure 3.3 shows an example of such a fit to an asymmetric resonance lineshape I measured on a TiN resonator (see Chapter 7). In this example, the number of iterations was 10^5.

In this thesis, I have mostly used the LSM fitting method with the Dual-Cavity Model to analyze my data. In my experience, this combination had some advantages over using Matlab's Lorentzian fitting function combined with the DCM

method. Although the two models are equivalent, when the values of Q_i and Q_e are very different ($Q_i \ll Q_e$ or $Q_i \gg Q_e$), the Dual-Cavity Model combined with the LSM method was able to extract the fitting parameters more reliably and accurately (see Fig. 8.3). Furthermore, the Dual-Cavity Model offers the ability to "weight" arbitrary parts of the resonance lineshape. This is particularly useful if an ultra-high-accuracy fit is needed to the bottom of the dip. This can be achieved by assigning a larger weight to this fitting area and/or increasing the number of Monte Carlo steps.

Chapter 4: Experimental setup and fabrication equipment

In this Chapter, I describe the tools and equipment that I used to fabricate and measure my devices. All the key measurements were performed at cryogenic temperatures in a dilution refrigerator, and I begin with a description of these systems. This is followed by a description of the device fabrication equipment. The device fabrication required mastering several tools, including those used for DC sputtering, plasma enhanced chemical vapor deposition (PECVD), reactive ion etching (RIE), inductively coupled plasma etching (ICP) and photolithography (stepper).

4.1 Dilution refrigerator setup

In a dilution refrigerator (DR), cryogenic temperatures are reached by continuously circulating a mixture of ^{3}He and ^{4}He isotopes [96]. At low temperatures, a phase separation occurs to form a phase that is rich in ^{3}He which floats on a phase that is dilute in ^{3}He and rich in ^{4}He. These two phases form at a temperature below approximately 0.6 K, and energy (latent heat) is required for ^{3}He to go from the ^{3}He-rich phase to the ^{4}He-rich phase. By pumping on the ^{4}He-rich phase (usually with a turbo or roots pump) at about 0.7 K in the "still" mostly ^{3}He is removed and the concentration of ^{3}He in the ^{4}He-rich phase is reduced. The required ^{3}He for

reaching equilibrium comes from the ^{3}He-rich phase, "evaporating" into the ^{4}He-rich phase in the mixing chamber, and this requires energy to do so. This energy is absorbed as heat from the mixing chamber, cooling down whatever is thermally anchored to it, including the device under test (DUT).

Most of the measurements I describe in this thesis were performed in a CF-650 cryogen-free dilution refrigerator, manufactured by Leiden Cryogenics BV. I helped with the installation, microwave wiring and maintenance of this refrigerator. The rest of my measurements were performed in an Oxford Instrument Kelvinox model 400 dilution refrigerator. I will only describe the Leiden CF-650 setup here, since I used this refrigerator in most of my measurements and details of the Oxford refrigerator can be found in Ref. [89].

The Leiden CF-650 has 5 cold plates with the nominal temperatures of 50 K, 3 K, 0.7 K, 50 mK and 10 mK (see Fig. 4.1a). The cooling power is 650 μW at 120 mK. The DR has a Joule-Thomson heat exchanger to condense the mix, followed by a continuous sintered heat exchanger. It has two circuits for ^{3}He condensation (one is auxiliary). A two-stage Cryomech CP-1000 pulse-tube refrigerator is anchored to the 50 K and 3 K plates and keeps them at their nominal temperatures in steady operation. The DR can be controlled remotely using software provided by the manufacturer.

A schematic of the microwave circuit in the refrigerator is shown in Fig. 4.1b. I used an Agilent N3383A PNA Series network analyzer. In the input half of the circuit, from the network analyzer to the DUT input, we have installed attenuators (Midwest Microwave model ATT-0298-10-HEX-02) on each plate to reduce mi-

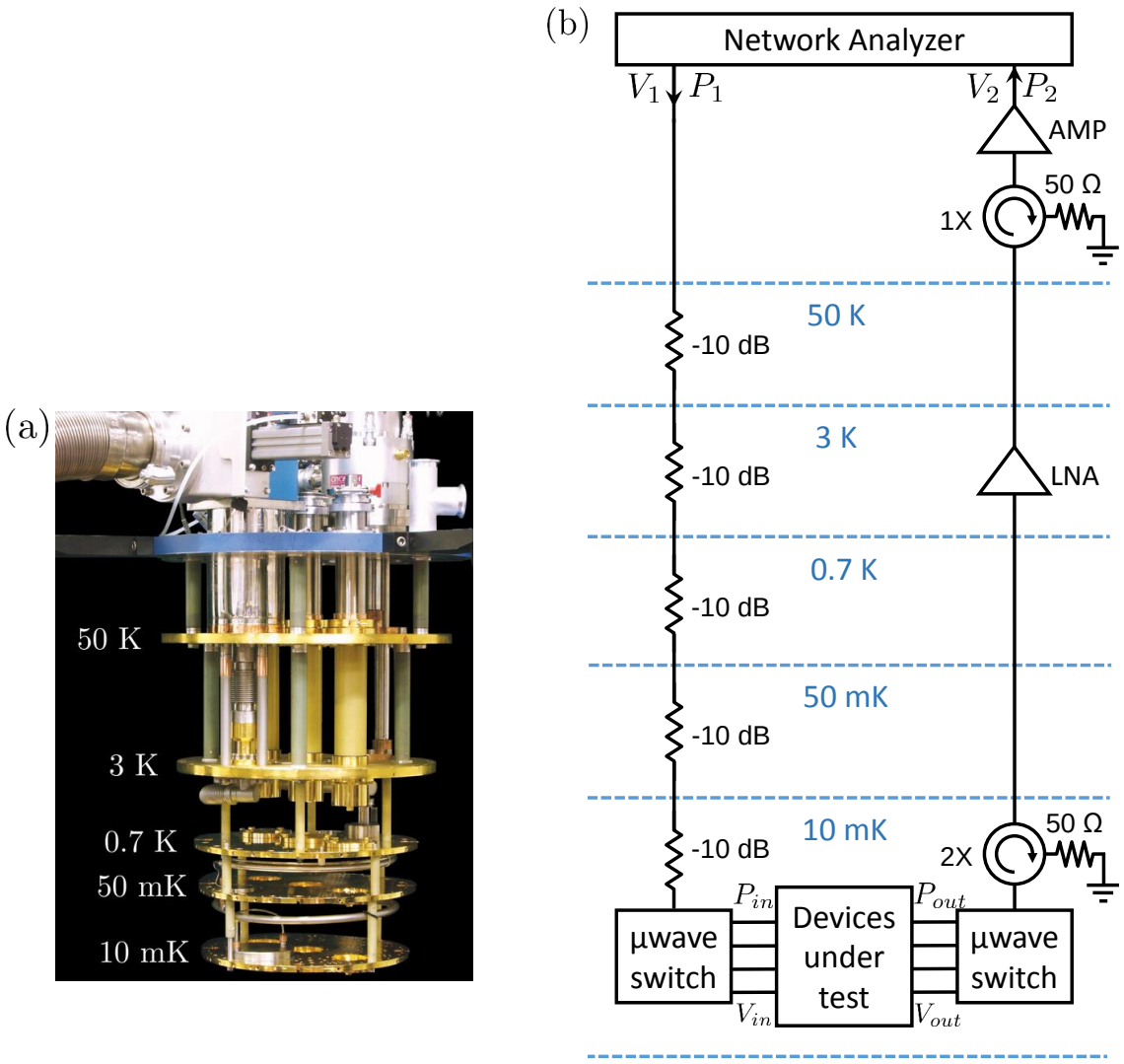

Figure 4.1: (a) Photograph of the cold plates on the Leiden CF-650 dilution refrigerator (courtesy of Leiden Cryogenics BV). (b) Schematic of microwave wiring in the refrigerator. V_{in} and V_{out} are the DUT input and output voltages, respectively.

crowave power coming from higher temperatures. These attenuators are thermally anchored to the plates using special copper anchors to allow the center conductor of the coaxial cable to cool. In the output half of the circuit, from the DUT output to the network analyzer, we have installed isolators (terminated circulators) to block microwave power and reflected waves from higher temperature stages. There is also a HEMT amplifier (LNA) model CIT-4254-077 on the 3 K plate. This LNA was purchased from the Weinreb group in Caltech, and has very low noise in the range 4-8 GHz. On the output at room temperature there is a low-phase-noise Miteq amplifier (model: AMF-5F-04000800-07-10P-LPN) with maximum noise figure of 0.7 dB and minimum gain of 50 dB in the frequency span of 4-8 GHz. Solenoid microwave switches (Radiall R573423600) are installed at the input and output of the devices under test, allowing us to connect up to six different cold samples without needing to warm up the DR. The group has continuously upgraded the DR wiring since purchase, and the current setup uses UT-85 copper-nickel coaxial cables, both for the input- and output lines.

4.2 Calibration of the input circuit

For many of my experiments, it was essential to know the total microwave attenuation on the input circuit (from the network analyzer to the DUT input). In other words, I needed to know the power P_{in} at the DUT as a function of the source frequency f and source power P_1. For example P_{in} was needed for TLS analysis while P_1 was the controllable variable. This calibration was critical because the

throughput for nonlinear systems depends on both the source frequency and the source power.

The calibration was performed by measuring the S_{21} throughput from the network analyzer to the device input in the frequency span of interest ($f = 4 - 7$ GHz) for three different source powers ($P_1 = -20, -10, 0$ dBm) with the DR at room temperature so that the connection to the DUT was accessible. For the calibrations, the dependence of P_{in} on f and was assumed to be log-linear (to first order), and P_{in} for an arbitrary f and P_1 was interpolated/extrapolated. Obviously, the calibration had to be redone each time the input circuit was modified.

Figure 4.2 shows the input calibration measurement of P_{in} versus f in the 4-7 GHz range for three applied powers P_1 as of May 2014. Each measurement of P_{in} versus f in Fig. 4.2a was fit to a log-linear expression to obtain the slopes α_i and the offsets β_i, $P_{in} = \alpha_i f + \beta_i$, where all powers are expressed in the $\log_{10}$ form (dBm). While the average of α_is (which I call $\bar{\alpha}$) determines the frequency dependence of P_{in}, the β_is are used to find the dependence of the power at the DUT (P_{in}) on the source power (P_1) as shown in Fig. 4.2b. The entire data set for different powers was then refit to the expression

$$P_{in} = \bar{\alpha} f + \alpha' P_1 + P', \tag{4.1}$$

and the slope α' and the offset P' were extracted. For the data shown in Fig. 4.2, I found $\bar{\alpha} = -1.8944$ dBm/GHz, $\alpha' = 1.0016$ and $P' = -68.9662$ dBm. Ideally, we expect $\alpha' = 1$, and there appears to be a small deviation that could be due to a small miscalibration of the network analyzer or nonlinearity of the circuit compo-

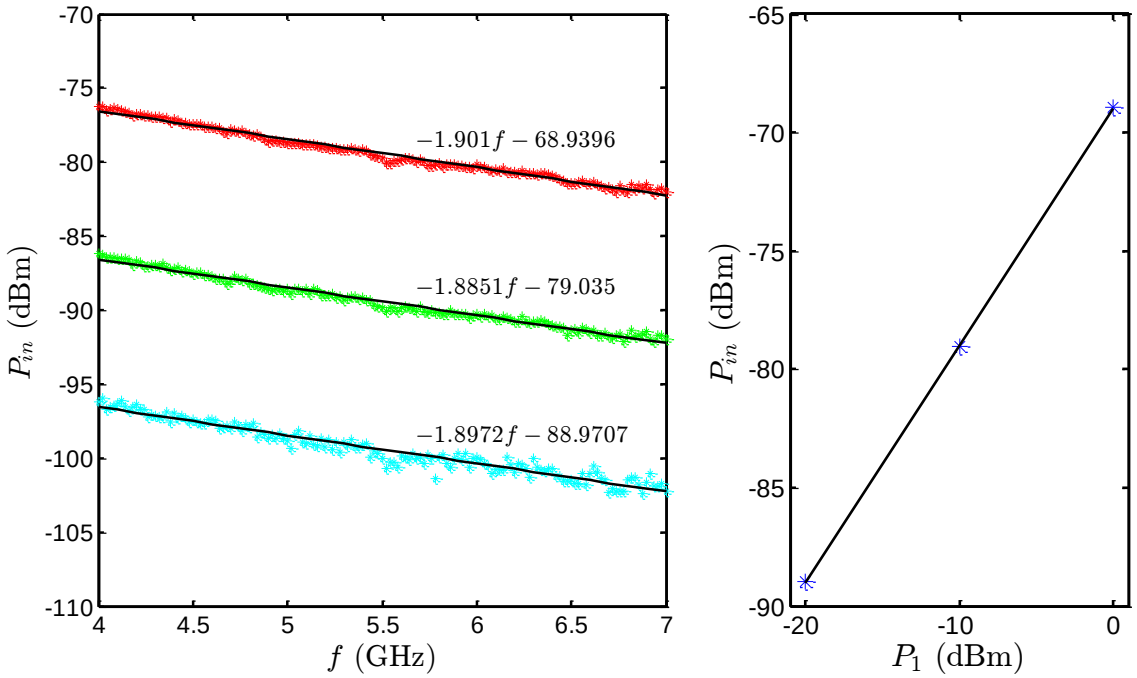

Figure 4.2: (a) Points show measured net throughput P_{in} (dBm) from the source to the DUT versus frequency f for different source powers P_1. Black lines are log-linear fits to data. The net throughput is obtained by subtracting the total throughput from the throughput of the coaxial cable that connects the device input channel to the network analyzer in the calibration setup. The data in cyan, green and red correspond to the measured net throughput at source powers of -20, -10 and 0 dBm, respectively. The frequency f in the calibration expressions is in GHz. (b) Power at DUT (P_{in}) and the linear fit versus source power (P_1).

nents. Although the attenuation from the input circuitry may depend weakly on temperature (most of the coax is stainless steel), I will assume that this dependence can be ignored and use Eq. 4.1 at cryogenic temperatures.

For the analysis of my TLS data, I needed to determine the DUT input voltage V_{in} and the electric field $\mathbf{E}$ in the dielectric under study for a given level of power at the source P_1 or the power at the DUT P_{in}. Since the thin-film microwave resonators I measured where all designed to have an input impedance of $Z_0 = 50\ \Omega$, we have

$$V_{in} = \sqrt{Z_0 P_{in}}. \tag{4.2}$$

Obviously, in order to use this, one must convert P_{in} from dBm to Watts.

To obtain the AC electric field $\mathbf{E}$ to which the TLSs are exposed, one needs to find the voltage across the capacitor $V_{\tilde{C}}$ (as introduced in Chapter 3) in terms of V_{in}. This can be done by referring to the Norton equivalent circuit of section 3.1. From Eqs. 3.3 and 3.4b and the definitions in that section, I can write

$$V_{\tilde{C}} = \frac{I_N}{\frac{1}{i\omega L} + i\omega\tilde{C} + G_T} = \frac{I_N}{\frac{1}{i\omega L} + \frac{1}{R} + \frac{1}{R_T} + i\omega\left(C + C_T\right)}. \tag{4.3}$$

According to Eqs. 3.5d and 3.5b, at resonance this becomes

$$V_{\tilde{C}}|_{\omega=\omega_0} = R_{eff} I_N. \tag{4.4}$$

Substituting this into Eq. 3.4a yields

$$V_{\tilde{C}}|_{\omega=\omega_0} = -\frac{V_{in} R_{eff}}{Z_0}\left(\frac{M}{L} - \frac{i\omega C_c Z_0}{i\omega C_c Z_0 + 1}\right). \tag{4.5}$$

The RMS voltage across $\tilde{C}$ is thus

$$V_{\tilde{C},RMS}\big|_{\omega=\omega_0} = \frac{R_{eff}}{Z_0}\left|\frac{M}{L} - \frac{i\omega C_c Z_0}{i\omega C_c Z_0 + 1}\right| V_{in,RMS}. \tag{4.6}$$

By using [89]

$$R_T = \frac{\omega^2 M^2}{2Z_0}, \tag{4.7}$$

and assuming $C_c \ll C$, we obtain

$$V_{\tilde{C},RMS}\big|_{\omega=\omega_0} = R_{eff}\sqrt{\frac{2}{Z_0 R_T}}V_{in,RMS}. \tag{4.8}$$

Equation 4.8 can be rewritten in terms of Q and Q_e as

$$V_{\tilde{C},RMS}\big|_{\omega=\omega_0} = \sqrt{\frac{2}{Z_0\omega_0 C Q_e}}QV_{in,RMS}. \tag{4.9}$$

From Eqs. 4.1, 4.2 and 4.9, I can find the RMS voltage across the capacitor $V_{\tilde{C},RMS}$ in terms of the source power P_1. If $\tilde{C}$ is a parallel-plate capacitor, the RMS electric field applied to the TLSs is simply $E_{RMS} = V_{\tilde{C},RMS}/d_0$, where d_0 is the dielectric thickness.

4.3 Fabrication apparatus

In this section, I briefly describe the tools that I used to fabricate devices. The processes I used for each experiment, including deposition, patterning, etching and characterization of metals and dielectrics, are described separately in the next chapters.

Sputtering

Figure 4.3a shows the Kurt J. Lesker model CMS-18 DC-sputtering system that I used for depositing aluminum and titanium nitride. It has a load lock with

oxidization capability and the 18" diameter by 15" high processing chamber accommodates three 3" diameter DC-sputtering guns. One of the guns is loaded with an aluminum target, and another with a titanium target (for reactive sputtering of titanium nitride). The third gun is currently unused. The guns are connected through a switch to a 1.5 kW/500 V DC power supply. The processing chamber is equipped with a cryopump which can pump the chamber to approximately 1×10^{-8} Torr. Three high-purity-gas inlets equipped with mass flow controllers are connected to the chamber to provide argon (for plasma generation), nitrogen and oxygen. The substrate is rotated by a speed-adjustable platen motor during deposition. The substrate can be heated up to 800°C, and temperature stabilization is automated using a PID controller integrated into the sputtering tool software.

There are also filaments installed inside the sputtering chamber to allow Ar ion-milling. These are connected to a separate power supply. The voltages used for ion milling is either 300 V (for substrate cleaning) or 800 V (for sputter etching). Also, an RF magnetron connected to a high-power RF source allows for RF-induced DC biasing of the substrate during sputtering. As I discuss in Chapter 7, varying the substrate DC bias (by changing the RF power) can significantly change the properties of reactively-sputtered titanium nitride films.

Photolithography

I did the patterning required for device fabrication using a 5X GCA stepper (see Fig. 4.3b) and 5" × 5" × 0.090" soda-lime reticles. Since most of the devices in

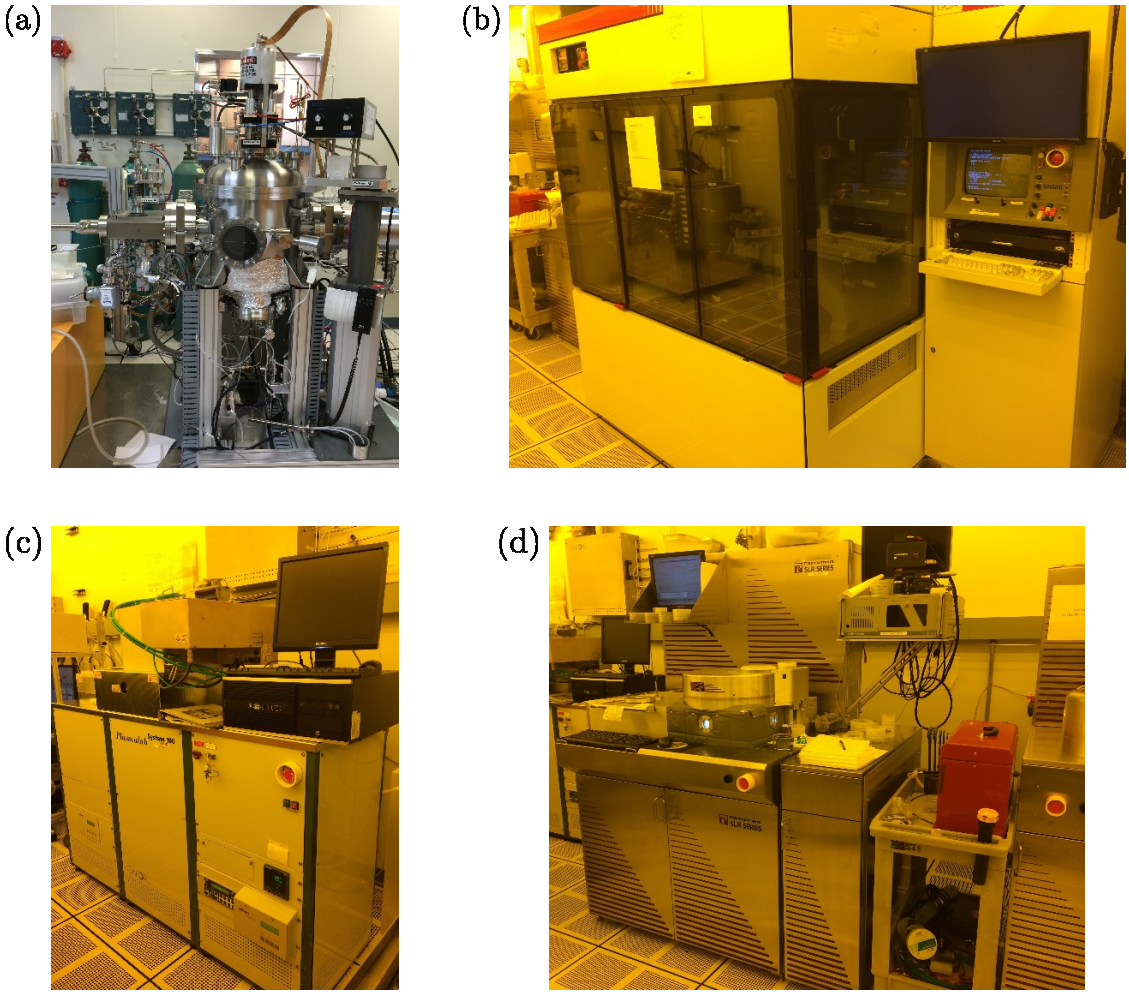

Figure 4.3: (a) Kurt J. Lesker model CMS-18 DC-sputtering system, (b) 5X GCA stepper, (c) Oxford Plasmalab System 100 PECVD and (d) Plasma-Therm SLR Series ICP in the LPS clean-room.

this thesis where formed from three layers, proper reticle alignment was crucial and I needed to calibrate the alignment before starting on a new wafer. I mostly used a positive photo resist (Fujifilm OiR 906-10), that I spun at 3000 rpm, pre-baked at 90°C, and post-baked at 120°C, each for 60 seconds. I used an exposure time of 0.25-0.35 seconds, depending on the type, age and performance of the UV lamp. The photo resist (PR) was developed using OPD 4262 developer. The PR removal followed my "standard organic cleaning" procedure: (i) acetone was sprayed onto the sample, (ii) the sample was then immersed in acetone and agitated in a sonicator for 1 minute, (iii) after removal from the acetone bath, the sample was rinsed with acetone, methanol and isopropanol, respectively, (iv) finally, nitrogen was used to blow-dry the sample.

Plasma-enhanced chemical vapor deposition

I used an Oxford Plasmalab System 100 (see Fig. 4.3c) for plasma-enhanced chemical vapor deposition (PECVD) to deposit SiN_x films using different recipes. These recipes differed in the flow rate ratio of SiH_4 to N_2, and resulted in films with different properties, most importantly the low-power microwave loss and the film stress. This has been investigated in detail by Paik *et al.* in Ref. [82]. In my devices, SiN_x was used either as capacitor dielectric, or insulator supporting superconducting bridges or spiral inductor cross-overs.

Inductively coupled plasma etching

For inductively coupled plasma (ICP) etching, I used a Plasma-Therm SLR Series machine (ICP/RIE) (see Fig. 4.3d). I used this system to etch titanium nitride (TiN), Al and AlO_x using chlorine based gases such as Cl_2 and BCl_3. The system has a load lock and automatically transfers samples from the load lock into the processing chamber.

Reactive ion etching

I also used a Plasma-Therm 790 Series reactive ion etching (RIE) system to etch SiN_x and TiN using SF_6-based recipes. The tool, shown in Fig. 4.4a, does not have a load lock, and the sample is directly loaded into the processing chamber.

Measurement of dielectric thickness and refractive index

Figure 4.4b shows the N&K 1500 Series spectrophotometer that I used for measuring SiN_x and AlO_x films. The system simultaneously measures film thickness, refractive index (N) and extinction coefficient (K) in the spectral wavelength range of 190-1000 nm. A baseline scan was required before every film measurement, using a reference bare Si wafer. The measurement spot size was 1 mm, and the tool was equipped with an automated X-Y stage for full sample mapping.

Profilometry

Figure 4.4c shows the Tencor P-10 profilometer. This highly-sensitive surface profiler drags a sharp stylus across the sample's surface while maintaining a constant downward force on the stylus. It features a vertical range from under 5 nm - 130 μm with better than 0.1 Å - 1 Å vertical resolution. The sample stage movement and rotation is controlled by software.

Film stress measurement

I used a Toho Technology FLX-2320-S stress measurement system (shown in Fig. 4.4d) to characterize the stress in thin films of metal or dielectric. Aside from characterization of TiN films, described in Chapter 7, this tool was very helpful for developing low-stress low-loss PECVD recipes for SiN_x. The tool determines the film stress by measuring the curvature change of a wafer between pre- and post-deposition measurements. The curvature difference of these two measurements is used to calculate stress by from Stoney's equation [97], which relates the stress to the biaxial modulus of the substrate, the thicknesses of the film and the substrate, and the radius of curvature of pre- and post-deposition wafers. Curvature was measured by directing a laser at the wafer surface at a known angle. The reflected beam was detected by a position-sensitive photodiode. The deflection was recorded while scanning the surface of the wafer. The wafer needs to be rotated manually by 180° using several smaller, but well-defined angle steps to map out the stress on the wafer. The resulting stress and deflection measurements can be visualized as

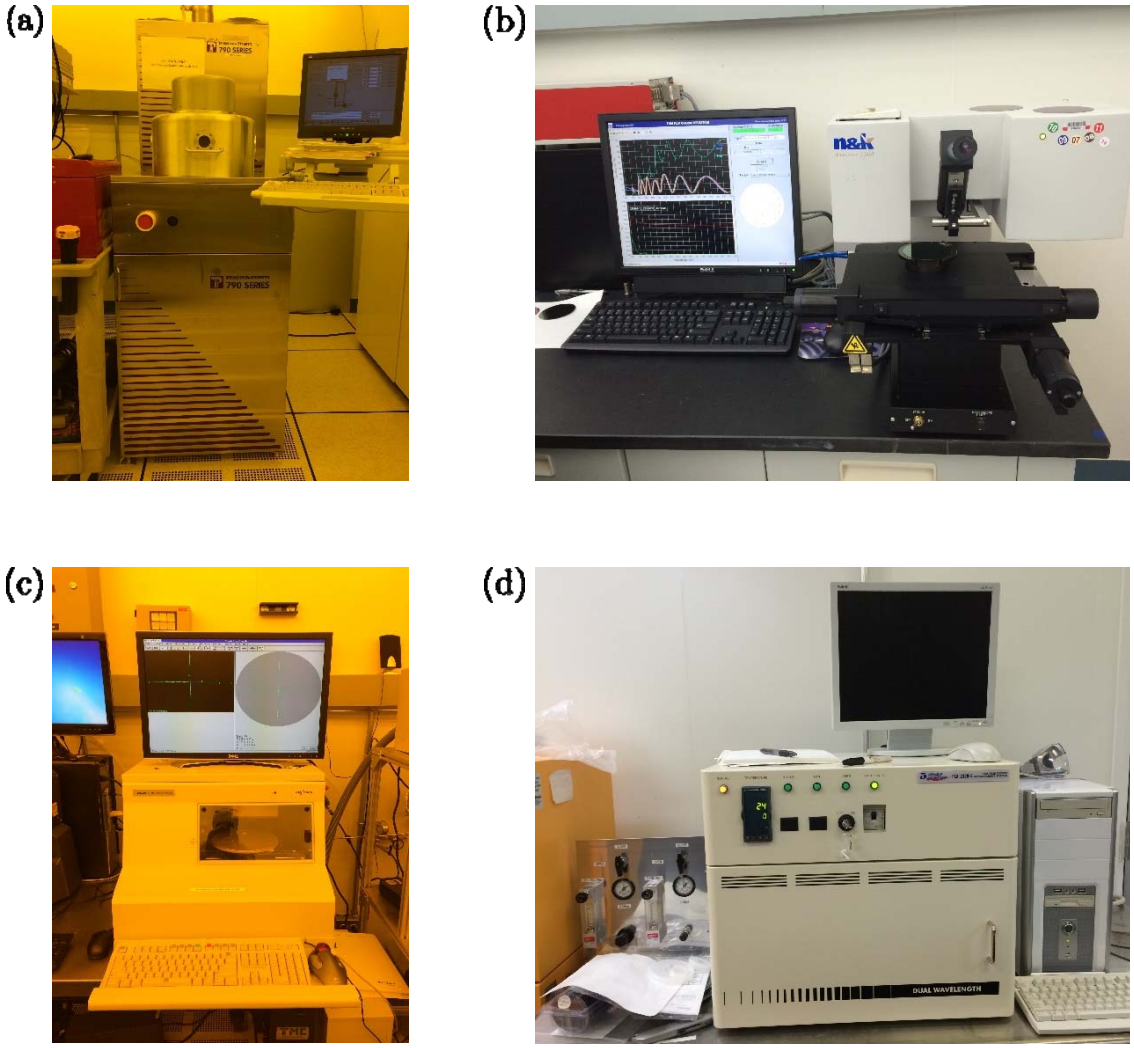

Figure 4.4: (a) Plasma-Therm 790 Series reactive ion etching (RIE) system, (b) N&K 1500 Series dielectric characterization system, (c) Tencor P-10 surface profiler and (d) Toho Technology FLX-2320-S stress measurement system.

3D plots provided by the system's software.

4.4 Integration and packaging

In this section I give brief descriptions of the device integration and sample preparation steps I followed to go from a fully-fabricated wafer to a sample mounted on the dilution refrigerator.

Integration

Figure 4.5 shows an example of a layout in which I integrate six resonators on the 6.35 mm $\times$ 6.35 mm die. This picture is from the circuit layout design program Cadence which I used for reticle design. This sample had a coplanar waveguide (CPW) in the middle with launchers at each end. The CPW width and spacing was designed for a 50 Ω impedance. I used two CPW geometries for my designs on sapphire or high-resistivity silicon substrates: width of 20 μm with spacing of 10 μm, or width of 10 μm with spacing of 5 μm. In general, my devices were coupled to the CPW both inductively and capacitively. When several resonators are coupled to the CPW, this results in a multi-band band-stop transmission through the same CPW, and I show examples of such devices in Chapters 5-8.

Dicing the wafer

For fabricating resonators, I used 2" (C-plane sapphire) and 3" (C-plain sapphire or high-resistivity silicon (100)) wafers and cut the final die size to 6.35 mm $\times$

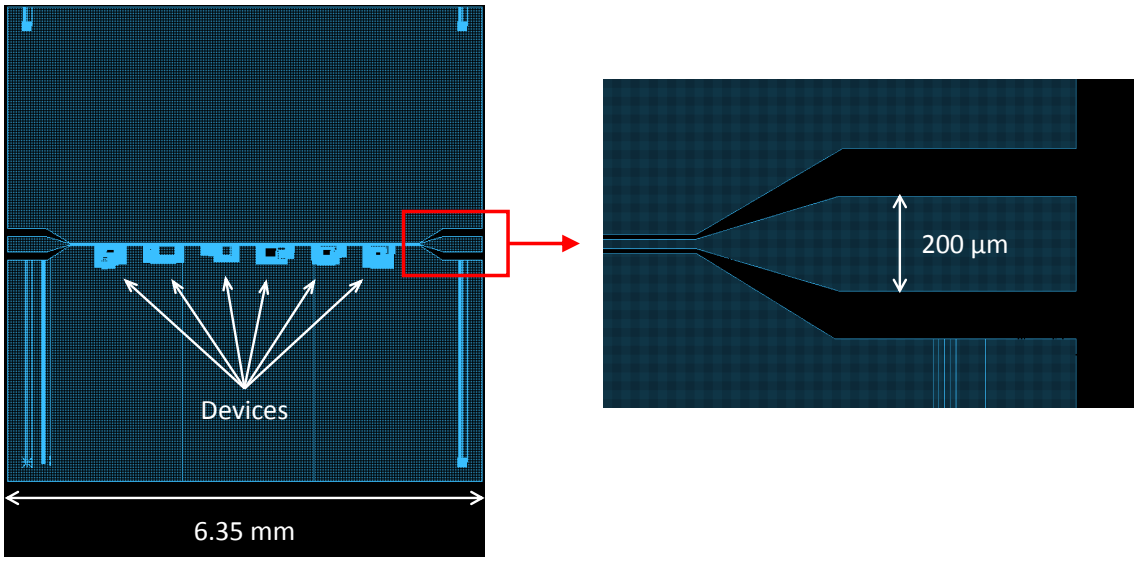

Figure 4.5: Device integration using Cadence. This Cadence layout is used for reticle fabrication. Only the first metal layer (blue) is shown here.

6.35 mm. Before dicing, wafers were coated with PR to protect the devices during dicing. For this purpose, I used Fujifilm OiR 906-10 PR baked at 120 °C for 120 seconds. Before dicing a wafer, a special dicing tape (Semiconductor Equipment Corp. Part Number: 18074) was carefully attached to the back of the wafer to hold the dies during and after the dicing. I used a Disco DAD 321 automatic dicing saw (see Fig. 4.6a) with the semi-automatic cut option. I used Dicing Blade Technology model CX-010-325-080-H and CX-010-600-080-H diamond blades to cut sapphire and high-resistivity Si wafers, respectively. This system requires a test cut on a dummy wafer for blade alignment followed by the alignment of the fabricated wafer and the saw. Finally, a number of cuts (depending on the die and wafer size) are

(a)

(b)

Figure 4.6: (a) Disco DAD 321 automatic dicing saw and (b) West-Bond model 7476E wedge bonder.

made in two directions. I used a cut speed for sapphire and silicon wafers of 0.5 mm/s and 3 mm/s, respectively, and the spindle speed was 30,000 rpm for both.

For my measurements, I tried to choose a die from the central area of the wafer, where the deposition/etch rates were well calibrated. The die was then cleaned using the standard organic cleaning process and optically inspected for flaws. Finally, I attached each test die to a sample box using GE low-temperature varnish. After letting the varnish dry for at least 2 hours, I wire-bonded to the ground plane and the CPW launchers.

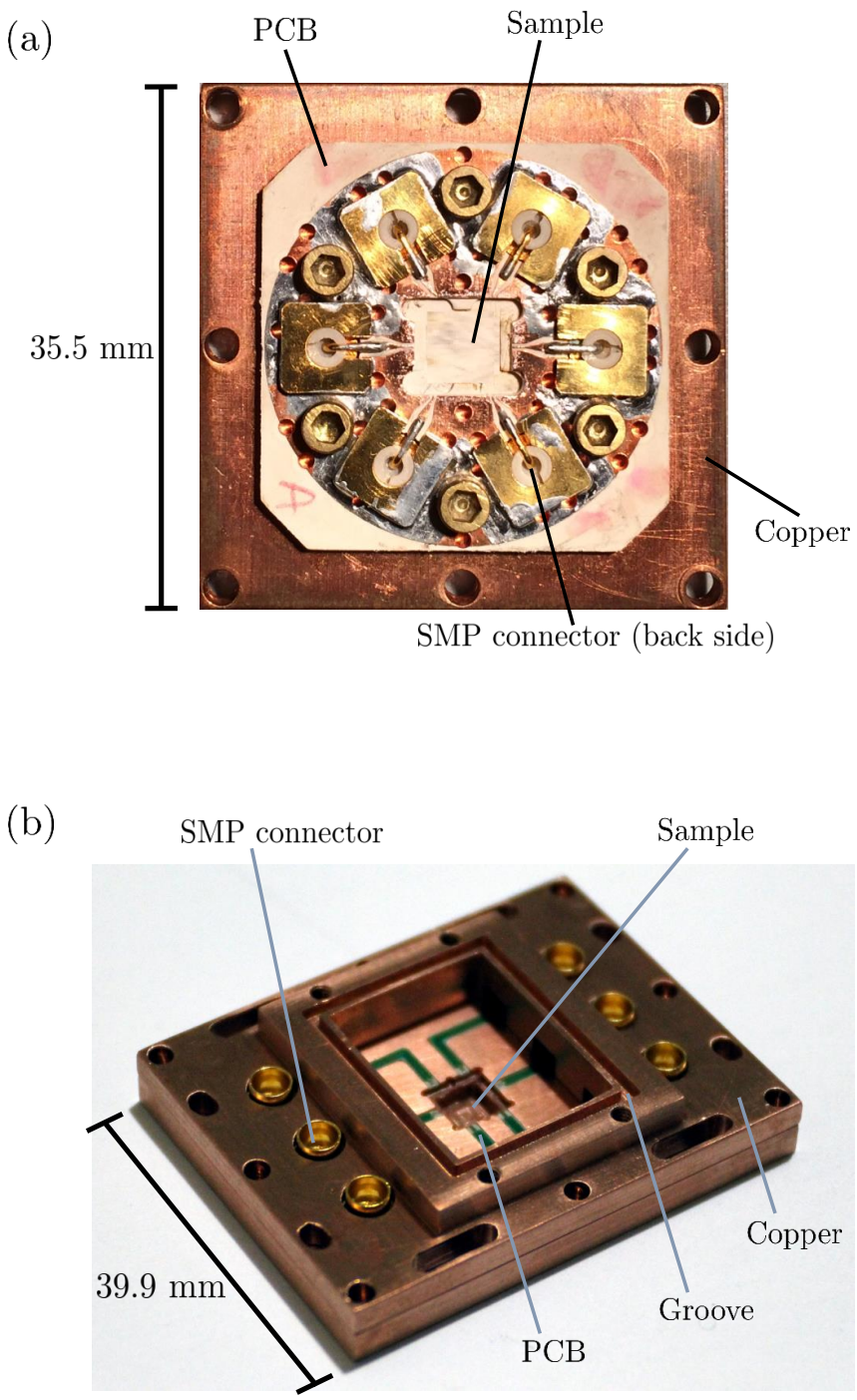

Figure 4.7: (a) Photograph of sample box type 1 and (b) sample box type 2 (designed by A. N. Ramanayaka).

Wire-bonding and sample boxes

Figure 4.6b shows the West-Bond model 7476E wedge bonder that I used to wire-bond my samples. I used SPM 1% Si/Al (aluminum) bond wire (Size: SIAL W-WI,.001).

I mainly used two types of sample boxes, shown in Fig. 4.7. Both sample boxes are made of copper and have a printed circuit board (PCB) insert. The type 2 sample box was most recently designed. It uses non-magnetic SMP connectors and has better infrared isolation than the type 1 sample box. The improved IR isolation is achieved by a matching groove and bump in the sample box and its lid (see Fig. 4.7b). I used Al wire-bonds to electrically connect the Cu sample box launchers (Cu) on the PCB to the sample's launcher (Al or TiN) on the sample chip. The sample chip sits in a well in the PCB (in the type 1 box) or in the copper (in the type 2 box) and is directly glued to the sample box with GE varnish.

Chapter 5: Cavity quantum electrodynamics of nanoscale TLSs

In this chapter, I describe my experiments that lead to the first CQED measurement of nanoscale TLSs [98].

5.1 Motivation

As discussed previously, TLSs have been found to be a major source of loss and noise in superconducting qubit circuits because of their coupling to the electric field. In 2004, Simmonds *et al.* observed individual TLSs in the JJ barrier of a phase qubit [67] (see Fig. 1.6) and later studied more TLSs in similar circuits [66]. Discrete TLSs in junction barriers were also seen in a Cooper-pair box [99]. Several other experiments have been performed to characterize individual TLSs and extract their coherence times [85, 86, 100].

Although these experiments and results from ensemble-averaged measurements [83, 101, 102] have provided much information about TLSs, the precise microscopic identity of TLSs remains unknown. This suggests the need for novel measurement techniques that can characterize individual TLSs and help search for materials with TLSs that have relatively long coherence times. In this chapter, I describe my direct CQED-based measurement of TLSs using a device that I call a micro-V

resonator. The micro-V resonator consists of a trilayer capacitor with SiN_x dielectric and a multi-turn (spiral) inductor. The capacitor (dielectric) volume is relatively small compared to previous devices used for resonator-TLS ensemble measurements [82, 83]. However, this volume is still at least three orders of magnitude larger than that of JJ barriers found in previous junction-based individual TLS measurements. As we will see, this meso-scale dielectric volume allows for CQED measurements of TLSs. This is due to the relatively small number of TLSs in the resonator bandwidth, their relatively long lifetimes and a relatively large TLS-resonator coupling due to the meso-scale SiN_x dielectric volumes.

5.2 Fully quantum-mechanical TLS-cavity model

I first consider a resonator (represented by a two-sided cavity c) and several TLSs, as shown in Fig. 5.1a. I assume that a coherent-state approximation can be used for photons in cavity c coupled to input field $\hat{a}_1$, output field $\hat{a}_2$. I represent the TLSs by the spin operator $\hat{S}_i^z$ due to the analogy between TLS theory and the spin-$\frac{1}{2}$ problem, as discussed in Chapter 2. Similar to the discussion in Section 3.2.2, the equation of motion for the cavity c photon annihilation operator $\hat{c}$ can be written as

$$\frac{d}{dt}\hat{c} = -\frac{i}{\hbar}[\hat{c}, \hat{\mathcal{H}}_{sys}] - \frac{1}{2}(\gamma_1 + \gamma_2)\hat{c} + \sqrt{\gamma_1}\hat{a}_{1,in} + \sqrt{\gamma_2}\hat{a}_{2,out}. \tag{5.1}$$

Here $\hat{\mathcal{H}}_{sys}$ is the system Hamiltonian, γ_1 and γ_2 are the cavity mode decay rates in input and output channels, and operators $\hat{a}_{1,in}$ and $\hat{a}_{2,out}$ represent the input and output fields in those channels respectively. The system Hamiltonian $\hat{\mathcal{H}}_{sys}$ can be

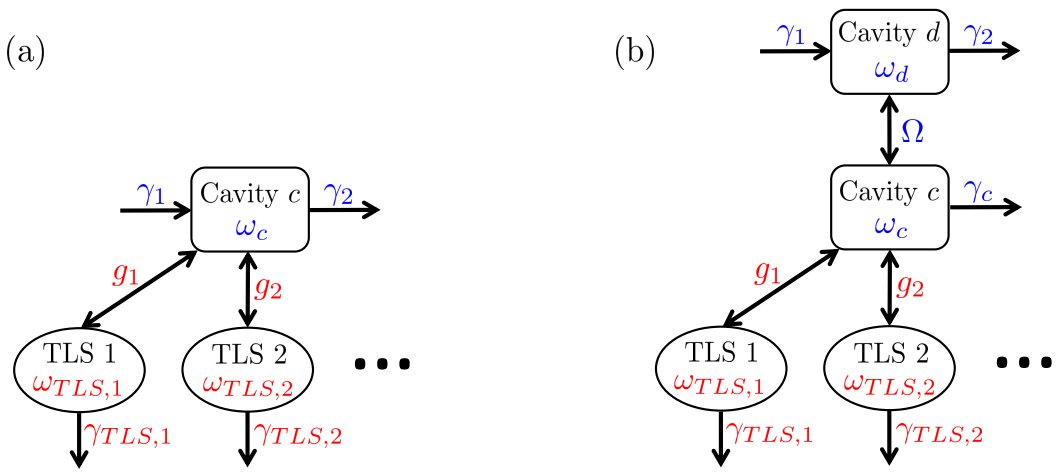

Figure 5.1: (a) The TLS-cavity quantum model with many TLSs and single cavity. (b) The Dual-Cavity Model with many TLSs coupled to cavity c.

written as

$$\hat{\mathcal{H}}_{sys} = \hbar\omega_c \hat{c}^\dagger \hat{c} - i\hbar \sum_{i=1}^{N} g_i (\hat{S}_i^- \hat{c}^\dagger + \hat{S}_i^+ \hat{c}) + \sum_{i=1}^{N} \mathcal{E}_i \hat{S}_i^z, \tag{5.2}$$

similar to the Jaynes-Cummings Hamiltonian (Eq. 1.50), except that there are N TLSs rather than just one. In Eq. 5.2, $\hat{S}_i^+$ and $\hat{S}_i^-$ are the TLS raising and lowering operators, respectively, ω_c is the resonant frequency of the cavity c mode, and the i-th TLS has energy $\mathcal{E}_i = \hbar\omega_{TLS,i} = \sqrt{\Delta_i^2 + \Delta_{0,i}^2}$ and resonant coupling g_i to the cavity field where

$$g_i = \frac{\Delta_{0,i}}{\mathcal{E}_i} p_i \cos\theta_i \sqrt{\frac{\omega}{2\epsilon_r \epsilon_0 \hbar V}}. \tag{5.3}$$

Equation 5.3 can be obtained from Eq. 2.33 and the cavity c (resonator) ground-state energy

$$C v_{RMS}^2 = \frac{1}{2}\hbar\omega. \tag{5.4}$$

Here p_i is the magnitude of the dipole moment $\mathbf{p}_i$ associated with TLS i, θ_i is the angle between $\mathbf{p}_i$ and the applied electric field $\mathbf{E}$, V is the dielectric volume, ϵ_r is its relative permittivity, and v_{RMS} is the RMS voltage across the capacitor C. Note the resemblance of Eq. 5.3 to Eq. 1.45 which comes from the fact that the effective cavity volume of the electric field for a resonator with a parallel-plate capacitor is simply the volume of the capacitor's insulator. If the input field is present in channel 1 only and it is harmonic with frequency ω, then one can represent the time evolution equation for the operator c as

$$i\omega\hat{c} = -i\omega_c\hat{c} - \frac{\gamma_c}{2}\hat{c} + i\sum_{i=1}^{N} g_i\hat{S}_i^- + \sqrt{\gamma_1}\hat{a}_{1,in}, \tag{5.5}$$

where $\gamma_c = \gamma_1 + \gamma_2$.

Similarly, one can write the equation for the time evolution of S_i^- operator using the Bloch equations approximation for relaxation and decoherence

$$-i\omega\hat{S}_i^- = -i\omega_{TLS,i}\hat{S}_i^- - \frac{\gamma_{TLS,i}}{2}\hat{S}_i^- - 2ig_i\hat{S}_i^z\hat{c}, \tag{5.6}$$

where

$$\gamma_{TLS,i} = k_{1,i} + 2k_{2,i}, \quad k_{1,i} = A\Delta_{0,i}^2\coth(\frac{\hbar\omega}{2k_BT}), \quad k_{2,i} \approx BT^2 \tag{5.7}$$

and rates $k_{1,i}$ and $k_{2,i}$ describe TLS i relaxation and phase decoherence rates associated with TLS-phonon and TLS-TLS interactions, and A and B are material-related constants. In the low temperature and low drive power limit ($k_BT \ll \hbar\omega$ and $\bar{n} \ll 1$), cavity c will be in its ground state or, with a much smaller probability, in its first excited state. This suggests we can replace the spin operator S^z in the product S^zc in Eq. 5.6 with the ground state value $-1/2$ since the TLS will have

a high probability to be in its ground state when the cavity is excited [103]. With these assumptions we obtain a closed system of linear equations which can be solved for the TLS operators:

$$S_i^- = \frac{ig_i c}{i(\omega_{TLS,i} - \omega) + \frac{\gamma_{TLS,i}}{2}}. \tag{5.8}$$

In the high-temperature case ($k_B T \sim \hbar\omega$), one can use a mean field approach replacing the operator S^z in Eq. (5.6) with its thermodynamic average value, *i.e.*

$$\langle S^z \rangle = -\frac{1}{2}\tanh(\frac{\hbar\omega}{2k_B T}) = -s. \tag{5.9}$$

This approach is consistent with previous analysis of sound and microwave absorption by TLSs [104, 105]. To proceed, I now substitute the solution for S_i^- (Eq. 5.8) into Eq. 5.5 to obtain a solution for the cavity c field in the form

$$c = \frac{\sqrt{\gamma_1} a_{1,in}}{i(\omega_c - \omega) + \frac{\gamma_c}{2} + 2s\sum_{i=1}^{N} \frac{g_i^2}{i(\omega_{TLS,i} - \omega) + \frac{\gamma_{TLS,i}}{2}}}. \tag{5.10}$$

Using this result one can find transmission and reflection coefficient using the boundary condition

$$a_{1,in}(+\infty) = a_{1,in}(-\infty) - \sqrt{\gamma_1} c. \tag{5.11a}$$

$$a_{2,out}(+\infty) = a_{2,out}(-\infty) - \sqrt{\gamma_2} c. \tag{5.11b}$$

One can use a single-photon scattering function and the Møller operator to find the transmission [106–108]

$$S_{21} = -\frac{\sqrt{\gamma_1 \gamma_2}}{i(\omega_c - \omega) + \frac{\gamma_1 + \gamma_2}{2} + 2s\sum_{i=1}^{N} \frac{g_i^2}{i(\omega_{TLS,i} - \omega) + \frac{\gamma_{TLS,i}}{2}}}. \tag{5.12}$$

For a more comprehensive model that better approximates the real system, I add a low-Q cavity (cavity d) which accounts for the coupling of cavity c to the transmission line and adds the required degree of freedom for asymmetric transmissions, as discussed in section 3.2.2. This model is shown in Fig. 5.1b. The above equations can be modified to include both cavities d and c and their mutual interaction, and can be written as

$$\hat{\mathcal{H}}_{sys} = \hbar\omega_d \hat{d}^\dagger \hat{d} + \hbar\omega_c \hat{c}^\dagger \hat{c} + \hbar\Omega(\hat{d}^\dagger \hat{c} + \hat{c}^\dagger \hat{d}) - i\hbar \sum_{i=1}^{N} g_i(\hat{S}_i^- \hat{c}^\dagger - \hat{S}_i^+ \hat{c}) + \sum_{i=1}^{N} \mathcal{E}_i \hat{S}_i^z, \quad (5.13)$$

Assuming only one input field $a_{1,in}$ (i.e. $a_{2,in} = a_{3,in} = 0$) and the cavity d to be two-sided (with decay rates of γ_1 and γ_2) and using the mean field approach for S^z operators, one finds the solution for the cavity mode d in the form

$$d = \frac{\sqrt{\gamma_1} a_{in}(0)}{i(\omega_d - \omega) + \frac{\gamma_d}{2} + \dfrac{\Omega^2}{i(\omega_c - \omega) + \frac{\gamma_c}{2} + 2s \sum\limits_{i=1}^{N} \dfrac{g_i^2}{i(\omega_{TLS,i} - \omega) + \frac{\gamma_{TLS,i}}{2}}}}. \quad (5.14)$$

Finally, the transmission coefficient is calculated as

$$S_{21} = \frac{\sqrt{\gamma_1 \gamma_2}}{i(\omega_d - \omega) + \frac{\gamma_d}{2} + \dfrac{\Omega^2}{i(\omega_c - \omega) + \frac{\gamma_c}{2} + 2s \sum\limits_{i=1}^{N} \dfrac{g_i^2}{i(\omega_{TLS,i} - \omega) + \frac{\gamma_{TLS,i}}{2}}}}. \quad (5.15)$$

Using Eq. 5.9 for the high-temperature case, we can reexpress the transmission as

$$S_{21} = \frac{\sqrt{\gamma_1 \gamma_2}}{i(\omega - \omega_d) + \frac{\gamma_1 + \gamma_2}{2} + \dfrac{\Omega^2}{i(\omega - \omega_c) + \frac{\gamma_c}{2} + \sum\limits_{i=1}^{N} \dfrac{g_i^2 \tanh(\hbar\omega / 2k_B T)}{i(\omega - \omega_{TLS,i}) + \frac{\gamma_{TLS,i}}{2}}}}, \quad (5.16)$$

where I have flipped the sign of $\mathrm{Im}(S_{21})$ arbitrarily.

Equation 5.16 can be understood as follows. The sum over i means there are multiple resonance ("rotating") terms of the form $i\Delta\omega$ representing the resonance of cavity c, cavity d and the TLSs, with the TLS resonance terms having a hyperbolic temperature dependence. In this equation, γ_c accounts for all cavity decay mechanisms *except* the TLS-induced loss, which is accounted for by the summation term.

Alternatively, we can interpret Eq. 5.16 in terms of the TLS coupling strengths. The idea is that one can divide TLSs into two categories: weakly-coupled TLSs and strongly-coupled TLSs. Assuming an ideal inductor and parallel-plate capacitor, only TLSs in the capacitor that lie in the resonator bandwidth can couple strongly to the cavity resonance. In the micro-V devices presented in this chapter and the next, the number of these strongly-coupled TLSs is on the order of unity. The rest of the TLSs are only weakly coupled to the resonator, and their ensemble effect can be represented by a constant cavity decay rate at a fixed drive power and temperature.

If the TLSs with nearly continuous spectral density produce the dominant loss and all other losses are negligible (which is the case for the micro-V devices), then the effect of the bath of weakly coupled TLSs can simply be represented by γ_c. In particular, if there is just one strongly-coupled TLS, the system Hamiltonian becomes

$$\hat{\mathcal{H}}_{sys} = \hbar\omega_d \hat{d}^\dagger \hat{d} + \hbar\omega_c \hat{c}^\dagger \hat{c} + \hbar\Omega(\hat{d}^\dagger \hat{c} + \hat{c}^\dagger \hat{d}) - i\hbar g(\hat{S}^- \hat{c}^\dagger - \hat{S}^+ \hat{c}) + \mathcal{E}\hat{S}^z, \qquad (5.17)$$

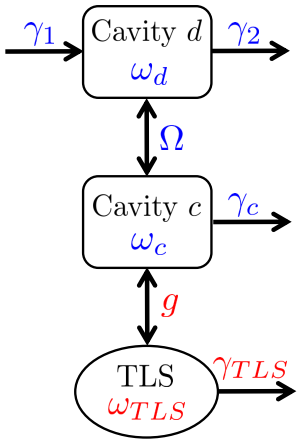

Figure 5.2: TLS-cavity quantum model with single strongly-coupled TLS and dual cavities.

and the transmission simplifies to

$$S_{21} = \frac{\sqrt{\gamma_1 \gamma_2}}{i\left(\omega - \omega_d\right) + \dfrac{\gamma_1 + \gamma_2}{2} + \dfrac{\Omega^2}{i\left(\omega - \omega_c\right) + \Gamma_c/2}}, \tag{5.18}$$

where

$$\Gamma_c = \gamma_c + \frac{2g^2 \tanh\left(\hbar\omega/2k_BT\right)}{i\left(\omega - \omega_{TLS}\right) + \gamma_{TLS}/2}. \tag{5.19}$$

We can consider Γ_c as a complex relaxation rate for cavity c which consists of a real term (γ_c) representing the bath of weakly-coupled TLSs and a "rotating" term due to the strongly-coupled TLS. Fig. 5.2 shows the corresponding model in a block diagram. Also, the TLS-cavity coupling rate simplifies to

$$g = \frac{\Delta_0}{\mathcal{E}} p \cos\theta \sqrt{\frac{\omega_0}{2\epsilon_r \epsilon_0 \hbar V}}, \tag{5.20}$$

From Eq. 2.31 and the low-temperature limit of Eq. 5.16, one can obtain the

average weakly-coupled TLS response

$$\gamma_{c,weak} = \left\langle \sum_{i,weak} \frac{g_i^2}{i(\omega - \omega_{TLS,i}) + \gamma_{TLS,i}/2} \right\rangle = \omega_c \frac{\pi P_0 p^2}{3\epsilon}. \tag{5.21}$$

Here I have used

$$\tan\delta = \frac{1}{Q_c} = \frac{\gamma_c}{\omega_c}, \tag{5.22}$$

where Q_c is the internal quality factor of cavity c. I can argue that one can distinguish a single TLS at resonance if the maximum single TLS response exceeds the average of Eq. 5.21, *i.e.*

$$\chi \equiv \frac{\pi P_0 \hbar V}{6\mathrm{T}_1} < 1, \tag{5.23}$$

where $\mathrm{T}_1 = 1/\gamma_{TLS}$ is the relaxation time of the strongly-coupled TLS.

5.3 Feasibility study

To achieve the limit where CQED effects can be seen for individual TLSs, two basic conditions must be fulfilled. First, the number of TLSs in the resonator bandwidth must be small enough such that they can be individually distinguished and measured. Second, the TLS-cavity coupling strength has to be large enough to produce measurable CQED effects.

To find the average number $\bar{N}$ of TLSs in the resonator bandwidth, I start from the standard distribution of TLSs described in Eq. 2.9. We need to integrate the standard distribution over energy and space, *i.e.*

$$\bar{N} = \int_V \int_{\mathcal{E}} \frac{P_0}{\Delta_0} d\Delta d\Delta_0 dV. \tag{5.24}$$

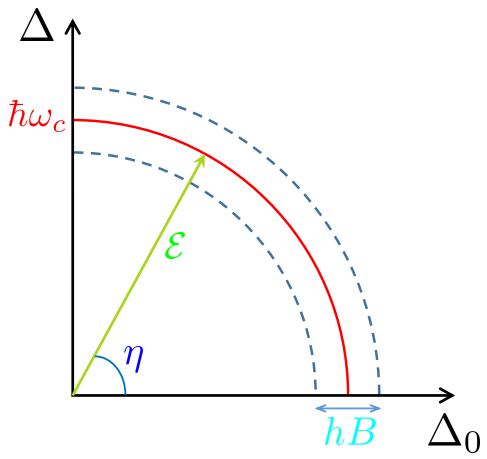

Figure 5.3: Δ-Δ_0 energy diagram. Dashed curves show the integration area.

Assuming a uniform spatial distribution, since the relevant TLSs lie in the capacitor dielectric only, the space integration simply yields a factor of V, the volume of the capacitor. The energy integration must be performed over the TLSs' asymmetry energy Δ and tunneling energy Δ_0 such that the TLS energy $\mathcal{E} = \sqrt{\Delta^2 + \Delta_0^2}$ is within energy hB (set by the resonator bandwidth B) around the resonance, shown by the dashed curves in the Δ-Δ_0 energy diagram of Fig. 5.3. Switching to polar variables $\mathcal{E} = \sqrt{\Delta^2 + \Delta_0^2}$ and $\eta = \arctan(\Delta/\Delta_0)$, the integration yields

$$\bar{N} = P_0 hBV \int_0^{\eta_{max}} \sec\eta d\eta = P_0 hBV \ln[\sec\eta_{max} + \tan\eta_{max}] \tag{5.25}$$

where η_{max} is an angle taken slightly smaller than $\pi/2$ to prevent the integral from diverging and to include only the strongest-coupled TLSs. In the discussion below, I use $\eta_{max} = 0.9 \times \frac{\pi}{2}$.

Next, I can estimate $P_0 = 8 \times 10^{42}$ J^{-1}m^{-3} from Eq. 2.31 and prior work

on Si-rich SiN_x [82]. For this estimation, I used $\epsilon = 6.5\epsilon_0$, $p = 7.9$ Debye and $\tan\delta_0 = 10^{-4}$, which are obtained from previous ensemble-averaged measurements [83]. Also, choosing $Q_e = 14000$, $\omega_c = 7$ GHz and using $Q_i = 10000$, I obtain $Q \simeq 6000$ and hence $B = 1.1$ MHz. Inserting the above values into Eq. 5.25, one finds that in order to get $\bar{N} = 1$, the dielectric volume must be $V \simeq 80\,\mu\text{m}^3$. This value corresponds to a very small parallel-plate capacitor compared to our group's previous resonators [82, 83], but it is at least three orders of magnitude larger than a typical JJ barrier volume in a qubit.

Regarding the coupling strength needed to see CQED effects from a TLS, one can see from Eq. 5.20 that $g \propto V^{-1/2}$, which means that shrinking the electric field volume not only reduces the number of TLSs, but it also increases the coupling. From this equation, the maximum TLS-cavity coupling that we can expect from TLSs in SiN_x with $p = 7.9$ Debye, $\omega_{TLS} = 7$ GHz and $V \simeq 80\,\mu\text{m}^3$ is $g_{max} = 5.6$ Mrad/s. Note that this implies the maximum splitting size is (see Fig. 1.3)

$$f_{g,max} = \frac{2g_{max}}{2\pi} = 1.8\,\text{MHz}. \tag{5.26}$$

This splitting size is more than enough to be distinguished in transmission data provided that the TLS coherence time is long enough to create a sharp resonance.

5.4 Device design

I designed five resonators with different dielectric volumes using AWR Microwave Office (see Fig. 5.4). The purpose of designing five resonators rather than one small-volume resonator was to see at what volume range the strong CQED

coupling of a TLS to the cavity can be observed. The areas of the parallel-plate capacitors were designed differently to accommodate dielectric volumes in the range of 80-5000 μm^3. I had to design the inductances differently too, as the resonance frequencies had to be in the range 4-8 GHz where the HEMT LNA provided optimum signal-to-noise ratio (SNR). I used multiturn (spiral) inductors, which have a larger inductance-per-length than a meandering inductor of the same line-width. The downside is that small cross-over capacitors are required in a multiturn geometry, making the circuit analysis and the measurement analysis slightly more complicated.

In addition to the five resonators shown in Figs. 5.4a-5.4e, I designed one extra resonator on the same chip. This extra resonator had the same geometry as the resonator shown in Fig. 5.4e, but it was placed closer to the transmission line to achieve higher coupling for an experiment on pulse-measurements of TLSs (analysis not included in this thesis). The resonators had resonance frequencies that differed by at least 250 MHz from each other (see Fig. 5.5) to create negligible shifts in frequency from resonator-resonator interactions and allow me to clearly identify a given resonance being due to a specific design.

The resonators were designed to have $11,000 < Q_e < 28,000$ except for the highly-coupled resonator, which was designed for $Q_e = 400$. I note that the AWR Microwave Office simulator does not directly give Q_e for a resonator. However, one can obtain the simulated value for the Q_e of a resonator by changing the Q_i in the simulation and looking at the depth of the resonance. If the resonator is critically coupled ($Q_e \simeq Q_i$), it will have a resonance lineshape with a depth of 6 dB, or $S_{21} =$

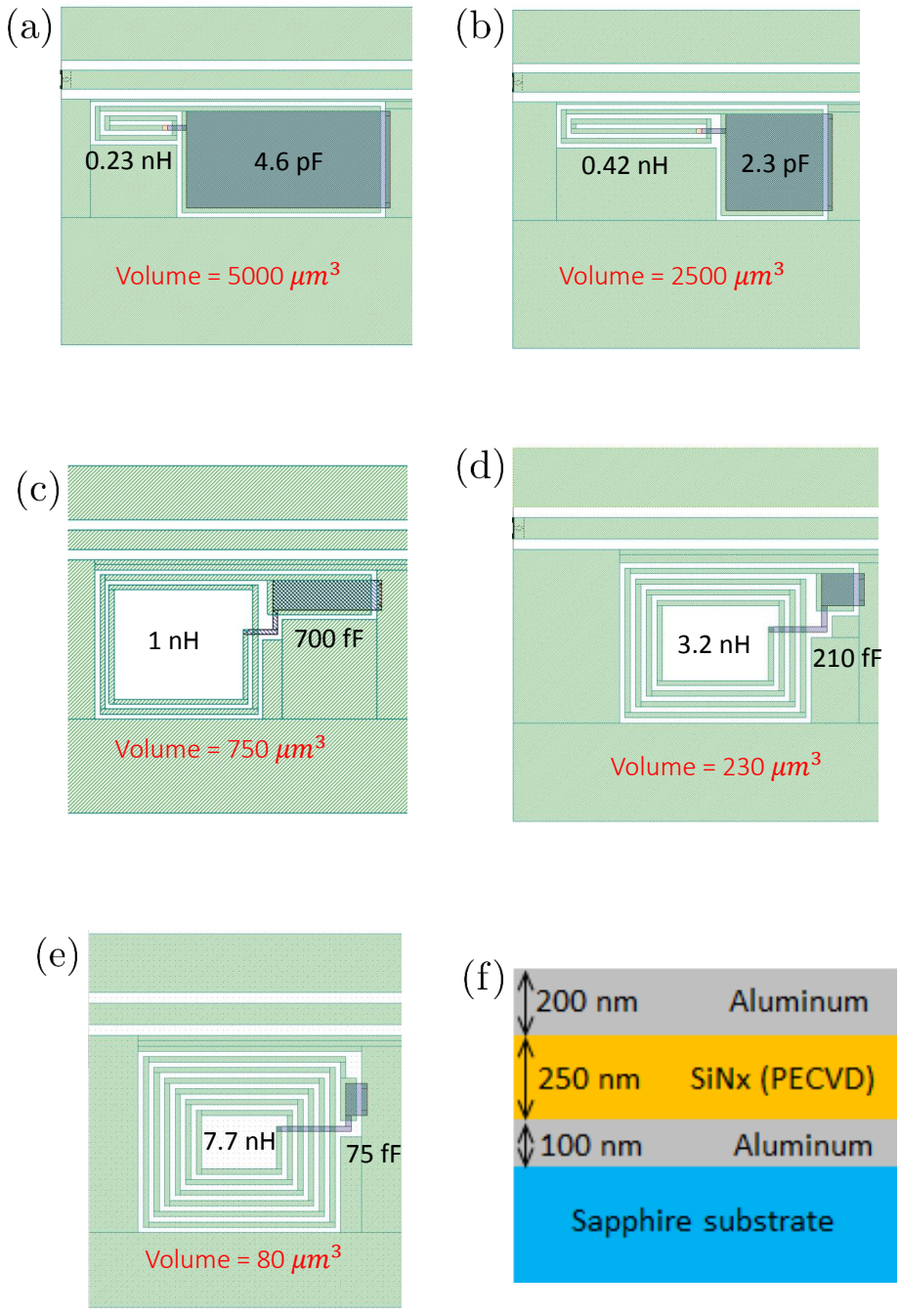

Figure 5.4: (a)-(e) Layout of five resonators with different dielectric volumes. (f) Capacitor cross section.

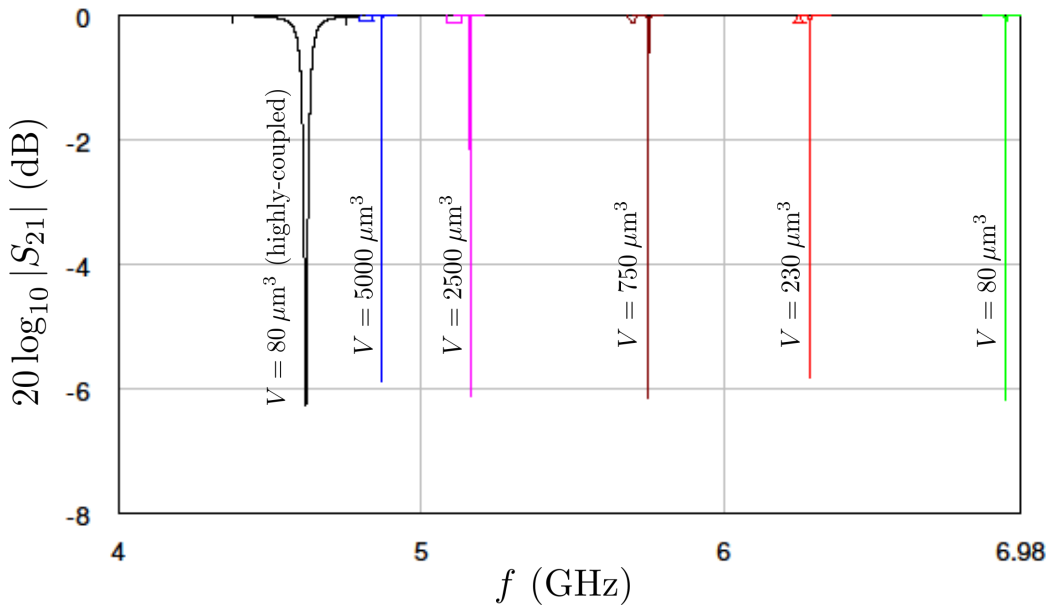

Figure 5.5: Device simulation results for $|S_{21}|$ versus frequency f for different capacitor volumes from AWR Microwave Office.

1/2 where it is defined as the output-input voltage ratio, $S_{21} \equiv 20\log_{10}(|V_{out}/V_{in}|)$. Thus, for my design of the resonators I chose a desired value for Q_e, set the dielectric loss tangent to $\tan\delta = 1/Q_e$ and adjusted the geometry of the resonator to get a ∼6 dB deep resonance lineshape. All of the resonances shown in Fig. 5.5 were simulated with $\tan\delta \simeq 1/Q_e$ for every resonator. In the simulation, the substrate loss tangent was set to zero.

5.5 Fabrication

I fabricated the resonators on a 3-inch sapphire wafer. The substrate was first inserted into the sputtering chamber and ion-mill cleaned at an Ar flow rate

of 6 sccm and beam voltage of 300 V for 30 s. Al was then DC-sputtered at 400 W (DC) with an Ar pressure of 5 mTorr. The sputtering lasted for 20 minutes and 30 s for a 100 nm thick Al film. This base metal layer was then coated with Fujifilm OiR 906-10 PR, exposed, developed and wet-etched to form the ground plane, the CPW, the spirals of the multiturn inductors, and the bottom capacitor plates. For wet-etching I used J.T.Baker Aluminum Etch 80-15-3-2. The PR was then removed using the standard organic cleaning process (see section 4.3) and the wafer was put inside the PECVD tool for dielectric deposition. A 250 nm thick film of amorphous hydrogenated silicon nitride (a-SiN_x:H) was then deposited using a relatively low-loss SiN_x recipe (PECVD) with SiH_4 and N_2 flow rates of 10 sccm and 9 sccm, respectively, at 300 °C. This dielectric film was covered with PR and photolithography was performed.

The film was etched to open the vias in the RIE tool using an SF_6-based recipe. For the RIE, the flow rates of SF_6 and O_2 were 20 sccm and 5 sccm respectively, and the processing chamber pressure was kept at 75 mTorr. After PR removal, the wafer was inserted back into the sputtering chamber, where the film was ion-milled using an Ar flow rate of 6 sccm and beam voltage of 800 V for 1 minute. The purpose of this step was to remove the native oxide formed on the base Al layer at the location of the vias. This ensures a continuous metal (superconducting) path between the via and the base metal layer. Next, without removing the wafer from vacuum, a 200 nm thick film of Al was DC-sputtered at a power of 400 W and the top metal layer and the vias were formed. By patterning this metal layer, the top capacitor plates were made.

Next the wafer went through photolithography and an SF_6-based etch to remove the SiN_x everywhere on the wafer, except for the areas supporting the top metal layer. This last step, performed using RIE, significantly reduces the stress caused by the SiN_x film and reduces stress-induced damage. For the same reason, the fabrication process, once started, needs to be completed as quickly as possible, typically within 8 hours. The sample was then diced and wire-bonded to the sample box type 1, shown in Fig. 4.7a.

Optical images of two devices I fabricated are shown in Fig. 5.6. I fabricated three sets (wafers) of these resonators. Each set was different in the SiN_x recipe used. The first set was made using N_2:SiH_4 flow rates of 9:10 sccm. This resulted in a relatively *low-loss*, high-stress, Si-rich film [82]. The second set was fabricated using N_2:SiH_4 flow rates of 12:10 sccm, resulting in a relatively *high-loss*, low-stress, N-rich film. For the third set, N_2:SiH_4 flow rates of 11:10 sccm were used, and resulted in a film with *medium-loss*, medium-stress and an intermediate stoichiometry with respect to the first two samples. Obviously, the first sample was best for CQED measurement of TLSs as it was made of a dielectric with the lowest TLS spectral density, which not only resulted in a relatively long cavity lifetime, but also facilitated individual TLS measurements. The high-loss sample was mostly used for ensemble-averaged measurements. The medium-loss sample was measured to study the feasibility of CQED with TLSs in lossier films.

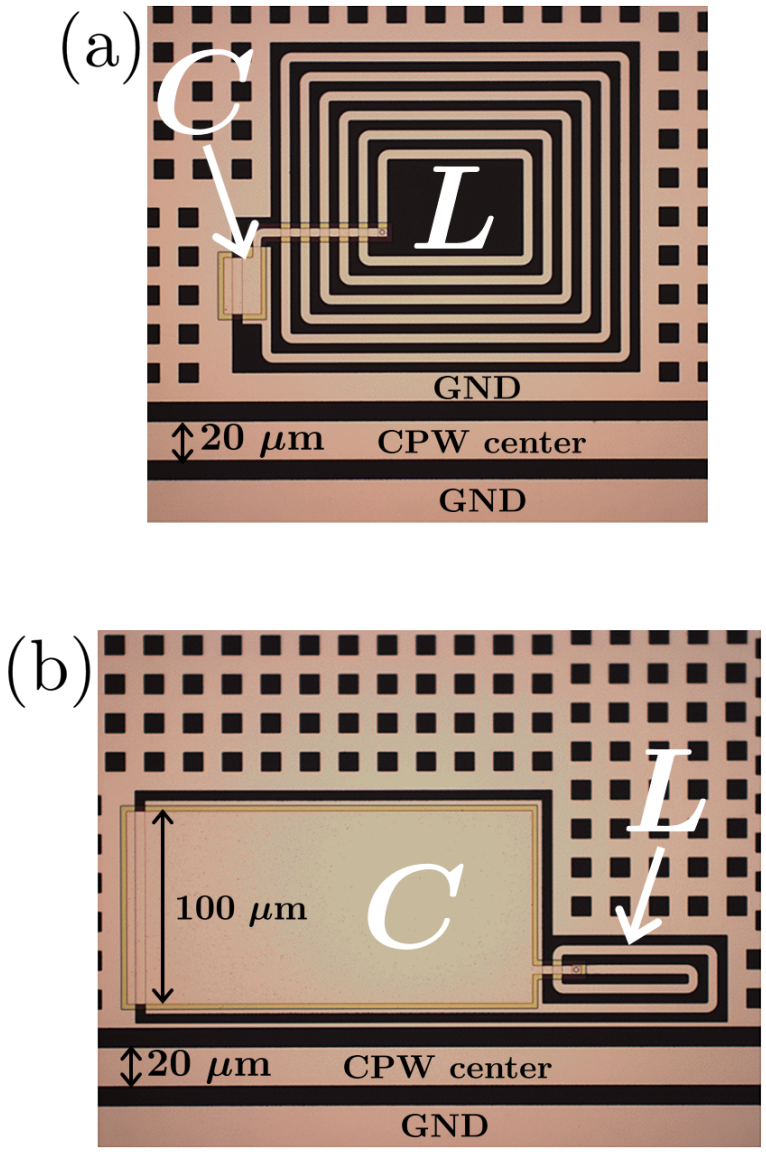

Figure 5.6: (a) Optical image of the smallest-volume and (b) the largest-volume resonators.

5.6 Large-V resonator measurements

I start with the analysis of the two largest-volume resonators ($V = 5000\,\mu\text{m}^3$ and $V = 2500\,\mu\text{m}^3$) on the low-loss sample. These resonators were first measured at

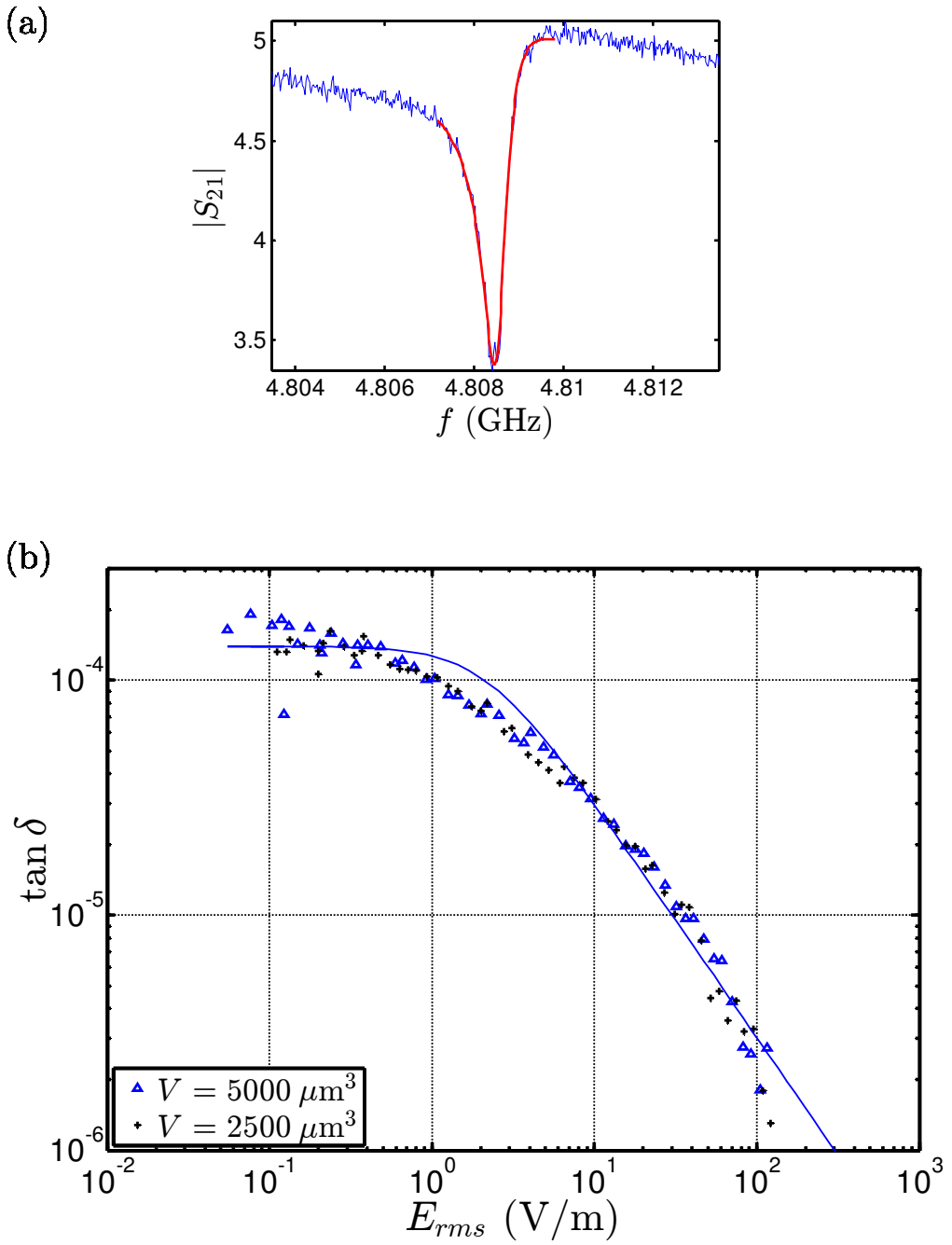

Figure 5.7: (a) Sample transmission data $|S_{21}|$ versus frequency f for the $V = 5000\ \mu\mathrm{m}^3$ resonator taken at an average photon occupancy of $\bar{n} \sim 0.1$. Data is shown in blue and the optimum fit is shown in red. (b) Black and blue points show measured loss tangent of the two largest-V resonators versus the RMS electric field in the capacitor. The solid blue line shows optimum fit to $\tan\delta = \tan\delta_0/\sqrt{1+(E/E_c)^2}$ for the $V = 5000\ \mu\mathrm{m}^3$ data.

25 mK, and at microwave powers corresponding to average cavity photon numbers ($\bar{n}$) of $\sim 10^{-4}$ to $\sim 10^{3}$. Due to the large dielectric volume, an average response due to many TLSs was observed, resulting in an asymmetric Lorentzian resonance lineshape throughout the entire measurement power span (see Fig. 5.7a). Figure 5.7b shows the loss tangent obtained from each resonator versus the RMS electric field E_{rms} inside the dielectric. Fitting these data to the standard power-dependent TLS ensemble response $\tan\delta = \tan\delta_0/\sqrt{1+(E/E_c)^2}$, I found that both resonators showed $\tan\delta_0 \simeq 1\times10^{-4}$ and $E_c = 4.6$ V/m which are similar to previous measurements of SiN_x [83]. The fact that both resonators show similar $\tan\delta_0$ and E_c indicates that these parameters are *intensive* in the corresponding volume range.

5.7 Micro-V device at low powers

The three smallest-volume resonators ($V = 750, 230, 80\,\mu\text{m}^3$) were measured next. At $T = 25$ mK and low powers for which the average number of photons in the cavity is $\bar{n} \ll 1$, one (or more) extra resonances were observed in the transmission S_{21} (see Fig. 5.8). The number and the clarity of these resonances seemed to be correlated with V, such that the smallest number of TLSs and the most clear splittings were seen in the smallest volume device. However, in order to reach a firm conclusion on this, a larger number of resonators with different volumes in the range $V < 750\,\mu\text{m}^3$ would be required. I note that when there are two or more clear resonances in the transmission, each resonance will correspond to a hybridized state which is, in general, a superposition of the cavity state and modes corresponding

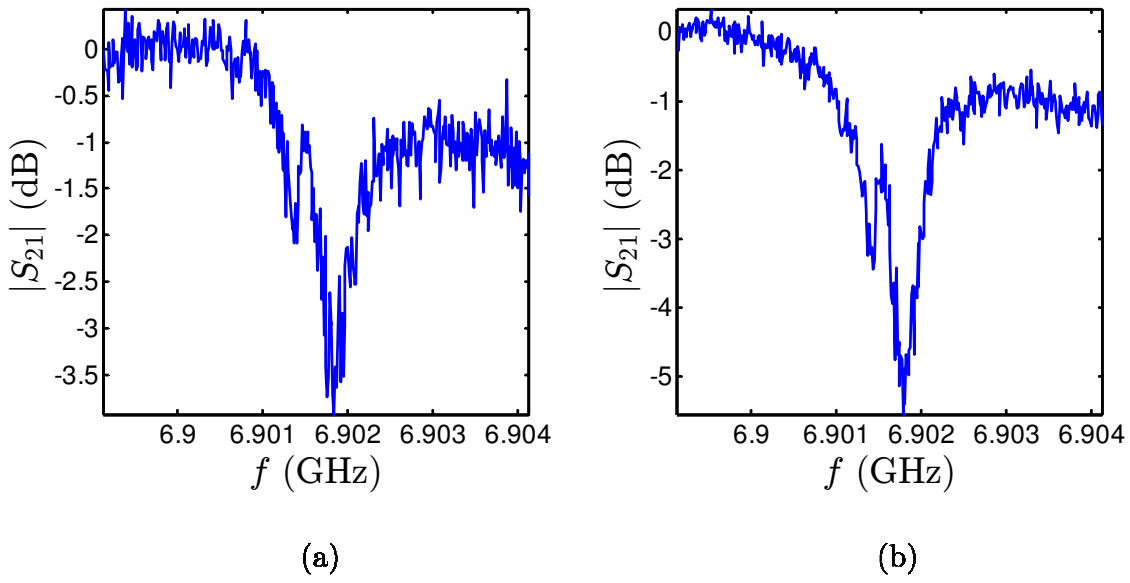

Figure 5.8: (a) Sample transmission data $|S_{21}|$ versus frequency f for the micro-V device with $V = 80\,\mu\text{m}^3$ taken at 25 mK and $\bar{n} \sim 0.01$ and (b) $\bar{n} \sim 0.1$.

to one or more TLSs. Since the mesoscale volume devices enable measurement on these hybridized states, we refer to them as micro-V devices. For the micro-V device with $V = 80\,\mu\text{m}^3$, usually no more than two clear resonances appeared, and they generally looked more clear than the resonances seen in the data of devices with $V = 750\,\mu\text{m}^3$ and $V = 230\,\mu\text{m}^3$.

These two resonances in the $V = 80\,\mu\text{m}^3$ device indicate that only one "dominant" TLS is strongly coupled to the resonator and any other TLSs in the bandwidth are only weakly coupled and result in a purely real cavity relaxation rate γ_c, as described in section 5.2. Figs. 5.8 and 5.10 show sample transmissions of this device. Since this micro-V device ($V = 80\,\mu\text{m}^3$) allowed for a simpler CQED analysis of a TLS due to strong coupling to only one TLS, I focus on this device for the rest of

this chapter.

One of the first measurements I performed on the micro-V device with $V = 80\ \mu\text{m}^3$ was a mode stability check. For this purpose, I swept the power back and forth in the range $0.01 \lesssim \bar{n} \lesssim 0.1$ for approximately 14 hours at 25 mK. The results, shown in Fig. 5.9a, revealed that the splitting was generally observed at all times, but there was a relatively slow TLS drift that caused occasional slight shifts in the mode frequencies. For comparison, a stability check was also performed on a large-V resonator ($V = 5000\ \mu\text{m}^3$) which exhibited one stable resonance (cavity mode) at all times, as expected. This is shown in Fig. 5.9b.

5.7.1 Analysis of $T = 25$ mK data

Since only one TLS was strongly coupled to the micro-V device, I can compare my data to the theoretical model shown in Fig. 5.2. The system Hamiltonian and transmission are described by Eqs. 5.17 and 5.18, respectively. I used the low temperature limit of the latter equation to fit the data taken at 25 mK shown in Fig. 5.10a-5.10c. I used a Least Squares Monte Carlo (LSM) method, similar to the fitting code described in section 3.2.2. For better accuracy, the fitting was performed on $\text{Re}(S_{21})$ and $\text{Im}(S_{21})$ separately (see Figs. 5.10b and 5.10c) rather than to $|S_{21}|$. For these fits, I assumed $Q_d = 20$ and $\gamma_1 = \gamma_2 = \gamma_d/2$. Also, the approximate values of ω_c, ω_{TLS} and g can be readily obtained from the transmission data and I used these for initial values in the Monte Carlo. Note that for a TLS that is strongly coupled to the resonator compared to the detuning, $2g = 2\pi f_g$, where f_g denotes

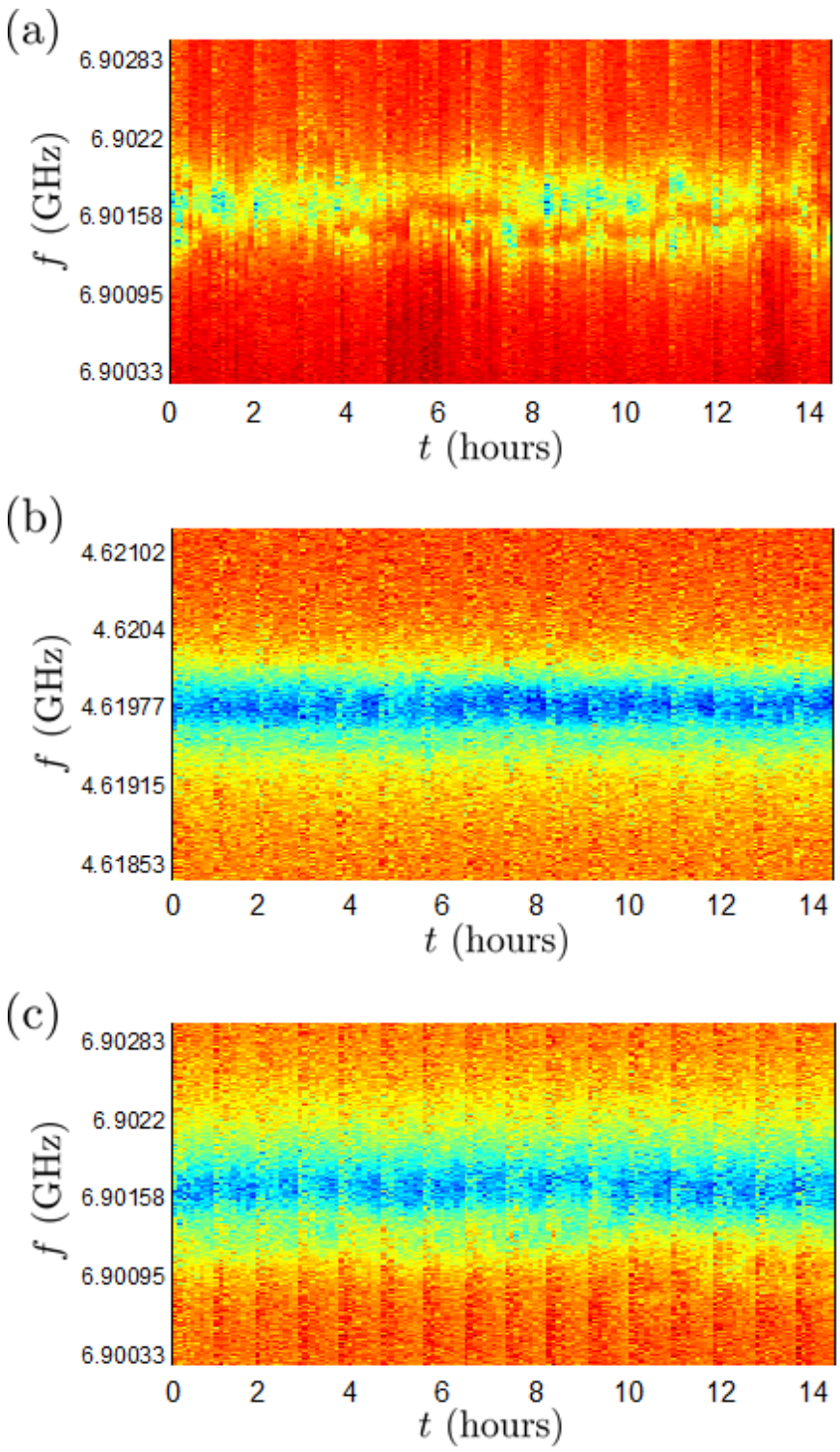

Figure 5.9: False-color plot of $|S_{21}|$ versus frequency f and time t showing the mode stability for (a) the $V = 80\,\mu\text{m}^3$ device at 25 mK, (b) the $V = 5000\,\mu\text{m}^3$ at 25 mK and (c) the $V = 80\,\mu\text{m}^3$ at 200 mK.

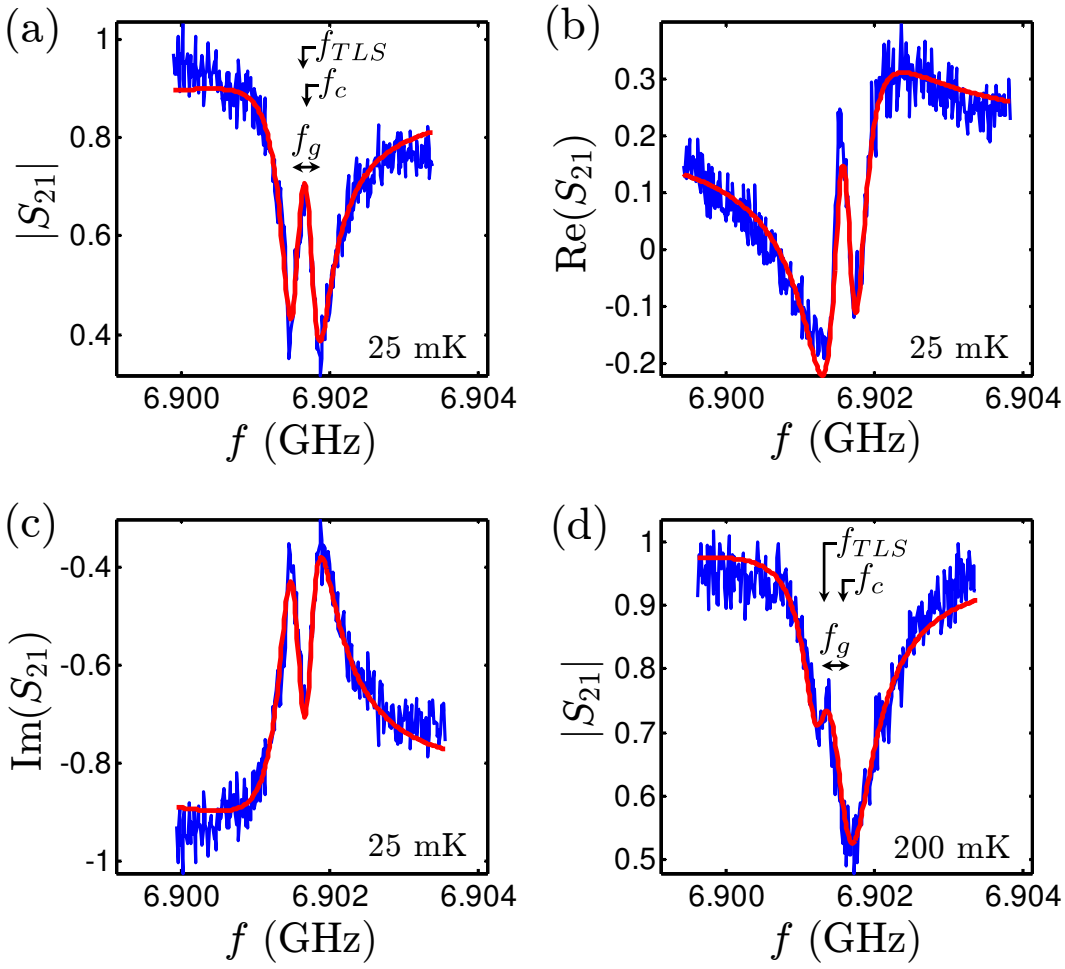

Figure 5.10: (a) Measured $|S_{21}|$ vs. frequency f (blue) and optimum fit (red) at 25 mK for the micro-V device with $V = 80\,\mu\mathrm{m}^3$. (b) and (c) show corresponding real and imaginary parts of S_{21}. (d) Measured (blue) and best fit (red) of $|S_{21}|$ vs. frequency at 200 mK. f_c and f_{TLS} are the cavity and TLS frequencies respectively, and $f_g = 2g/2\pi$ shows the vacuum Rabi frequency and the splitting width.

the splitting width.

The fit yielded $\omega_d/2\pi = 6.978419$ GHz and $\gamma_d = 2.19$ GHz for cavity d, and $f_c = \omega_c/2\pi = 6.901689$ GHz and $\gamma_c = 1.92$ MHz for cavity c. The intercavity coupling rate was $\Omega = 41.9$ MHz, $Q_e \simeq 14000$, and the coupling of cavity c to the TLS under consideration was $g = 1.15$ Mrad/s. For the TLS I obtain $f_{TLS} = \omega_{TLS}/2\pi = 6.901629$ GHz, and hence a detuning of $\Delta_\omega = 60$ kHz which is less than $g/2\pi$.

The fit also revealed $\mathrm{T}_2 = 2/\gamma_{TLS} = 3.2\mu$s as the coherence time of the resonant TLS including the decay at rate γ_{TLS} from spontaneous emission and neglecting dephasing, *i.e.* $\mathrm{T}_2 = 2\mathrm{T}_1$. This value for T_2 is at least 3 times larger than previously found for individual TLSs in JJ alumina tunnel barriers [85,100]. In fact, it is similar to the coherence time of the original transmon qubit [64].

This remarkably long coherence time is possibly caused by the properties of the silicon nitride film. That is, the SiN_x film may contain TLSs of a different physical nature than those found in alumina. Also, it could be due to better isolation of TLSs in the bulk from surface effects at the superconductor-dielectric interface. TLSs in JJ barriers are in close proximity to the superconducting electrodes which can potentially result in a faster decoherence due to a possible enhanced strain field (phonon) coupling to the TLSs [109].

From g and Eq. 5.20, I can obtain a lower limit for the dipole size of the strongly-coupled TLS. The minimum dipole size in this case satisfies $p_{min} = (\Delta_0/\mathcal{E})p\cos\theta = 1.6$ Debye, which is consistent with previous work on SiN_x [83].

5.7.2 Analysis of $T = 200$ mK data

I also measured the micro-V device with $V = 80\,\mu\text{m}^3$ at $T = 200$ mK where $\hbar\omega/2k_BT \simeq 0.8$. The mode stability test result shown in Fig. 5.9c, revealed a much more frequency-stable mode compared to the low-temperature case where two modes where observed. The apparent stability is likely due to the strongly coupled TLS being close to thermal saturation, which causes the splitting to become barely visible. Therefore, the remaining stable mode is a "cavity-like" mode, or bare cavity rather than the dressed cavity.

An individual 200 mK transmission curve is shown in Fig. 5.10d. I fit this curve to Eq. 5.18 and extracted the parameters for the 200 mK case. For the fit, I kept ω_d, γ_d and Ω equal to their low-temperature values, while the rest of the parameters where permitted to change. I extracted $g = 1.13$ Mrad/s which was almost the same as at 25 mK. However, $f_{TLS} = 6.901318$ GHz and $f_c = 6.901576$ GHz show a small shift due to weak influence from TLSs, as expected. The detuning $\Delta_\omega = 258$ kHz shows a considerable increase compared to the low temperature case, and becomes comparable to the TLS-cavity coupling rate g. According to Eq. 1.63, this would produce coupled modes with an uneven superposition of the bare states, and causes the transition to the high-energy cavity-like state $E_+(n = 0)$ to have a larger amplitude than $E_-(n = 0)$ (see Eq. 1.61). In the transmission data, this shows up as a "deep" resonance on the higher frequency side and a shallow one on the lower frequency side.

Using Eq. 5.20 with the remaining fit values, $\text{T}_1(200\text{ mK}) = 0.57\,\mu$s and γ_c,

allows me to calculate the ratio of the TLS-like state signal on the background of the cavity-like state as $4g^2 \tanh(\hbar\omega_{TLS}/2k_BT)\mathrm{T}_1/\gamma_c = 0.67$, where $\tanh(\hbar\omega/2k_BT) = 0.68$. The T_1(200 mK) value reveals a faster TLS decay than expected from the increased phonon emission which scales as $\tanh(\hbar\omega/2k_BT)$ and would give $\mathrm{T}_1(200\ \mathrm{mK}) = 1.1\,\mu$s. However, this is qualitatively consistent with spectral diffusion, which causes TLS dephasing [110], and with the parabolic temperature dependence of TLS coherence times found in alumina tunneling barriers [100].

5.8 Micro-V device power sweep

After examining a TLS in the micro-V device with $V = 80\,\mu\mathrm{m}^3$ at low powers ($\bar{n} \ll 1$) and two temperatures (25 mK and 200 mK), the next measurement I did was a power sweep at low-temperature (25 mK). This enabled me to observe the power saturation of an individual TLS (see Fig. 5.11a). The power measurement was performed in a separate cooldown (approximately one year later) than the measurements of section 5.7, and this resulted in a different TLSs strongly coupled to the resonator. The input power at the device (P_{in}) was swept in the range $-170 < P_{in} < -100$ dBm, which corresponded to average photon numbers in the cavity of $10^{-4} \lesssim \bar{n} \lesssim 10^3$.

Figure 5.11a shows a false-color plot of the measured $|S_{21}|$ as a function of frequency f and input power P_{in}. At low powers, $\bar{n} \lesssim 1$, the splitting is clearly observed, which is expected from a low-power probe of the $n = 0 \rightarrow 1$ (single photon) excitation of the system. At power levels corresponding to more than a

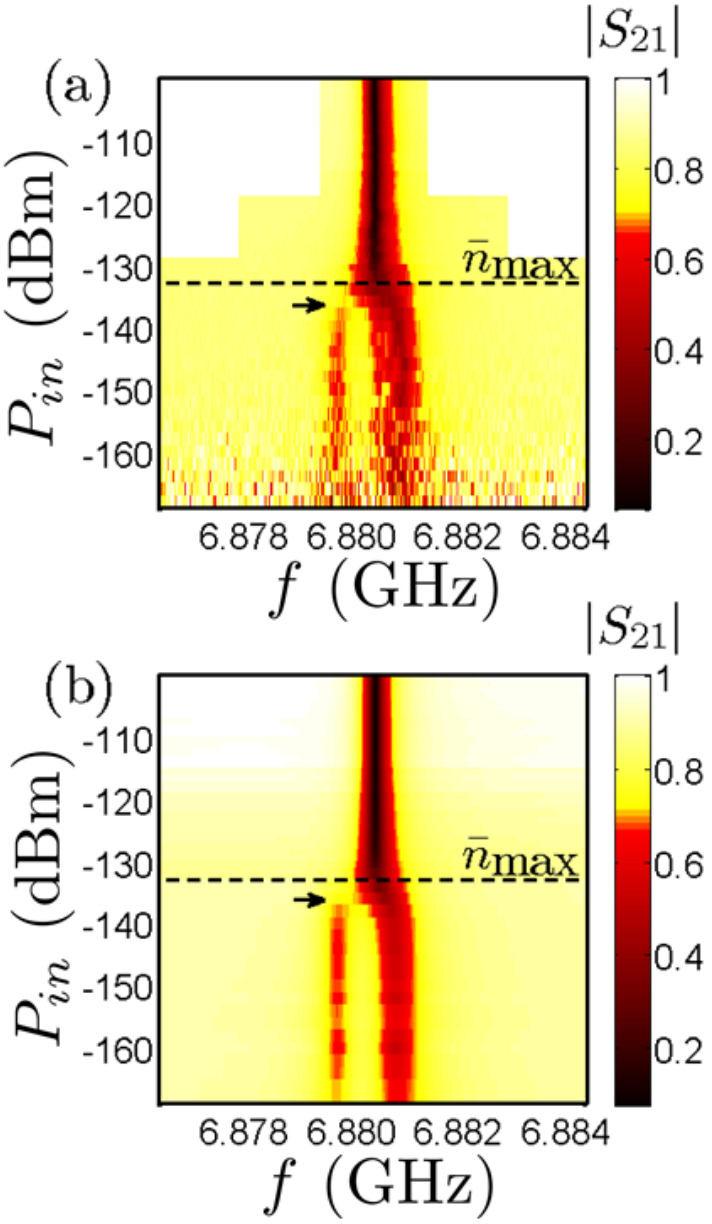

Figure 5.11: (a) False-color plot showing measured transmission $|S_{21}|$ vs. input power P_{in} and frequency f for the micro-V resonator with $V = 80\,\mu\text{m}^3$. (b) Simulated power dependence from theoretical fit to model. Dashed line at $\bar{n}_{\max} \simeq 7$ indicates the photon number above which the simplified Dual-Cavity Model is used and the arrow shows the break corresponding to $n > 1$ transitions.

single photon in the cavity, the splitting merges into a single resonance, which is the bare cavity mode. I note that at higher powers, we generally expect photon number peaks due to the Poissonian distribution of the photon number n in cavity c (see section 1.2.2) although these are not apparent in Fig. 5.11a. The Jaynes-Cummings Hamiltonian gives transition energies

$$\Delta E_{\pm\pm}(n>0) = \hbar\omega_c \pm \hbar\sqrt{g^2(n+1)+(\Delta_\omega/2)^2} \mp \hbar\sqrt{g^2 n+(\Delta_\omega/2)^2}, \qquad (5.27)$$

from the nth hybridized pair $\{|n,\mathrm{g}\rangle, |n-1,\mathrm{e}\rangle\}$ to that of the next higher energy. The high-power central dip corresponds to the $\Delta E_{++}(n>0)$ and $\Delta E_{--}(n>0)$ transitions, which asymptotically approach a single frequency ($\hbar\omega_c$) for large n. In contrast to the $\Delta E_{++}(n>0)$ and $\Delta E_{--}(n>0)$ case, the $\Delta E_{+-}(n>0)$ and $\Delta E_{-+}(n>0)$ transitions do not converge, but diverge in energy as the power is increased.

With the low power ($\bar{n} \ll 1$) and high-power ($\bar{n} \gg 1$) regimes understood, I next focus on the crossover ($\bar{n} \sim 1$). I note that Fig. 5.11a shows a clear break on the left part of the "wishbone" in this regime. This break is marked in Fig. 5.11a by an arrow. At low powers, there is a larger amplitude for the high frequency transition, and once again this is caused by a cavity-like transition for $\Delta E_{+}(n=0)$. This is similar to the case of Fig. 5.10d (see section 5.7). In addition, the high-power transition $\Delta E_{++}(n>0)$ is closer to $\Delta E_{+}(n=0)$, than $\Delta E_{--}(n>0)$ is to $\Delta E_{-}(n=0)$, for a given $n>0$. The apparent break of the low frequency crossover from low to high power is expected due to the more spectrally diffuse transition energies than the other high frequency one.

Similar to the analysis in section 5.7, I also characterized the strongly-coupled TLS in the power sweep. This analysis was more comprehensive and included the power dependence of the micro-V transmission. In the following, I will describe the steps in the full analysis of this data for a wide range of input powers corresponding to $10^{-4} \lesssim \bar{n} \lesssim 10^{3}$.

Step 1: High-power analysis

For the full analysis of the data shown in Fig. 5.11a, I started with the high power regime. In this regime, the strongly-coupled TLS is saturated and a classical-field analysis is allowed, reducing the theoretical model to one without a dominant TLS. This is depicted in Fig. 3.2 with the Hamiltonian given by Eq. 3.26 and the transmission given by Eq. 3.42. In this regime, $|S_{21}|$ is given by Eq. 5.18 with $g = 0$. However, I note that the TLSs are still the dominant loss mechanism and result in the power-dependent photon decay rate γ_c in the cavity. The analysis of the high-power regime allowed me to extract the cavity d parameters, the bare cavity c resonance frequency, the photon decay rate (γ_c), and the intercavity coupling Ω.

Each horizontal slice of Fig. 5.11a corresponds to a small range of $\bar{n}$, and when I assign a $\bar{n}$ value to a slice, it corresponds to the maximum of the average photon number in the cavity within that particular horizontal slice. I chose $\bar{n} \gtrsim \bar{n}_{max} = 7$ as a high enough power to saturate the dominant TLS. $\bar{n}_{max}$ was also close to our computational limit for the low-power analysis (described later in section 5.8). This analysis was performed on separate transmission data (33 S_{21} curves)

taken at $\bar{n}_{max} < \bar{n} < 10^3$. This data set corresponds to horizontal slices of Fig. 5.11a above $\bar{n} = \bar{n}_{max}$. As before, I assumed $Q_d = 20$ and $\gamma_1 = \gamma_2 = \gamma_d/2$. The parameters of the fit were $\gamma_d = 2.17$ GHz and $\Omega = 41.6$ MHz, showing excellent consistency with the values given in section 5.7.1. I also extracted γ_c, and found that it decreases with power due to saturation of the weakly coupled TLSs. Also, I obtained $\omega_c/2\pi = 6.880434$ GHz and $\omega_d/2\pi = 6.899807$ GHz. The small shift in ω_c with respect to that reported in section 5.7.1 could be explained by a 0.6% change in the aluminum inductance relative to that found during the cooldown from that section. This should have little effect except to make the micro-V device sensitive to TLSs with slightly lower energy.

Figure 5.11b shows the simulation results of $|S_{21}|$ versus frequency and power using the best fit values. Note that only the $\bar{n} > \bar{n}_{max}$ part corresponds to the fit obtained in this section.

Step 2: Low-power analysis

For photon numbers $\bar{n} \lesssim \bar{n}_{max} = 7$, the dominant TLS must be considered. The theoretical model in this regime is shown in Fig. 5.2 and the Hamiltonian is given by Eq. 5.17. However, we can not use the transmission of Eq. 5.18, as it was derived assuming $\bar{n} \ll 1$. To proceed, I consider the photon density matrix ρ_{ph}. The time evolution of ρ_{ph} was obtained from the Lindblad equation [111] and $\mathcal{H}_{sys}$. From the photon density matrix, each transmission curve is calculated using an iterative method with 10^5 iterations. The initial Lindblad equation code was developed by

A. Burin at the Department of Chemistry, Tulane University.

Once again a separate fitting code was required to extract the parameters in this regime. I used the LSM method, with 10^4 guesses. Note that this number of Monte Carlo guesses is in addition to the density matrix iterations, making these fits extremely time consuming. Therefore, I used parallel computing (Matlab) on a 12-core computer with dual-Xeon CPUs and 96 GB of RAM.

I started fitting an S_{21} curve at around $\bar{n} \simeq 0.1$ where the splitting is clear yet the signal-to-noise ratio is large enough for a reasonably good fit. I used the extracted values of γ_d, ω_d, Ω and ω_c from step 1, and this allowed for a fairly accurate extraction of γ_c, ω_{TLS}, γ_{TLS} and g. Next, I used the extracted ω_{TLS}, γ_{TLS} and g as initial Monte Carlo values to fit the rest of the low-power $|S_{21}|$ curves. However, in order to increase the fitting accuracy, I used an expected functional form of $\gamma_c \propto (1 + E/E_c)^{-1/2}$ for γ_c as the initial guess, such that it depends on the average cavity photon number at which the transmission data is taken. The 18 S_{21} curves I analyzed correspond to horizontal slices of the false-color plot of Fig. 5.11a in the range $10^{-4} < \bar{n} < \bar{n}_{max}$. The parameters γ_c, ω_{TLS}, γ_{TLS} and g were extracted for each curve, and the results for each parameter were almost identical at different powers, except for γ_c which decreased with power due to saturation of TLSs.

Step 3: Low-power γ_c extraction

High- and low-power values of γ_c were extracted in steps 1 and 2, respectively. However, since we are particularly interested in the cavity loss tangent $\tan\delta = \gamma_c/\omega_c$,

I also tried a more accurate low-power extraction of γ_c. Once again I fixed the values of γ_d, ω_d, Ω and ω_c to those obtained in step 1. The almost-identical values (for different low-power curves) of the parameters ω_{TLS}, γ_{TLS} and g obtained in step 2 were averaged, and then fixed at $\omega_{TLS}/2\pi = 6.880106$ GHz, $\gamma_{TLS} = 3.08$ MHz and $g = 3.14$ MHz. The only remaining fitting parameter was γ_c, which I extracted using a similar fitting code to that used in step 2. This step ended the fitting procedure.

Having extracted all the parameters (all are power-independent except γ_c), Fig. 5.11b shows a simulated false-color plot of $|S_{21}|$ versus frequency and power. I note that there is excellent correspondence with the data shown in Fig. 5.11a.

With γ_c extracted for the entire measurement power span, I can now obtain $\tan\delta$ as a function of $\bar{n}$. This is plotted in red in Fig. 5.12. On the same plot, I have included the loss tangent data for the largest volume resonator ($V = 5000\,\mu\text{m}^3$) for comparison. The solid curves show the optimum fit of Eq. 2.35 to the data. I describe the details of this fitting code in more detail in Chapter 7. While both devices showed a similar low-power loss tangent of $\tan\delta_0 \simeq 1 \times 10^{-4}$, they exhibited different critical electric fields (E_c). The micro-V resonator showed $E_c = 13.6$ V/m, which is 3 times larger than that of the large-volume device. In terms of the average cavity photon number on resonance $\bar{n}$, an intrinsic E_c means that the critical average cavity photon number $\bar{n}_c$ is proportional to V. The ratio of device volumes in this case is 62.5, whereas the ratio of the two values for $\bar{n}_c$ is about 9. This suggests that the micro-V device is in a regime in which E_c is not an intrinsic property of the system.

Interestingly, for the micro-V device, the critical number of photons calculated

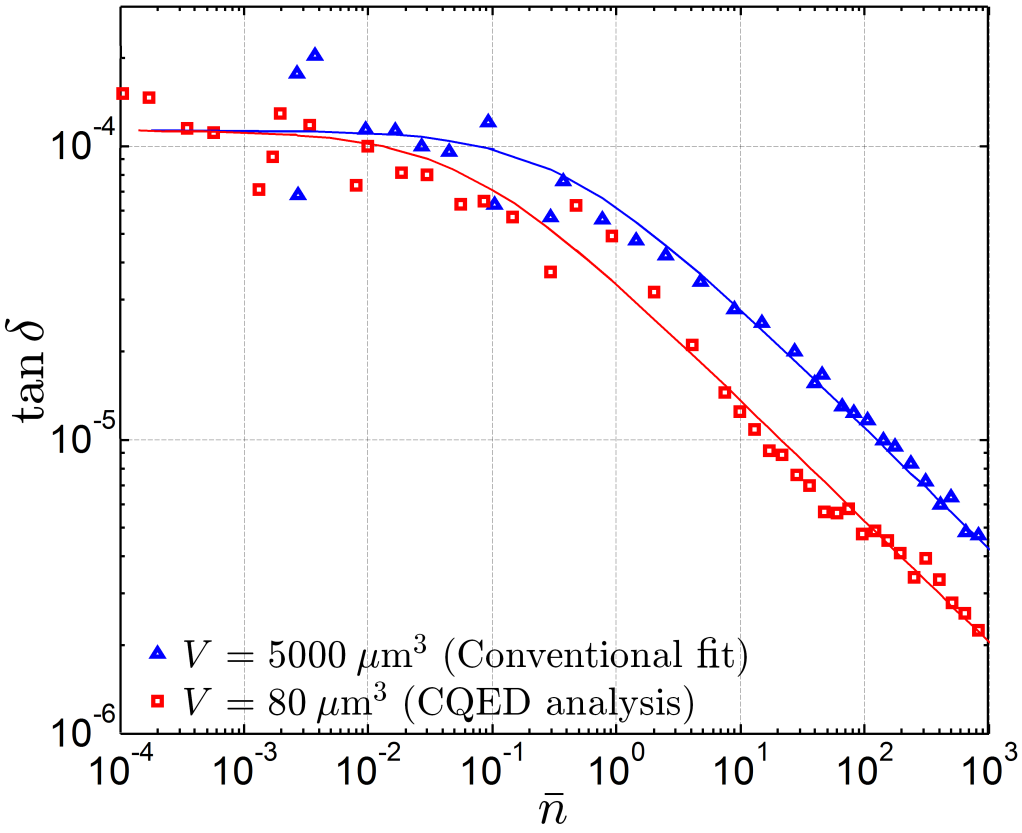

Figure 5.12: Red squares show measured loss tangent versus average cavity photon number $\bar{n}$ for the micro-V device with $V = 80\,\mu\mathrm{m}^3$ extracted from CQED power-dependent analysis. Blue triangles show measured loss tangent of the largest volume resonator with $V = 5000\,\mu\mathrm{m}^3$ obtained from the Dual-Cavity (conventional) fitting. The solid curves are corresponding optimum fit to data.

from E_c is $\bar{n}_c = 0.2$, such that the beginning of saturation for the TLS environment is reached in a quantum regime. While quantum effects on the weakly-coupled TLSs must be present, we expect inherent TLS-sampling variations to cause $\bar{n_c}$ to vary such that it may be desirable to try many TLS configurations using electric field bias control in the future [83]. I note that quantum effects of loss saturation have been theoretically analyzed previously only for a single TLS [112]. This may be interesting because the saturation may depend on the details of a complex set of TLSs coupled to the cavity, and these complex dynamics are related to famously-difficult coupled spin problems [113, 114].

5.9 Conclusion

In this Chapter I introduced a new TLS measurement technique that offers a few advantages over previous techniques. My measurement is based on direct CQED strong coupling of an individual TLS to a linear superconducting resonator cavity, forming a micro-V device. I described a full temperature- and power-dependent analysis of a TLS using a theoretical model developed for the micro-V devices. I showed how to extract the coupling and relaxation parameters of the cavity and the dominant TLS within a wide range of average cavity photon numbers ($10^{-4} \lesssim \bar{n} \lesssim 10^3$). A TLS measured at $T = 25$ mK in a SiN_x micro-V device showed a coherence time of $T_2 = 3.2\ \mu$s which is considerably longer than those of TLSs measured previously in alumina tunnel barriers [85]. Possible reasons for this remarkably long coherence time were discussed. In a photon-intensity study, the two low-energy

transitions, which reveal the vacuum Rabi splitting, are observed to crossover to the high-power cavity transitions, with a break between these regimes on the low-frequency side resulting in a wishbone shape.

From these results it is clear that this CQED measurement technique can be used to characterize individual TLSs in a wide range of materials and this could lead to the discovery of materials with TLSs with even longer coherence times. This approach offers a significant advantage compared to measuring individual TLSs in a JJ tunnel barrier, where only the TLSs within the tunnel barrier could be measured and one faces severe limitations on the materials that can be used as JJ barriers. Before this study, to the best of my knowledge, only TLSs from alumina tunneling barriers had been measured individually.

Finally, I note that the micro-V device opens up the possibility for the CQED operation of long-lived nanoscale TLSs in quantum information circuits. In the next Chapter, I describe a device that makes us one step closer to this ambitious goal.

Chapter 6: Spectroscopy of nanoscale TLSs

6.1 Motivation

As I discussed in previous chapters, the precise identity of nanoscale TLSs in amorphous solids is unknown, but this means there are opportunities for novel measurement methods to reveal new information about TLSs. While TLSs cause decoherence in superconducting qubits [66], there is a possibility that they could serve as quantum memory bits [88]. Clearly, this would require finding long-lived, well-characterized and strongly-coupled TLSs. In Chapter 5, I showed a new measurement technique together with temperature and power dependent analyses for characterizing individual TLSs in different amorphous solids. In the micro-V device that was measured, one TLS on average was strongly coupled to the cavity (resonator), allowing CQED study of the TLS. Of course, this also meant that I could only characterize an average of one TLS per cooldown. In order to study a larger number of TLSs, I developed a tunable micro-V device which I discuss in this Chapter.

In addition to allowing a search for TLSs with long coherence times, a tunable micro-V device can enable characterization of TLSs in an insulating film by their dipole sizes and yield a distribution of this parameter. The tunable device also

raises the possibility of CQED operation of nanoscale TLSs in quantum information circuits and quantum manipulation of TLSs [98]. A clear challenge however, is the inherent randomness of the TLS distribution in energy and space, which complicates the coupling to a TLS with the desired properties. However, this might also be achieved with tunability.

In order to add tunability to a superconducting resonator, one could use the nonlinear inductance of JJs. In fact, tunable JJ-based devices that measure individual TLSs have been developed and used previously [66, 86]. However, in such techniques, the cavity acquires nonlinearity which complicates measurements and analysis.

In this chapter, I describe a device which adds TLS tunability to the micro-V device, without destroying its harmonicity. In this tunable micro-V device, the TLSs rather than the cavity are tuned. This is achieved by electric field biasing the TLSs, which tilts the TLS potential. As discussed in Chapter 2, this potential is generally believed to be a double-well. This type of tuning has been previously applied to TLS *ensembles* by Khalil *et al.* in the context of Landau-Zener population control of TLSs [83].

6.2 DC-tuning the TLSs

To understand the tunable micro-V device, I consider a parallel-plate capacitor with an amorphous dielectric between its electrodes (see Fig. 6.1a). In addition to the applied ac voltage V_{ac}, an additional quasi-static voltage V_{bias} is applied. For

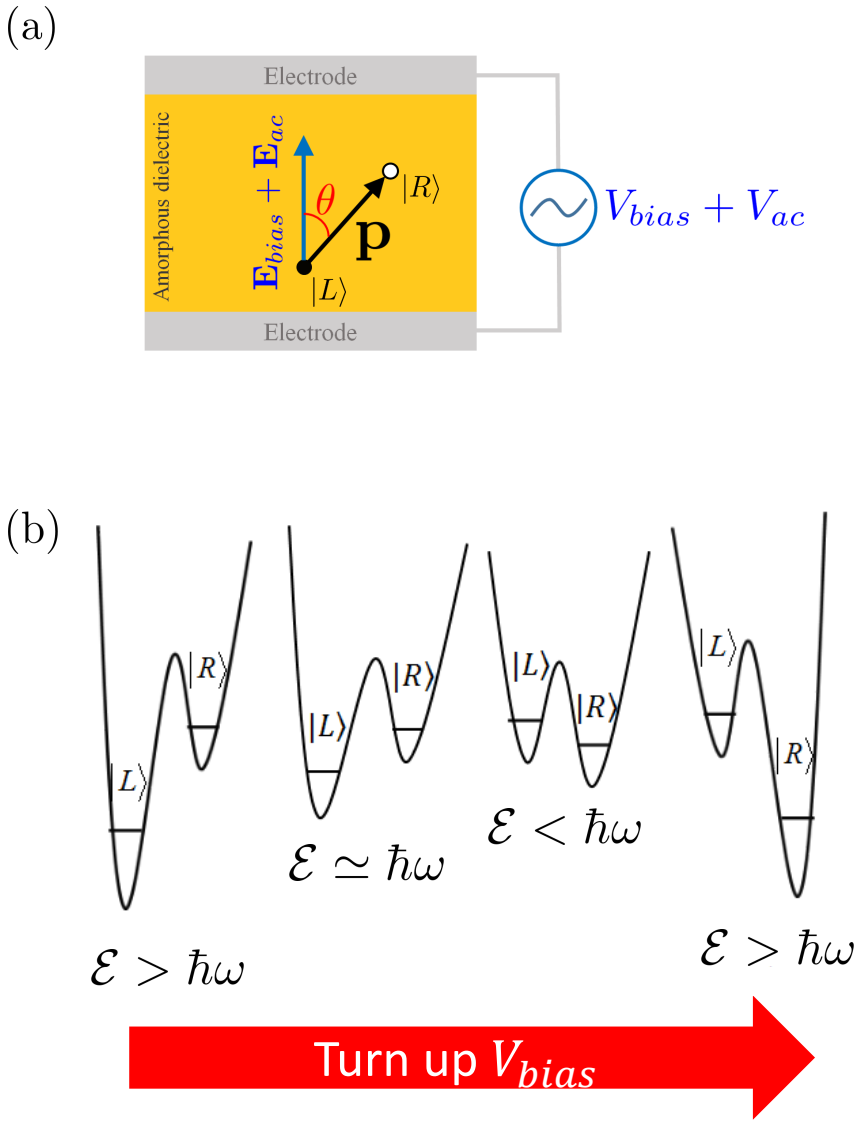

Figure 6.1: (a) A TLS with dipole moment $\mathbf{p}$ exposed to external AC and DC electric fields, $\mathbf{E}_{ac}$ and $\mathbf{E}_{bias}$. (b) The potential energy diagram of a TLS that is brought into resonance with the cavity by applying $\mathbf{E}_{bias}$. Further increasing $\mathbf{E}_{bias}$ can take the TLS far out of resonance with the cavity, and possibly even change the direction of the double-well asymmetry.

now, I assume $V_{ac} = 0$ and look into the effect of V_{bias}. According to Eq. 2.12a, upon application of V_{bias}, the asymmetry energy of a TLS double-well potential changes to

$$\Delta' = \Delta + 2\mathbf{p} \cdot \mathbf{E}_{bias}, \tag{6.1}$$

where $\mathbf{p} = q\mathbf{a}/2$, $E_{bias} = V_{bias}/d$, q is the charge of the TLS, a is the charge hopping distance, d is the separation between the capacitor plates, and Δ is the asymmetry energy for $V_{bias} = 0$. Then I can write the TLS energy as

$$\mathcal{E} = \sqrt{\Delta_0^2 + \Delta'^2} = \sqrt{\Delta_0^2 + |\Delta + 2\mathbf{p} \cdot \mathbf{E}_{bias}|^2}. \tag{6.2}$$

If we drive the TLSs by adding V_{ac} at frequency ω with $V_{bias} = 0$, the TLSs with $\mathcal{E} \simeq \hbar\omega$ will be resonantly excited by $\mathbf{E}_{ac}$ while the TLSs with energies sufficiently smaller or larger than $\hbar\omega$ will not be excited. According to Eq. 6.2, one can tune the TLS energies and bring TLSs in and out of resonance with the applied electric field by changing V_{bias} (see Fig. 6.1b).

I note that the change of the asymmetry could be in either direction depending on the direction of the TLS dipole and electric field. For the special case of $\theta = \pi/2$, the TLS can not be tuned using a bias field because $\mathbf{p} \cdot \mathbf{E}_{bias} = 0$. In contrast, TLSs with $\theta = 0$ or π have the highest bias sensitivity.

6.3 Device design

A simple way to isolate the applied AC voltage from the DC bias voltage is to use a microwave bridge resonator [83]. Figure 6.2 shows a schematic of an "ideal" tunable micro-V device with a capacitor bridge. If the device is designed such that

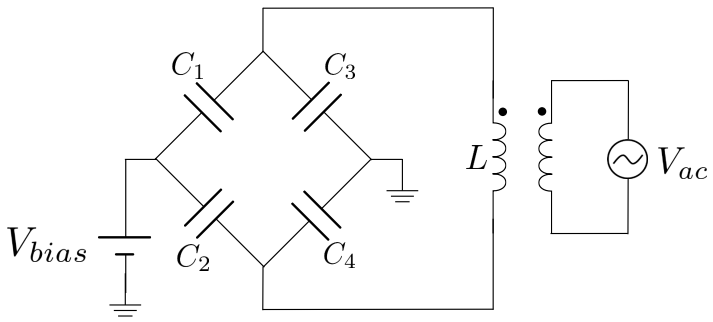

Figure 6.2: Schematic of ideal tunable micro-V bias bridge resonator.

$C_1 = C_2 = C_3 = C_4 = C$, then the equivalent (total) capacitance of the bridge is $C_{tot} = C$ and the DC voltage across each capacitor, C_1 through C_4, is $V_{bias}/2$.

As discussed in Chapter 5, a sufficiently small dielectric volume is necessary for CQED measurements of TLSs. I note though that by using a bias bridge with total capacitance C, the dielectric volume is four times larger than for a single capacitor of the same dielectric thickness. In order to compensate this four-fold increase in volume, I used a dielectric thickness of $d = 125$ nm, which is half the dielectric thickness of the micro-V device described in Chapter 5, and leads to a two-times smaller volume. I also used a relatively large double-loop spiral inductor which allowed me to use smaller capacitors, further decreasing the dielectric volume.

Figure 6.3a shows the layout for the device, rendered using AWR Microwave Office. In order to increase the inductance-per-length, a spiral inductor with 2.5 μm linewidth was used. This is half the linewidth I used for the inductors of the devices

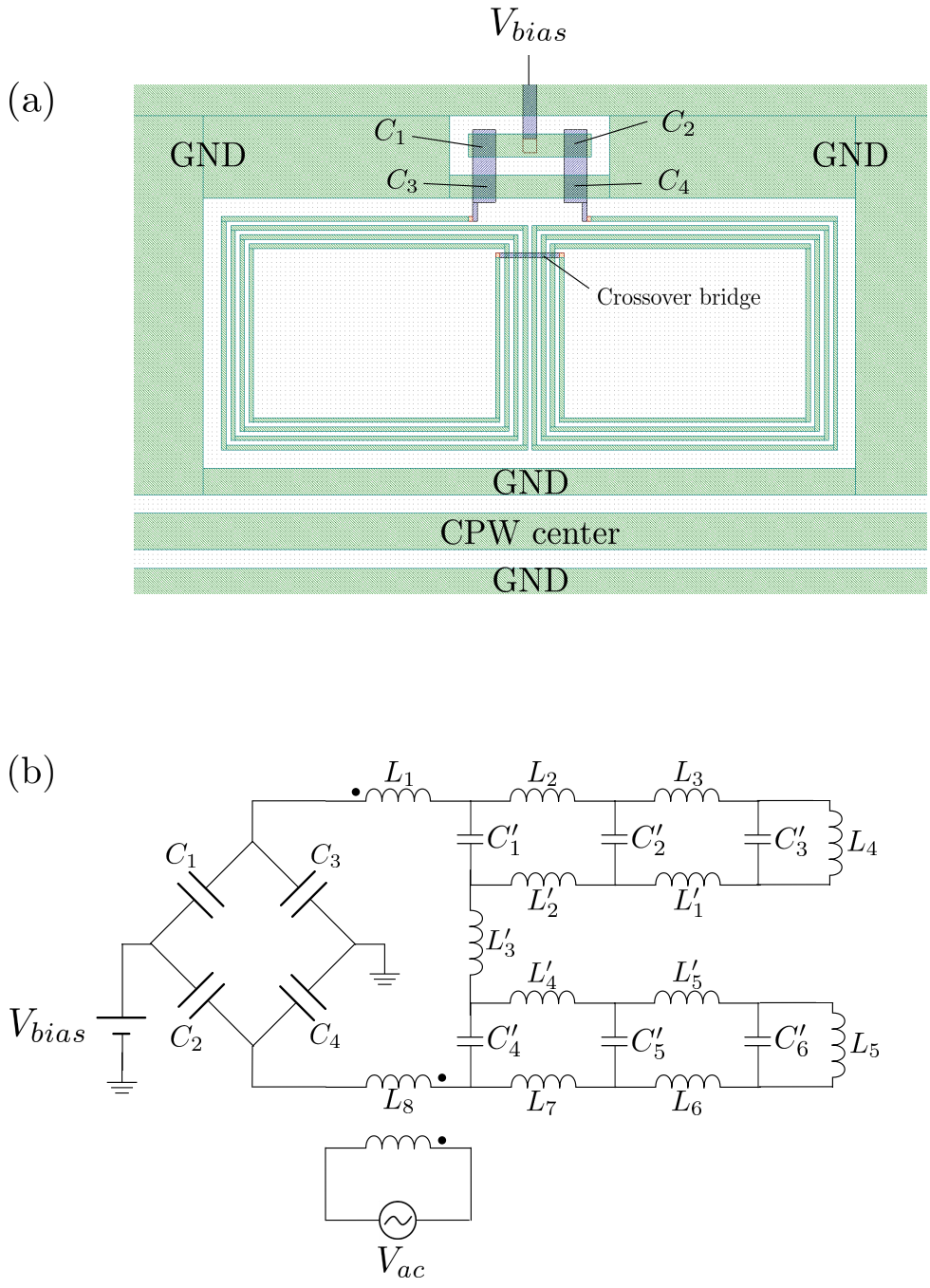

Figure 6.3: (a) Layout of the tunable micro-V device with $V = 78\,\mu\text{m}^3$ and $Q_e \simeq 10000$ from AWR Microwave Office. (b) Schematic of a tunable micro-V device including cross-over capacitors.

described in Chapter 5. For efficient isolation of DC and AC voltages, I designed the circuit to be symmetric, such that, ideally, the DC bias line was attached to the circuit at an AC voltage node (ground). I designed two tunable micro-V devices with different external quality factors. I could achieve dielectric volumes V of 63 μm^3 and 78 μm^3 with $d = 125$ nm corresponding to total bridge capacitances of $C_{tot} = 58$ fF and 72 fF, respectively. I used $\epsilon_r = 6.5$ (SiN_x) for the simulation.

A more complete schematic of a tunable micro-V device is shown in Fig. 6.3b. This schematic includes the crossover capacitors which are formed where the multiturn inductor crosses itself. Obviously, there will be some coupling to the TLSs in the crossover capacitors. However, this coupling is expected to be much weaker than the coupling to TLSs in the bridge capacitors. More importantly, the schematic shows that the crossover capacitors are DC shorted, so that the TLSs within are not expected to be tuned by V_{bias}.

In addition to the two tunable micro-V devices mentioned above, I designed two regular micro-V devices that had a single parallel-plate capacitor rather than a capacitor bridge. Since the inductance was larger than the micro-V device of Chapter 5, I could achieve dielectric volumes of 27 μm^3 and 12 μm^3. I have not included the analysis of these two devices in this thesis, as it is similar to that studied in detail in Chapter 5.

The simulated resonances for the four designs are shown in Fig. 6.4 and the key device parameters are listed in Table 6.1.

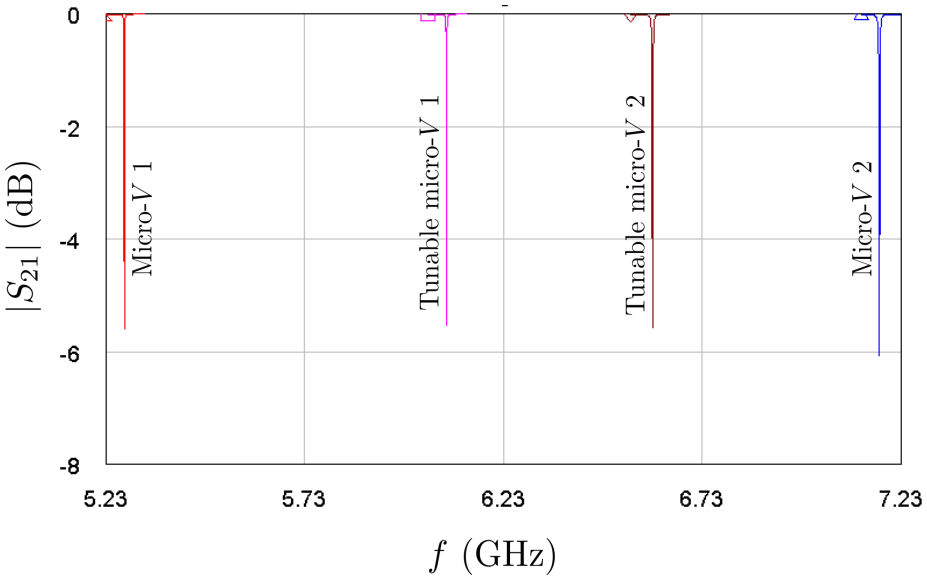

Figure 6.4: AWR Microwave office simulation results for four devices showing resonance lineshape of the devices on a die. In this simulation, a constant and real loss tangent of $\tan\delta = 1/Q_e$ was assumed for SiN_x to get a resonant depth of approximately 6 dB.

6.4 Fabrication

To make tunable micro-V devices, I followed a fabrication procedure that was similar to that described in Section 5.5. However, the fabrication was more challenging in several ways. The most challenging part was that I needed to fabricate a 125 nm thick low-loss SiN_x film on top of the first (bottom) Al layer. The problem was that low-loss SiN_x tended to have a high tensile stress ($1 - 2.8$ GPa) and this tends to cause the film to peel off within a few minutes after it is removed from the PECVD chamber. This happened whether I used Si or sapphire substrates. I also

Table 6.1: List of device parameters.

Device label	V (μm^3)	C_{tot} (fF)	Q_e	f_0 (GHz)
Micro-V-1	12	43	5000	5.276
Tunable Micro-V-1	78	72	10000	6.087
Tunable Micro-V-2	63	58	5000	6.605
Micro-V-2	27	100	10000	7.175

tried techniques to improve SiN_x-Al adhesion, such as ion-milling the Al layer prior to PECVD. The alternative I used was to compromise and use a somewhat lossier SiN_x film with lower stress. In this case I used a film which was fabricated by a different PECVD tool than I used for the micro-V samples described in Chapter 5. The tool was an Oxford Plasmalab System 100 in the Nanofab Lab in the Kim Building (University of Maryland - College Park). This system has a 13.56 MHz driven parallel plate reactor and offered frequency mixing (modulation) with a kHz-range drive. The resulting film had a 263 MPa compressive stress.

Another challenge compared to the fabrication of devices in Chapter 5, was that I needed to use a narrower inductor linewidth. This left only a small area for the vias that required a much more accurate reticle alignment and careful etch rate calibrations for the Al and SiN_x patterning.

I fabricated the devices on a 3-inch C-plane sapphire wafer. After Ar ion-

mill cleaning the substrate in the sputtering chamber, a 100 nm thick Al layer was sputtered in the sputtering system described in section 4.3. I used a DC sputtering power of 400 W (DC) and an Ar pressure of 5 mTorr for 20 minutes and 30 s. After defining a photolithographic resist on the base metal layer, Al was wet-etched to form the ground plane, the CPW center, bottom capacitor plates and the spiral inductor (except the crossover bridge shown in Fig. 6.3a). For wet-etching I used J.T.Baker Aluminum Etch 80-15-3-2. After removing the PR, the wafer was inserted in the Oxford Plasmalab System 100 and a 125 nm thick SiN_x film was deposited. After completing photolithography, I performed an RIE process to remove SiN_x at the location of the vias using a Plasma-Therm 790 Series RIE system. For the RIE, the flow rates of SF_6 and O_2 were 20 sccm and 5 sccm respectively, and the processing chamber pressure was kept at 75 mTorr. The wafer was then transferred back to the sputtering chamber, where it was exposed to a high-voltage Ar ion-milling process (described in Section 5.5) with a beam voltage of 800 V for 1 minute. Without removing the wafer from vacuum, I then sputtered a 200 nm thick Al layer. This was then patterned to form the vias, crossover bridges, DC bias lines and top capacitor plates. After PR removal, I executed a final photolithography step followed by an RIE process to remove SiN_x everywhere except for the areas covered by the top metal plate and within approximately 1 μm from them. An optical image of a tunable micro-V resonator is shown in Fig. 6.5.

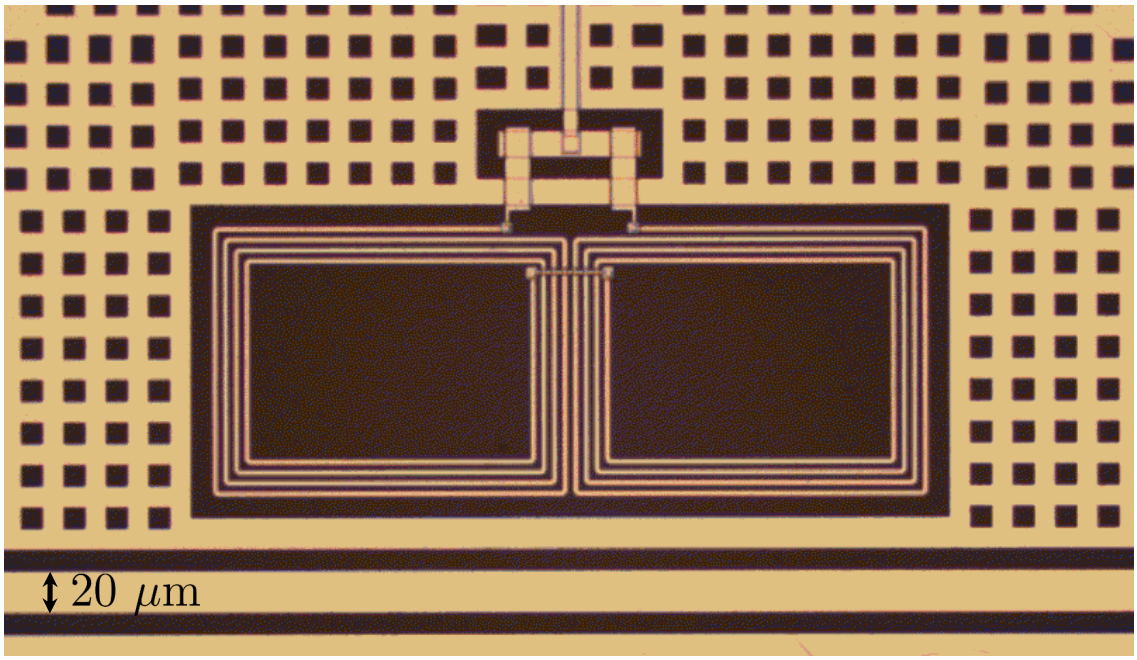

Figure 6.5: Optical image of the tunable micro-V resonator with $Q_e \simeq 10000$.

6.5 Device measurement

In order to tune the TLSs in a controlled way, the DC bias circuit had to provide a relatively stable V_{bias}. Ideally, the noise voltage amplitude V_{noise} should be much smaller than that required to shift the energy of a TLS by an amount comparable to the resonator bandwidth B. Quantitatively, this translates into

$$V_{noise} \ll hBd/p, \tag{6.3}$$

where d is the separation between the capacitor plates and p is the dipole moment of the TLS. For a device with a resonance frequency of $\omega_0/2\pi = 6$ GHz, $Q_e = 10000$, $Q_i = 1000$, $d = 125$ nm and using $p = 7.9$ Debye (estimated in a previous study of

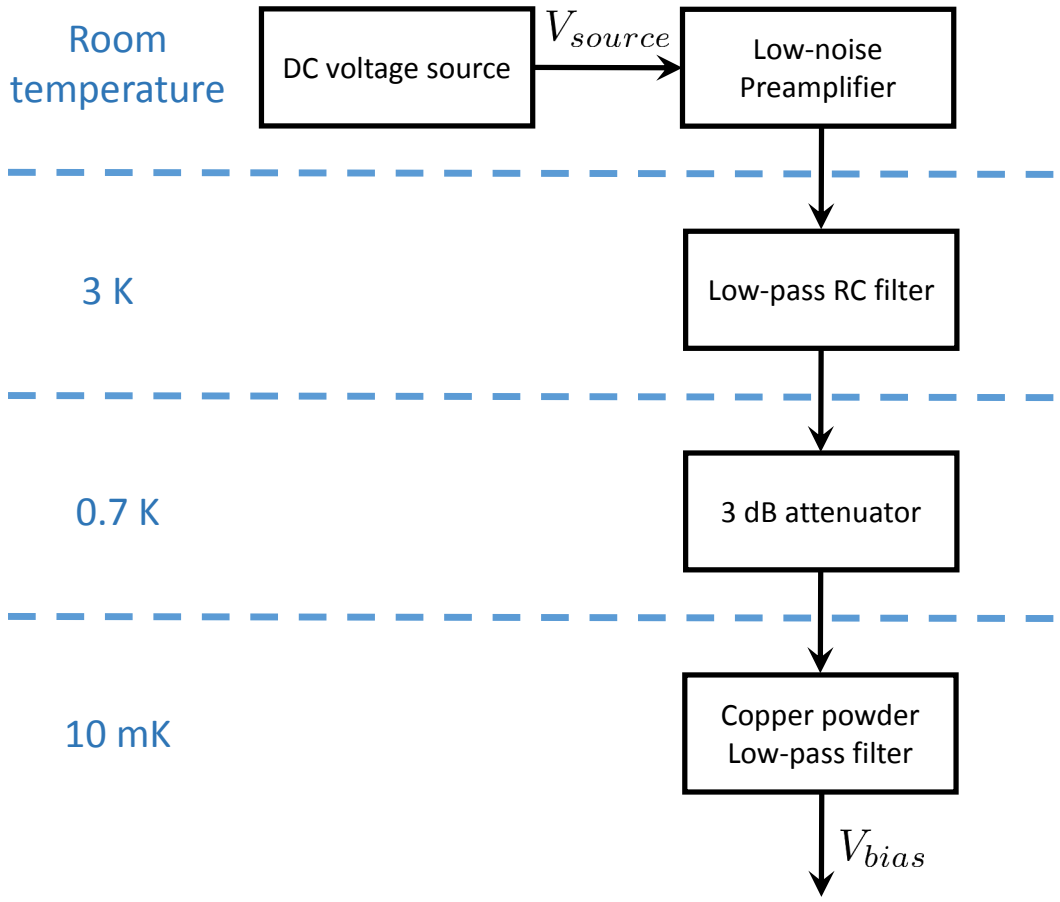

Figure 6.6: Filtering of the DC bias line for the tunable micro-V measurement. The DC voltage source is a Yokogawa GS200 and the preamplifier is a Stanford Research Systems SR560.

SiN$_x$ [83]), I obtain $V_{noise} \ll 20\ \mu$V. This means that the noise voltage amplitude from 0 to a few GHZ should not exceed a few microvolts. If the noise has a white spectrum, this implies $\sqrt{S_N(f)} \lesssim 200\ \text{pV}/\sqrt{\text{Hz}}$.

In order to suppress noise on V_{bias}, I tried modifying the filtering on the DC bias line. The final version of the setup I used is shown in Fig. 6.6. The DC voltage source was connected to a SR560 preamplifier that had an integrated tunable low-

pass filter (I used a cutoff frequency of 30 Hz) and operates on internal battery for better isolation from 60-Hz noise. I did not use amplification, *i.e.* the gain was 1. The output of the preamplifier goes to a low-pass RC filter with a cutoff frequency of ∼30 Hz which is installed on the 3 K plate to reduce the Johnson noise. Next the DC line goes through a 3 dB microwave attenuator installed on the 0.7 K plate to thermalize the center conductor carrying the DC voltage and reduce Johnson noise from higher temperature stages. The series and parallel resistances of the 3 dB attenuator at room temperature were 8.5 Ω and 142 Ω, respectively. Finally, a copper powder low-pass filter with cutoff frequency of ∼100 kHz was installed at the 10 mK plate to filter noise from higher-temperature stages. The DC voltage was carried by UT-85 coaxial cables from the DC source to the copper powder filter. I used a Cu twisted pair cable from the copper powder filter to the device input for better filtering of the high-temperature noise. With this arrangement, the DC voltage V_{bias} across the capacitor is a fraction of the DC voltage at the source V_{source}. For the setup of Fig. 6.6 I found $V_{bias} = 0.01507 V_{source}$.

I note that if $V_{noise} \gtrsim hBd/p$, some TLS-induced features will not appear clearly in an S_{21} measurement. I also note that because the coupling to a TLS depends on the dipole angle θ with respect to the electric field, for a given TLS dipole size, TLSs with $\theta \lesssim \theta_{min}$ where θ_{min} is an angle depending on V_{noise}, will not clearly appear in the data. In other words, high V_{noise} can hide some TLSs in the spectroscopy.

Figure 6.7 shows some of my first spectroscopy results on the device Tunable Micro-V-1 when I did not use a preamplifier, filter or attenuator and the DC voltage

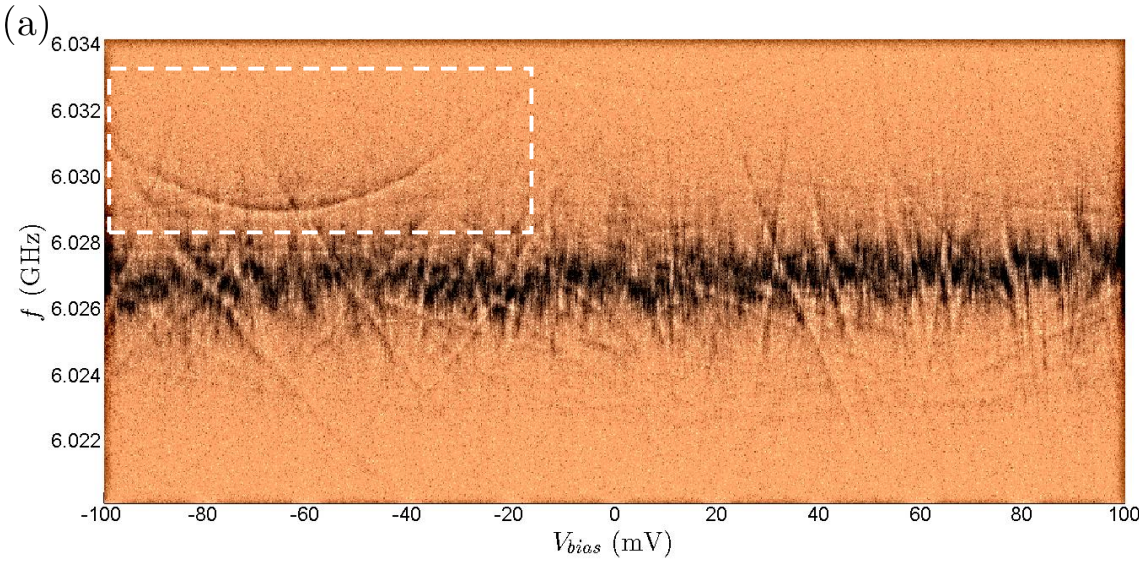

(b)

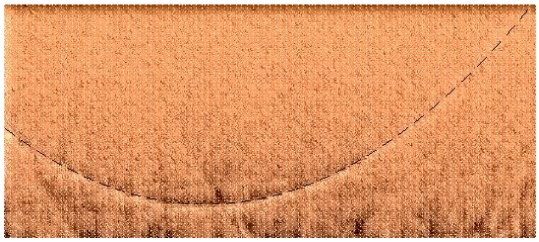

Figure 6.7: (a) False-color plot of measured $|S_{21}|$ of the Tunable Micro-V-1 versus frequency f and DC bias voltage V_{bias} without filtering the DC line for $-100\,\mathrm{mV} \leq V_{bias} \leq +100\,\mathrm{mV}$. Light copper and black correspond to $|S_{21}| = 1.16$ and $|S_{21}| = 0.77$, respectively. (b) Dashed curve shows theoretical fit to a hyperbola highlighted in (a).

source was directly connected to the sample through coaxial cables. Most of the TLS-like features appear as fairly straight tracks entering and exiting the relatively broad cavity resonance (the black horizontal portion in the middle of the plot). These straight tracks can be approximated as asymptotes of hyperbolas described by Eq. 6.2 and are the direct result of the TLS energies changing with V_{bias}.

In addition to the straight tracks, several hyperbolas can also be seen (most clearly, one on the top left in Fig. 6.7a). The hyperbolas correspond to TLSs with $\Delta_0 \cong \mathcal{E} \cong \hbar\omega_c$ where ω_c corresponds to the bare cavity mode. For these TLSs, one can approximate Δ_0 as the energy corresponding to the minimum frequency. By fitting the hyperbolas to Eq. 6.2, I can extract the projection of the TLS dipole moment on the electric field ($p\cos\theta$), and the asymmetry energy Δ' at $V_{bias} = 0$. I show a fit to a hyperbola in Fig. 6.7b. The parameters of the fit are $\Delta_0/h = 6.029015$ GHz, $\Delta'|_{V_{bias}=0} = 1.23\ \mu$eV and $p\cos\theta = -0.113$ Debye. If I assume $p = 7.9$ Debye from Ref. [83], then $\theta = 1.009 \times \pi/2$. This dipole angle is remarkably close to $\pi/2$ suggesting that significant V_{noise} may be suppressing the TLSs with a similar dipole moment but a smaller dipole-field angle which are more sensitive to V_{bias}.

I note that a wide-range V_{bias} sweep performed using large V_{bias} step size can also miss TLSs with dipole-field angles smaller than a certain angle as their frequencies may sweep through the measurement bandwidth from one step to the next.

Figure 6.8 shows a different bias sweep on the device Tunable Micro-V-1 in a smaller range than that of Fig. 6.7a but for the same wiring arrangement. There are no clear hyperbolas or TLS features "crossing" the cavity resonance. The reason is that Eq. 6.3 does not hold.

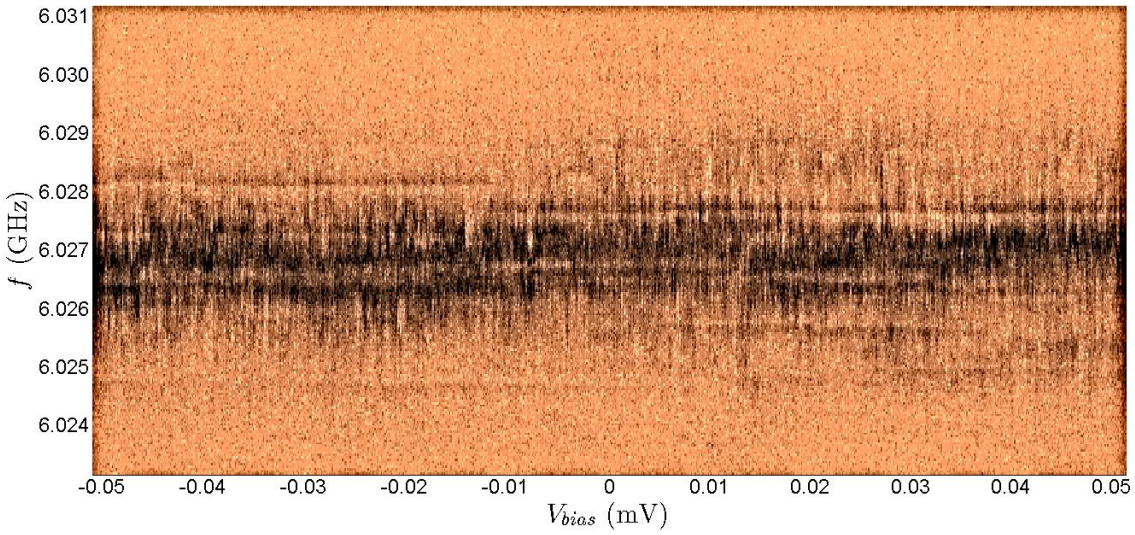

Figure 6.8: False-color plot of measured $|S_{21}|$ of the Tunable Micro-V-1 versus frequency f and DC bias voltage V_{bias} without filtering the DC line for $-50\,\mu\text{V} \leq V_{bias} \leq +50\,\mu\text{V}$. Light copper and black correspond to $|S_{21}| = 0.59$ and $|S_{21}| = 0.40$, respectively.

It is interesting to note that, however, several clear horizontal features can be seen in the spectroscopy. Most likely, these are either induced by TLSs with dipole-field angle extremely close to $\pi/2$, or they are due to TLSs in the crossover capacitors. Given the quantitative unlikeliness of the former and the fact that such TLSs would produce very weak spectroscopic features in S_{21}, I suspect that most if not all of these horizontal features are due to TLSs in the crossover capacitors. As I described in Section 6.3, these TLSs can produce strong features in S_{21} but they are insensitive to V_{bias} and as a result, V_{noise} does not smear out their transitions or hide them in the S_{21} measurement.

After I realized that V_{noise} could be affecting the visibility of the TLSs, I

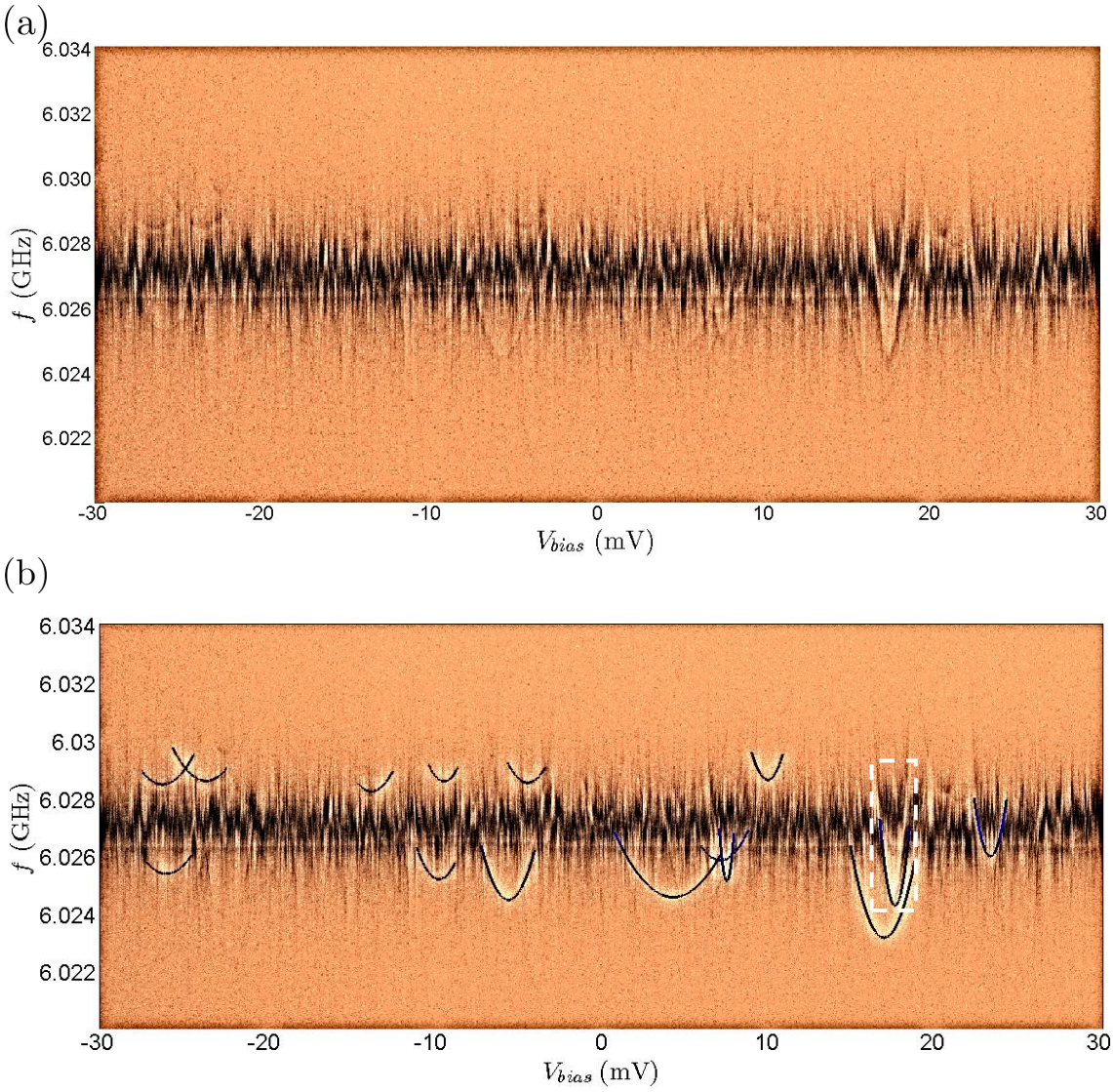

Figure 6.9: (a) False-color plot of measured $|S_{21}|$ of device Tunable Micro-V-1 versus frequency f and DC bias voltage V_{bias} after filtering the DC line for -30 mV $\leq V_{bias} \leq +30$ mV. Light copper and black correspond to $|S_{21}| = 0.62$ and $|S_{21}| = 0.41$, respectively. (b) Theoretical curves fit and superimposed on the measured hyperbolas (15 total). The hyperbola in the highlighted box is shown in detail in Fig. 6.14a.

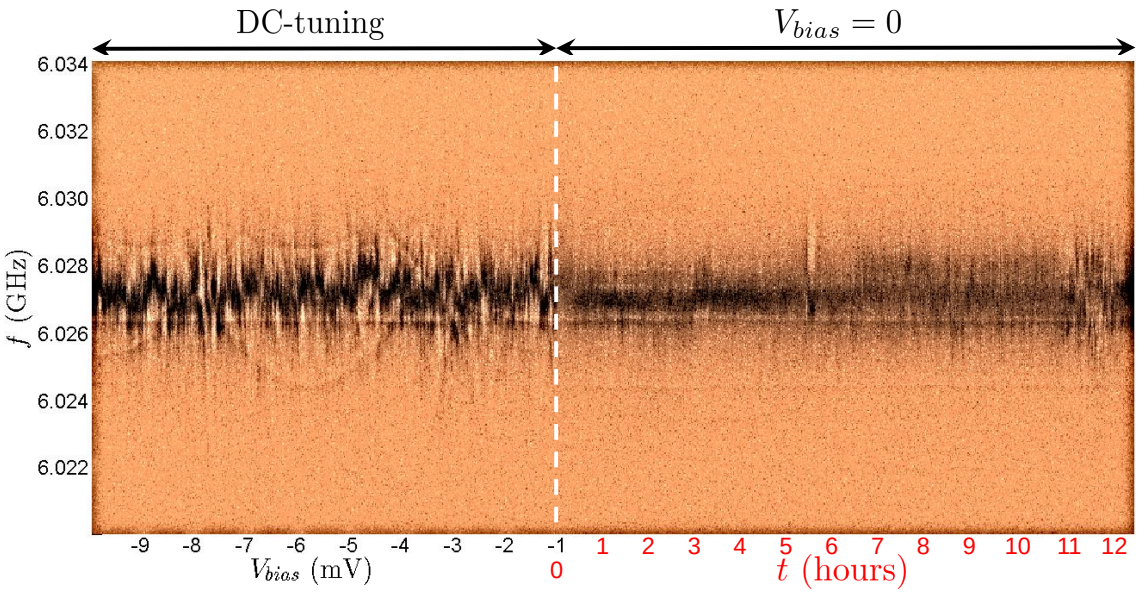

Figure 6.10: False-color plot of measured $|S_{21}|$ of device Tunable Micro-V-1 versus frequency f, and DC bias voltage V_{bias} or time t, showing DC-tuning versus stability test. The white dashed line shows the point at which V_{bias} was set to zero.

warmed up the system and installed the setup shown in Fig. 6.6 to improve the filtering on the DC line. The Tunable Micro-V-1 was remeasured and Fig. 6.9a shows the result of a wide-range DC sweep. Although the range was approximately 1/3 of that in Fig. 6.7a, a much larger number of TLS features as well as more hyperbolas were observed. I note however that the features do not appear as clearly as those in Fig. 6.7a, which could be because many weak TLSs were not visible in the earlier sweep due to larger V_{noise} in the earlier sweep.

In order to examine drift in the measurements I compared the DC tuning results to results of a "stability" test, which involved measuring the transmission while V_{bias} was fixed. This is shown in Fig. 6.10, where V_{bias} was initially swept, and

then set to zero. The difference in the left and the right parts of this figure shows how TLS-crossings can be distinguished from instability in the cavity resonance. I also note that both Figs. 6.9a and 6.9b show a prominent horizontal feature which, almost certainly, is due to a TLS in the crossovers.

6.6 Spectroscopy analysis

Figure 6.11a shows a high-resolution sweep of the device Tunable Micro-V-1 in a later cooldown than Fig. 6.9a. The hyperbolas are fit in Fig. 6.11b. Together with the hyperbolas from Fig. 6.9b and a third set of spectroscopy data (shown in Fig. 6.12), I was able to identify 60 TLSs with $\Delta_0 \cong \hbar\omega_c$. A histogram of the number of observed hyperbolas $\mathcal{N}_w$ versus $p|\cos\theta|$ corresponding to these TLSs is plotted in Fig. 6.13a. Table 6.2 shows the fit parameters for all 60 TLSs I fit. I note that this histogram shows a *weighted* TLS number $\mathcal{N}_w$ due to the fact that TLSs with larger $p|\cos\theta|$ will have a higher chance to appear in the spectroscopy data as a result of Eqs. 6.1 and 6.2. In other words, the bias sweep range between $V_{bias,min}$ and $V_{bias,max}$ corresponds to a larger asymmetry energy range for TLSs with larger $p|\cos\theta|$, and I can take $\mathcal{N} = (p|\cos\theta|_{max}/p|\cos\theta|) \times \mathcal{N}_w$ as the number distribution of $p|\cos\theta|$ by removing the energy-range dependence on $p|\cos\theta|$. The histogram of $\mathcal{N}$ is shown in Fig. 6.13b.

If I assume that the electric dipole moment of the TLSs has no preferred direction, the distribution of $\cos\theta$ would be uniform and hence $\langle|\cos\theta|\rangle = 1/2$. Using this, from the histogram of Fig. 6.13b I can find an effective (mean) value for

(a)

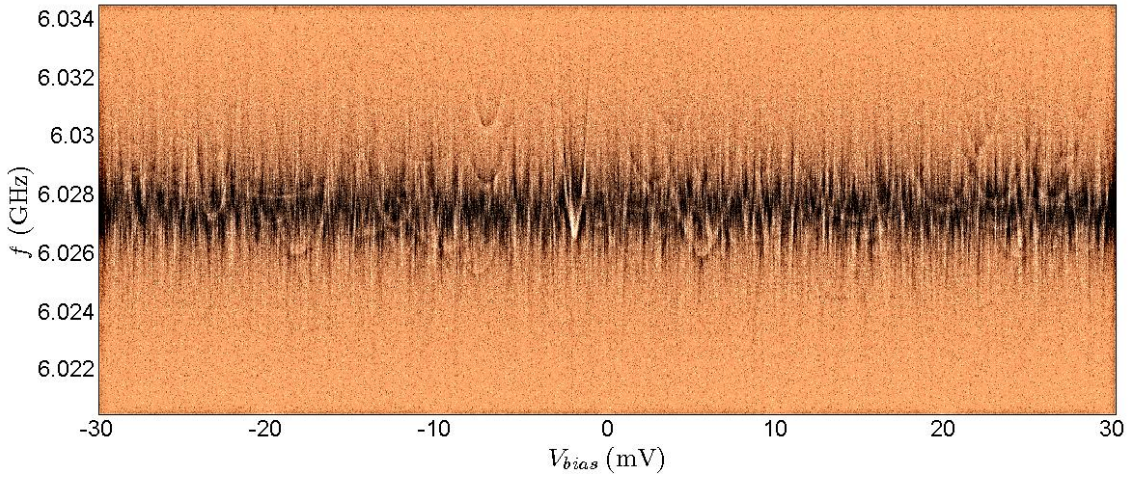

(b)

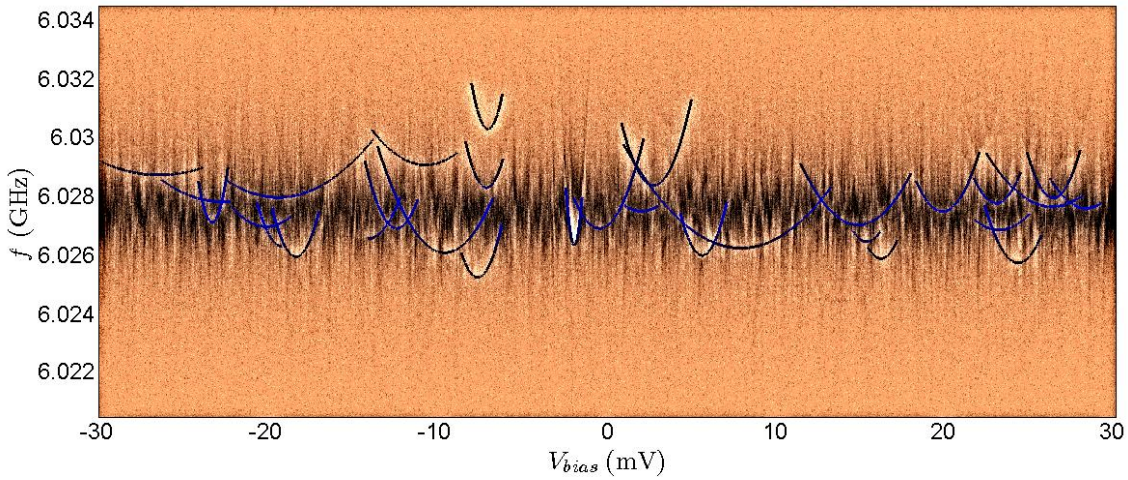

Figure 6.11: (a) False-color plot of measured $|S_{21}|$ of device Tunable Micro-V-1 versus frequency f and DC bias voltage V_{bias} after filtering the DC line for $-30\text{mV} \leq V_{bias} \leq +30$ mV. Light copper and black correspond to $|S_{21}| = 0.58$ and $|S_{21}| = 0.40$, respectively. (b) Theoretical curves fit and superimposed on the measured hyperbolas (30 total).

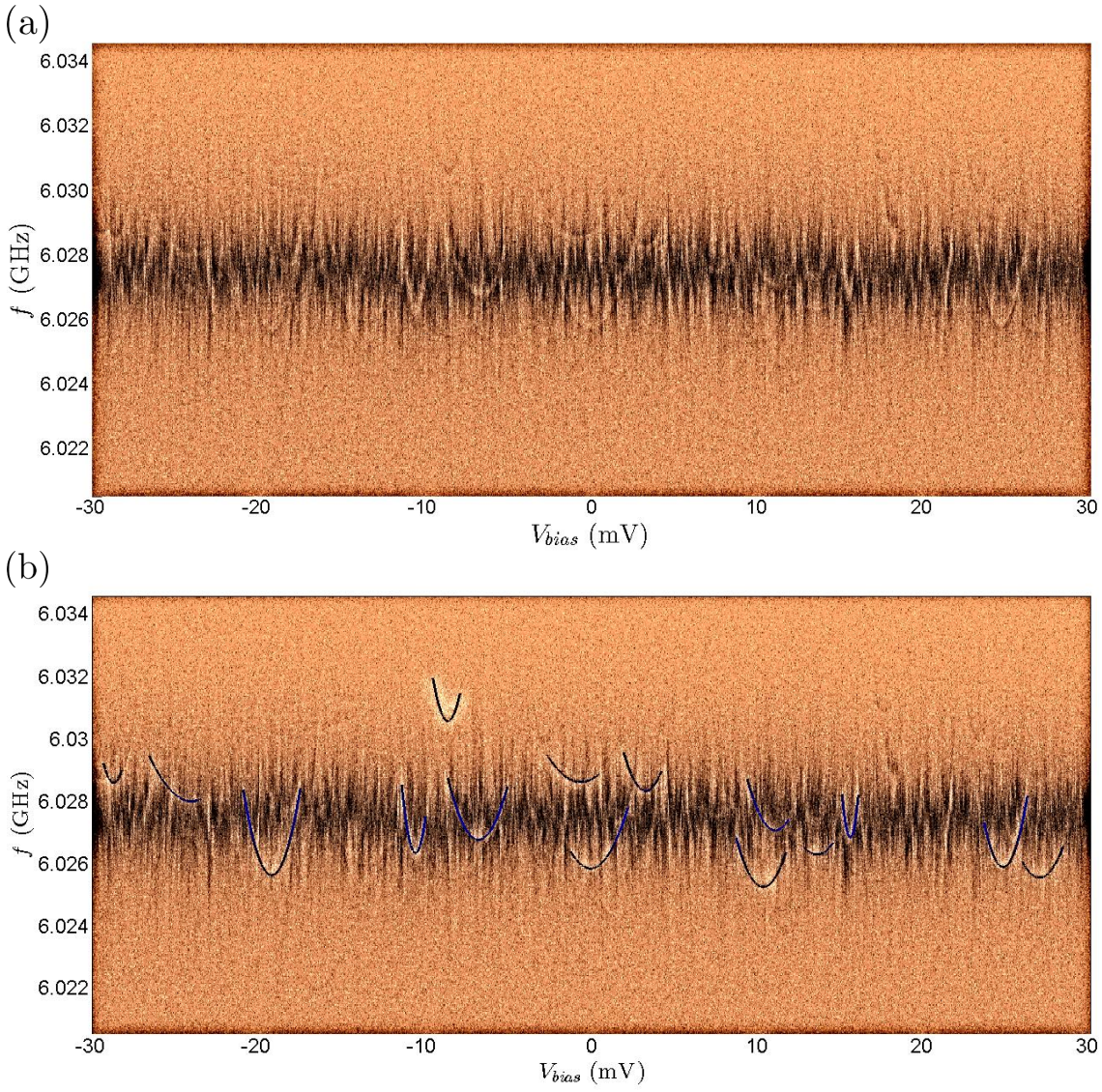

Figure 6.12: (a) False-color plot of measured $|S_{21}|$ of device Tunable Micro-V-1 versus frequency f and DC bias voltage V_{bias} after filtering the DC line for $-30\text{mV} \leq V_{bias} \leq +30$ mV. Light copper and black correspond to $|S_{21}| = 0.61$ and $|S_{21}| = 0.36$, respectively. (b) Theoretical curves fit and superimposed on the measured hyperbolas (15 total).

the dipole size as $p_{eff} = \langle p \rangle = 3.4$ Debye.

However, examination of the histogram in Fig. 6.13b suggests that there are more than one TLS dipole sizes: a distribution of large number of TLSs possibly with a triangular distribution for $p|\cos\theta| \lesssim p_1 = 3.25$ Debye, and a uniform distribution of TLSs with a dipole size of $p = p_2 \simeq 8$ Debye, as shown in Fig. 6.13b. In a previous dipole size measurement using Landau-Zener population control of TLSs, a dipole size of 7.9 Debye was extracted for SiN_x [83], a value very close to p_2.

I fit a combination of a triangular function and a Heaviside step function to the histogram of Fig. 6.13b.I took $p_2 = 8.25$ Debye corresponding to the central value of the rightmost bin in the histogram, and I ignored the distribution of TLSs with $p|\cos\theta| \leq 1$ Debye for the fitting as these TLSs are hardly visible in the spectroscopy because their coupling to the cavity is relatively small. I also weighted the fit according to the contribution of each dipole size to the loss tangent (see Eq. 6.4). The optimum fit gave $p_1 = 3.32$ Debye.

I also attempted to calculate the loss tangent based on the exact TLS distribution data in Table 6.2. I used [108]

$$\tan\delta_0 = \frac{\pi}{\epsilon_r \epsilon_0} \frac{\hbar\omega}{hBV} \frac{2d}{2(V_{bias,max} - V_{bias,min})} \sum_{i=1}^{60} (p|\cos\theta|)_i, \tag{6.4}$$

similar to Eq. 2.31 and considering the weighted style of the measurement discussed above. Here V and d are the total dielectric volume and dielectric film thickness, respectively, and the bandwidth B was calculated from the minimum and maximum Δ_0 extracted from the spectroscopy data. Equation 6.4 yielded $\tan\delta_0 = 7.8 \times 10^{-4}$.

I also extracted a loss tangent from an average of 2001 resonance lineshapes

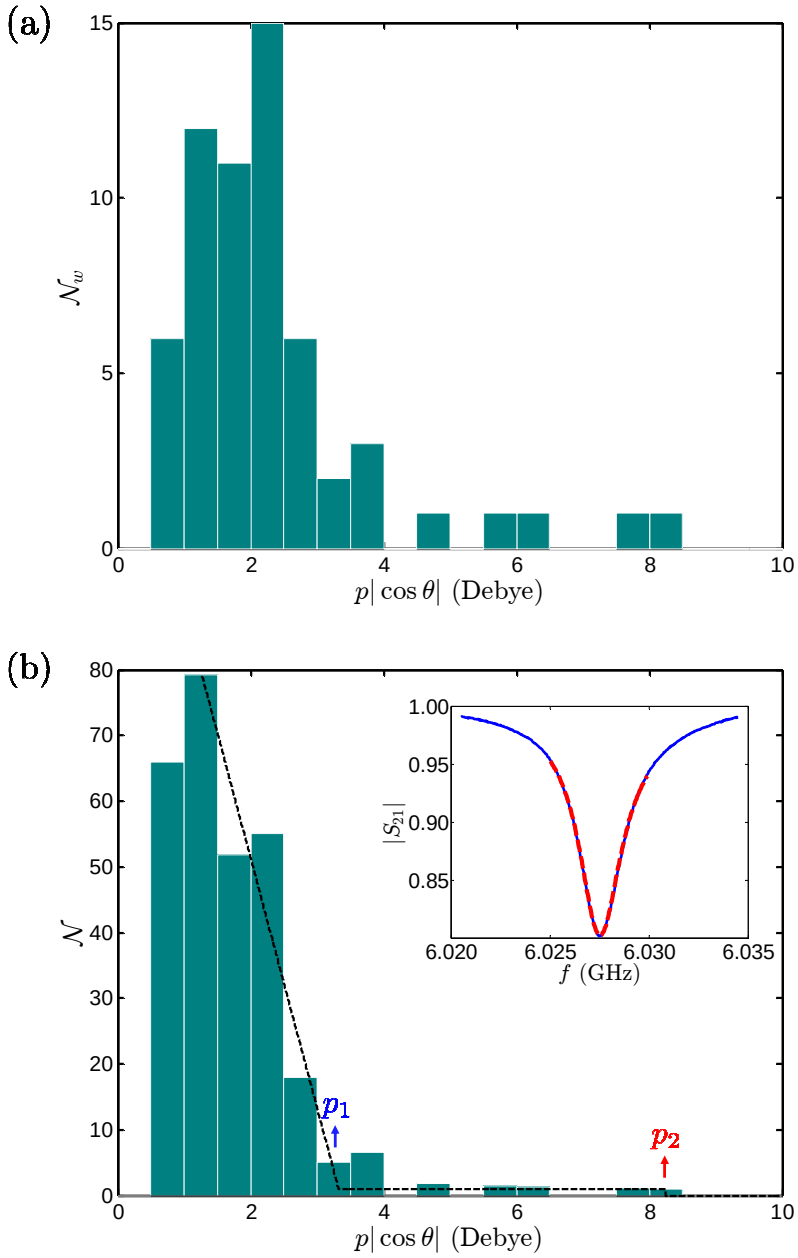

Figure 6.13: (a) Histogram of the observed (weighted) distribution $\mathcal{N}_w$ of $p|\cos\theta|$ for 60 hyperbolic trajectories from three spectroscopy sweeps performed in separate cooldowns. (b) Histogram of the distribution $\mathcal{N}$ of $p|\cos\theta|$ where $\mathcal{N} = (p|\cos\theta|_{max}/p|\cos\theta|) \times \mathcal{N}_w$ is proportional to the dipole distribution in the material. Black dashed line shows optimum fit to data from a triangular distribution of relatively small dipole sizes with $p|\cos\theta| < p_1$ and a uniform distribution of a dipole size $p = p_2$. Inset shows an average over 2001 resonance lineshapes (blue) and optimum fit (red dashed curve).

in the spectroscopy of Fig. 6.11a (see the inset of Fig. 6.13b). I used the Dual-Cavity Model (see Section 3.2.2) and extracted $\tan\delta_0' = 3.8\times10^{-4}$, which is slightly smaller than $\tan\delta_0$ obtained from the histogram of Fig. 6.13b. I note that since the measurement is performed at an average photon number of $\bar{n} \simeq 0.4$ in the cavity at not really at a low-power limit, $\tan\delta_0'$ only represents a lower limit for $\tan\delta_0$, in agreement with $\tan\delta_0$ obtained above. I also note that in the limit of large number of TLS-induced hyperbolic trajectories detected in the spectroscopy, the above-mentioned method using the $p|\cos\theta|$ distribution gives an exact value for $\tan\delta_0$.

I also attempted to analyze one of the strongest-coupled TLSs that appeared in my spectroscopy data, highlighted in Fig. 6.9b and re-plotted in Fig. 6.14a. I used Eq. 5.18 combined with Eq. 6.2 where the former models the CQED strong coupling to the TLS and weak coupling of the bath of TLSs to the cavity, and the latter describes tuning of ω_{TLS} due to V_{bias}. I wrote a LSM fitting code which allowed for fitting the 3D data of Fig. 6.14a, with the fitting parameters g, $p|\cos\theta|$, Δ_0, Δ and the parameters shown in Fig. 5.2. I used the data for a fixed V_{bias} to find the initial Monte Carlo values for some of the fitting parameters.

The optimum fit is shown in Fig. 6.14b. The key extracted parameters were $\Delta_0/h = 6.024540$ GHz, $\Delta'|_{V_{bias}=0} = 17.64\,\mu$eV, $g/2\pi = 753$ kHz, $p|\cos\theta| = 5.977$ Debye and $T_2 = 2/\gamma_{TLS} = 313$ ns where the latter is the TLS coherence time assuming negligible dephasing. From the extracted g and detuning, I was able to

Table 6.2: Extracted key parameters for 60 TLSs.

TLS number	Δ_0 (μeV)	$\Delta_{V_{bias}=0}$ (μeV)	$p\,\lvert\cos\theta\rvert$ (Debye)	TLS number	Δ_0 (μeV)	$\Delta_{V_{bias}=0}$ (μeV)	$p\,\lvert\cos\theta\rvert$ (Debye)
1	24.91606	0.833806	1.161	31	24.92545	0.145355	1.818
2	24.91035	6.749631	2.389	32	24.9315	0.94627	2.077
3	24.91451	17.30437	5.947	33	24.92787	0.3968	1.179
4	24.93283	4.648576	2.795	34	24.92164	2.349467	2.516
5	24.92131	1.998893	1.675	35	24.92264	0.970712	0.737
6	24.92198	15.27476	3.926	36	24.92591	2.872135	1.161
7	24.91841	10.21927	8.149	37	24.92357	5.238811	2.049
8	24.93218	6.524694	1.488	38	24.92121	5.942372	2.204
9	24.93266	5.706305	1.445	39	24.92777	5.902082	1.786
10	24.91941	6.283698	1.446	40	24.92903	7.318905	1.910
11	24.91862	3.489143	2.149	41	24.92965	9.659426	2.197
12	24.9157	2.105047	2.266	42	24.9206	7.794448	1.925
13	24.93243	1.385744	1.884	43	24.92524	4.298467	1.113
14	24.9326	3.615406	2.297	44	24.92851	4.109734	0.937
15	24.93119	4.05029	1.762	45	24.92827	6.109205	1.295
16	24.93294	2.362307	0.535	46	24.92998	5.104598	1.271
17	24.9292	2.463116	0.649	47	24.92308	8.562549	4.843
18	24.92635	15.55782	3.991	48	24.92487	2.33758	2.063
19	24.92979	2.209302	0.681	49	24.93242	16.7754	3.494
20	24.92569	3.662113	1.088	50	24.9325	0.134832	1.250
21	24.92288	7.051111	2.201	51	24.92107	0.016811	1.684
22	24.92154	7.548242	2.458	52	24.93132	1.240327	2.277
23	24.92403	3.973177	1.685	53	24.92131	11.59411	2.803
24	24.92546	4.546895	2.187	54	24.94051	5.167786	3.583
25	24.92203	2.083589	1.299	55	24.91862	3.621278	2.098
26	24.93436	1.663045	0.928	56	24.92611	3.799433	2.056
27	24.93116	3.284287	2.754	57	24.91989	8.432944	1.875
28	24.93941	4.085125	3.469	58	24.92015	8.499584	2.645
29	24.91859	3.273252	2.559	59	24.92518	16.72467	6.434
30	24.92301	2.509118	7.675	60	24.92291	3.912873	1.728

extract the low-power Jaynes-Cummings eigenenergies

$$E_{\pm} = \frac{1}{2}\hbar(\omega_c + \omega_{TLS}) \pm \hbar\sqrt{g^2 + (\Delta_\omega/2)^2}, \tag{6.5}$$

which are shown by the white dashed curves in Fig. 6.14b.

From $g = (\Delta_0/\mathcal{E})\mathbf{p}\cdot\mathbf{E}/\hbar$ (see Eq. 2.33) and the extracted values for Δ_0, Δ, g and $p|\cos\theta|$, I estimated the RMS electric filed within the dielectric as $E_{rms} = 25$ V/m. I estimated another value for the electric field within the dielectric from Eq. 5.4 as $E'_{rms} = \hbar\sqrt{\omega_c/(2\epsilon_r\epsilon_0\hbar V)} = 21$ V/m (see also Eq. 5.20), in reasonably close agreement with E_{rms}. The difference between E_{rms} and E'_{rms} can well be due to ignoring the cross-over capacitors and stray capacitances in estimating E'_{rms}.

I note that this TLS is listed as TLS number 3 in Table 6.2. The extracted value for $p|\cos\theta|$ using the fully-quantum-mechanical approach (Fig. 6.14b) versus the naive hyperbola model which ignores the TLS-cavity coupling (Fig. 6.9b), differs by less than 1%. One important implication of this agreement is that the DC dipole moment that produces the hyperbola shape as I tune the DC bias voltage V_{bias} is consistent with the ac coupling g between the cavity and the TLS. That is, the cavity is coupled to the TLS through its electric dipole moment.

6.7 Simulation of the results

In order to better understand the spectroscopy results, I simulated the transmission S_{21} of the tunable micro-V device in the presence of a distribution of TLSs. As the first step in the simulation I generated a random distribution of TLSs in asymmetry energy (Δ), tunneling energy (Δ_0) and dipole-field angle (θ). I started

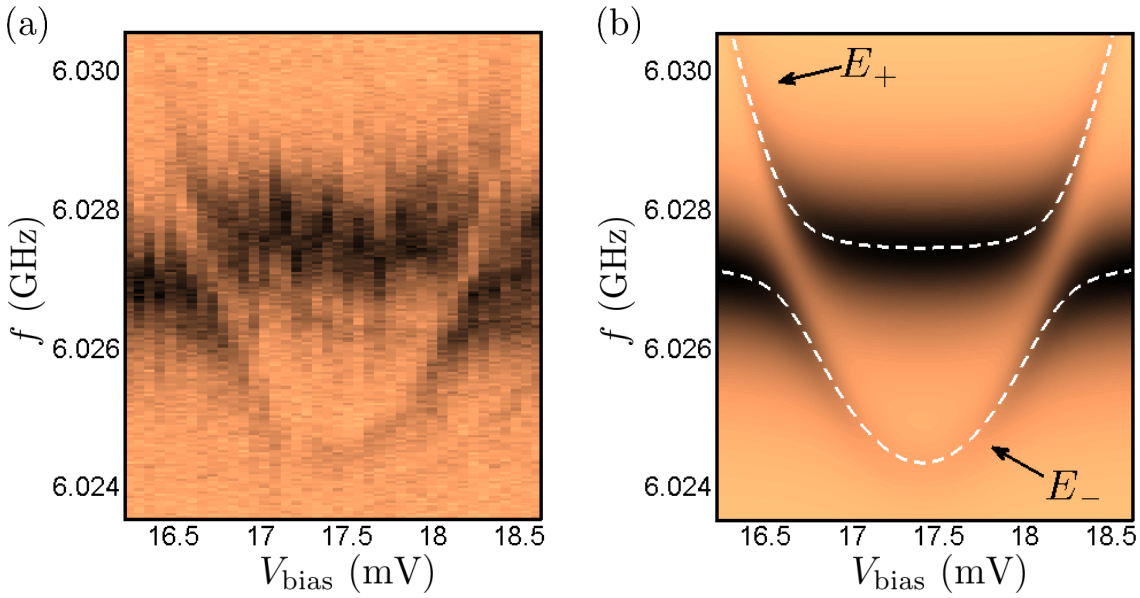

Figure 6.14: (a) False-color plot of measured $|S_{21}|$ vs. frequency f and bias voltage V_{bias} showing avoided crossings due to a TLS with $\Delta_0 \cong \hbar\omega_c$. Light copper and black correspond to $|S_{21}| = 0.60$ and $|S_{21}| = 0.43$, respectively. (b) Optimum fit to data. White dashed curves show the extracted low-power Eigenenergies E_+ and E_- of the Jaynes-Cummings Hamiltonian.

by assuming the distribution of each property according to the standard model of TLSs, as discussed in Chapter 2.

First, the spectral spatial density of TLSs needed to be estimated using Eq. 2.31. For simplicity, I assumed two distinct dominant dipole sizes of $p_1 = 3$ Debye and $p_2 = 8$ Debye. I took $\epsilon_r = 6.5$ for SiN_x and used $\tan\delta_0 = 3.8 \times 10^{-4}$ which was measured for this dielectric, and assumed that TLSs with p_1 and p_2 contribute equally to the loss tangent. The total number of TLSs within the crossover capacitors ($V = 78\,\mu\text{m}^3$) and energy band of $\mathcal{E}_{min} < \mathcal{E} < \mathcal{E}_{max}$ was calculated from Eqs. 5.24

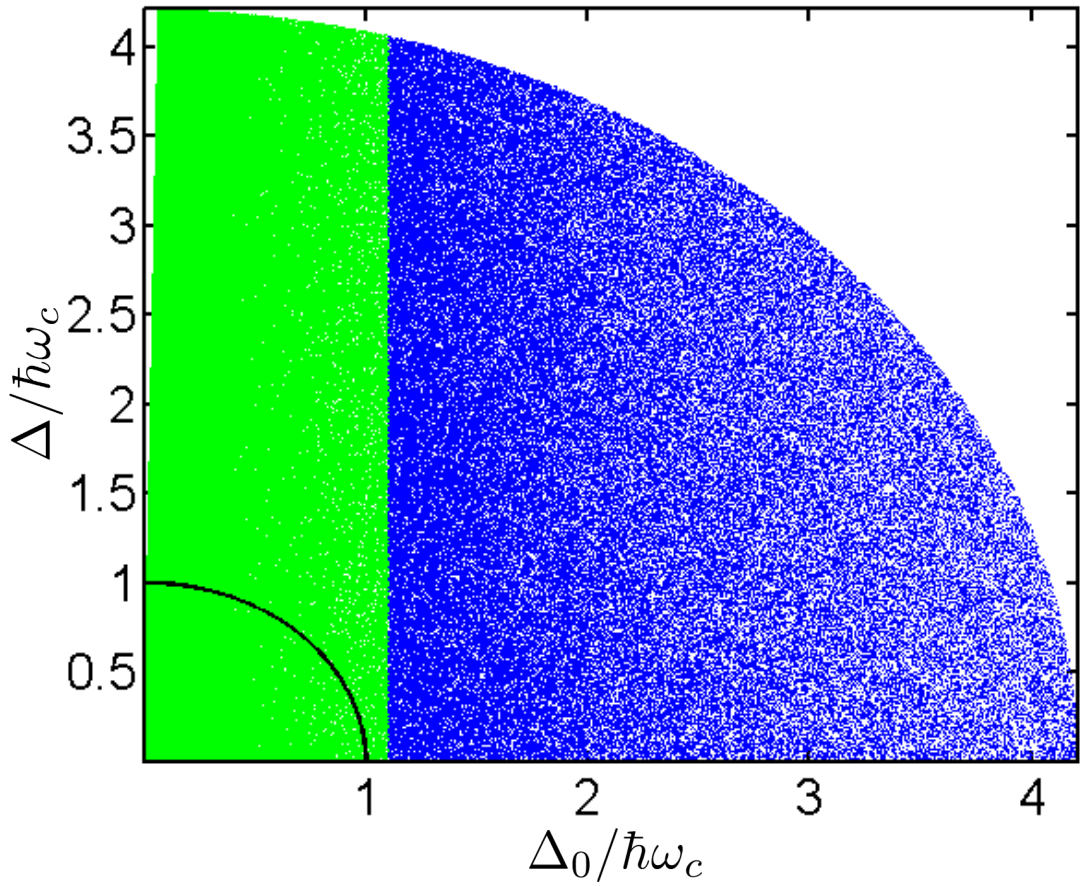

Figure 6.15: Δ-Δ_0 diagram showing simulated energy distribution of $\sim 700,000$ TLSs with $p_1 = 3$ Debye and $p_2 = 8$ Debye in bridge capacitors for $V_{bias,max} = 30$ mV. The green dots represent TLSs that are taken into account for CQED interaction in the simulation, and the TLSs in blue are ignored. The black curve corresponds to $\mathcal{E} = \hbar\omega_c$.

and 5.25 to get

$$N = P_0 V(\mathcal{E}_{max} - \mathcal{E}_{min}) \int_0^{\eta_{max}} \sec\eta d\eta. \tag{6.6}$$

I note that this number corresponds to TLSs in one quarter of the Δ-Δ_0 energy diagram with Δ defined as the absolute value of the asymmetry energy, $\Delta \equiv |\mathcal{E}_L -$

$\mathcal{E}_R|$. In this case, one should assume a uniform distribution of $\cos\theta$ between -1 and 1 for the TLSs. I note that, assuming both the AC and DC fields to be along the z-direction, only the projection of $\mathbf{p}$ on the z-axis matters and the dynamics are independent of the azimuthal angle.

However, if instead one defines $\Delta \equiv \mathcal{E}_L - \mathcal{E}_R$, then the N TLSs must be distributed in two quarters of the Δ-Δ_0 energy diagram (each quarter having $N/2$ TLSs). In this case, $\cos\theta$ must be uniformly distributed between 0 and 1. The TLSs with $-1 < \cos\theta \leq 0$ are already accounted for by the TLSs with negative Δ. TLSs with a specific physical double-well asymmetry direction map to a positive $\cos\theta$, whereas TLSs with the inverse asymmetry direction map to a negative $\cos\theta$.

I note that, however, either choice is physically acceptable and when dealing with many randomly-distributed TLSs, rather than one or few TLSs, taking $\Delta \equiv \mathcal{E}_L - \mathcal{E}_R$ together with $-1 < \cos\theta \leq 0$ does not change the resulting S_{21}.

For these simulations, I chose $\eta_{max} = 99\pi/200$ and $\mathcal{E}_{min}/h = 10$ MHz. I choose $\mathcal{E}_{max} = \hbar\omega_0 + 2pV_{bias,max}/d$ to cover the maximum shifting range of the TLSs, where $V_{bias,max}$ was the maximum applied bias voltage for the given data set being analyzed. Next, I distributed N TLSs uniformly in Δ and logarithmically in Δ_0 according to Eq. 2.9. This distribution is shown in Fig. 6.15.

I also chose $\mathrm{T}_{1,min} = 70$ ns and 120 ns for TLSs with dipole sizes of p_1 and p_2, respectively. I assigned relaxation rates to the TLSs according to $\gamma_{TLS} = 1/\mathrm{T}_1$ and Eq. 2.24, and I neglected dephasing. The TLS-cavity coupling rate g was assigned according to Eq. 5.20. I also set the resonator decay rate to $\gamma_c = \tan\delta_0/\omega_c = 10^{-5}/\omega_c$ which approximately corresponds to the loss tangent associated with an

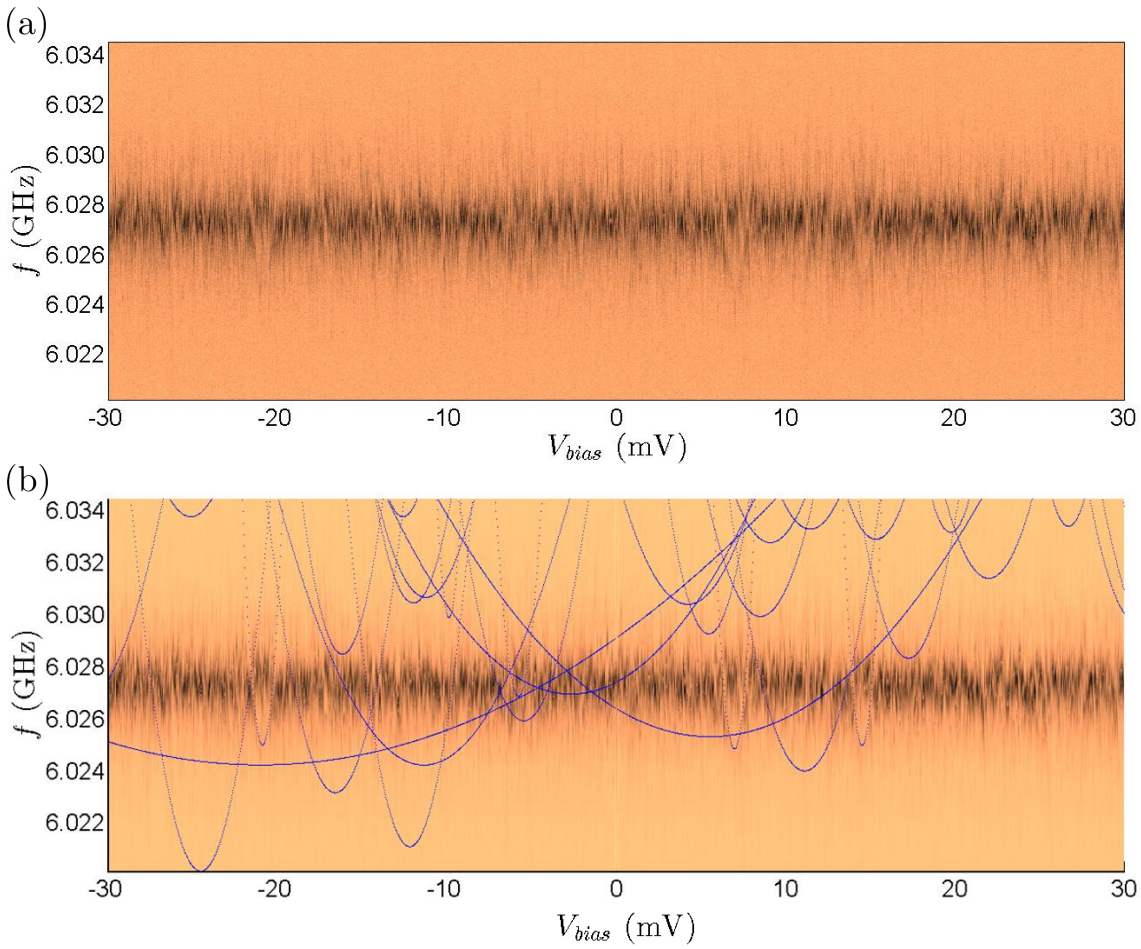

Figure 6.16: (a) False-color simulation of $|S_{21}|$ from Eq. 5.16 with $T_{1,min} = 70$ ns and 120 ns for distribution of TLSs with dipole sizes of $p_1 = 3$ Debye and $p_2 = 8$ Debye, respectively. White Gaussian noise is added to $|S_{21}|$ to allow a better comparison with data. Light copper and black correspond to $|S_{21}| = 0.53$ and $|S_{21}| = 0.36$, respectively. (b) Same simulation data as in (a) with the hyperbolas that have $\Delta_0 \cong \hbar\omega_c$ marked with blue, and with no gaussian noise added to $|S_{21}|$.

aluminum coplanar resonator on sapphire. In other words, I assumed a constant background loss of $\tan\delta = 10^{-5}$ from weakly-coupled TLSs, and that *all* TLSs in SiN_x interact with the cavity based on CQED. Given a large number of TLSs, we expect the resonator's average resonance lineshape to be Lorentzian. To find S_{21}, I

used Eq. 5.16.

For a simulation of the data shown in Fig. 6.9a, I set $-30\,\mathrm{mV} \leq V_{bias} \leq 30\,\mathrm{mV}$. For better comparison of simulation with data, I added white Gaussian noise to the simulated $|S_{21}|$, to produce a SNR similar to the experimental data. I also included TLSs within the crossover capacitors and assumed that they are not sensitive to V_{bias}. Figure 6.16 shows results from the simulation.

Examination of Fig. 6.16 reveals some interesting points. Qualitatively, the simulation is very similar to the data. Clearly, an average Lorentzian-like lineshape *can* be achieved by the CQED interaction of many TLSs with the cavity (even if $\gamma_c = 0$), just as if a constant loss tangent was assumed for the resonator. Second, despite the similarities between Figs. 6.16 and Fig. 6.9a, some significant differences are noticeable. One major difference is that the hyperbolas (TLSs) with $\mathcal{E} \simeq \Delta_0$ appear more clearly in the data than in the simulation. The reason may be that the number of TLSs in the simulation is too few, or some parameters (*e.g.* $\mathrm{T}_{1,min}$) are not estimated correctly, or a different distribution (*e.g.* triangular distribution) must be considered for the TLSs with small values of $p\cos\theta$.

6.8 Conclusion

In this chapter, I presented results on a micro-V device (Tunable Micro-V-1) that in addition to measurements of individual TLSs, allows for DC-tuning of the TLSs. A DC electric field changes the asymmetry energy of the TLS double-well potential, allowing tuning of the TLS transition frequency. This device was realized

by incorporating a capacitor bridge in the resonator and using a relatively large spiral inductor to reduce the electric field volume. To suppress noise on the DC-bias line, several filtering stages were used.

I found that the measured microwave spectrum showed clear tracks entering and exiting the cavity's bandwidth. Most of these tracks were straight asymptotes of hyperbolas generated by the CQED coupling of TLSs to the resonator, as discussed in Chapter 5. For TLSs with tunneling energy Δ_0 close to the resonator resonance frequency, the minimum frequency of the hyperbola appears in the spectroscopy. For these TLSs, one can accurately extract the asymmetry energy Δ in the absence of the DC field, the tunneling energy Δ_0, and $p\cos\theta$, the projection of the dipole moment on the electric field direction.

Analysis of 60 fitted hyperbolas in spectroscopy results from three DC-bias sweeps on the device Tunable Micro-V-1 suggested at least two dipole sizes for TLSs. One of the dipole sizes was in agreement with a recent ensemble study of SiN_x [83]. My ability to distinguish a distribution of dipole sizes may be due to the inherent advantages of being able to measure $p|\cos\theta|$ of individual TLSs compared to ensemble measurements or individual measurements of $(\Delta_0/\mathcal{E}) \times p|\cos\theta|$. It can also be due to different types of defects in SiN_x deposited using different recipes.

I note that this type of study could be performed on other amorphous dielectrics. The combination of direct TLS-cavity coupling and DC-tuning of the TLSs, can give us a deeper and more complete understanding of TLSs in amorphous solids.

Finally, I note that the study in this Chapter tests the double-well potential

model for the TLSs, and confirms it to good accuracy. However, the presence of other potentials including soft anharmonic single wells has been suggested for nanoscale TLSs [115]. Further measurements using this device type may well reveal additional insight into the nature of TLSs in SiN_x.

Chapter 7: TiN film growth at different RF-induced DC biases

7.1 Motivation

In recent years, superconducting titanium nitride (TiN) has become an important subject of research because of its unusual properties when used in superconducting microwave resonators [116], superconducting qubits [117] and microwave kinetic inductance detectors (MKIDs) [118]. Thin-film TiN has several characteristic make it an attractive material for superconducting microwave devices, including:

(a) TiN films can show remarkably low loss at microwave frequencies. TiN superconducting resonators with single-photon internal quality factors of $Q_i = 5 \times 10^6$ have been reported [119].

(b) The critical temperature of TiN films can be tuned in the range $0 \lesssim T_c \lesssim 5$ K, with composition controlled by partial N_2 pressure (or mass flow rate) during deposition. This is useful for MKIDs because, in general, lower-T_c materials are needed for sensitive detectors [118].

(c) The normal-state resistivity is relatively high, on the order of $\rho_n \sim 100\ \mu\Omega$ cm [118].

(d) Due to relatively large resistivity, the London penetration depth is large and

sufficiently thin TiN films show remarkably high kinetic inductance. Other potentially useful non-linear effects can also be observed [120].

(e) TiN films are very hard and mechanically robust [118].

(f) TiN has a high corrosion resistance and stoichiometric TiN does not grow a native oxide at room temperature when it is exposed to air [121].

Although TiN appears to be a promising material for certain applications in quantum computing and astrophysics, there are some challenges. For example, many of these applications require tuning the structural and low-temperature microwave properties of the reactively-sputtered films. Previous work has shown that some of these properties can be tuned by nitrogen (N_2) flow [122], substrate temperature [123, 124], sputtering chamber pressure, or distance between the target and the substrate [119].

The overall goal of the work I describe here was to develop a TiN process that was suitable for incorporating TiN in some future devices at LPS. In the first stage of the TiN process development, I attempted to obtain a film with the right visual properties, *e.g.* color (orange / brown) and shininess, which were indicators that nitrogen was being incorporated into the film. During this stage, I mainly adjusted the N_2 flow during reactive sputtering in Ar. I used a 3"-diameter titanium (Ti) planar sputtering target and DC sputtering power of 400 W and substrate temperature of 500 °C in the sputtering chamber described in section 4.3. I found that a film with the right color could be obtained by using nitrogen and argon (Ar) flows of 10 sccm and 15 sccm respectively into the sputtering chamber. My approach

was based on a similar recipe reported by Sandberg *et al.* [125].

To my surprise the first films I deposited did not look shiny. This could have been an indication that the films were amorphous or had μm-scale surface nonuniformity. To fix this, I tried adding an RF bias to the substrate using RF forward powers of $0 < P_{RF} < 55$ W during DC sputtering. This RF power induced a DC voltage on the substrate which depended on P_{RF}. Also, a higher P_{RF} resulted in a brighter plasma inside the processing chamber. I found that for RF-induced DC bias of $V_{sub} \gtrsim 250$ V on the substrate, the films look shinier with a slightly lighter color (more orange than brown), indicating a change in their physical properties. This result motivated me to perform a more detailed investigation of the effect of V_{sub} on the properties of TiN at room- and millikelvin-temperatures [126].

The short-term goal of this study was to investigate TiN film composition (elements and phases), stress, critical temperature, uniformity, kinetic inductance, *etc.* as a function of the RF-induced DC bias during deposition. The long-term goal, however, was to obtain low-loss TiN films with the desired electrical properties, and to reduce the TiN-Si interface loss in TiN resonator circuits by functionalizing the Si surface prior to TiN film deposition.

7.2 Resonator design

For this study, I designed a chip with three resonators coupled to a single transmission line. One of the resonators (Res 3) was a lumped-element LC circuit with a meandering inductor and an interdigitated capacitor (IDC). The other two

Table 7.1: Table of TiN resonators with designed values for line width LW, line spacing LS and resonance frequency f_0.

Device label	Device type	LW (μm)	LS (μm)	f_0 (GHz)
Res 1	quarter-wave	3	3	6.932
Res 2	quarter-wave	20	15	7.516
Res 3	lumped-element	10	10	7.941

resonators (Res 1 and 2) were quarter-wave resonators with significantly different line width (LW) and line spacing (LS). According to a previous study, for a similar resonator design, using smaller LW and LS increases the impact of surface loss on a resonator's internal quality factor Q_i [127].

Table 7.1 summarizes the design values for LW, LS and the resonance frequency f_0 for the three designs. For Res 3, the LW and LS correspond to the IDC fingers only. The frequencies in Table 7.1 were based on just the geometrical inductance, *i.e.* the London penetration depth is assumed to be zero. The operating bandwidth of the HEMT LNA was 4-8 GHZ, therefore, in order to account for possible shifts in resonance frequencies due to a large kinetic inductance (L_k) of the TiN films, I designed the resonators to have resonance frequencies in the upper part of this span. Also, the resonance frequencies were designed to be about 0.5 GHz apart in order to conveniently distinguish the resonators in the experiments. All three resonators were designed to have $Q_e \simeq 1 \times 10^5$. The layout of the devices is shown in Fig. 7.1.

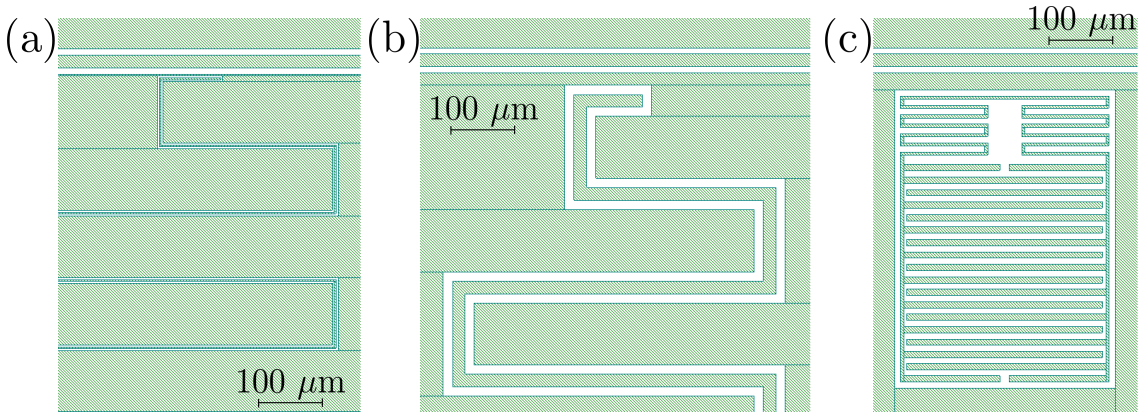

Figure 7.1: Layout of (a) Res 1, (b) Res 2, and (c) Res 3 from AWR Microwave Office.

7.3 Fabrication

Two sets of samples where fabricated, each set containing 6 samples deposited at different V_{sub} (see Table 7.2). The first set (TiN-only set) was made of TiN films only. For the second set (hybrid TiN-Al set), the coplanar transmission line was made of aluminum while the devices where made of TiN. This reduced the kinetic inductance of the transmission line and enabled these chips to operate with a matched input/output line. I describe the fabrication steps in the next two sections.

7.3.1 TiN-only design

I used 3-inch diameter float-zone silicon substrates with high-resistivity (> 20000 $\mu\Omega$-cm) manufactured by Topsil. First, the substrates where dipped in an HF solution to remove the SiO_2 layer formed on the surface due to exposure to

Table 7.2: Table of the fabricated TiN samples.

Sample label	Fabrication set	V_{sub} (V)
TiN-RF-65	TiN-only	0
TiN-RF-66	TiN-only	110
TiN-RF-67	TiN-only	175
TiN-RF-54	TiN-only	250
TiN-RF-60	TiN-only	325
TiN-RF-64	TiN-only	400
TiN-RF-72	Hybrid TiN-Al	0
TiN-RF-68	Hybrid TiN-Al	110
TiN-RF-75	Hybrid TiN-Al	175
TiN-RF-73	Hybrid TiN-Al	250
TiN-RF-74	Hybrid TiN-Al	325
TiN-RF-70	Hybrid TiN-Al	400

the atmosphere. From my previous low-temperature measurements on resonators, I found that dipping the substrate in 49% HF for 30 s removed the substrate native oxide more effectively than using 1% HF for 3 minutes. After HF-dipping, the substrate was rinsed with DI water for less than 10 s and transferred into the sputtering load-lock as quickly as possible, which was pumped out immediately to prevent formation of a thick and lossy SiO_2 layer. The time interval between taking out the substrate from the HF solution to the beginning of pumping on the load-lock was approximately 2 minutes.

After transferring the wafer to the CMS-18 sputtering chamber (see section 4.3), the chamber was pumped to $\sim 10^{-8}$ Torr and the PID temperature controller was set to 500 °C and allowed to stabilize in about 30 minutes. Constant flow rates of N_2 (10 sccm) and Ar (15 sccm) were used, which resulted in a chamber pressure of

Table 7.3: Magnitude of the RF-induced DC biases on the substrate V_{sub}, and deposition times t_{dep} as a function of the applied forward RF power P_{RF} to the substrate. All films were about 62 nm thick.

P_{RF} (W)	0	4	10	20	37	52
V_{sub} (V)	0	110	175	250	325	400
t_{dep} (min.)	29	34	40.5	39	41	39

approximately 4.3 mTorr with the main gate valve to the cryo-pump throttled. The DC magnetron sputtering power of 400 W was used to sputter the 3-inch diameter Ti target (purity: 99.995%). Before opening the substrate shutter, pre-sputtering was performed for 1 minute without the RF-bias, and an additional 30 s with the RF power applied to the substrate. The substrate shutter was then opened and TiN was deposited to obtain 62 nm thick films. The target-substrate distance was about 20 cm.

The deposition time and the substrate DC voltage depended on P_{RF} (see Table 7.3). Six samples were deposited using RF-induced DC bias magnitudes (V_{sub}) of 0 V (nominal), 110 V, 175 V, 250 V, 325 V and 400 V. I note that the sample with $V_{sub} = 0$ V has no DC voltage due to P_{RF} since no RF power was applied, but there was a relatively small DC voltage on it as a result of the chamber plasma and the sputtering gun voltage.

Once the deposition was finished, the wafer was taken out of the chamber

and cooled down close to room temperature in the load-lock (no exchange gas was used). I then patterned the wafers using my standard photolithography procedure: resist coating using Fujifilm OiR 906-10 photo resist, pre-baking at 90 °C for 60 s, exposure for 0.35 s, post-backing at 120 °C for 1 minute and developing in OPD 4262 developer for 40 seconds. the samples were then transferred into the ICP tool described in Chapter 4, and etched for 2 minutes using a chlorine-based recipe with the following parameters: BCl_3 flow: 12.5 sccm, Cl_2 flow: 2.5 sccm, Chamber pressure: 3.5 mTorr, RIE power: 50 W, ICP power: 500 W. This recipe also etched the Si substrate. However, etching for 2 minutes did not cause noticeable narrowing of the lines.

After taking out the samples from the ICP tool, they were dipped in phosphoric acid for 1 minute to remove chlorine residue [128]. Finally, the samples were cleaned using my standard organic cleaning process, described in Chapter 4. After this process, energy-dispersive X-ray spectroscopy showed no trace of Cl.

The above procedure completed the fabrication of the first set of six TiN samples at the wafer level, which I refer to as the TiN-only set.

7.3.2 Hybrid TiN-Al design

Another set of six samples were fabricated using the procedure described in section 7.3.1, plus an additional photolithography and deposition step (described below) to create the CPW out of aluminum. I refer to this set of six samples as the hybrid TiN-Al set. The purpose of the Al CPW is to reduce possible impedance

mismatch from the sample box PC board CPW to the on-chip TiN CPW due to a large kinetic inductance in the TiN films.

To avoid contact between Al and the TiN in the resonators, a lift-off process was used to deposit Al on the TiN CPW transmission line only. The prepared TiN wafer was coated with MicroChem LOR-5A photoresist (spun at 4000 rpm for 1 minute), and pre-baked for 1 minute at 195 °C. Then another layer of photoresist (Fujifilm OIR-906-10) was spun at 3000 rpm for 1 minute, and pre-baked at 90 °C for 1 minute. The wafer was then exposed (for 0.35 seconds), post-baked (at 120 °C for 1 minute) and developed in OPD4262 (for 60 seconds).

The wafer was then transferred to the E-beam evaporation tool to deposit 100 nm of Al. E-beam evaporation is more directional than sputtering and reduces fencing at the edges compared to the case if sputtering is used with a lift-off. The samples where then soaked in MicroChem Remover PG (at 70 °C) for > 75 minutes. Next, the wafer was soaked in a second Remover PG (at 70 °C) for about 10 minutes to ensure that all the resist and the Al above it was lifted off. The wafer was cleaned using my standard organic cleaning process.

After the lift-off process, SEM imaging and profilometry confirmed that no fencing occurred on the edges. Figure 7.2 shows optical images of the three finished hybrid TiN-Al resonators.

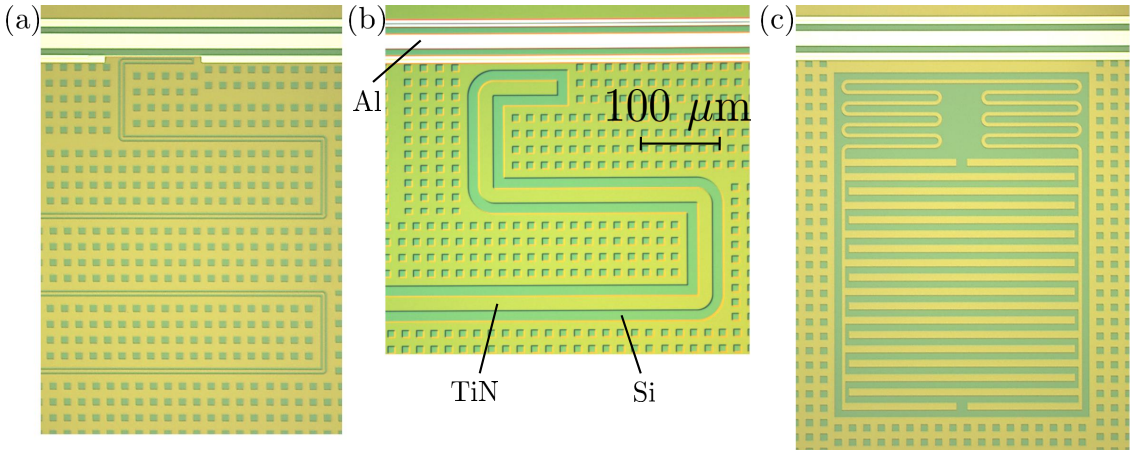

Figure 7.2: Optical images of the hybrid TiN-Al resonators: (a) Res 1 (b) Res 2 (c) Res 3.

7.4 Structural and compositional properties

Several structural and compositional properties of the *unpatterned* TiN films sputtered with different V_{sub} were investigated as part of the process development, as I describe below.

Crystalline structure

C. Richardson from LPS used X-ray diffraction (XRD) to determine the crystalline structure and phases of the deposited films. A θ-2θ scan in the range 27°-60° was performed on the unpatterned samples (see Fig. 7.3a). All six films showed a Si peak at 33°-34° due to the substrate. For the V_{sub} = 0 V film, XRD indicated the presence of α-Ti, TiO_2 and TiN with a texture of (111) and (200) orientations.

For the $V_{sub} = 110$ V film, weak peaks from both (111) and (200) planes indicated a lack of dominant crystal orientation and possibly an amorphous microstructure. The presence of the (111) direction for $V_{sub} \leq 110$ V could be due to lower strain energy from this phase [129]. For films with $V_{sub} \geq 175$ V, the (111) peak disappears and the δ-TiN (200) peak becomes dominant as V_{sub} is increased. These samples show only a small peak due to the tetragonal phase, Ti_2N, which is a normal conductor. Finally, for the $V_{sub} = 400$ V film, the (200) peak broadened and reduced in intensity.

Film stress

The film stress was measured for the six TiN wafers before patterning. This required making two measurements on each wafer: once before the film deposition to measure the initial substrate deflection, and one after the deposition to measure the combined substrate-film deflection. Details on the stress measurements are discussed in Section 4.3.

The results of the stress measurements are shown in Fig. 7.3b where the film stress S is plotted as a function of V_{sub} in blue. The green curve shows the δ-TiN (200) peak height normalized to the background value from the XRD measurements. The results indicate that stress is tunable in a wide range - from slightly tensile (negative stress) to highly compressive (positive stress). Also, this data shows a strong correlation between stress and the changes in crystal orientation.

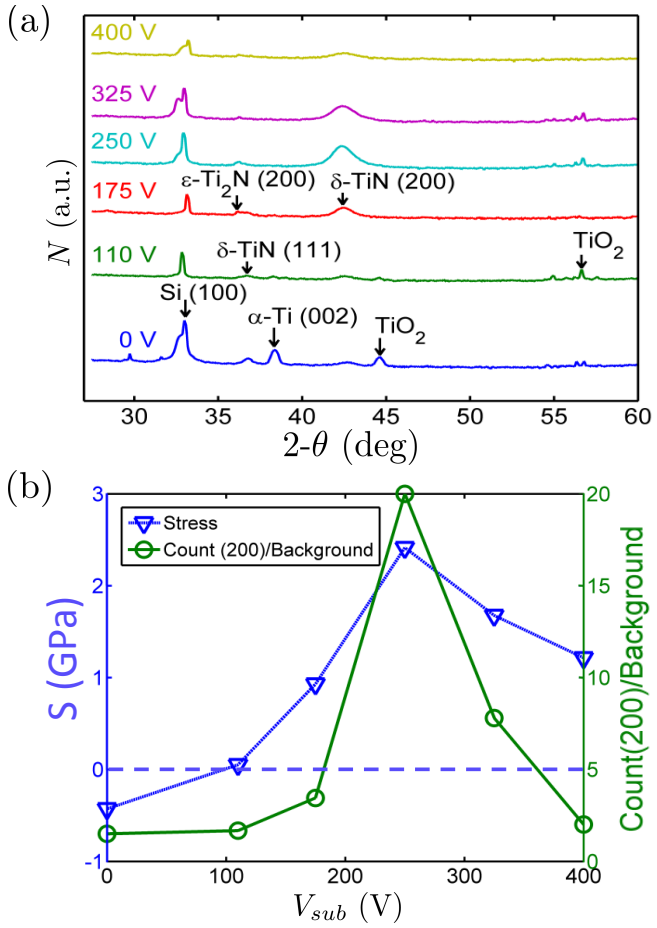

Figure 7.3: From Ref. [126] (a) XRD counts N versus angle 2-θ for films with different V_{sub}. (b) Film stress S versus V_{sub} showing correlation with the δ-TiN (200) phase.

Table 7.4: Elemental concentrations, superconducting critical temperature T_c and resistivity ρ for sputtered TiN films at different V_{sub}. The XPS elemental composition was obtained at 30 nm below the TiN film surfaces.

V_{sub} (V)	Ti (at. %)	N (at. %)	O (at. %)	C (at. %)	T_c (K)	ρ ($\mu\Omega$-cm)
0	47.9	44.7	7.2	0.2	4.12	436
110	47.8	47.5	3.7	0	4.37	96
175	49.7	50.1	0.1	0	4.36	64
250	49.3	50.7	0	0	4.45	29
325	50	50	0	0	4.58	22
400	50	50	0	0	4.35	32

Elemental composition

E. Lock at the Naval Research Laboratory performed sputter elemental depth profiles using a K-Alpha X-ray photoelectron spectroscopy (XPS) system. Figures 7.4 and 7.5 show the atomic percentage of titanium, nitrogen, oxygen, carbon and silicon as a function of the sputter-etch time for all six samples. Table 7.4 gives the elemental concentrations in 30 nm depth inside of the films.

Although significant carbon concentration was found on the surfaces of the films, almost no carbon was found in the bulk. The carbon on the surfaces is believed to be due to exposure to air. For the films with $V_{sub} = 0$ V and $V_{sub} = 110$ V, oxygen content generally decreases as a function of depth, suggesting diffusion

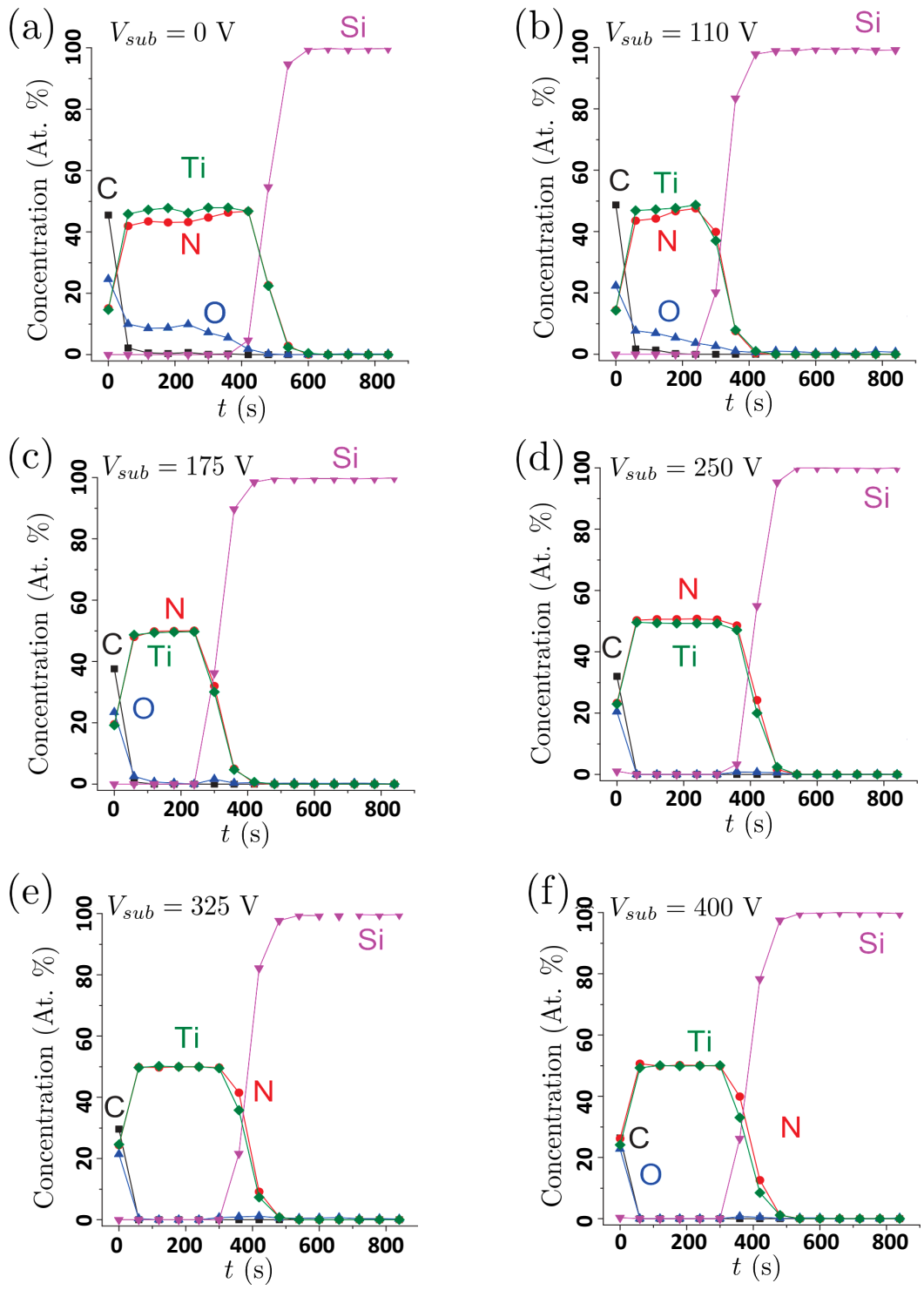

Figure 7.4: XPS results for TiN films with (a) $V_{sub} = 0$ V (TiN-RF-65) (b) $V_{sub} = 110$ V (TiN-RF-66) (c) $V_{sub} = 175$ V (TiN-RF-67) (d) $V_{sub} = 250$ V (TiN-RF-54) (e) $V_{sub} = 325$ V (TiN-RF-60) (f) $V_{sub} = 400$ V (TiN-RF-64). Courtesy of E. Lock, Naval Research Laboratory.

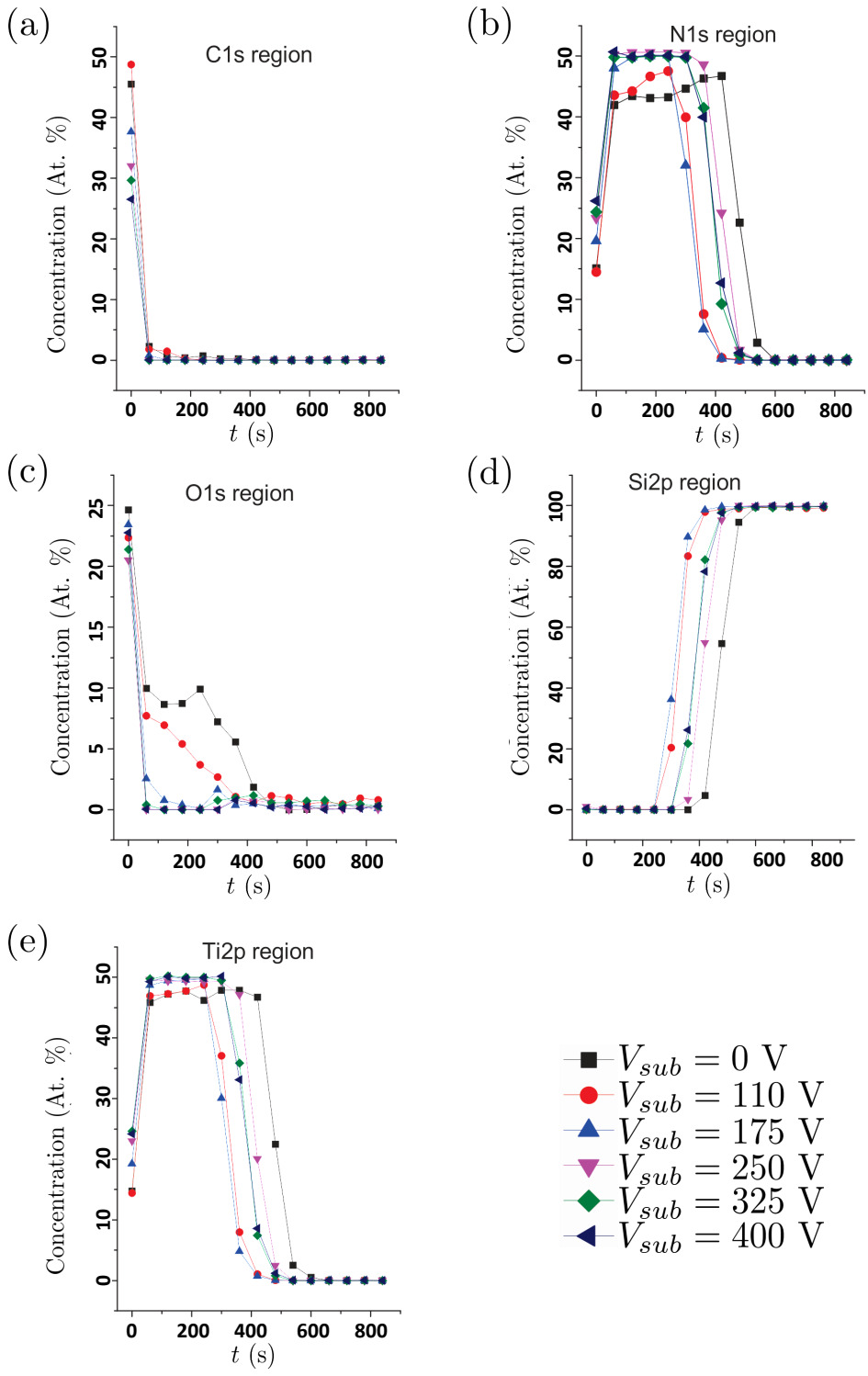

Figure 7.5: XPS depth profiles showing atomic-percent concentration of (a) carbon (b) nitrogen (c) oxygen (d) silicon and (e) titanium for six sputtered samples (TiN-RF-65, TiN-RF-66, TiN-RF-67, TiN-RF-54, TiN-RF-60 and TiN-RF-64). Courtesy of E. Lock, Naval Research Laboratory.

from the atmosphere into the film via grain boundaries. For the films with $V_{sub} > 110$ V, negligible oxygen was detected in the bulk, probably because the films were denser with fewer voids and open structures for oxygen diffusion [130].

Resistivity

The room-temperature resistivity ρ was measured using a 4-point probe (courtesy of H. M. I. Jaim and J. A. Aguilar). The variation in ρ was approximately 2% across a single wafer for all measured wafers, and about 2% for different films sputtered at the same V_{sub}. There was a strong correlation between the resistivity at room temperature and oxygen content as shown in Fig. 7.6. The highest resistivity was 436 $\mu\Omega$-cm observed in the 0 V bias film which had 7.2% oxygen at 30 nm below the surface. As V_{sub} was increased, a gradual reduction in oxygen content and resistivity was observed. When the oxygen concentration at 30 nm reached 0%, the resistivity dropped to approximately 28 $\mu\Omega$-cm, approximately 50% above the bulk crystalline TiN value of 18 $\mu\Omega$-cm [131]. I note that these observations are consistent with previous reports [130].

Uniformity of thickness and index of refraction

The uniformity of the film thicknesses and the complex indices of refraction $\tilde{n} = n + ik$ were measured (courtesy of Y. Rosen) by broadband spectrophotometry using the N&K analyzer described in section 4.3. The thickness across a 3-inch wafer showed a relative standard deviation of less than 2% indicating very uniform

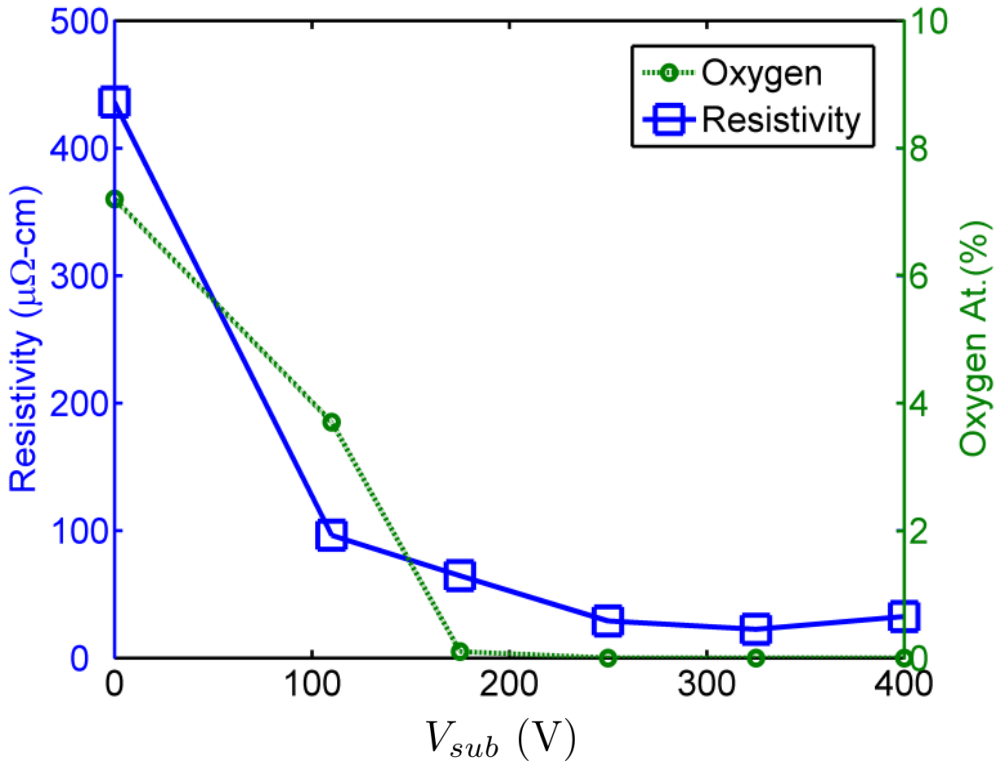

Figure 7.6: Correlation between resistivity and oxygen content for different films (from Ref. [126])

films. Also, the relative standard deviation in n and k was less than 5% and 2%, respectively.

7.5 Low-temperature properties

This section includes the measurement of critical temperature T_c of the films sputtered with different V_{sub}, as well as some results from millikelvin microwave measurements.

Critical temperature

The critical temperatures T_c of the films were measured on small diced sections of the wafer using a probe which was dipped in liquid ^{4}He. By pumping on ^{4}He, temperatures of approximately 1 K could be reached. Similar to the room temperature measurements, a 4-point measurement technique was used. The T_c was measured using a 90%-resistance criteria. Table 7.4 includes the T_c for the films with different V_{sub}. I note that increasing V_{sub} caused T_c to increase slightly, but T_c was generally in the range $4\,\mathrm{K} < T_c < 4.5\,\mathrm{K}$. By comparing T_c of the samples taken from the centers and edges of the wafers, it was found that T_c varied by less than 2% across the 3-inch wafers, independent of V_{sub}. I note that a previous experiment using a different growth method showed a T_c variation of $\pm 15\%$ across a 3-inch wafer [132].

Quality factors

After cooling to $\sim$20 mK the resonance frequencies of all the resonators were found to be significantly lower than the design values given in Table 7.1 due to a high kinetic inductance. This caused some complications. In particular, it was difficult to identify which resonator produced which resonance as there was a possibility of shifts in the order of resonance frequencies.

Regardless of the resonator type, all resonators on films with different V_{sub} were measured and analyzed. Each resonator transmissions S_{21} curve was fit to the Dual-Cavity Model described in section 3.2.2, using the LSM method. All resonators showed single-photon internal quality factors of $1 \times 10^5 \lesssim Q_{i,0} \lesssim 3 \times 10^5$. As an

example, Fig. 7.7a shows Q_i versus the average photon number $\bar{n}$ for resonators Res 1, Res 2 and Res 3 which were made from the $V_{sub} = 250$ V film (TiN-RF-54). The curves are labeled according to the best guess as to which resonator was responsible.

I also fit the characteristic loss tangent $\tan\delta = 1/Q_i$ versus the electric field amplitude for all resonators to theory to extracted the limiting low-power value. The model that I used was a modified low-temperature version of Eq. 2.35, *i.e.*

$$\frac{1}{Q_i} = \frac{1}{Q_{i,0}} \frac{1}{\left(\sqrt{1+(E/E_c)^2}\right)^{1-\beta}}. \tag{7.1}$$

Here β is a variable that allows for a weaker E-dependence than E^{-1} in the high-power limit. While the standard TLS theory described in Chapter 2 predicts $\beta = 0$, all the TiN resonators showed $0.7 \lesssim \beta \lesssim 1$, indicating a shallower slope (than the predicted slope of -1) on a logarithmic plot of loss tangent versus E. This could be due to an unusual TLS distribution or a loss mechanism producing a significant background loss, or possibly due to a TLS-related effect not included in the standard TLS theory.

As an example, Fig. 7.7b shows $1/Q_i$ versus the electric field amplitude E for Res 2. This film had $V_{sub} = 250$ V from the TiN-only design. I performed the fitting using the LSM method and the theory described by Eq. 7.1. The extracted parameters were $Q_{i,0} = 3.2 \times 10^5$ and $\beta = 0.71$. I note that this extracted $Q_{i,0}$ represents all internal loss mechanisms including the TLS-induced loss.

In order to help me distinguish the resonators for the hybrid TiN-Al samples, I shorted out the interdigitated capacitor of Res 3 by wire-bonding the capacitor fingers. This allowed me to clearly distinguish Res 1 and Res 2 in the experiments.

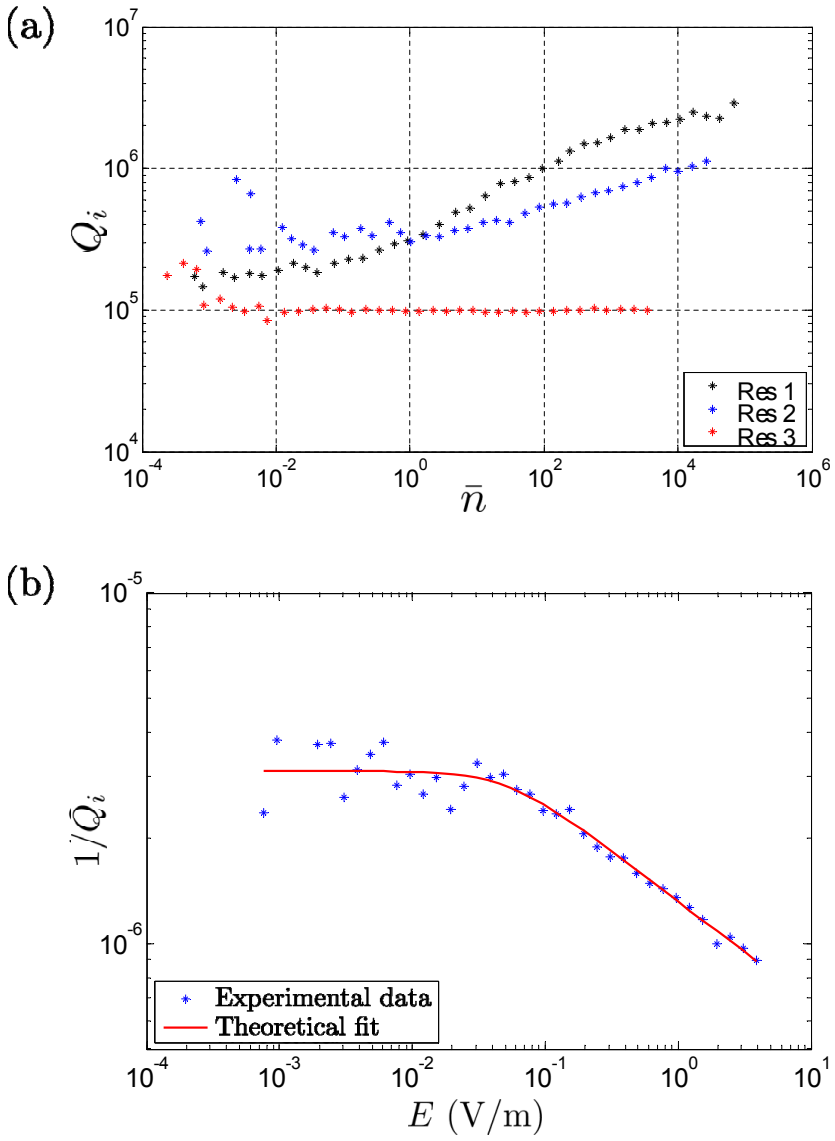

Figure 7.7: (a) Internal quality factors Q_i versus the average number of photons $\bar{n}$ for three resonators made from the V_{sub} = 250 V film (TiN-RF-54). (b) Loss tangent $1/Q_i$ versus electric field amplitude E applied to the TLSs for Res 2, with theoretical fit to data (red curve).

The TLS-induced loss tangent was extracted using the temperature dependence of the resonance frequencies. For this purpose, resonance frequencies of Res 1 and Res 2 were measured in the range $0.03 < T < 1.3$ K. The fractional frequency shift versus temperature for the resonators made from the $V_{sub} = 400$ V film (TiN-RF-70) are plotted in Fig. 7.8a. Both resonators were measured at the same input power, which corresponded to less than about 50 photons in the resonator.

The increase in frequency in the low-temperature part of the data, $T < 0.25$ K, is believed to be a TLS-related effect. The TLS-induced fractional frequency shift is given by [80]

$$\frac{\Delta f}{f_0} = \frac{1}{\pi Q_{i,TLS}} \left[\mathrm{Re}\Psi \left(\frac{1}{2} - \frac{\hbar\omega}{2i\pi k_B T} \right) - \log \frac{\hbar\omega}{2\pi k_B T} \right]. \tag{7.2}$$

The logarithmic term in Eq. 7.2 is dominant at low temperatures, and the term containing the digamma function Ψ is negligible in this regime. The low-temperature fits are shown more clearly in Fig. 7.8b. I note that the resulting internal quality factors in the fits are solely due to TLSs, and in this temperature regime the frequency shift is believed to be a purely TLS-induced effect. The fits yielded $Q_{i,TLS} = 3 \times 10^5$ and $Q_{i,TLS} = 1 \times 10^6$ for Res 1 and Res 2. This is in qualitative agreement with our expectations. Given the larger line-width and line-spacing of Res 2 compared to those of Res 1, the fractional filling factor of the TLS-containing surfaces is smaller in Res 2, resulting in a higher $Q_{i,TLS}$. Of course, this only accounted for a portion (approximately 50% to 90%) of the total loss seen in these devices. There might be additional losses due to coupling to low-Q sample box modes which can be reduced by improving the sample box design.

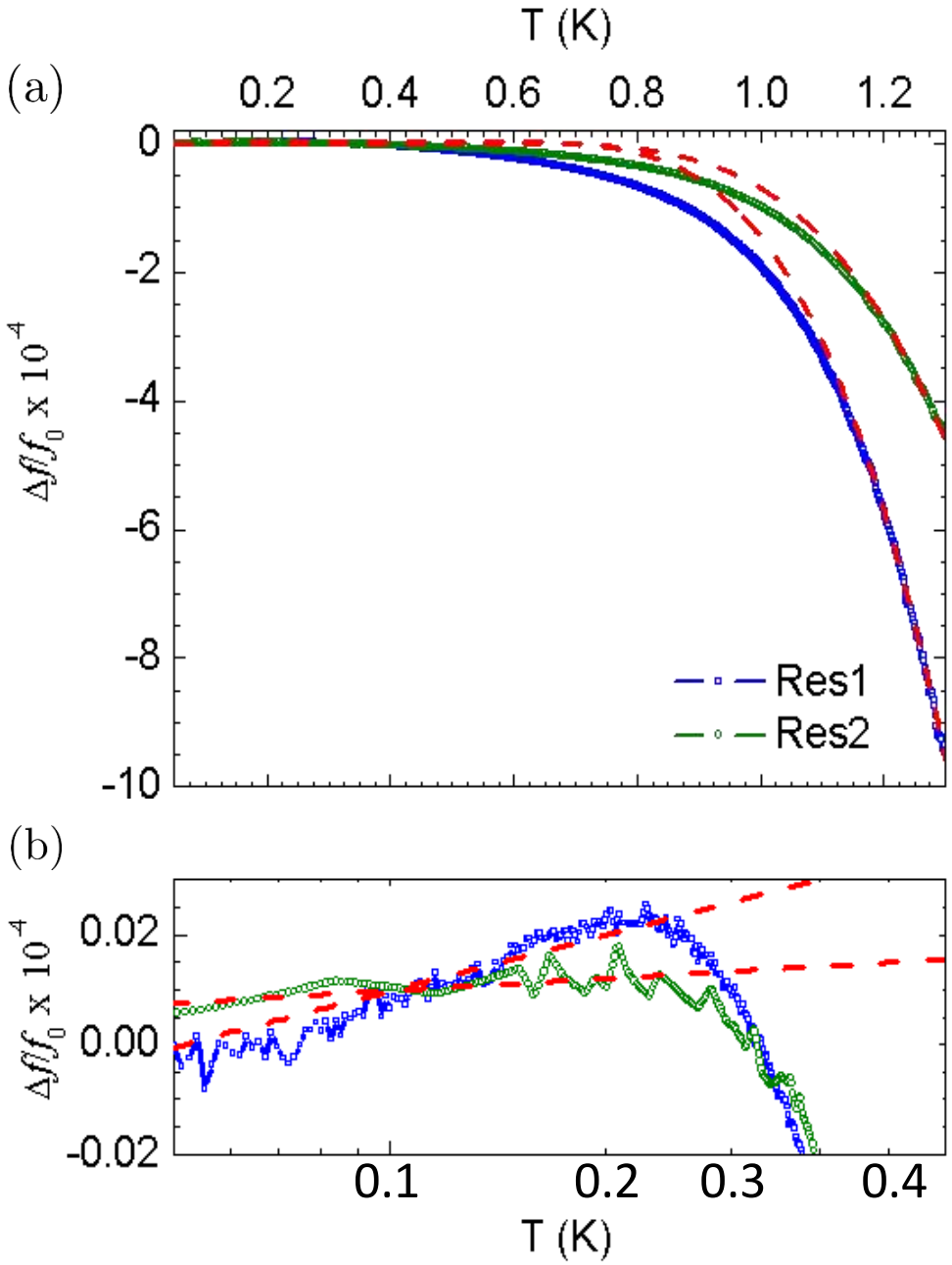

Figure 7.8: From Ref. [126]. (a) The measured fractional frequency shift for Res 1 and Res 2 as a function of the temperature for the TiN-RF-70 sample with V_{sub} = 400 V (courtesy of A. Ramanayaka). Red dashed lines are fits to high and low temperature theory. (b) Detailed view of low temperature frequency shift data showing non-monotonic behavior of fractional frequency shift at low temperatures. Red dashed curves are fits to the TLS-induced frequency shift.

Kinetic inductance

The thickness of the TiN films in all fabricated samples was about 62 nm, which is much smaller than the reported London penetration depth for TiN films (λ = 250 nm - 700 nm) [116]. Therefore, as mentioned before, all films showed significant kinetic inductance, and this made it hard for me to identify which of the resonators was creating a given resonance.

The kinetic inductance fraction $\alpha = L_k/L_{tot}$ denotes the fraction of the total inductance L_{tot} that is due to kinetic inductance L_k. In order to extract α, the fractional frequency shift was fit to a model that combines the low-temperature TLS-induced effects (mentioned above) and the Mattis-Bardeen formula [133],

$$\frac{\lambda(T) - \lambda(0)}{\lambda(0)} = \frac{L_k(T) - L(0)}{L(0)} = \sqrt{\frac{\pi\Delta_s}{2k_BT}} \exp\left(-\Delta_s/k_BT\right). \tag{7.3}$$

Here Δ_s is the superconducting energy gap (not to be confused with the TLS asymmetry energy). The fit was performed in the range $0.03 < T < 1.3$ K (see Fig. 7.8a). In the fitting procedure, the TLS contribution was kept unchanged from that described above. The fit yielded a kinetic inductance fraction of $\alpha_{MB} = 47\%$ for Res 1 and 23% for Res 2. The fit also yielded a superconducting energy gap $2\Delta_s/k_BT_c = 4.0$ (with $T_c = 4.32$ K), which was a bit high compared to the weak-coupling BCS values.

The simulated resonance frequencies of Res 1 and Res 2 (assuming $\lambda = 0$) are listed in Table 7.1. An approximate value for α can also be found from the

measured- and simulated resonance frequencies, f_{meas} and $f_{\lambda=0}$, as [80]

$$\alpha_{approx} = 1 - \left(\frac{f_{meas}}{f_{\lambda=0}}\right)^2. \tag{7.4}$$

Eq. 7.4 yielded $\alpha_{approx} = 70\%$ and 29% for Res 1 and Res 2 respectively. However, I note that α_{approx} is a good approximation of α only if the geometric inductance, $L_g = L_{tot} - L_k$, is well-known and does not depend on the penetration depth. This is consistent with some simulation data [80] but is not generally true [134]. Here we assumed that the geometric inductance does not differ from the value obtained from a simulation of the resonator treating the superconductor as a perfect conductor. Res 2 has a significantly smaller α due to a significantly larger linewidth compared to the 2D screening length [134]. Res 2 also has a smaller L_g, and therefore I expect α_{approx} to be a better approximation for α_{MB} compared to the case of Res 1.

Finally, I note that the film with $V_{sub} = 110$ V (TiN-RF-66) showed the largest α_{approx}, with $\alpha_{approx} = 85\%$. This unusually large kinetic inductance might be due to possible nonlinear effects other than the usual contribution from low superfluid density, including for example grain boundaries which create weak links [120].

7.6 Conclusion

In this chapter, I discussed my work on TiN films, including effects on the film properties produced by the RF-induced DC voltage (V_{sub}) on the substrate during reactive sputtering. I showed that several structural properties (crystallography, stress, resistivity, *etc.*) can be tuned with the substrate DC bias.

Most importantly, the film stress was related to the TiN (200) crystalline

phase, which in turn could be tuned with V_{sub}. Also, a strong correlation between resistivity and oxygen content was observed. The TiN films deposited with small DC bias voltages showed large room-temperature resistivity and high kinetic inductance, making them potentially attractive for detector applications. Furthermore, the deposition conditions resulted in highly uniform films (across the wafer) in terms of the thickness, resistivity, critical temperature and complex index of refraction.

Two sets of coplanar resonators were fabricated. One was made from TiN films only, while the other was based on a hybrid TiN-Al design. Low-temperature measurements of these resonators revealed relatively high internal quality factors (Q_i) and a large kinetic inductance fraction. These parameters where extracted by measuring the resonator frequency shifts as a function of the temperature.

Chapter 8: Perimeter effects in ALD-Al_2O_3 trilayer resonators

8.1 Motivation

Aluminum is currently the most commonly used superconductor in qubit circuits. This is mostly due to the prevalence of aluminum / aluminum oxide / aluminum Josephson junctions (JJs) as aluminum oxide can be formed in a controlled way by thermal oxidization to create suitable tunnel barriers. Also, native oxide forms very rapidly on surfaces of aluminum that are exposed to air. Although aluminum oxide is a crucial dielectric for the superconducting quantum computing community, regardless of whether aluminum oxide occurs in a JJ barrier or as a surface native oxide, its presence can cause qubit decoherence because it contains nanoscale two-level systems.

More than 30 years ago, it was suggested that OH groups in oxides act as charged TLS defects [135–138]. Some of these experiments showed two distinct dipole sizes in silica that contain OH groups, with dipole moments differing by a factor of 6. The larger dipole size was associated with rotation of the proton in OH^-, while the smaller dipole size was assumed to be intrinsic to silica [138]. In another study, it was suggested that hydrogenated cation vacancy defects form a significant density of GHz frequency TLSs in alumina which create a dipole moment between

adjacent potential energy minima of the hydrogen atom [139]. More recently, hydrogen concentration measured by secondary ion mass spectrometry (SIMS) was found to correlate with low-temperature microwave oxide dielectric loss [101]. Currently, hydrogen defects are commonly believed to be the dominant cause of microwave loss in oxides at low temperatures.

Atomic layer deposition (ALD) [140] is a thin film deposition method that allows for mono-layer thickness control and results in extremely uniform films. In this method, gas precursors enter the deposition chamber in a sequential manner, causing alternative self-limiting chemical reactions that lead to layer-by-layer deposition of a film.

The ability to achieve a controlled uniform thickness suggests that ALD-grown alumina might be attractive for JJ barriers in qubit circuits. For this purpose, *in-situ* trilayer fabrication must be employed, where the JJ electrodes and its tunnel barrier are deposited without breaking the vacuum. This would be essential to prevent atmospheric contaminants such as water from being incorporated into the oxide layer.

In this Chapter, I introduce a set of trilayer resonators designed to study atmospheric contamination effects in ALD-grown alumina. These devices can help us better understand the formation of OH defects in this material by air-exposing different cross-sectional areas of the dielectric.

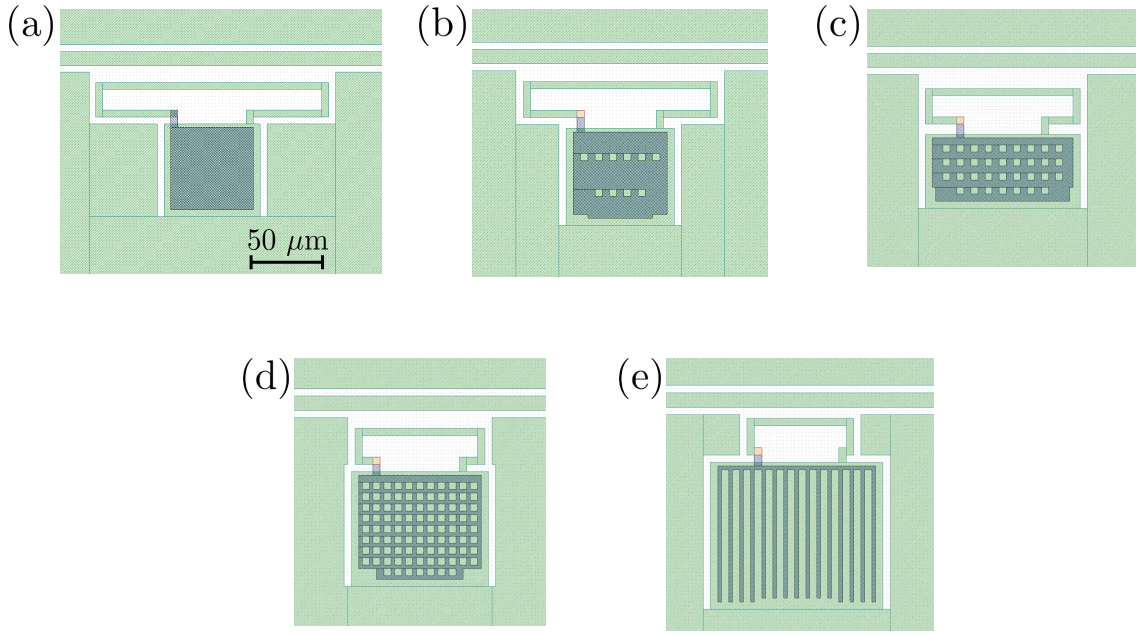

Figure 8.1: AWR Microwave Office layout for five resonators with different capacitor perimeters. The perimeter lengths P are (a) P_1, (b) $2P_1$, (c) $4P_1$, (d) $9P_1$ and (e) $12P_1$ where $P_1 = 240\ \mu$m. The bottom (base) metal layer is shown in light green, while the top (capacitor) plate is shown in dark green. The transmission line is 10 μm wide with 5 μm spacing with the ground plane.

8.2 Resonator design

For this study I designed a set of five microwave resonators with parallel-plate capacitors with somewhat unusual looking top capacitor plates (see Fig. 8.1). The devices were designed to have approximately identical capacitances and dielectric volumes. However, the "perimeter" of the trilayer capacitor was different for each device. The different capacitor perimeters led to different dielectric cross-sectional areas on each device being exposed to air. In some of the devices, the perimeter lengths of the capacitors were effectively increased by punching holes or slots in the

Table 8.1: Table of the designed values for capacitance C, inductance L and resonance frequency f_0 for the resonators with different perimeters P.

Device name	P	C (pF)	L (pH)	f_0 (GHz)
R1	P_1	5.12	308	5.027
R2	$2P_1$	5.12	255	5.518
R3	$4P_1$	5.12	214	6.026
R4	$9P_1$	5.12	183	6.51
R5	$12P_1$	5.12	159	6.991

capacitor top plate. One device had no holes or slots and had an effective perimeter length $P_1 = 240\,\mu$m. The other devices had perimeter lengths of $2P_1$, $4P_1$, $9P_1$ and $12P_1$.

The resonator layouts from AWR Microwave Office are shown in Fig. 8.1 and the key device parameters are given in Table 8.1. Figure 8.1a shows the resonator with the smallest perimeter P_1 (square capacitor), while resonators in Figs. 8.1b-d have holes on the top capacitor plate through the ALD-Al_2O_3 layer to increase the perimeter. The resonator shown in Fig. 8.1e had the largest perimeter due to the fins (not to be confused with fingers of an interdigitated capacitor). The resonators were designed to be built using a trilayer fabrication process. This process yields devices that always have a bottom (base) metal layer (shown in light green) that is under any structures made of the top metal layer (shown in dark green) with the

top and bottom layers separated by ALD-grown aluminum oxide.

The internal quality factor for alumina grown with this ALD process was measured in the single photon limit in a separate experiment [101]. That film, which was exposed to air prior to measurement, showed $330 < Q_{i,0} < 500$, slightly dependent on the resonator geometry [89]. Based on this result, I designed the resonators for the perimeter experiments to have a coupling quality factor of $Q_e \sim 1000$. This was sufficiently close to the $Q_{i,0}$ of the air-exposed film, but slightly larger so as to allow measurements of $Q_{i,0}$ in lower-loss *in-situ* grown films that the group might build in the future. I note that the Q_i extraction is most accurate if $Q_i = Q_e$, and, in general, the uncertainty in Q_i increases as Q_i and Q_e deviate.

8.3 Fabrication

The perimeter resonators were fabricated on a 3-inch C-plane sapphire wafer in an *ex-situ* process. The sapphire substrate was first transferred into the CMS-18 sputtering chamber and ion-mill cleaned at a beam voltage of 300 V and an Ar flow of 6 sccm for 30 seconds. 100 nm of Al was then sputtered using a DC gun power of 400 W and an Ar pressure of 5 mTorr for 20 minutes and 30 seconds. Next, the sample was transferred to the ALD processing chamber to deposit a 50 nm thick layer of Al_2O_3. The ALD step was performed by A. Kozen in the Rubloff group's deposition system at the University of Maryland. Al_2O_3 is formed layer-by-layer by

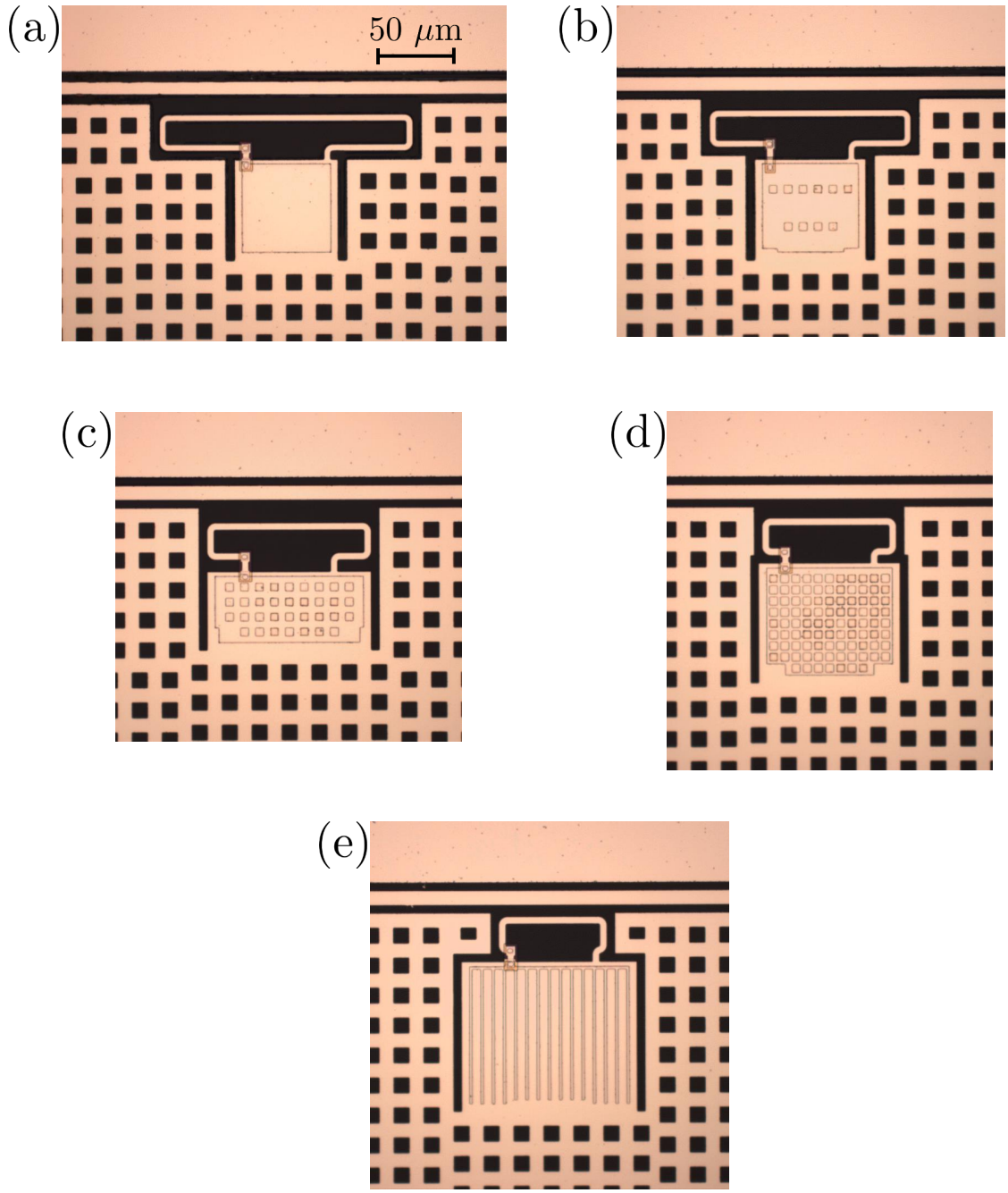

Figure 8.2: Optical image of the fabricated perimeter resonators. The capacitor perimeters are (a) P_1, (b) $2P_1$, (c) $4P_1$, (d) $9P_1$ and (e) $12P_1$. Both the top and bottom metal layers appear light orange, and sapphire appears black.

chemical exchange between $Al(CH_3)_3$ and H_2O:

$$\text{Step1}: \quad Al - OH^* + Al(CH_3)_3 \rightarrow Al - O - Al(CH_3)_2^* + CH_4$$

$$\text{Step2}: \quad Al - O - Al(CH_3)_2^* + H_2O \rightarrow Al - O - Al(OH)_2 + 2CH_4$$

Each step was repeated approximately 500 times, and the deposition took about 14 hours. After the ALD process, the sample was taken out of the vacuum and transferred into the sputtering chamber described in Section 4.3. The ALD layer was exposed to air for about 24 hours before it was placed in the sputtering chamber. Another 100 nm thick layer of Al was deposited using the deposition conditions described above. The Al/ALD-Al_2O_3/Al trilayer wafer was then processed using five photolithography steps.

In the first photolithography step, the top Al layer (for the top capacitor plates) was formed. After photolithography, this layer was wet-etched in a standard Al-etch solution (J.T.Baker Aluminum Etch 80-15-3-2). The 50 nm thick Al_2O_3 acted as an etch-stop for this solution, while the thin native oxide layer was not. After the wet etch, the wafer was rinsed with DI water. Without removing the patterned photo resist (PR), the wafer was transferred to the same sputtering chamber to dry-etch Al_2O_3 using Ar ion-milling. Ion-milling was performed with an 800 V beam voltage and an Ar flow of 6 sccm for 11 minutes to etch through the ALD layer. Due to the high-power and relatively long ion-milling process, the PR was hard to remove after the ion-mill step; I had to soak the wafer in an acetone bath in a sonicator for 12 minutes and 30 seconds (rather than the standard 1 minute) to remove the PR completely.

After PR removal, the second photolithography step was performed followed

by wet-etching the bottom (base) Al layer. In this step, the bottom capacitor plates, inductors, microwave transmission line and the ground plane were formed. After etching, the PR was removed using the standard organic cleaning described in Chapter 4.

In the next step, SiN_x was deposited to support metal bridges (see Fig. 8.2) that were deposited in a later step. I used a low-loss SiN_x recipe (PECVD) with SiH_4 and N_2 flow rates of 10 sccm and 9 sccm respectively, performed at 300 °C. The measured thickness of the SiN_x layer was 266 nm.

Next, the third photolithography step was performed followed by an SF_6-based RIE recipe to etch through the SiN_x at the location of the vias. For the RIE, the mass flow rates of SF_6 and O_2 were 20 sccm and 5 sccm, respectively, and the processing chamber pressure was 75 mTorr.

After the RIE, the sample was transferred to the sputtering chamber, and I used 1 minute of ion-milling at an 800 V beam voltage and 6 sccm Ar flow rate to remove the native oxide on the top and bottom Al layers at the location of the vias. 200 nm of Al was then deposited using a gun power of 400 W and a chamber pressure of 5 mTorr. this deposition was done in the sputtering chamber described in Section 4.3 and took 41 minutes.

After removing the sample from the sputtering chamber, a fourth photolithography step was performed followed by wet-etching the last deposited Al layer to create the bridges.

Finally, I removed the resist and did a final photolithography step and RIE etch to remove SiN_x from everywhere except under the bridges. The wafer was then

diced and packaged in a type 2 sample box (see Fig. 4.7).

8.4 Measurements

The sample was stored at room temperature in a dry box with desiccant for approximately 5 weeks after the fabrication was completed and then measured in the Leiden CF-650 dilution refrigerator. A frequency sweep at 30 mK in the range 4-8 GHz showed only four resonances rather than five. The measured resonance frequencies were 5.190 GHz, 5.764 GHz, 6.365 GHz, 7.354 GHz for R1, R2, R3 and R5, respectively. The missing resonance corresponded to R4 with perimeter $P = 9P_1$. This problem probably occurred because of a broken bridge connection caused by the high-stress SiN_x film underneath. But it could also be due to a bad via connection to the base Al layer.

A power sweep at 30 mK was performed on the four functional resonators. The transmission $|S_{21}|$ was fit using two different methods: the Diameter Correction Method [90] and the Dual-Cavity Method described in detail in sections 3.2.1 and 3.2.2, respectively. In my analysis, all the electric energy was assumed to be within the ALD layer due to the parallel-plate geometry and I took $\tan\delta = Q_i^{-1}$.

Figure 8.3 shows a comparison of $\tan\delta$ versus the RMS voltage V_{rms} across the capacitor extracted using these two methods for the resonator R1 with $P = P_1$. While the results from both methods agree when $Q_i \sim Q_e$, the Dual-Cavity Method does a much better job, especially in the high-power region where $Q_i \gg Q_e$, as mentioned in section 3.2.2. Therefore, I analyzed the rest of the data using the

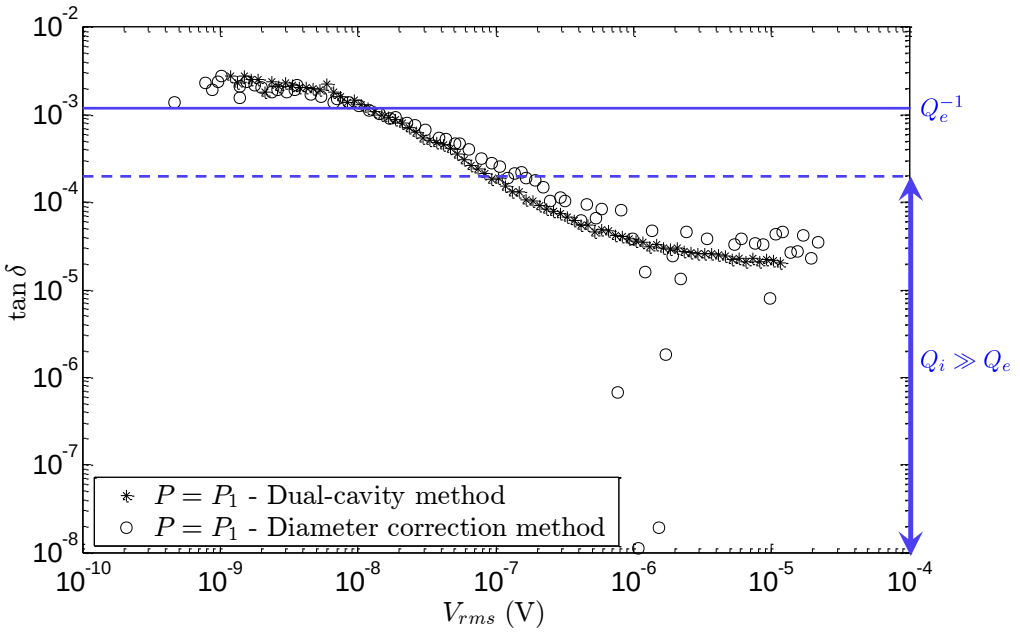

Figure 8.3: Measured loss tangent (extracted using two different methods) versus the RMS voltage V_{rms} across the capacitor for device R1 with perimeter P_1. The data was taken at 30 mK and the measured external quality factor was $Q_e \simeq 900$. The Dual-Cavity Method combined with the Least-Squares Monte Carlo method shows a better extraction than the Diameter Correction Method combined with Matlab's automated fitting, especially when Q_i deviates from Q_e.

Dual-Cavity Method.

The results for the loss versus power at $T = 30$ mK for the four working resonators, devices R1, R2, R3 and R5, are shown in Fig. 8.4. Again, the loss tangent was extracted using the Dual-Cavity Method. The resonators were also measured at higher temperatures, *i.e.* $T = 100$ mK and $T = 200$ mK (see Fig. 8.5).

The power-dependent loss tangent was fit to a modified version of Eq. 2.35 or

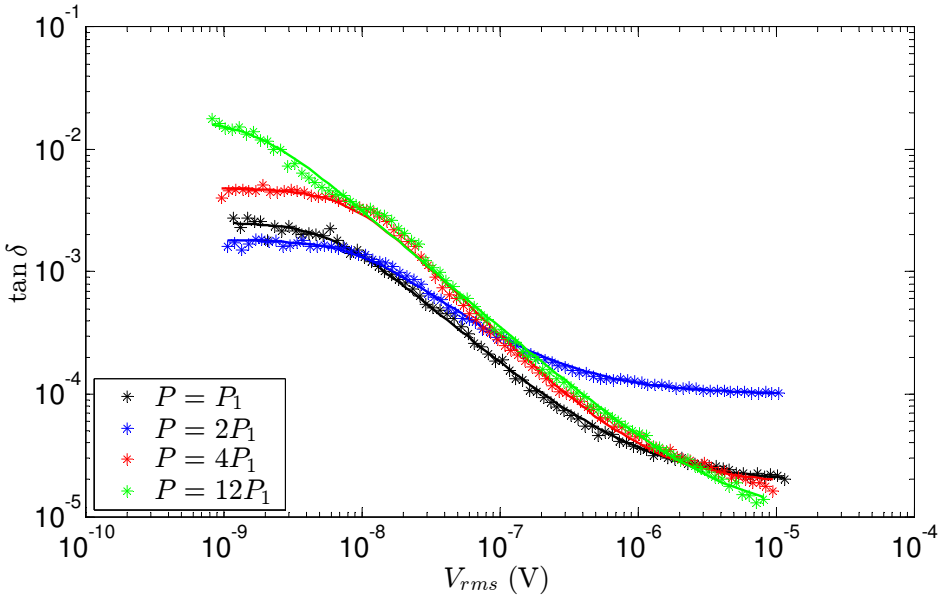

Figure 8.4: Measured loss tangent versus the RMS voltage V_{rms} across the capacitor for devices R1 (black), R2 (blue), R3 (red) and R5 (green) at $T = 30$ mK. Loss tangent was extracted using the Dual-Cavity Method. Solid curves show optimum fit to data.

Eq. 7.1, *i.e.*

$$\tan\delta = \frac{\tan\delta_0}{\left(\sqrt{1+2\left(V_{rms}/dE_c\right)^2}\right)^{1-\beta}} + \tan\delta_{bg}, \tag{8.1}$$

where $d = 50$ nm is the dielectric thickness and $\tan\delta_{bg}$ denotes a constant "background loss" that appears most clearly at the high-power limit of the measurement as a flattening of the loss tangent curve at high powers. Whatever its cause, this background loss sets a lower limit for the loss tangent that I can measure, and it represents some type of non-TLS loss mechanism (*e.g.* quasi-particle loss or radiative loss).

To fit the theory described by Eq. 8.1 to data, I wrote a fitting code using the

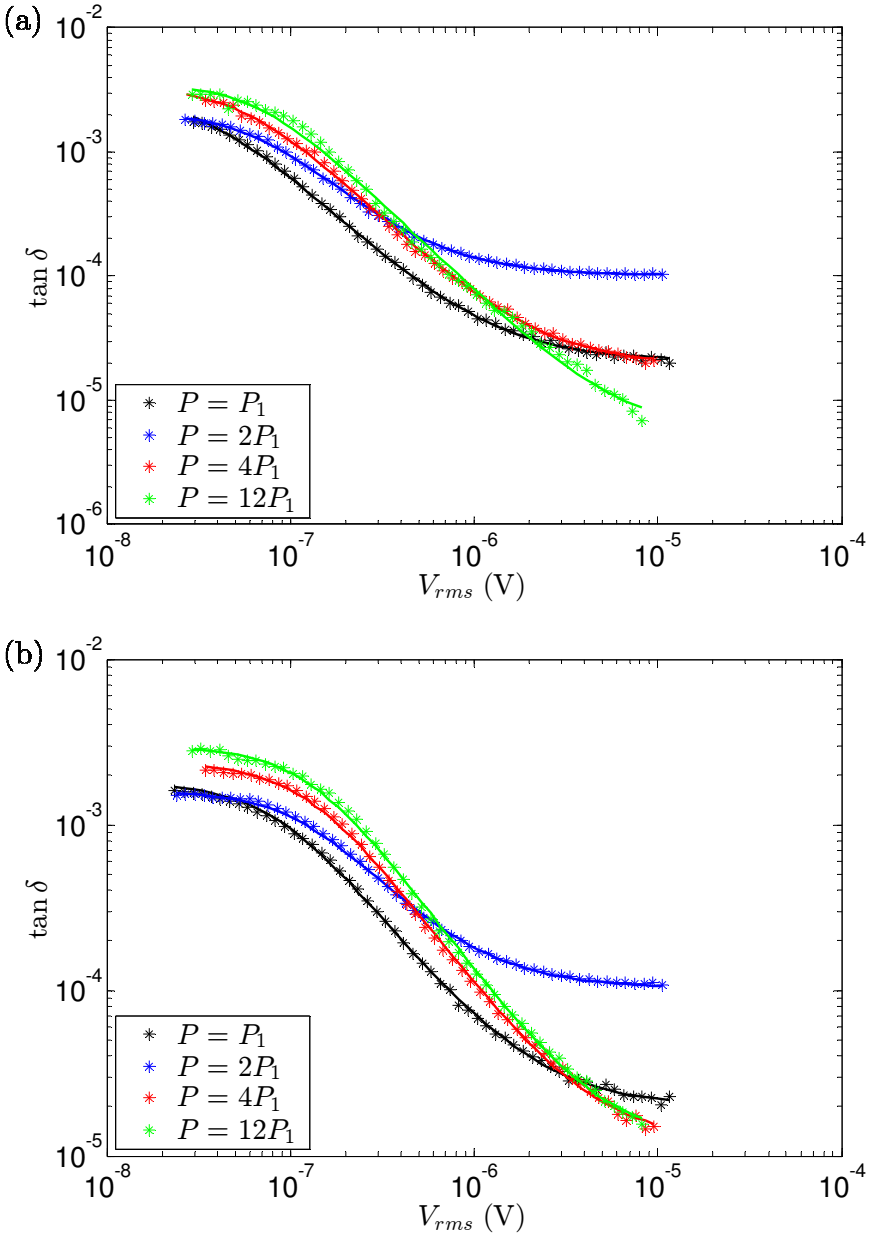

Figure 8.5: Measured loss tangent versus the RMS voltage V_{rms} across the capacitor at (a) $T = 100$ mK and (b) $T = 200$ mK for devices R1 (black), R2 (blue), R3 (red) and R5 (green). Loss tangent was extracted using the Dual-Cavity Method. Solid curves show optimum fit to data.

Table 8.2: Extracted loss parameters for four devices at three temperatures.

		30 mK				100 mK				200 mK			
Device name	P	$\tan\delta_0 \times 10^3$	E_c (V/m)	β	$\tan\delta_{bg} \times 10^6$	$\tan\delta_0 \times 10^3$	E_c (V/m)	β	$\tan\delta_{bg} \times 10^6$	$\tan\delta_0 \times 10^3$	E_c (V/m)	β	$\tan\delta_{bg} \times 10^6$
R1	P_1	2.52	0.17	0.03	19.06	2.68	1.01	-0.37	21.03	1.76	2.31	-0.40	20.03
R2	$2P_1$	1.70	0.28	0.08	99.31	2.00	1.82	-0.42	101.54	1.49	3.24	-0.35	102.61
R3	$4P_1$	4.82	0.24	-0.14	18.50	3.32	1.61	-0.43	19.42	2.35	3.50	-0.50	12.18
R5	$12P_1$	17.62	0.05	0.03	9.53	3.63	1.91	-0.45	5.17	2.94	3.64	-0.54	11.84

least-squares Monte Carlo (LSM) method (see Section 3.2.2). The fitting parameters were $\tan\delta_0$, E_c, β and $\tan\delta_{bg}$. I used 10^6 Monte Carlo steps to obtain the optimum fit shown by solid curves in Figs. 8.4 and 8.5. The fitting parameter values are listed in Table 8.2 and plotted in Fig. 8.6.

From Fig. 8.6a it is clear that $\tan\delta_0$ typically increases with the perimeter length P, as expected. This effect is most clearly seen at $T = 30$ mK, where $k_BT \ll \hbar\omega$ and the TLSs are not saturated. At this temperature, the dependence of $\tan\delta_0$ on P is approximately linear with zero intercept. The same qualitative behavior was observed at 100 mK and 200 mK, although with a much smaller dependence on the perimeter length. This is consistent with lesser TLS participation in coherent photon absorption/emission as a result of thermal saturation of the TLSs.

Figure 8.6b shows a clear increase in E_c with temperature. This behavior was also observed in a previous study of SiN_x [102]. This increase in E_c is believed to be due to a reduction in the coherence time T_2 of the TLSs (see Eq. 2.34). T_2 decreases when T_1 is affected by stimulated emission and absorption of phonons.

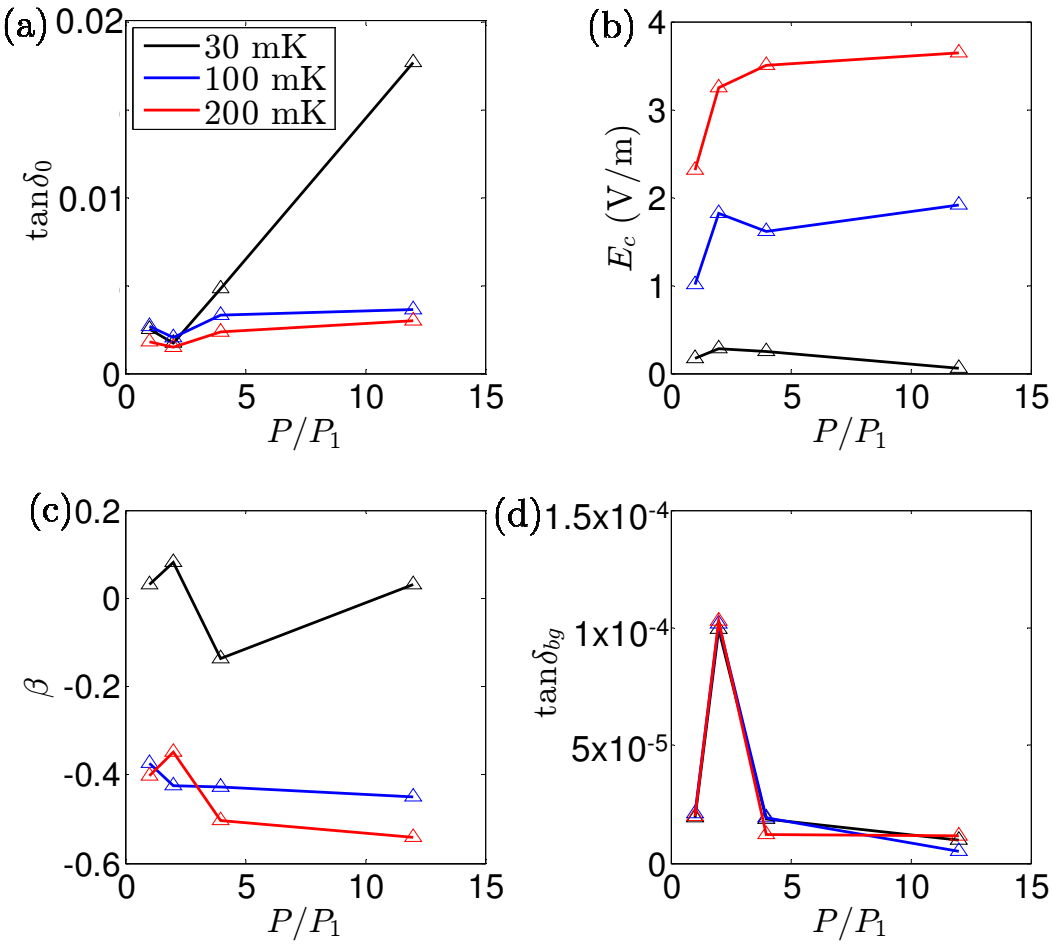

Figure 8.6: Loss parameters versus normalized capacitor perimeter length P/P_1 for $T = 30$ mK (black), $T = 100$ mK (blue) and $T = 200$ mK (red). (a) Single-photon loss tangent $\tan\delta_0$ versus normalized capacitor perimeter P/P_1, (b) critical electric field amplitude E_c versus normalized capacitor perimeter P/P_1, (c) TLS power-saturation factor β versus normalized capacitor perimeter P/P_1 and (d) background loss tangent $\tan\delta_{bg}$ versus normalized capacitor perimeter P/P_1.

Also, additional dephasing can occur due to spectral diffusion [110]. At a fixed temperature, E_c shows a weak dependence on the perimeter length.

Figure 8.6c shows that the TLS power-saturation factor β does not show a significant dependence on the perimeter. However, the TLS power-saturation slope

tends to become steeper at higher temperature. This may be related to the temperature contribution to TLS saturation, which causes the higher temperature TLSs to saturate faster as power is increased. I note that $\beta \simeq 0$ at $T = 30$ mK, which agrees better than many silicon nitride film types with the standard TLS model [108].

Finally, Figure 8.6d shows that the background loss does not correlate with temperature or perimeter. This suggests that the background loss is not a TLS-induced effect. It is most probably dependent on the resonator geometry.

8.5 Conclusion

In this Chapter, I introduced five trilayer resonators with parallel plate capacitors made from Al and ALD-grown Al_2O_3 using an *ex-situ* process. The capacitor on each device had a unique perimeter length. This allowed different amounts of atmospheric water vapor to diffuse into the oxide layer (after device fabrication) in the devices, resulting in different effective TLS defect densities.

The devices were measured at 30 mK, 100 mK and 200 mK and I analyzed the power dependence of the loss tangent. I found that the loss tangent in the low-power limit increased with perimeter length, consistent with a larger defect density in the larger perimeter devices. Also, the dependence of the critical electric field E_c on the temperature showed qualitative agreement with the previous measurements of other amorphous solids.

Finally, I note that the ALD layer had been exposed to air for about 24 hours before it was covered with Al, and the measurement was performed about 5 weeks

after the device fabrication was completed. Together with the measurement results, this supports the idea that hydrogen defect formation in ALD-grown Al_2O_3 layer is a continuous and relatively slow process, and can take place in a diffusion process that is longer than 24 hours. The correlation of loss with the air-exposed area was stronger at measurement temperatures T when $k_B T \ll \hbar\omega$.

Chapter 9: Conclusion

9.1 Summary of key results

In Chapter 1, I discussed the motivation for studying nanoscale tunneling two-level systems in amorphous solids. One aim was to determine their precise identity as this would help the development of practical superconducting qubits (small-footprint qubits with sufficiently long coherence times). Superconducting qubits are microscale, artificial two-level systems that are promising candidates for future quantum computers. This promise is based on their scalability and the fact that they can be easily coupled to each other, and to the read, write and control lines. However, they also couple relatively easily to the environment, which is a source of loss, noise and dephasing.

In recent years, much research conducted by the superconducting quantum computing community has been devoted to improving qubit coherence. It is now known that amorphous dielectrics used in qubit circuits have been a major source of loss and can cause significant qubit decoherence. Dielectrics contain nanoscale tunneling two-level systems (also referred to as two-level system defects or TLSs) that couple to the electric field within the qubit circuit, absorb energy and cause qubit decoherence. Despite progress made in recent years to understand the ensemble-

averaged response of many TLSs and the behavior of individual TLSs, the precise identification of TLSs in superconducting qubits is still unknown. Aside from the interesting underlying physics of TLS phenomena, a deeper understanding of their physical nature could help in the design and fabrication of superconducting qubits to reduce dielectric loss and subsequently increase coherence. In Chapter 1, I discussed the Hamiltonian for a TLS-cavity system known as the Jaynes-Cummings Hamiltonian. I also described the splittings that occur in the energy levels of this hybrid system as a result of TLS-cavity coupling.

In Chapter 2, I discussed details of the standard theoretical model of TLS dynamics as well as the TLS ensemble-averaged response. I started by introducing the influence of TLSs on low-temperature properties of amorphous solids. I then discussed the double-well potential of a tunneling TLS. By using the Bloch equations and the analogy between a TLS and a spin-$\frac{1}{2}$ particle in a magnetic field, I derived the dynamics of a TLS in an electric field. I also derived the response of an ensemble of TLSs interacting with an external electric field, and explained how power-saturation of TLSs reduces the TLS-induced dielectric loss at high applied microwave powers.

In Chapter 3, I described three models to analyze the resonance lineshape of superconducting microwave resonators in my studies of TLSs. The first model was a naive model which assumed perfectly symmetric transmissions. The second model (Diameter Correction Method) included a correction to the first model to take into account the asymmetric transmissions caused by the non-ideal experimental setup [90]. The third model (Dual-Cavity Model) was based on two cavities, one representing the resonator and the other modeling its coupling to the microwave

transmission line [91]. A fitting code based on the least-squares Monte Carlo (LSM) method was developed based on the Dual-Cavity Model. I found that the Dual-Cavity Model with the LSM method allowed for, in general, more accurate parameter extraction compared to the first two models.

In Chapter 4, I described the fabrication tools and some of the techniques that I used to build the devices described in Chapters 5-8.

9.1.1 CQED of TLSs and the discovery of TLSs with long T_2

In Chapter 5, I introduced a method that enables measurements of individual TLSs based on direct TLS-cavity coupling. In this method, strong CQED coupling between a TLS and a cavity is achieved by reducing the electric field volume in a thin-film lumped element superconducting microwave resonator to a mesoscopic scale. I showed experimental S_{21} data (taken at 25 mK and 200 mK) of the splitting in a resonator's transmission caused by strong coupling of a cavity to a single TLS. This data was analyzed using a theoretical model that I described in detail. Furthermore, I showed results of S_{21} from a power sweep of the hybrid TLS-cavity system. The S_{21} results showed two distinct quantum states (dressed states) at single-photon powers, which merged into the bare cavity mode at higher powers. The power-dependent data were fit and analyzed using a photon density matrix combined with the Lindblad equations to find the time evolution of the Hamiltonian for the TLS-cavity system for the entire measurement power span. This allowed for extraction of the hybrid system's coupling and relaxation parameters, including the TLS-cavity

coupling rate and the TLS coherence time, for a wide range of average photon numbers in the cavity. These CQED measurements of individual TLSs within a SiN_x film revealed TLSs with coherence times on the order of microseconds, raising the possibility of deliberately employing CQED information exchange with TLSs. This study also opened up the possibility of making individual TLS measurements in a wide range of amorphous solids, as the technique was not limited to materials that were suitable for JJ barriers.

9.1.2 TLS spectroscopy results and distribution statistics

In Chapter 6, I introduced a method to perform individual TLS spectroscopy in insulating films. In this method, in addition to the small volume CQED measurement of TLSs, a DC electric field tunes the TLSs in and out of the cavity resonance. This was realized using a thin-film resonator design with a capacitor bridge arrangement that isolated the DC bias voltage from the AC (microwave) resonance and the coupled AC transmission line. By combining this with a restively large double-loop spiral inductor, I developed the tunable micro-V devices. Low-power measurements of the device transmission versus frequency and bias voltage showed clear TLS-induced modes crossing the cavity resonance. For the cases where the TLS asymmetry energy was sufficiently close to zero and the tunneling energy was close to the resonator's resonance frequency, hyperbolic-shape (including the vertex) double-well induced modes of the TLSs were measured and fit to theory. For these TLSs, several parameters could be extracted, including the projection of the dipole

moment on the electric field direction $p|\cos\theta|$. By performing three high-resolution DC-bias sweeps (from three separate cool-downs), I found 60 TLS-induced hyperbolas in a SiN_x film. The distribution statistics of $p|\cos\theta|$ could be interpreted as more than one dipole size: a distribution of large number of TLSs with $p < 3.32$ Debye possibly with a triangular distribution, and a uniform distribution of TLSs with a dipole size of $p \simeq 8.25$ Debye.

I note that this study marked the first spectroscopy of individual TLSs in a thin film with a thickness that was typically used for insulating layers. To the best of my knowledge this was also the first individual spectroscopy measurement of TLSs in a material other than thermally grown alumina. This TLS spectroscopy technique could readily be extended to other materials. In Chapter 6, I also described the theoretical model that I used to simulate the spectroscopy data. I found that the simulations could explain some features in the data, but not everything I observed.

9.1.3 Process development for TiN film deposition

In Chapter 7, I described my approach for finding the reactive sputtering parameters to deposit superconducting TiN films with relatively high quality factors. I showed that some of the structural and compositional properties of TiN thin films can be tuned by using an RF-induced DC bias on the substrate during reactive sputtering. I reported on six films sputtered at different substrate DC biases. The films' crystalline phases, elemental composition, stress, resistivity and superconducting critical temperature were measured and compared. The room temperature resis-

tivity was strongly correlated with the oxygen content. Also, stress was correlated with the (200) peak height in the XRD results. The deposition process produced highly-uniform films in terms of thickness and resistivity across 3-inch diameter Si wafers.

In order to investigate the low-temperature properties of the TiN films, I designed two sets of resonators. The first set was designed for a TiN-only fabrication process, while the second set was designed for hybrid TiN-Al devices. I showed some experimental results on Q_i and resonance frequency shift with temperature. I also showed an example where my colleague (A. Ramanayaka) and I extracted the kinetic inductance fraction α from the data, and compared it with an approximative method estimating α from the difference in the simulated- and measured resonance frequencies. Generally, the measured TiN films showed high Q_is and αs.

9.1.4 Hydrogen diffusion in ALD-Al_2O_3

In Chapter 8, I introduced a set of microwave resonators with different capacitor perimeter lengths that I used to investigate the correlation of the air-exposed cross-sectional area (edges) of the parallel-plate capacitor with the low-temperature microwave loss. The dielectric was ALD-grown Al_2O_3 and the trilayer wafer was made in an *ex-situ* process.

Measurement and analysis of the resonators showed a higher (single-photon) loss tangent in resonators with larger perimeters. Higher temperature measurements showed the same qualitative behavior, but with a smaller dependence of $\tan\delta_0$ on

perimeter. The critical electric field E_c and the TLS power-saturation factor β showed strong correlation with temperature, but relatively small dependence on perimeter. Given the time interval between ALD and the deposition of the top (protective) layer, and the interval between the completion of device fabrication and the low-temperature measurements, I concluded that the TLS defect formation in ALD-grown Al_2O_3 as a result of air-exposure, is a slow process, and has significant effects on the low-temperature microwave properties of this material.

9.2 Future work

9.2.1 CQED of TLSs in different amorphous dielectrics

Individual TLSs within tunnel barriers have been measured in previous studies using qubits, and several TLS properties such as TLS density and coherence times have been extracted [66, 85]. However, such studies of individual TLSs in dielectrics were limited by the necessity of incorporating the material into JJ barriers. Due to the limited choice of materials and processes that yield reliable JJs, all such studies have previously been limited to TLSs in 1-2 nm thick aluminum oxide.

Over the past two decades, cavity quantum electrodynamics (CQED) phenomena have proven to be extremely useful for studying coherent quantum phenomena in atoms, ions and superconducting qubits. I showed in Chapter 5 that TLSs in SiN_x films can also display CQED effects in a so-called micro-V device. This sensitivity is achieved by reducing the dielectric volume V in a high-Q lumped-element superconducting microwave resonator. Under certain conditions, one TLS in the

dielectric can strongly couple to the resonator (cavity). This direct TLS-cavity coupling allows an individual TLS to be observed based on its effect on the resonator's transmission S_{21}. The parameters of such a hybrid TLS-cavity system, including the TLS lifetime and TLS-cavity coupling rate, can be extracted by fitting the S_{21} data to a theoretical model that has been developed based on this work [103].

It is clear that this type of study could be extended to other dielectrics, including amorphous silicon (a-Si), low-loss silicon nitride (SiN_x), and atomic-layer-deposited aluminum oxide (ALD-Al_2O_3). Studying a-Si and low-loss SiN_x is interesting because these dielectrics have shown unexpected deviations in TLS density compared to other solids [82, 141]. ALD-Al_2O_3 would be interesting because the layer-by-layer controlled deposition allows for the growth of very thin insulating layers (as thin as a few nanometers). This could enable the fabrication of cavities with extremely small electric field volumes ($\sim 1\ \mu m^3$), further enhancing CQED effects with individual TLSs.

I note that there will likely be some challenges when fabricating devices from other materials. To achieve CQED with TLSs, the dielectric volume has to be sufficiently small. This requires relatively thin dielectric layers and careful fabrication. For example, in the case of low-loss SiN_x where the film stress can be larger than 1 GPa [82], this may require special pre-deposition surface treatments for better dielectric adhesion. On the other hand, this will probably not be an issue for ALD-Al_2O_3. Clearly it would be best to use trilayer fabrication techniques. This will allow for *in-situ* film growth, effectively preventing the dielectric from being exposed to air, and reducing contaminants.

9.2.2 Spectroscopy of TLSs in different insulating films

I note that Ustinov's group in 2012 reported on strain-dependent TLS spectroscopy in alumina in JJ tunnel barriers [142]. They tuned the TLSs by varying the strain field and read out a signal via coupling to a qubit, with obvious limitations in materials, spectroscopy range, *etc.* In contrast, In Chapter 6 I introduced a device which was tunable and was able to perform TLS spectroscopy in the CQED limit. I note that if I had made the cavity (resonator) tunable, it might have imposed non-linearity, destroying the possibility of CQED measurements. Instead, I tuned the TLSs in- and out of the cavity resonance, rather than tuning the cavity itself [143]. This was accomplished by exposing the TLSs to an external DC electric field generated by a DC voltage V_{bias} across a capacitor bridge. The TLS-cavity coupling at microwave drive frequencies was observed via S_{21}, similar to the non-tunable devices mentioned previously. By tuning V_{bias}, the "dressed" modes were tuned resulting in "tracks" crossing the cavity resonance. These modes appeared as hyperbolas, as expected from perturbation of TLS double-well potential due to V_{bias}.

The exacts shape of the TLS tracks as well as their width and brightness depend on the TLSs' dipole size, the dipole angle with respect to the external electric field, the lifetime, the tunneling rate and the coupling strength to the cavity. Therefore, this type of measurement can not only reveal specific information for a single TLS, but also provide crucial information about the distribution and statistics of the TLS parameters.

It would be interesting in the future to design, fabricate, measure and analyze

tunable micro-V devices made using other dielectrics. Fabrication of such devices could be more challenging than for the devices suggested in section 9.2.1 because of the need for a capacitor bridge which results in a four-times larger electric field volume. To compensate for this, one could decrease the dielectric thickness compared to a single-capacitor device. Due to the capability of ALD in reliable deposition of thin layers, an experiment with ALD-Al_2O_3 trilayer devices would be interesting. Of course the TLS-cavity coupling could be stronger or weaker in different materials, and the density of TLSs could be higher or lower than in SiN_x, so different dielectric volumes may be needed to resolve individual TLSs.

As described in Chapter 6, I developed a comprehensive simulation code to better understand the spectroscopy results. This program can potentially be applied to any dielectric used in future devices. Also, in order to facilitate extracting the distribution of TLS parameters mentioned above, a 2-dimensional Fourier transform code has been developed [144] to analyze data similar to those of Figs. 6.7, 6.8, 6.9 and 6.11. Nevertheless, it is unclear how much of the analysis can be readily automated.

9.2.3 CQED operation of TLSs

Despite the obvious differences between TLS defects and qubits, a TLS defect with a long enough coherence time could in principle be used as a quantum coherent resource. For example, it has been reported that TLSs within alumina tunnel barriers can operate as quantum memory bits [88]. In this work, Neeley *et al.* transferred

quantum information to a TLS, stored the information in it for a while, and then retrieved it. F. Nori has made similar proposals [145, 146].

As I mentioned in Chapter 5, the longest lived individual TLS that I measured by CQED in SiN_x showed a coherence time of $T_2 = 3.2\,\mu$s, probably limited by the Purcell effect [98]. I note that this value is similar to that of the original transmon coupled to a cavity [64]. The studies described in sections 9.2.1 and 9.2.2 have the potential to discover materials that host TLSs with even longer coherence times.

With a long-lived tunable TLS, it would be interesting to perform a feasibility study of coherent manipulation of individual TLSs via the TLS-cavity coupling. Manipulation of an ensemble of TLSs has been recently performed [83]. As the first step towards this study, one could try tuning a TLS with sufficiently large coherence time to interact strongly with the cavity and prepare it with a desired detuning using the TLS DC-tuning technique described in Chapter 6. Applying a second tone at the TLS transition frequency ω_{TLS} would allow measurement of the TLS spectrum via its effect on the cavity resonance. Next, one can apply microwave pulses at $\omega \simeq \omega_{TLS}$ to see if the quantum state can be manipulated. Relevant properties to measure include Rabi oscillations, the TLS relaxation time T_1, the Ramsey-fringes and spin echo experiments [147].

9.2.4 TiN tunable resonators, and MKIDs

In Chapter 7, I described a method for controlling TiN film properties by RF-induced DC biasing the substrate during reactive sputtering. I reported an un-

usually high kinetic inductance fraction for some deposition conditions. The large kinetic inductance could potentially be used to make DC magnetic field tunable resonators. The field could be created by passing a DC current through the microwave transmission line, significantly changing the effective kinetic inductance of the inductor and shifting the resonance frequency.

Moreover, it is interesting to investigate if the oxygen content in TiN correlates with kinetic inductance. High kinetic inductance is attractive for constructing MKIDs [118]. One could try adding oxygen to the sputtering chamber during reactive sputtering to create higher kinetic inductance films.

9.2.5 *In-situ* ALD-Al_2O_3 trilayer resonators

The resonators described in Chapter 8 for investigating hydrogen diffusion into ALD-grown Al_2O_3 were made using an *ex-situ* trilayer process, meaning that the ALD layer was exposed to air before it was covered by a protective (top) metal layer. The water/hydrogen diffusion process, although believed to be slow, starts immediately after air exposure, and degrades the Q_i of the film. Despite this effect, the measured resonators showed significant dependence of loss to the air-exposed cross-sectional area (edges) set by the capacitor perimeter.

It would be interesting to try to sort out some of the unknowns, including the diffusion rates and the diffusing species. One could try to fabricate and measure devices using an *in-situ* process, where the ALD layer is covered by the top metal layer before it is taken out of the vacuum. It is expected that the loss tangent of

such a device would be smaller than the same device made in an *ex-situ* process. It has been shown that plasma O_2 ALD process has a lower number of entrained defects compared to the H_2O ALD process which was used in Chapter 8 [148]. Also, compared to the *ex-situ* case, the dependence of $\tan\delta_0$ on the perimeter length is expected to be stronger due to a lower TLS spectral density in areas far from capacitor edges.

Bibliography

[1] B. D. Josephson. Possible new effects in superconductive tunnelling. *Physics Letters*, 1(7):251 – 253, 1962.

[2] James Nicol, Sidney Shapiro, and Paul H. Smith. Direct measurement of the superconducting energy gap. *Phys. Rev. Lett.*, 5:461–464, Nov 1960.

[3] P. W. Anderson and J. M. Rowell. Probable observation of the Josephson superconducting tunneling effect. *Phys. Rev. Lett.*, 10:230–232, Mar 1963.

[4] K. K. Likharev and V. K. Semenov. RSFQ logic/memory family: a new Josephson-junction technology for sub-terahertz-clock-frequency digital systems. *IEEE Transactions on Applied Superconductivity*, 1(1):3–28, March 1991.

[5] Kris Gaj, Eby G. Friedman, and Marc J. Feldman. Timing of multi-gigahertz rapid single flux quantum digital circuits. In Eby G. Friedman, editor, *High Performance Clock Distribution Networks*, pages 135–164. Springer US, 1997.

[6] Q. P. Herr and P. Bunyk. Implementation and application of first-in first-out buffers. *IEEE Transactions on Applied Superconductivity*, 13(2):563–566, June 2003.

[7] Bahman Sarabi and Anna Y. Herr. Compensating the RSFQ clock jitter using a FIFO buffer. *Unpublished*.

[8] Bahman Sarabi. Design and Optimization of the RSFQ FIFO Register and Experimental Verification of RSFQ Circuits. Master's thesis, Chalmers University of Technology, Gothenburg, Sweden, 2008.

[9] Quentin P. Herr, Anna Y. Herr, Oliver T. Oberg, and Alexander G. Ioannidis. Ultra-low-power superconductor logic. *Journal of Applied Physics*, 109(10):103903, 2011.

[10] O. A. Mukhanov. Energy-efficient single flux quantum technology. *IEEE Transactions on Applied Superconductivity*, 21(3):760–769, June 2011.

[11] R. Landauer. Irreversibility and heat generation in the computing process. *IBM Journal of Research and Development*, 5(3):183–191, July 1961.

[12] C. H. Bennett. Logical reversibility of computation. *IBM Journal of Research and Development*, 17(6):525–532, Nov 1973.

[13] Michael P. Frank. The physical limits of computing. *Computing in Science & Engineering*, 4(3):16–26, 2002.

[14] V. K. Semenov, G. V. Danilov, and D. V. Averin. Negative-inductance SQUID as the basic element of reversible Josephson-junction circuits. *IEEE Transactions on Applied Superconductivity*, 13(2):938–943, June 2003.

[15] Roman S. Ingarden. Quantum information theory. *Reports on Mathematical Physics*, 10(1):43 – 72, 1976.

[16] Yuri I. Manin. Vychislimoe i nevychislimoe (computable and noncomputable), 1980.

[17] Richard P. Feynman. Simulating physics with computers. *International Journal of Theoretical Physics*, 21(6-7):467–488, 1982.

[18] Göran Wendin and V. S. Shumeiko. Superconducting quantum circuits, qubits and computing. *arXiv preprint cond-mat/0508729*, 4(1), 2005.

[19] Jarryd J. Pla, Kuan Y. Tan, Juan P. Dehollain, Wee H. Lim, John J. L. Morton, David N. Jamieson, Andrew S. Dzurak, and Andrea Morello. A single-atom electron spin qubit in silicon. *Nature*, 489(7417):541–545, 2012.

[20] Bruce E. Kane. A silicon-based nuclear spin quantum computer. *Nature*, 393(6681):133–137, 1998.

[21] Carlo Ottaviani, David Vitali, Maurizio Artoni, Francesco Cataliotti, and Paolo Tombesi. Polarization qubit phase gate in driven atomic media. *Phys. Rev. Lett.*, 90:197902, May 2003.

[22] Andreas Wallraff, David I. Schuster, Alexandre Blais, L. Frunzio, R.-S. Huang, J. Majer, S. Kumar, Steven M. Girvin, and Robert J. Schoelkopf. Strong coupling of a single photon to a superconducting qubit using circuit quantum electrodynamics. *Nature*, 431(7005):162–167, 2004.

[23] John M. Martinis. Superconducting phase qubits. *Quantum Information Processing*, 8(2-3):81–103, 2009.

[24] Tsuyoshi Yamamoto, Yu A. Pashkin, Oleg Astafiev, Yasunobu Nakamura, and Jaw-Shen Tsai. Demonstration of conditional gate operation using superconducting charge qubits. *Nature*, 425(6961):941–944, 2003.

[25] D. P. DiVincenzo and D. Loss. Quantum information is physical. *Superlattices and Microstructures*, 23(34):419 – 432, 1998.

[26] David P. DiVincenzo and Daniel Loss. Quantum computers and quantum coherence. *Journal of Magnetism and Magnetic Materials*, 200(13):202 – 218, 1999.

[27] Lydia L. Sohn, Leo P. Kouwenhoven, and G. Schön. *Mesoscopic Electron Transport: Proceedings of the NATO Advanced Study Institute, 25 June-5 July 1996, Curacao, Netherlands Antilles*, volume 345. Springer, 1997.

[28] David P. DiVincenzo. Topics in quantum computers. *arXiv:cond-mat/9612126v2*, 1996.

[29] David P. DiVincenzo. The physical implementation of quantum computation. *Fortschritte der Physik*, 48(9-11):771–783, 2000.

[30] D. Deutsch. Quantum theory, the church-turing principle and the universal quantum computer. *Proceedings of the Royal Society of London. A: Mathematical and Physical Sciences*, 400(1818):97–117, 1985.

[31] David Deutsch and Richard Jozsa. Rapid solution of problems by quantum computation. *Proceedings of the Royal Society of London. Series A: Mathematical and Physical Sciences*, 439(1907):553–558, 1992.

[32] D. R. Simon. On the power of quantum computation. In *Foundations of Computer Science, 35th Annual Symposium on Proceedings*, pages 116–123, Nov 1994.

[33] P. W. Shor. Algorithms for quantum computation: discrete logarithms and factoring. In *Foundations of Computer Science, 35th Annual Symposium on Proceedings*, pages 124–134, Nov 1994.

[34] Andrew M. Childs and Wim van Dam. Quantum algorithms for algebraic problems. *Rev. Mod. Phys.*, 82:1–52, Jan 2010.

[35] Andrew M. Childs, Richard Cleve, Enrico Deotto, Edward Farhi, Sam Gutmann, and Daniel A. Spielman. Exponential algorithmic speedup by a quantum walk. In *Proceedings of the Thirty-Fifth Annual ACM Symposium on Theory of Computing*, STOC '03, pages 59–68, New York, NY, USA, 2003. ACM.

[36] Gilles Brassard, Peter Hoyer, Michele Mosca, and Alain Tapp. Quantum amplitude amplification and estimation. *arXiv preprint quant-ph/0005055*, 2000.

[37] E. M. Purcell. Spontaneous emission probabilities at radio frequencies. *Physical Review*, 69:681, 1946.

[38] P. Goy, J. M. Raimond, M. Gross, and S. Haroche. Observation of cavity-enhanced single-atom spontaneous emission. *Phys. Rev. Lett.*, 50:1903–1906, Jun 1983.

[39] Serge Haroche and Daniel Kleppner. Cavity quantum electrodynamics. *Phys. Today*, 42(1):24–30, 1989.

[40] E. T. Jaynes and F. W. Cummings. Comparison of quantum and semiclassical radiation theories with application to the beam maser. *Proceedings of the IEEE*, 51(1):89–109, Jan 1963.

[41] Bruce W. Shore and Peter L. Knight. The Jaynes-Cummings Model. *Journal of Modern Optics*, 40(7):1195–1238, 1993.

[42] Ying Wu and Xiaoxue Yang. Strong-coupling theory of periodically driven two-level systems. *Phys. Rev. Lett.*, 98:013601, Jan 2007.

[43] F. W. Cummings. Stimulated emission of radiation in a single mode. *Phys. Rev.*, 140:A1051–A1056, Nov 1965.

[44] Pierre Meystre and Murray Sargent. *Elements of quantum optics*, volume 3. Springer, 1990.

[45] Chung Liang Tang. *Fundamentals of quantum mechanics: for solid state electronics and optics*. Cambridge University Press, 2005.

[46] Christopher Gerry and Peter Knight. *Introductory quantum optics*. Cambridge University Press, 2005.

[47] Marlan O. Scully. *Quantum optics*. Cambridge University Press, 1997.

[48] Mark Fox. *Quantum Optics: An Introduction: An Introduction*, volume 15. Oxford University Press, 2006.

[49] Andrei B. Klimov and Sergei M. Chumakov. *A Group-Theoretical Approach to Quantum Optics*. John Wiley & Sons, 2009.

[50] Jun John Sakurai and San Fu Tuan. *Modern quantum mechanics*, volume 104. Addison-Wesley, Reading, Mass., 1994.

[51] C. A. Blockley, D. F. Walls, and H. Risken. Quantum collapses and revivals in a quantized trap. *Europhysics Letters*, 17(6):509, 1992.

[52] M. D. Lukin and P. R. Hemmer. Quantum entanglement via optical control of atom-atom interactions. *Phys. Rev. Lett.*, 84:2818–2821, Mar 2000.

[53] Richard F. Voss and Richard A. Webb. Macroscopic quantum tunneling in 1-μm Nb Josephson junctions. *Phys. Rev. Lett.*, 47:265–268, Jul 1981.

[54] L. D. Jackel, J. P. Gordon, E. L. Hu, R. E. Howard, L. A. Fetter, D. M. Tennant, R. W. Epworth, and J. Kurkijärvi. Decay of the zero-voltage state in small-area, high-current-density Josephson junctions. *Phys. Rev. Lett.*, 47:697–700, Aug 1981.

[55] W. C. Stewart. Current-voltage characteristics of Josephson junctions. *Applied Physics Letters*, 12(8), 1968.

[56] D. E. McCumber. Effect of ac impedance on dc voltage-current characteristics of superconductor weaklink junctions. *Journal of Applied Physics*, 39(7), 1968.

[57] T. A. Fulton and L. N. Dunkleberger. Lifetime of the zero-voltage state in Josephson tunnel junctions. *Phys. Rev. B*, 9:4760–4768, Jun 1974.

[58] John M. Martinis, Michel H. Devoret, and John Clarke. Energy-level quantization in the zero-voltage state of a current-biased Josephson junction. *Phys. Rev. Lett.*, 55:1543–1546, Oct 1985.

[59] P. Lafarge, P. Joyez, D. Esteve, C. Urbina, and M. H. Devoret. Two-electron quantization of the charge on a superconductor. *Nature*, 365(6445):422–424, 1993.

[60] M. Büttiker. Zero-current persistent potential drop across small-capacitance Josephson junctions. *Phys. Rev. B*, 36:3548–3555, Sep 1987.

[61] T. A. Fulton and G. J. Dolan. Observation of single-electron charging effects in small tunnel junctions. *Phys. Rev. Lett.*, 59:109–112, Jul 1987.

[62] Michel H. Devoret, A. Wallraff, and J. M. Martinis. Superconducting qubits: A short review. *arXiv preprint cond-mat/0411174*, 2004.

[63] Jens Koch, Terri M. Yu, Jay Gambetta, A. A. Houck, D. I. Schuster, J. Majer, Alexandre Blais, M. H. Devoret, S. M. Girvin, and R. J. Schoelkopf. Charge-insensitive qubit design derived from the Cooper pair box. *Phys. Rev. A*, 76:042319, Oct 2007.

[64] A. A. Houck, Jens Koch, M. H. Devoret, S. M. Girvin, and R. J. Schoelkopf. Life after charge noise: recent results with transmon qubits. *Quantum Information Processing*, 8(2-3):105–115, 2009.

[65] I. Chiorescu, Y. Nakamura, C. J. P. M. Harmans, and J. E. Mooij. Coherent quantum dynamics of a superconducting flux qubit. *Science*, 299(5614):1869–1871, 2003.

[66] John M. Martinis, K. B. Cooper, R. McDermott, Matthias Steffen, Markus Ansmann, K. D. Osborn, K. Cicak, Seongshik Oh, D. P. Pappas, R. W. Simmonds, and Clare C. Yu. Decoherence in Josephson qubits from dielectric loss. *Phys. Rev. Lett.*, 95:210503, Nov 2005.

[67] R. W. Simmonds, K. M. Lang, D. A. Hite, S. Nam, D. P. Pappas, and John M. Martinis. Decoherence in Josephson phase qubits from junction resonators. *Phys. Rev. Lett.*, 93:077003, Aug 2004.

[68] Peter K. Day, Henry G. LeDuc, Benjamin A. Mazin, Anastasios Vayonakis, and Jonas Zmuidzinas. A broadband superconducting detector suitable for use in large arrays. *Nature*, 425(6960):817–821, 2003.

[69] P. Flubacher, A. J. Leadbetter, J. A. Morrison, and B. P. Stoicheff. The low-temperature heat capacity and the Raman and Brillouin spectra of vitreous silica. *Journal of Physics and Chemistry of Solids*, 12(1):53 – 65, 1959.

[70] R. C. Zeller and R. O. Pohl. Thermal conductivity and specific heat of non-crystalline solids. *Phys. Rev. B*, 4:2029–2041, Sep 1971.

[71] S. Hunklinger and W. Arnold. Chapter 3 - Ultrasonic properties of glasses at low temperatures. volume 12 of *Physical Acoustics*, pages 155 – 215. Academic Press, 1976.

[72] Erode Subramanian Raja Gopal. *Specific heats at low temperatures*. Heywood London, 1966.

[73] S. Hunklinger, W. Arnold, St. Stein, R. Nava, and K. Dransfeld. Saturation of the ultrasonic absorption in vitreous silica at low temperatures. *Physics Letters A*, 42(3):253 – 255, 1972.

[74] W. A. Phillips. Tunneling states in amorphous solids. *Journal of Low Temperature Physics*, 7(3-4):351–360, 1972.

[75] P. W. Anderson, B. I. Halperin, and C. M. Varma. Anomalous low-temperature thermal properties of glasses and spin glasses. *Philosophical Magazine*, 25(1):1–9, 1972.

[76] Amorphous solids: Low temperature properties, edited by W. A. Phillips. *Topics in Current Physics*, 24, 1981.

[77] C. Enss, S. Hunklinger. *Low-Temperature Physics*, Springer, 2005.

[78] Anatole Abragam. *The principles of nuclear magnetism*. Number 32. Oxford University Press, 1961.

[79] F. Bloch. Nuclear induction. *Phys. Rev.*, 70:460–474, Oct 1946.

[80] Jiansong Gao. *The physics of superconducting microwave resonators*. PhD thesis, California Institute of Technology, 2008.

[81] M. Von Schickfus and S. Hunklinger. Saturation of the dielectric absorption of vitreous silica at low temperatures. *Physics Letters A*, 64(1):144 – 146, 1977.

[82] Hanhee Paik and Kevin D. Osborn. Reducing quantum-regime dielectric loss of silicon nitride for superconducting quantum circuits. *Applied Physics Letters*, 96(7), 2010.

[83] M. S. Khalil, S. Gladchenko, M. J. A. Stoutimore, F. C. Wellstood, A. L. Burin, and K. D. Osborn. Landau-Zener population control and dipole measurement of a two-level-system bath. *Phys. Rev. B*, 90:100201, Sep 2014.

[84] M. Von Schickfus and S. Hunklinger. The dielectric coupling of low-energy excitations in vitreous silica to electromagnetic waves. *Journal of Physics C: Solid State Physics*, 9(16):L439, 1976.

[85] Yoni Shalibo, Yaara Rofe, David Shwa, Felix Zeides, Matthew Neeley, John M. Martinis, and Nadav Katz. Lifetime and coherence of two-level defects in a Josephson junction. *Phys. Rev. Lett.*, 105:177001, Oct 2010.

[86] M. J. A. Stoutimore, M. S. Khalil, C. J. Lobb, and K. D. Osborn. A Josephson junction defect spectrometer for measuring two-level systems. *Applied Physics Letters*, 101(6), 2012.

[87] J. Q. You and Franco Nori. Superconducting circuits and quantum information. *arXiv preprint quant-ph/0601121*, 2006.

[88] Matthew Neeley, M. Ansmann, Radoslaw C. Bialczak, M. Hofheinz, N. Katz, E. Lucero, A. Oconnell, H. Wang, A. N. Cleland, and John M. Martinis. Process tomography of quantum memory in a Josephson-phase qubit coupled to a two-level state. *Nature Physics*, 4(7):523–526, 2008.

[89] Moe S. Khalil. *A study of two-level system defects in dielectric films using superconducting resonators*. PhD thesis, University of Maryland - College Park, 2013.

[90] M. S. Khalil, M. J. A. Stoutimore, F. C. Wellstood, and K. D. Osborn. An analysis method for asymmetric resonator transmission applied to superconducting devices. *Journal of Applied Physics*, 111(5), 2012.

[91] M. J. Collett and C. W. Gardiner. Squeezing of intracavity and traveling-wave light fields produced in parametric amplification. *Phys. Rev. A*, 30:1386–1391, Sep 1984.

[92] Chunqing Deng, Martin Otto, and Adrian Lupascu. An analysis method for transmission measurements of superconducting resonators with applications to quantum-regime dielectric-loss measurements. *Journal of Applied Physics*, 114(5), 2013.

[93] H. Haus and W-P Huang. Coupled-mode theory. *Proceedings of the IEEE*, 79(10):1505–1518, Oct 1991.

[94] H. Haken. *Laser Theory*. Springer, 1970.

[95] C. W. Gardner. Handbook of stochastic methods for physics, chemistry and the natural sciences, 1983.

[96] P. Das, R. Bruyn de Ouboter, and K. W. Taconis. A realization of a London-Clarke-Mendoza type refrigerator. In J.G. Daunt, D.O. Edwards, F.J. Milford, and M. Yaqub, editors, *Low Temperature Physics LT9*, pages 1253–1255. Springer US, 1965.

[97] *FLX-2320-S Stress Measurement System*, Operation Manual.

[98] B. Sarabi, A. N. Ramanayaka, A. L. Burin, F. C. Wellstood, and K. D. Osborn. Cavity quantum electrodynamics of nanoscale two-level systems. *arXiv preprint arXiv:1405.0264v2*, 2014.

[99] Z. Kim, V. Zaretskey, Y. Yoon, J. F. Schneiderman, M. D. Shaw, P. M. Echternach, F. C. Wellstood, and B. S. Palmer. Anomalous avoided level crossings in a Cooper-pair box spectrum. *Phys. Rev. B*, 78:144506, Oct 2008.

[100] J. Lisenfeld, C. Müller, J. H. Cole, P. Bushev, A. Lukashenko, A. Shnirman, and A. V. Ustinov. Measuring the temperature dependence of individual two-level systems by direct coherent control. *Phys. Rev. Lett.*, 105:230504, Dec 2010.

[101] M. S. Khalil, M. J. A. Stoutimore, S. Gladchenko, A. M. Holder, C. B. Musgrave, A. C. Kozen, G. Rubloff, Y. Q. Liu, R. G. Gordon, J. H. Yum, S. K. Banerjee, C. J. Lobb, and K. D. Osborn. Evidence for hydrogen two-level systems in atomic layer deposition oxides. *Applied Physics Letters*, 103(16), 2013.

[102] S. Gladchenko, M. S. Khalil, D. A. Braje, F. C. Wellstood, and K. D. Osborn. Oxygen impurities and deviations from universal glass dielectric loss in silicon nitride. *In prep.*

[103] A. L. Burin. Private communication.

[104] S. Hunklinger and A. K. Raychaudhuri. Thermal and elastic anomalies in glasses at low temperatures. *Prog. Low Temp. Phys.*, 9:267–344, 1986.

[105] J. Classen, C. Enss, C. Bechinger, G. Weiss, and S. Hunklinger. Low frequency acoustic and dielectric measurements on glasses. *Annalen der Physik*, 506(5):315–335, 1994.

[106] A. A. Clerk, M. H. Devoret, S. M. Girvin, Florian Marquardt, and R. J. Schoelkopf. Introduction to quantum noise, measurement, and amplification. *Reviews of Modern Physics*, 82(2):1155, 2010.

[107] Shanhui Fan, Şükrü Ekin Kocabaş, and Jung-Tsung Shen. Input-output formalism for few-photon transport in one-dimensional nanophotonic waveguides coupled to a qubit. *Phys. Rev. A*, 82:063821, Dec 2010.

[108] K. D. Osborn. Private communication.

[109] Lara Faoro and Lev B. Ioffe. Quantum two level systems and kondo-like traps as possible sources of decoherence in superconducting qubits. *Phys. Rev. Lett.*, 96:047001, Jan 2006.

[110] J. L. Black and B. I. Halperin. Spectral diffusion, phonon echoes, and saturation recovery in glasses at low temperatures. *Phys. Rev. B*, 16:2879–2895, Sep 1977.

[111] G. Lindblad. On the generators of quantum dynamical semigroups. *Communications in Mathematical Physics*, 48(2):119–130, 1976.

[112] M. Bhattacharya, K. D. Osborn, and Ari Mizel. Jaynes-Cummings treatment of superconducting resonators with dielectric loss due to two-level systems. *Phys. Rev. B*, 84:104517, Sep 2011.

[113] Lara Faoro and Lev B. Ioffe. Internal loss of superconducting resonators induced by interacting two-level systems. *Phys. Rev. Lett.*, 109:157005, Oct 2012.

[114] Jiushu Shao and Peter Hänggi. Decoherent dynamics of a two-level system coupled to a sea of spins. *Phys. Rev. Lett.*, 81:5710–5713, Dec 1998.

[115] V. G. Karpov, M. I. Klinger, and F. N. Ignatiev. Theory of low-temperature anomalies in thermal-properties of amorphic structures. *Zhurnal Eksperimental'noi i Teoreticheskoi Fiziki*, 84(2):760–775, 1983.

[116] M. R. Vissers, J. Gao, D. S. Wisbey, D. A. Hite, C. C. Tsuei, A. D. Corcoles, M. Steffen, and D. P. Pappas. Low loss superconducting titanium nitride coplanar waveguide resonators. *Applied Physics Letters*, 97(23), 2010.

[117] Josephine B. Chang, Michael R. Vissers, Antonio D. Crcoles, Martin Sandberg, Jiansong Gao, David W. Abraham, Jerry M. Chow, Jay M. Gambetta, Mary Beth Rothwell, George A. Keefe, Matthias Steffen, and David P. Pappas. Improved superconducting qubit coherence using titanium nitride. *Applied Physics Letters*, 103(1), 2013.

[118] Henry G. Leduc, Bruce Bumble, Peter K. Day, Byeong Ho Eom, Jiansong Gao, Sunil Golwala, Benjamin A. Mazin, Sean McHugh, Andrew Merrill, David C. Moore, Omid Noroozian, Anthony D. Turner, and Jonas Zmuidzinas. Titanium nitride films for ultrasensitive microresonator detectors. *Applied Physics Letters*, 97(10), 2010.

[119] S. Ohya, B. Chiaro, A. Megrant, C. Neill, R. Barends, Y. Chen, J. Kelly, D. Low, J. Mutus, P. J. J. O'Malley, P. Roushan, D. Sank, A. Vainsencher, J. Wenner, T. C. White, Y. Yin, B. D. Schultz, C. J. Palmstrøm, B. A. Mazin, A. N. Cleland, and John M. Martinis. Room temperature deposition

of sputtered TiN films for superconducting coplanar waveguide resonators. *Superconductor Science and Technology*, 27(1):015009, 2014.

[120] L. J. Swenson, P. K. Day, B. H. Eom, H. G. Leduc, N. Llombart, C. M. McKenney, O. Noroozian, and J. Zmuidzinas. Operation of a titanium nitride superconducting microresonator detector in the nonlinear regime. *Journal of Applied Physics*, 113(10), 2013.

[121] A. W. Groenland, I. Brunets, A. Boogaard, A. A. I. Aarnink, A. Y. Kovalgin, and J. Schmitz. Thermal and plasma-enhanced oxidation of ALD TiN. 2008.

[122] Yasuhiro Igasaki, Hiroji Mitsuhashi, Koichi Azuma, and Tokio Muto. Structure and electrical properties of titanium nitride films. *Japanese Journal of Applied Physics*, 17(1):85, 1978.

[123] P. Patsalas, C. Charitidis, and S. Logothetidis. The effect of substrate temperature and biasing on the mechanical properties and structure of sputtered titanium nitride thin films. *Surface and Coatings Technology*, 125(13):335 – 340, 2000.

[124] R. Chowdhury, R. D. Vispute, K. Jagannadham, and J. Narayan. Characteristics of titanium nitride films grown by pulsed laser deposition. *Journal of Materials Research*, 11:1458–1469, 6 1996.

[125] Martin Sandberg, Michael R. Vissers, Jeffrey S. Kline, Martin Weides, Jiansong Gao, David S. Wisbey, and David P. Pappas. Etch induced microwave losses in titanium nitride superconducting resonators. *Applied Physics Letters*, 100(26), 2012.

[126] H. M. Jaim, J. A. Aguilar, B. Sarabi, Y. J. Rosen, A. N. Ramanayaka, E. H. Lock, C. J. K. Richardson, and K. D. Osborn. Superconducting TiN films sputtered over a large range of substrate DC bias. *IEEE Transactions on Applied Superconductivity*, PP(99):1–1, 2014 (arXiv:1408.3177v2).

[127] K. Geerlings, S. Shankar, E. Edwards, L. Frunzio, R. J. Schoelkopf, and M. H. Devoret. Improving the quality factor of microwave compact resonators by optimizing their geometrical parameters. *Applied Physics Letters*, 100(19), 2012.

[128] M. J. A. Stoutimore and W. Berk. Private communication.

[129] Joshua Pelleg, L. Z. Zevin, S. Lungo, and N. Croitoru. Reactive-sputter-deposited TiN films on glass substrates. *Thin Solid Films*, 197(12):117 – 128, 1991.

[130] N. Kumar, K. Pourrezaei, B. Lee, and E.C. Douglas. Failure mechanisms of TiN thin film diffusion barriers. *Thin Solid Films*, 164(0):417 – 428, 1988.

[131] B. O. Johansson, J. E. Sundgren, J. E. Greene, A. Rockett, and S. A. Barnett. Growth and properties of single crystal TiN films deposited by reactive magnetron sputtering. *Journal of Vacuum Science & Technology A*, 3(2), 1985.

[132] Michael R. Vissers, Jiansong Gao, Jeffrey S. Kline, Martin Sandberg, Martin P. Weides, David S. Wisbey, and David P. Pappas. Characterization and in-situ monitoring of sub-stoichiometric adjustable superconducting critical temperature titanium nitride growth. *Thin Solid Films*, 548(0):485 – 488, 2013.

[133] J. P. Turneaure, J. Halbritter, and H. A. Schwettman. The surface impedance of superconductors and normal conductors: The Mattis-Bardeen theory. *Journal of Superconductivity*, 4(5):341–355, 1991.

[134] John R. Clem. Inductances and attenuation constant for a thin-film superconducting coplanar waveguide resonator. *Journal of Applied Physics*, 113(1), 2013.

[135] W. A. Phillips. OH in vitreous silica. *Philosophical Magazine Part B*, 43(5):747–764, 1981.

[136] B. Golding and J. E. Graebner. Amorphous solids: Low temperature properties, edited by W. A. Phillips. *Topics in Current Physics*, 24, 1981.

[137] Brage Golding, M. v. Schickfus, S. Hunklinger, and K. Dransfeld. Intrinsic electric dipole moment of tunneling systems in silica glasses. *Phys. Rev. Lett.*, 43:1817–1821, Dec 1979.

[138] W. A. Phillips. Two-level states in glasses. *Reports on Progress in Physics*, 50(12):1657, 1987.

[139] Aaron M. Holder, Kevin D. Osborn, C. J. Lobb, and Charles B. Musgrave. Bulk and surface tunneling hydrogen defects in alumina. *Phys. Rev. Lett.*, 111:065901, Aug 2013.

[140] V. B. Aleskovskii. Chemistry and technology of solids. *Journal of Applied Chemistry of the USSR*, 47(10):2207–2217, 1974.

[141] D. R. Queen, X. Liu, J. Karel, T. H. Metcalf, and F. Hellman. Excess specific heat in evaporated amorphous silicon. *Phys. Rev. Lett.*, 110:135901, Mar 2013.

[142] Grigorij J. Grabovskij, Torben Peichl, Jürgen Lisenfeld, Georg Weiss, and Alexey V. Ustinov. Strain tuning of individual atomic tunneling systems detected by a superconducting qubit. *Science*, 338(6104):232–234, 2012.

[143] B. Sarabi, A. N. Ramanayaka, A. L. Burin, F. C. Wellstood, and K. D. Osborn. Spectroscopy of two-level systems in insulating films. *In prep.*

[144] A. N. Ramanayaka. Private communication.

[145] A. M. Zagoskin, S. Ashhab, J. R. Johansson, and Franco Nori. Quantum two-level systems in Josephson junctions as naturally formed qubits. *Phys. Rev. Lett.*, 97:077001, Aug 2006.

[146] S. Ashhab, J. R. Johansson, and Franco Nori. Rabi oscillations in a qubit coupled to a quantum two-level system. *New Journal of Physics*, 8(6):103, 2006.

[147] D. Vion, A. Aassime, A. Cottet, P. Joyez, H. Pothier, C. Urbina, D. Esteve, and M. H. Devoret. Rabi oscillations, ramsey fringes and spin echoes in an electrical circuit. *Fortschritte der Physik*, 51(4-5):462–468, 2003.

[148] Alexander C. Kozen, Marshall A. Schroeder, Kevin D. Osborn, C. J. Lobb, and Gary W. Rubloff. Examining the role of hydrogen in the electrical performance of in situ fabricated metal-insulator-metal trilayers using an atomic layer deposited Al_2O_3 dielectric. *Applied Physics Letters*, 102(17), 2013.